

Local Structural Studies of Oriented High Temperature
Superconducting Cuprates by Polarized XAFS Spectroscopy

by

Daniel Haskel

A dissertation submitted in partial fulfillment of the requirements for the degree of

Doctor of Philosophy

University of Washington

1998

Approved by _____
(Chairperson of Supervisory Committee)

Program Authorized
to Offer Degree _____

Date _____

In presenting this dissertation in partial fulfillment of the requirements for the Doctoral degree at the University of Washington, I agree that the Library shall make its copies freely available for inspection. I further agree that extensive copying of this dissertation is allowable only for scholarly purposes, consistent with "fair use" as prescribed in the U. S. Copyright Law. Requests for copying or reproduction of this dissertation may be referred to University Microfilms, 1490 Eisenhower Place, P. O. Box 975, Ann Arbor, MI 49106, to whom the author has granted "the right to reproduce and sell (a) copies of the manuscript in microform and/or (b) printed copies of the manuscript made from microform."

Signature_____

Date_____

University of Washington

Abstract

Local Structural Studies of Oriented High Temperature Superconducting Cuprates by Polarized XAFS Spectroscopy

by Daniel Haskel

Chairperson of Supervisory Committee: Professor Edward A. Stern
Department of Physics

Doping (Sr,Ba) in $\text{La}_{2-x}(\text{Sr,Ba})_x\text{CuO}_4$ induces high T_c superconductivity in addition to profound changes in structural, magnetic and normal state electronic properties. The purpose of this thesis is to investigate the structural characteristics accompanying this doping by performing orientation dependent x-ray absorption fine structure (XAFS) measurements on magnetically aligned powders. This type of measurements allowed obtaining critical information at the La/(Sr,Ba) site previously unavailable, as detailed below.

The measurements show that hole carriers introduced with Sr are polaronic in nature as evident from the *two* site configuration found for the O(2) apical neighboring Sr and the lack of temperature dependence in the O(2) distribution, which indicates that the hole states associated with each site are not discrete but rather broader than $k_B T$ up to $T=300\text{K}$. There is a good theoretical argument suggesting each O(2) site is associated with holes being doped into O(1) $2p_{x,y}$ -Cu $3d_{x^2-y^2}$ in-plane and O(2) $2p_z$ -Cu $3d_{3z^2-r^2}$ out-of-plane electronic bands resulting in two different Jahn-Teller distortions of the CuO_6 octahedra neighboring Sr, where the doped holes are peaked. Based on this argument, the predominance of out-of-plane character for the doped holes, as evidenced from the concentration dependence of the relative population of O(2) sites, would imply that theories of high T_c relying only on in-plane character of the doped holes are not complete in describing the properties of these cuprates.

Our measurements showed that all structural phase transitions in $\text{La}_{2-x}(\text{Sr,Ba})_x\text{CuO}_4$ have a significant order-disorder component, as opposed to the purely displacive models found in crystallographic studies. The CuO_6 octahedra are *locally* tilted in the

high-doping, high-temperature phases but fail to order over long range resulting in the average structures of the crystallographic studies. A critical parameter in assessing the plausibility of a density of states (DOS) effect causing T_c suppression in $\text{La}_{1.875}\text{Ba}_{0.125}\text{CuO}_4$, the tilt angle of the CuO_6 octahedra in the LTT phase, was directly measured and found to be *locally* larger than the average value measured by diffraction techniques. This result strengthens the theoretical case for a DOS effect at the basis of T_c suppression at $x = 0.125$.

TABLE OF CONTENTS

List of Figures	v
List of Tables	xi
Chapter 1: Introduction	1
1.1 The phase diagram of $\text{La}_{2-x}\text{Sr}_x\text{CuO}_4$	3
1.2 The LTO and HTT structural modifications	6
1.3 Jahn-Teller distortion of the CuO_6 octahedra	7
1.4 The LTO to HTT structural phase transition and T_c	12
1.5 Deviations from the conventional model	13
1.6 The phase diagram of $\text{La}_{2-x}\text{Ba}_x\text{CuO}_4$	15
1.7 The LTT structural modification	19
1.8 Evidence for an unusual structural ground state in $\text{La}_{2-x}\text{Ba}_x\text{CuO}_4$	19
Chapter 2: XAFS: THEORETICAL CONCEPTS AND DATA ANALYSIS USING THEORETICAL STANDARDS	22
2.1 Theoretical concepts	22
2.1.1 The origin of XAFS	22
2.1.2 The XAFS equation: single scattering	25
2.1.3 Multiple scattering	29
2.1.4 Applications of MS XAFS in this thesis	30
2.2 Data analysis: Isolating and interpreting the XAFS signal	32
2.2.1 Isolating $\chi(k)$	32
2.2.2 Fitting $\chi(k)$ using FEFFIT and theoretical standards from FEFF6	35
2.2.3 Evaluating the correctness of a model	39
Chapter 3: EXPERIMENTAL SETUP FOR TRANSMISSION XAFS MEASUREMENTS	42
3.1 The measurement of $\mu(E)$	42

3.2	The double crystal monochromator and vertical slits	43
3.3	The ion chambers	45
3.4	Polarization dependent measurements	47
3.5	Low temperature measurements	49
Chapter 4: Sample preparation and characterization for polarized XAFS measurements		50
4.1	Magnetically aligned powder	50
4.2	The $\text{La}_{2-x}\text{Sr}_x\text{CuO}_4$ system	51
4.2.1	Determining degree of alignment with x-ray diffraction	55
4.2.2	Electron diffraction study of $\text{La}_{1.85}\text{Sr}_{0.15}\text{CuO}_4$	59
4.3	The $\text{La}_{2-x}\text{Ba}_x\text{CuO}_4$ system	65
4.3.1	Fitting of x-ray powder diffraction patterns	68
4.3.2	Magnetic measurements of superconducting transition temperatures	70
4.3.3	Obtaining very fine powder in $\text{La}_{2-x}\text{Ba}_x\text{CuO}_4$	73
4.4	Why not single crystals?	78
Chapter 5: XAFS MEASUREMENTS OF $\text{La}_{2-x}\text{Sr}_x\text{CuO}_4$: ANALYSIS AND RESULTS		81
5.1	The nature of the Sr-induced LTO to HTT structural phase transition	81
5.1.1	Experimental results	81
5.1.2	Discussion	102
5.2	The nature of the temperature-induced LTO to HTT structural phase transition	104
5.2.1	Experimental results	104
5.2.2	Discussion	114
5.3	Sr induced distortions in $\text{La}_{2-x}\text{Sr}_x\text{CuO}_4$	120
5.3.1	Experimental results	120
5.3.2	On Sr substitution at the La site	125
5.3.3	On the nature of the Sr-O(1) distortions	128
5.3.4	Implications of the Sr-O(1) distortions	130
5.3.5	The O(2) apical oxygen to Sr: experimental results	132

5.3.6	The O(2) apical oxygen to Sr: discussion	138
Chapter 6:	XAFS MEASUREMENTS OF $\text{La}_{2-x}\text{Ba}_x\text{CuO}_4$: ANALYSIS AND RESULTS	144
6.1	La K -edge measurements	144
6.1.1	Experimental results	144
6.1.2	Discussion	152
6.2	Ba K -edge measurements	160
6.2.1	Experimental results	160
6.2.2	Discussion	164
6.3	Cu K -edge measurements	178
6.3.1	Experimental results	178
6.3.2	Discussion	189
6.3.3	Measuring the CuO_6 octahedra tilt angle	198
6.3.4	Comparing <i>local</i> and <i>average</i> buckling angles	205
6.3.5	On the relation between buckling and tilt angles	205
6.3.6	Implications for T_c suppression at $x = 0.125$	206
6.3.7	On the nature of the temperature-induced LTT \rightarrow LTO \rightarrow HTT structural phase transitions	208
Chapter 7:	Summary and conclusions	212
7.1	On the nature of the dopant and temperature induced structural phase transitions in $\text{La}_{2-x}(\text{Sr},\text{Ba})_x\text{CuO}_4$	212
7.1.1	The $\text{La}_{2-x}\text{Sr}_x\text{CuO}_4$ system: Dopant and temperature induced LTO \rightarrow HTT structural transitions	212
7.1.2	The $\text{La}_{2-x}\text{Ba}_x\text{CuO}_4$ system: temperature induced LTT \rightarrow LTO \rightarrow HTT structural phase transitions	215
7.2	On the nature of local distortions around (Sr, Ba) dopant atoms . . .	218
7.2.1	Polaronic nature of the Sr induced holes in $\text{La}_{2-x}\text{Sr}_x\text{CuO}_4$. .	219
7.2.2	On the effect of (Sr, Ba) distortions on the magnetic properties	222
7.3	On the origin of T_c suppression in $\text{La}_{2-x}\text{Ba}_x\text{CuO}_4$ with $x = 0.125$. . .	223
Bibliography		225

Appendix A: Measuring buckling angles with XAFS	237
Appendix B: Angular averaging in XAFS	248
Appendix C: XAFS Debye Waller factors	256

LIST OF FIGURES

1.1	Phase diagram of $\text{La}_{2-x}\text{Sr}_x\text{CuO}_4$	4
1.2	LTO and HTT structural modifications	8
1.3	Electronic energy levels of Cu^{+2} ion in octahedral environment and the Jahn-Teller effect	11
1.4	Phase diagram of $\text{La}_{2-x}\text{Ba}_x\text{CuO}_4$	16
1.5	The LTT structural modification	20
2.1	Schematic energy diagram of the photo-absorption process	23
2.2	Schematics of the origin of XAFS	24
2.3	Multiple scattering in solving structural issues	31
3.1	Experimental transmission setup	42
4.1	La and Sr K -edges in $\text{La}_{1.85}\text{Sr}_{0.15}\text{CuO}_4$; polarized absorption raw data	54
4.2	Schematics of the procedure for magnetic alignment	56
4.3	Determining degree of alignment using x-ray diffraction	57
4.4	X-ray powder diffraction before and after alignment	58
4.5	Schematic view of the TEM used for the electron diffraction experiments	60
4.6	Schematics of electron diffraction pattern formation in the TEM	62
4.7	Electron diffraction patterns of $\text{La}_{1.85}\text{Sr}_{0.15}\text{CuO}_4$ in the LTO and HTT phases	64
4.8	LTO superstructure reflections vanishing in HTT phase	66
4.9	Camera length calibration of the TEM	67
4.10	Fitting of the x-ray powder diffraction pattern of $\text{La}_{1.85}\text{Ba}_{0.15}\text{CuO}_4$	69
4.11	Zero field cooled magnetic susceptibility of $\text{La}_{2-x}\text{Ba}_x\text{CuO}_4$	70
4.12	M/H curves for $\text{La}_{2-x}\text{Ba}_x\text{CuO}_4$ system	73
4.13	SEM picture of $\text{La}_{1.875}\text{Ba}_{0.125}\text{CuO}_4$ with typical grain size $2 - 5\mu\text{m}$	75
4.14	Comparison of degree of alignment by sieving and sedimentation methods in $\text{La}_{1.875}\text{Ba}_{0.125}\text{CuO}_4$	77

4.15	Examples of La, Ba, Cu K -edge polarized raw absorption data in $\text{La}_{1.875}\text{Ba}_{0.125}\text{CuO}_4$	79
5.1	LTO modification of $\text{La}_{2-x}\text{Sr}_x\text{CuO}_4$ and comparison of interatomic distances in LTO and HTT phases	83
5.2	La K -edge in $\text{La}_{1.8}\text{Sr}_{0.2}\text{CuO}_4$ at $T=20\text{K}$; polarized absorption raw data	85
5.3	La K -edge in $\text{La}_{1.8}\text{Sr}_{0.2}\text{CuO}_4$: polarized $\chi(k)$ and reproducibility . . .	86
5.4	Effect of Sr substitution in fourth shell on backscattering amplitudes and phases of first and third shells	91
5.5	Fit results: La K -edge, $x = 0.075$, $T=20\text{K}$, $\hat{e} \parallel \hat{b}$	92
5.6	Fit results: La K -edge, $x = 0.075$, $T=20\text{K}$, $\hat{e} \perp \hat{b}$	93
5.7	Fit results: La K -edge, $x = 0.20$, $T=20\text{K}$, $\hat{e} \parallel \hat{b}$	94
5.8	Fit results: La K -edge, $x = 0.20$, $T=20\text{K}$, $\hat{e} \perp \hat{b}$	95
5.9	Fit results for La-O(2) and planar La-La distances as function of x in $\text{La}_{2-x}\text{Sr}_x\text{CuO}_4$ at $T=20\text{K}$	97
5.10	Fit results for La-O(1) distances as function of x in $\text{La}_{2-x}\text{Sr}_x\text{CuO}_4$ at $T=20\text{K}$	98
5.11	Comparison of fit results using LTO and HTT models for La K -edge, $x = 0.3$, $T=20\text{K}$, $\hat{e} \perp \hat{b}$ in $\text{La}_{2-x}\text{Sr}_x\text{CuO}_4$	101
5.12	Temperature dependence of $\chi(k)$ and $\tilde{\chi}(r)$ of $\text{La}_{1.85}\text{Sr}_{0.15}\text{CuO}_4$	106
5.13	Fit results: La K -edge, $x = 0.15$, $T=20\text{K}$, $\hat{e} \parallel \hat{b}$	107
5.14	Fit results: La K -edge, $x = 0.15$, $T=20\text{K}$, $\hat{e} \perp \hat{b}$	108
5.15	Fit results: La K -edge, $x = 0.15$, $T=285\text{K}$, both polarizations	109
5.16	Fit results for La-O(2) and planar La-La distances for $x = 0.15$ at temperatures in both LTO and HTT phases	110
5.17	Fit results for La-O(1) distances for $x = 0.15$ at temperatures in both LTO and HTT phases	111
5.18	XAFS Debye-Waller factors of La-O, La-Cu and La-La distances for $x = 0.15$ at several temperatures together with fits to Einstein model	112
5.19	Local \hat{b} lattice constant measured for $x = 0.15$ versus temperature . .	113
5.20	Comparison of fits to $x = 0.15$ at $T=285\text{K}$ using both LTO and HTT models	115

5.21	Comparison of planar La-La distances as function of x and temperature in both LTO and HTT phases of $\text{La}_{2-x}\text{Sr}_x\text{CuO}_4$	116
5.22	Effect of LTO versus hypothetical LTT tilts on planar La-O(2) distances in $\text{La}_{2-x}\text{Sr}_x\text{CuO}_4$	118
5.23	Sr K edge in $\text{La}_{1.9}\text{Sr}_{0.1}\text{CuO}_4$ at $T=17\text{K}$: raw absorption data	121
5.24	Sr K -edge $\chi(k)$ and reproducibility scans for $\text{La}_{1.9}\text{Sr}_{0.1}\text{CuO}_4$ at $T=17\text{K}$, both polarizations	122
5.25	Comparison of theoretical mean free path for Sr and La K -edges in $\text{La}_{2-x}\text{Sr}_x\text{CuO}_4$	123
5.26	Fit results: Sr K -edge, $x = 0.1$, $T=17\text{K}$, $\hat{e} \parallel \hat{b}$	126
5.27	Fit results: Sr K -edge, $x = 0.1$, $T=17\text{K}$, $\hat{e} \perp \hat{b}$	127
5.28	Isolated Sr-O signal for $x = 0.1$, \hat{b} -polarization, $T=17\text{K}$	129
5.29	Fit results for Sr-O(1) and planar Sr-O(2) distances as function of x , $T \approx 20\text{K}$	131
5.30	FEFF6 comparison of Sr-O(2)-Cu SS and MS signals with and without O(2) apical	134
5.31	Schematic representation of SS and MS paths in Sr-O(2)-Cu	136
5.32	Fits to isolated Sr-O(2) apical signal for $x = 0.075$ and $x = 0.2$ at $T=20\text{K}$	137
5.33	Distance and mean square disorder fit results using single site model for O(2) apical	139
5.34	Distances and population of site closer to Sr obtained in fits to isolated Sr-O(2) signal using two sites model	140
5.35	Schematic representation of pattern of atomic displacements induced by Sr substitution	143
6.1	LTT structural modification and bond lengths	146
6.2	La K -edge in $\text{La}_{2-x}\text{Ba}_x\text{CuO}_4$ with $x = 0.125$, $T=10\text{K}$, \hat{e} -polarization: raw absorption data	147
6.3	La K -edge $\chi(k)$ data and reproducibility scans for $\text{La}_{1.875}\text{Ba}_{0.125}\text{CuO}_4$ at $T=10\text{K}$ in both polarizations	148
6.4	Fit results: La K -edge, $x = 0.125$, $T=10\text{K}$, $\hat{e} \parallel \hat{c}$	153
6.5	Fit results: La K -edge, $x = 0.125$, $T=10\text{K}$, $\hat{e} \perp \hat{c}$	154

6.6	Fit results: La K -edge, $x = 0.15$, $T=10\text{K}$, $\hat{e} \parallel \hat{c}$	155
6.7	Fit results: La K -edge, $x = 0.15$, $T=10\text{K}$, $\hat{e} \perp \hat{c}$	156
6.8	Comparison of Sr doped ($x = 0.075$, $T=20\text{K}$) and Ba-doped ($x = 0.125$, $T=10\text{K}$) La K -edge \hat{c} -polarized data and FEF6 calculations	159
6.9	Ba K -edge in $\text{La}_{1.875}\text{Ba}_{0.125}\text{CuO}_4$ at $T=10\text{K}$, both polarizations: raw absorption data	161
6.10	Ba K -edge for $x = 0.125$ and $x = 0.15$ at $T=10\text{K}$: $\chi(k)$ and reproducibility scans, both polarizations	162
6.11	Comparison between La and Ba K -edges $\chi(k)$ for $x = 0.125, 0.15$ in $\text{La}_{2-x}\text{Ba}_x\text{CuO}_4$; both polarizations	163
6.12	Fit results: Ba K -edge, $x = 0.125$, $T=10\text{K}$, $\hat{e} \parallel \hat{c}$	165
6.13	Fit results: Ba K -edge, $x = 0.125$, $T=10\text{K}$, $\hat{e} \perp \hat{c}$	166
6.14	Fit results: Ba K -edge, $x = 0.15$, $T=10\text{K}$, $\hat{e} \parallel \hat{c}$	167
6.15	Fit results: Ba K -edge, $x = 0.15$, $T=10\text{K}$, $\hat{e} \perp \hat{c}$	168
6.16	Magnitude of local atomic displacements induced by Ba substitution	171
6.17	Schematic representation of planar La-O(2) and La-La configurations in LTT, LTO, and HTT phases	175
6.18	Schematic representation of O(2) and correlated La/Ba in-plane atomic displacements found in Ba K -edge fits	177
6.19	Pattern of atomic displacements induced by Ba substitution	179
6.20	Cu K -edge in $\text{La}_{1.875}\text{Ba}_{0.125}\text{CuO}_4$ at $T=10\text{K}$. Raw absorption data, both polarizations	180
6.21	Cu K -edge, $x = 0.125$, $T=10\text{K}$: $\chi(k)$ data and reproducibility scans, both polarizations	181
6.22	Fit results: Cu K -edge, $x = 0.125$, $T=10\text{K}$, $\hat{e} \parallel \hat{c}$	185
6.23	Fit results: Cu K -edge, $x = 0.125$, $T=10\text{K}$, $\hat{e} \perp \hat{c}$	186
6.24	Fit results: Cu K -edge, $x = 0.15$, $T=10\text{K}$, $\hat{e} \parallel \hat{c}$	187
6.25	Fit results: Cu K -edge, $x = 0.15$, $T=10\text{K}$, $\hat{e} \perp \hat{c}$	188
6.26	Fit results for Cu-O(1), Cu-O(2) and Cu-Cu distances for $x = 0.125, 0.15$ at several temperatures	190
6.27	Fit results for Cu-La (SS) and Cu-O(2)-La (MS) distances for $x = 0.125$ at several temperatures	191

6.28	Fit results for mean squared disorder in Cu-O(1), Cu-O(2) and Cu-Cu distances at several temperatures together with fits to Einstein model	192
6.29	Fit results for mean square disorder in Cu-La and Cu-O(2)-La distances at several temperatures together with fits to Einstein model	193
6.30	\hat{c} -axis atomic environment of Cu atoms nearby La/Ba atoms	197
6.31	Schematic representation of buckling angles	199
6.32	Fit results for buckling angles of Cu-O(1)-Cu and Cu-O(2)-La configurations	202
6.33	Comparison of fits with buckling angles set to average structure values and varied	203
6.34	$\tilde{\chi}(r)$ of La K -edge data for $x = 0.125, 0.15$, $\hat{e} \perp \hat{c}$, for temperatures across LTT, LTO and HTT phases	210
6.35	$\tilde{\chi}(r)$ of La K -edge simulated using FEFF6 for LTT and LTO phases of $\text{La}_{2-x}\text{Ba}_x\text{CuO}_4$	211
7.1	Schematic representation of thermally induced order-disorder in the structural phase transitions of $\text{La}_{2-x}\text{Ba}_x\text{CuO}_4$	217
7.2	Schematic representation of the two Jahn-Teller polarons associated with holes doped by Sr in $\text{La}_{2-x}\text{Sr}_x\text{CuO}_4$	221
A.1	Nearly collinear multiple scattering paths	238
A.2	Parameterization of path leg-length as function of buckling angle . . .	240
A.3	<i>Paths.dat</i> file corresponding to $\theta_{\text{avg}} = 5.9^\circ$	240
A.4	<i>Paths.dat</i> file corresponding to $\theta_{\text{avg}} = 14.0^\circ$	241
A.5	Buckling angle parameterization of effective scattering amplitude for $k = 8 \text{ \AA}^{-1}$	242
A.6	k -dependent coefficients used in buckling angle parameterization of effective scattering amplitude	243
A.7	Relevant variables in <i>feffit.inp</i> used in fitting buckling angles	244
A.8	Relevant PATH paragraphs in <i>feffit.inp</i> used in fitting buckling angles	245
A.9	Dependence of effective scattering amplitude on buckling angle	246
A.10	Dependence of effective scattering phase on buckling angle	247

B.1	Relative orientation of bonds and electric field used in angular averaging of XAFS	253
C.1	Schematic representation of collinear MS paths for which σ^2 relations are derived	256
C.2	Average versus instantaneous positions in MS paths	257
C.3	XAFS σ^2 versus disorder about lattice sites	259

LIST OF TABLES

1.1	Lattice parameters and atomic coordinates for the LTO phase of La_2CuO_4 at 10K	9
1.2	Lattice parameters and atomic coordinates for $\text{La}_{1.85}\text{Sr}_{0.15}\text{CuO}_4$ at T=300K, HTT phase	9
1.3	Comparison of basal plane and apical distances of CuO_6 and NiO_6 octahedra in La_2CuO_4 and La_2NiO_4	12
1.4	Lattice parameters and atomic coordinates for $\text{La}_{2-x}\text{Ba}_x\text{CuO}_4$ in the LTT phase	19
3.1	Ion chamber gases mixtures used for the different energy edges	47
4.1	First five fundamental reflections allowed for both LTO and HTT phases in $\langle -110 \rangle$ zone axis	63
4.2	Experimental versus theoretical reciprocal lattice vector ratios for first five fundamental reflections	63
4.3	Experimental versus theoretical angles formed by reciprocal lattice vectors for first five fundamental reflections	65
4.4	Lattice parameters of $\text{La}_{2-x}\text{Ba}_x\text{CuO}_4$ with $x = 0.125, 0.15$ at T=300K obtained by fittings of powder x-ray diffraction	69
4.5	Bulk onset values for T_c 's of $\text{La}_{2-x}\text{Ba}_x\text{CuO}_4$ with $x = 0.125, 0.15$ from magnetic susceptibility measurements	71
4.6	Desired sample thickness for $\text{La}_{1.875}\text{Ba}_{0.125}\text{CuO}_4$ at all La, Ba and Cu K -edges	76
5.1	Background removal parameters for La K -edge in $\text{La}_{2-x}\text{Sr}_x\text{CuO}_4$, \hat{b} -polarization	85
5.2	Theoretical SS paths used in fitting La K -edge data in $\text{La}_{2-x}\text{Sr}_x\text{CuO}_4$	88
5.3	Theoretical MS paths used in fitting La K -edge data in $\text{La}_{2-x}\text{Sr}_x\text{CuO}_4$	89

5.4	Fourier transform parameters and fitting regions for La K -edge in $\text{La}_{2-x}\text{Sr}_x\text{CuO}_4$	96
5.5	XAFS σ^2 and quality of fits factors obtained for fits to La K -edge data in $\text{La}_{2-x}\text{Sr}_x\text{CuO}_4$ as function of x , $T=20\text{K}$	99
5.6	XAFS σ^2 and fit quality factors for HTT model of La K -edge in $\text{La}_{2-x}\text{Sr}_x\text{CuO}_4$, $x = 0.3$, $T=20\text{K}$	100
5.7	Fit quality factors for La K -edge fits of $\text{La}_{1.85}\text{Sr}_{0.15}\text{CuO}_4$ at several temperatures	111
5.8	Fit quality factors and σ^2 for HTT model of La K -edge, $x = 0.15$ in $\text{La}_{2-x}\text{Sr}_x\text{CuO}_4$, $T=285\text{K}$	114
5.9	La-O distances for $\langle 100 \rangle$ and hypothetical $\langle 101 \rangle$ tilts for $x = 0.075$ in $\text{La}_{2-x}\text{Sr}_x\text{CuO}_4$ at 20K	119
5.10	Background removal parameters for Sr K -edge in $\text{La}_{2-x}\text{Sr}_x\text{CuO}_4$, $\hat{a}\hat{c}$ -polarization	122
5.11	Additional theoretical paths required in fitting Sr K -edge data in $\text{La}_{2-x}\text{Sr}_x\text{CuO}_4$	124
5.12	Fit results to Sr-O(2)-Cu SS and MS signal with and without O(2) apical to Sr	133
6.1	Background removal parameters for La K -edge in $\text{La}_{2-x}\text{Ba}_x\text{CuO}_4$, \hat{c} -polarization	148
6.2	Theoretical SS paths used in fitting La K -edge data in $\text{La}_{2-x}\text{Ba}_x\text{CuO}_4$	150
6.3	Theoretical MS paths used in fitting La K -edge data in $\text{La}_{2-x}\text{Ba}_x\text{CuO}_4$	151
6.4	Fourier transform parameters and fitting regions for La K -edge fits in $\text{La}_{2-x}\text{Ba}_x\text{CuO}_4$	152
6.5	Fit results for interatomic distances at La K -edge, $x = 0.125, 0.15$, $T=10\text{K}$	157
6.6	Fit results for XAFS σ^2 at La K -edge, $x = 0.125, 0.15$, $T=10\text{K}$	158
6.7	Background removal parameters for Ba K -edge in $\text{La}_{2-x}\text{Ba}_x\text{CuO}_4$, both polarizations	162
6.8	Fit results for interatomic distances at Ba K -edge in $\text{La}_{2-x}\text{Ba}_x\text{CuO}_4$ with $x = 0.125, 0.15$ at $T=10\text{K}$	169

6.9	Fit results for XAFS σ^2 at Ba K -edge in $\text{La}_{2-x}\text{Ba}_x\text{CuO}_4$ with $x = 0.125, 0.15$ at $T=10\text{K}$	170
6.10	Background removal parameters for Cu K -edge in $\text{La}_{2-x}\text{Ba}_x\text{CuO}_4$, both polarizations	178
6.11	Theoretical SS paths used in fitting Cu K -edge in $\text{La}_{2-x}\text{Ba}_x\text{CuO}_4$	182
6.12	Theoretical MS paths used in fitting Cu K -edge in $\text{La}_{2-x}\text{Ba}_x\text{CuO}_4$	183
6.13	Fourier transform parameters, fitting regions and quality of fit factors for Cu K -edge fits in $\text{La}_{2-x}\text{Ba}_x\text{CuO}_4$	184
6.14	Comparison of fit results to Cu-O(1)-Cu and Cu-O(2)-La MS paths with different models for buckling angles	204
A.1	First leg length r_1 as function of θ and its deviation from the average structure, Δr_1	239

ACKNOWLEDGMENTS

I would like to thank Edward Stern for having taught me so much about so many different aspects of Physics and for having guided me during these years in a way that allowed me to complete my thesis research but yet to explore other research interests.

I thank Bruce Ravel and Matthew Newville who contributed so much to my knowledge and experience here. I would like to thank Anatoly Frenkel, Victor Polinger, Hanan Shechter, Shelly Kelly, John Rehr, Yitzhak Yacoby, Joseph Budnick, Steve Heald and John Tranquada for many important discussions. I learned a lot from all of you.

I thank Mehmet Sarikaya and Maoxu Qian for introducing me to the world of transmission electron microscopy and for the productive collaboration. Many thanks to D. G. Hinks, A. W. Mitchell and Jim Jorgensen for providing the $\text{La}_{2-x}\text{Sr}_x\text{CuO}_4$ ceramic samples used in the measurements. I thank Fatih Dogan for providing the $\text{La}_{2-x}\text{Ba}_x\text{CuO}_4$ ceramic samples and for teaching me some basics of ceramic processing. A special thanks to Mas Suenaga for letting me use the superconducting magnet to align the powders and Frank Perez for technical help and the good coffee. To Arnie Moodenbaugh for the SQUID magnetization measurements on $\text{La}_{2-x}\text{Ba}_x\text{CuO}_4$ and useful discussions.

I benefited greatly from interactions with other faculty/students at UW: Julie Cross, Kyungha Kim, Bob Ingalls, Oscar Vilches, Alexei Ankudinov, Ana Poiarkova.

Finally I thank my family. To Ofelie and Chame for their encouragement throughout these years. To my mom Miriam and my dad Elias for teaching me to search for the best in myself, to always move forward and not to be afraid. Thanks for being there for me, always. To my brothers Carlos, Ariel and Yoel: thank you for being the best brothers one can have. To my wife Ili, all these years were so much better because I had you. To our son Ilan, whose arrival made my last year as a graduate student the best of all. I love you both and this thesis is dedicated to you.

Chapter 1

INTRODUCTION

Since the discovery in 1986 of high T_c superconductivity in $\text{La}_{2-x}(\text{Ba},\text{Sr})_x\text{CuO}_4$ by Bednorz and Müller [1] a tremendous amount of theoretical and experimental effort has been devoted to understanding the nature of the superconducting pairing mechanism. Even though superconducting transition temperatures as high as $T_c \sim 130\text{K}$ have been achieved since then in $\text{Hg}_{1-x}\text{Pb}_x\text{Ba}_2\text{Ca}_2\text{Cu}_3\text{O}_8$ and $\text{Tl}_2\text{Ca}_2\text{Ba}_2\text{Cu}_3\text{O}_{10}$ compounds [2–6], the nature of the basic interaction leading to pairing is still an open question.

At present, several leading theories of high T_c superconductivity exist. These invoke (i) pure magnetic interactions as *spin-fluctuation exchange* between planar quasiparticles [7]; (ii) magnetic induced interactions due to spatial arrangements of the doped holes into 1-D metallic *stripes* embedded in antiferromagnetic insulating environment (local separation of spin and charge) [8]; (iii) a combination of magnetic and coulombic interactions like in the *resonating valence bond* (RVB) state, a mixture of singlet pairings of holes on different sites whose excitations (boson holes) can undergo Bose condensation [9, 10] or as in the $t - J - \epsilon$ model [11]; (iv) lattice involvement such as in *electron-phonon coupling* [12, 13] and *polaron* mediated superconductivity. [14–16]

The knowledge of the structure of the high T_c superconductors is basic to a fundamental understanding of their pairing mechanism, as all the theories listed above rely on knowledge of the interatomic distances and structural symmetries. The aim of the work presented in this thesis is to accurately measure the underlying structure in a way that should provide important and unique information. As the superconducting coherence length (pair size) in the high T_c cuprates is very short [17, 18], on the order of $10 - 20 \text{ \AA}$, the *local* structure on a similar scale length is of primary importance in determining the superconducting properties. As an example, nanophase separation or local structural inhomogeneities, which could have profound effects on the

superconducting properties, can go undetected by the more conventional diffraction techniques. This is due to diffraction requiring a coherence length of several tens of angstroms in order to be sharp enough to give a Bragg peak, resulting in a measurement of the *average* atomic positions over the same length scale. The technique employed here, x-ray absorption fine structure (XAFS), determines *local* structure up to a length of $\sim 10 \text{ \AA}$ (see chapter 2) and hence is ideal for the problem at hand. Average structure (diffraction) and local structure (XAFS) are the same if no disorder is present. However, if disorder on a local scale is present, the average structure is not the same as the actual local structure. As I described in reference 19 and further detailed here, the short range local structure revealed a different underlying atomic arrangement than commonly assumed, indicating disorder is present.

A related aspect that has been thoroughly addressed in this thesis is the role played by the dopant atoms in determining the structural properties. In $\text{La}_{2-x}(\text{Ba},\text{Sr})_x\text{CuO}_4$, Sr and Ba introduce hole carriers into the otherwise insulating La_2CuO_4 parent compound leading to superconductivity for $x \gtrsim 0.05$ [20]. It is being assumed in most of the current theories that the dopant atoms only change the hole occupation but are otherwise passive players in the phenomenon of high T_c . The mere presence of the dopant atoms destroys the perfect periodicity of the crystal adding extra difficulty to an already hard theoretical problem. But what mostly contributed to the absence of an appropriate treatment of the effect of the dopant atoms is the lack of experimental information on their actual atomic environments. Since these dopant atoms reside at the same crystallographic site as the La atoms, diffraction techniques measure a Sr/Ba contribution which is only a few percent of the total signal at the (Sr,Ba)/La site, making it impossible to obtain significant information on the actual environment of the dopant atoms.

XAFS can selectively tune to the dopant atoms and hence isolate their contribution from that of the majority host La atoms. In this way the local atomic arrangement about the Sr and Ba atoms is determined leading to very valuable information for addressing their role in high T_c and in determining the ground state structural properties. I described some of the results on the Sr atomic environment at low Sr content in reference 21. Those, together with newer results, are described in this thesis.

In what follows relevant information on the structural and superconducting properties of the $\text{La}_{2-x}\text{Sr}_x\text{CuO}_4$ and $\text{La}_{2-x}\text{Ba}_x\text{CuO}_4$ systems is presented, which should

help identify the nature of the questions at hand.

1.1 The phase diagram of $\text{La}_{2-x}\text{Sr}_x\text{CuO}_4$

Figure 1.1 shows the phase diagram of $\text{La}_{2-x}\text{Sr}_x\text{CuO}_4$ in the doping-temperature plane. It consists of a very rich mixture of magnetic, electronic and structural phases. The parent compound, La_2CuO_4 , shows 3D antiferromagnetic (AF) ordering of the Cu^{+2} magnetic moments [22], with a Néel temperature highly sensitive to oxygen stoichiometry, typically $T_N \sim 200-300\text{K}$. Strong 2D dynamic AF correlations persist above T_N in the CuO_2 planes [22, 23], with instantaneous correlation lengths as long as 200Å . Doping with Sr destroys the AF long range order for $x \gtrsim 0.02$, but spin-spin 2D AF correlations between the Cu^{+2} moments in the CuO_2 planes persist for higher Sr concentrations, even in the superconducting state. [24] These correlations are dynamical, as in pure La_2CuO_4 above T_N , with the correlation length decreasing from $\sim 35\text{Å}$ to $\sim 8\text{Å}$ in going from $x = 0.02$ to $x = 0.18$. [24] The size of the magnetic moment at the Cu^{+2} sites was found to be nearly independent of doping, so the doping destroys the long range AF $\text{Cu}^{+2}\text{-Cu}^{+2}$ spin correlations but doesn't change the Cu^{+2} magnetic moment itself. [24] The dependence of the 2D AF correlation length, ζ_{2D} , on Sr doping relates quite well to the average distance between holes, $\zeta_{2D} \sim 3.8/\sqrt{x}\text{Å}$ (3.8Å being the Cu-Cu in-plane interatomic distance), assuming the holes are doped predominantly into the CuO_2 planes (since each Sr introduces one hole, x is the concentration of holes per Cu site).

As shown by polarized x-ray absorption near edge structure (XANES) measurements [25, 26], a significant fraction of the doped holes in $\text{La}_{2-x}\text{Sr}_x\text{CuO}_4$ have $O(1)$ $2p_{x,y}\text{-Cu } 3d_{x^2-y^2}$ in-plane orbital character. Numerical solutions of extended Hubbard Hamiltonians [27] show about 70% weight of these holes being on oxygen derived planar orbitals. Following this observation, Aharony *et. al* [28] proposed that the extra spin associated with a hole localized on a planar O site introduces a local *ferromagnetic* (F) exchange coupling between the Cu spins, resulting in frustration of the 3D ordering of the parent compound and the decrease in ζ_{2D} with Sr content.

Since the AF and F exchange coupling results from overlap integrals over Cu-O and Cu-Cu in-plane distances, it is of importance to determine the local atomic configuration of the Cu-O planes as a function of Sr doping. In particular, since the loss of AF correlations is so closely related to Sr content, it is of interest to look at the structure of the CuO_2 planes in the vicinity of the Sr atoms, as the hole wave function

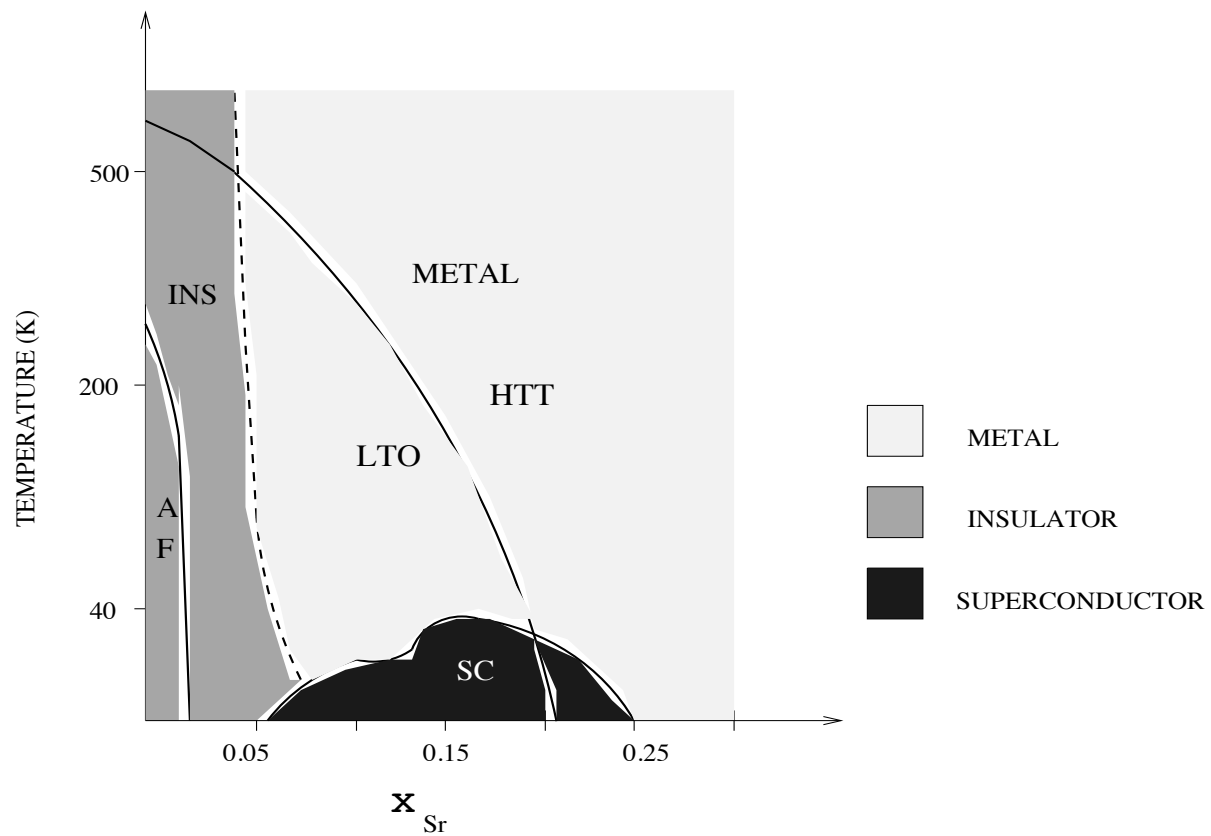


Figure 1.1: Phase diagram of $\text{La}_{2-x}\text{Sr}_x\text{CuO}_4$ in the temperature-doping plane. AF=Antiferromagnet, LTO and HTT stand for low temperature orthorhombic and high temperature tetragonal, respectively.

is expected to have significant weight near the dopant atoms. This is certainly true for x values in the insulating regime (denoted “INS” in fig. 1.1), where the low temperature resistivity ($T \lesssim 100K$) is of the “variable range hopping” [29], a type of conduction in which carriers are mostly localized near individual impurities and hopping between impurities results in conductivity.

The electrical properties of these materials are quite remarkable. The pure and slightly doped materials display hopping conductivity. As the concentration of holes is increased, the system undergoes an *insulator-metal* transition at $x \sim 0.05$ for $T \sim 300K$. At low temperatures the insulating phase leads to a superconducting state, with T_c increasing with x in the “underdoped” regime, reaching its maximum value of $T_c \sim 40K$ at “optimal” doping for $x = 0.15$ and decreasing in the “overdoped” regime until superconductivity is destroyed for $x \gtrsim 0.26$, but the material retains its normal-state metallic conductivity.

The normal state (non-superconducting) properties of these cuprates are highly anisotropic: for x values in the underdoped and optimal regions of the superconducting phase the in plane resistivity, ρ_{ab} , exhibits “metallic” behavior ($d\rho/dt > 0$) while the out-of-plane resistivity, ρ_c exhibits “insulating” behavior ($d\rho/dt < 0$) [30,31]. The values of ρ_c are about 2 orders of magnitude larger than ρ_{ab} for every x and decrease with increasing x , as does ρ_{ab} . If the cuprate is sufficiently overdoped $x \gtrsim 0.2 - 0.25$, a 2D \rightarrow 3D crossover is found for which both $\rho_{ab,c}$ exhibit “metallic” behavior. [30,32]

The decrease in c -axis resistivity with Sr content deserves attention. If Sr introduces random disorder in the LaO layers (the place where it resides), an *increase* in resistivity with Sr would be expected, as the LaO layers intervene between CuO_2 planes, where most of the carriers reside. In addition diffraction shows [20] that the distance between CuO_2 adjacent planes *increases* with Sr. Again, in a band picture, this would be unfavorable for hole transfer between CuO_2 planes. The unusual dependence of ρ_c on x might be indicative of changes in the electronic structure as doping proceeds. As determined from polarized XANES studies [25,26], doped holes in $\text{La}_{2-x}\text{Sr}_x\text{CuO}_4$ have a significant amount of O $2p_z$ orbital character, most likely associated with the apical oxygens. The relative importance of these out-of-plane orbitals *increases* with Sr content and hence they could play a significant role in the c -axis coupling between CuO_2 layers, as the apical oxygens bridge the LaO planes with the CuO_2 ones. Whether these symmetry-dependent occupational changes are coupled to structural modifications introduced with Sr is an open question. It is then

of importance to quantitatively determine the structural changes introduced with Sr doping in its immediate atomic environment, in particular its apical oxygens, in order to fully understand the x -dependence of ρ_c .

1.2 The LTO and HTT structural modifications

The crystal structure of $\text{La}_{2-x}\text{Sr}_x\text{CuO}_4$ has been thoroughly studied by x-ray and neutron diffraction techniques. [20, 33, 34] As shown in fig. 1.1, at low x and T $\text{La}_{2-x}\text{Sr}_x\text{CuO}_4$ crystallizes in a low temperature orthorhombic (LTO) structure. This structure is characterized by the presence of a cooperative tilt of the CuO_6 octahedra (see fig. 1.2). As x and T are increased, the orthorhombic strain, together with the tilt angle of the CuO_6 octahedra gradually decrease, giving rise to the high temperature tetragonal (HTT) phase, also shown in fig. 1.2. The orthorhombic LTO deformation is currently understood as a strain-releasing response to the lattice mismatch between LaO and CuO_2 layers: the ideal, preferred, Cu-O and La-O bond lengths, as obtained from the sum of Cu^{+2} , O^{-2} and La^{+3} ionic radii [35] are $R_{\text{Cu-O}} = 2.13 \text{ \AA}$ and $R_{\text{La-O}} = 2.55 \text{ \AA}$, respectively. The degree of mismatch, defined as [36] $t = \sqrt{2}(\text{La} - \text{O})/2(\text{Cu} - \text{O})$, is $t \sim 0.85$ for the undoped structure indicating that a layered packing with the preferred distances will result in significant strain as the preferred $\sqrt{2}(\text{La-O})$ distance is too short compared to the preferred $2(\text{Cu-O})$ distance.

This strain can be partially relieved by distorting the structure in the LTO way shown in fig. 1.2: the O(1) oxygen atoms are displaced out of the CuO_2 planes resulting in a shorter Cu-Cu distance while the La-O distances become splitted in such a way that longer than ideal La-O bond lengths are obtained. Since the CuO_6 octahedra are nearly rigid units (mainly in their basal planes) and are coupled to each other by the vertexes, the out of plane motion of the O(1) atoms results in a coherent buckled pattern of the CuO_2 planes. As pointed out by Radaelli *et al* [20], the ‘‘tilt’’ distortion doesn’t exactly correspond to a rigid tilt of the octahedra units, as the $\angle \text{O}(1)\text{-Cu-O}(1)$ angle departs from 90° (only by about 1°) to allow a not-so-longer than ideal La-O distance in the \hat{a} direction (the \hat{a} direction is perpendicular to the plane of the paper in fig. 1.2). In addition the Cu-O(2) vector deviates slightly from being perpendicular to the inclined basal plane (again by less the 1°). Since the CuO_2 planes are highly covalent (Cu-O in plane bonding are hybrids of Cu $3d_{x^2-y^2}$ and O(1) $2p_{x,y}$ orbitals) while the LaO planes are highly ionic [37], the largest distortion

of the system in terms of atomic displacements occurs in the LaO planes, resulting in a splitting of La-O(2) bond lengths as large as 0.5 Å.

When x is increased by Sr substitution, holes are introduced into the top of the valence band which is composed of *antibonding* combinations of Cu $3d_{x^2-y^2}$ and O(1) $2p_{x,y}$ orbitals [37]. Removing electrons from antibonding orbitals causes a decrease in Cu-O bond length and a reduction in the mismatch (t gets closer to 1), resulting in a gradual decrease of the tilt distortion to zero. The x -induced LTO to HTT phase boundary at low temperature is found by neutron diffraction [20] at $x \sim 0.21$. A similar reduction in lattice mismatch can be obtained by increasing the temperature. This is due to the different thermal expansions of the La-O and Cu-O bond lengths, La-O bonds expanding faster and leading to a decrease in lattice strain and a decrease of the resulting distortions. As introduction of Sr stabilizes the HTT phase at lower temperatures, the T -induced LTO to HTT phase boundary depends on x , as given in fig. 1.1.

Throughout this thesis, two different space group notations for the LTO and HTT structures are used. For the LTO phase, the standard $Cmca$ space group (No. 64) has the \hat{b} axis as the long axis of the unit cell while the isomorphic, non-standard $Bmab$ space group has the \hat{c} axis as the long axis. The HTT phase can be described by the standard $I4/mmm$ space group (No. 139) or by the non-standard $F4/mmm$ space group. Both tetragonal space groups have the \hat{c} axis as the long axis of the unit cell. The $Cmca$ and $Bmab$ notations are related by $x(Cmca) = x(Bmab)$; $y(Cmca) = z(Bmab)$; $z(Cmca) = -y(Bmab)$. Tables 1.1& 1.2 show lattice parameters and unit cell atomic positions for $x = 0$ at 10K (LTO) and $x = 0.15$ at 300K (HTT) based in neutron diffraction results of Radaelli *et. al.*

1.3 Jahn-Teller distortion of the CuO_6 octahedra

When a Cu^{+2} ion in a $3d^9$ atomic configuration is placed in a cubic octahedral environment (symmetry O_h , see fig. 1.3), the resulting coulombic interaction with the cubic field lifts the five-fold degeneracy of the 3d level and splits it into triple-degenerate, t_{2g} , and double-degenerate, e_g , levels. [38] The electronic wavefunctions in the t_{2g} -manifold have symmetry yz , zx and xy while the ones in the e_g manifold have symmetry $3z^2 - r^2$ and $x^2 - y^2$. For the case here, where the octahedra is formed of negatively charged oxygen atoms, the t_{2g} manifold is lower since the angular dependence of the wavefunctions making up the e_g manifold results in a large amplitude in

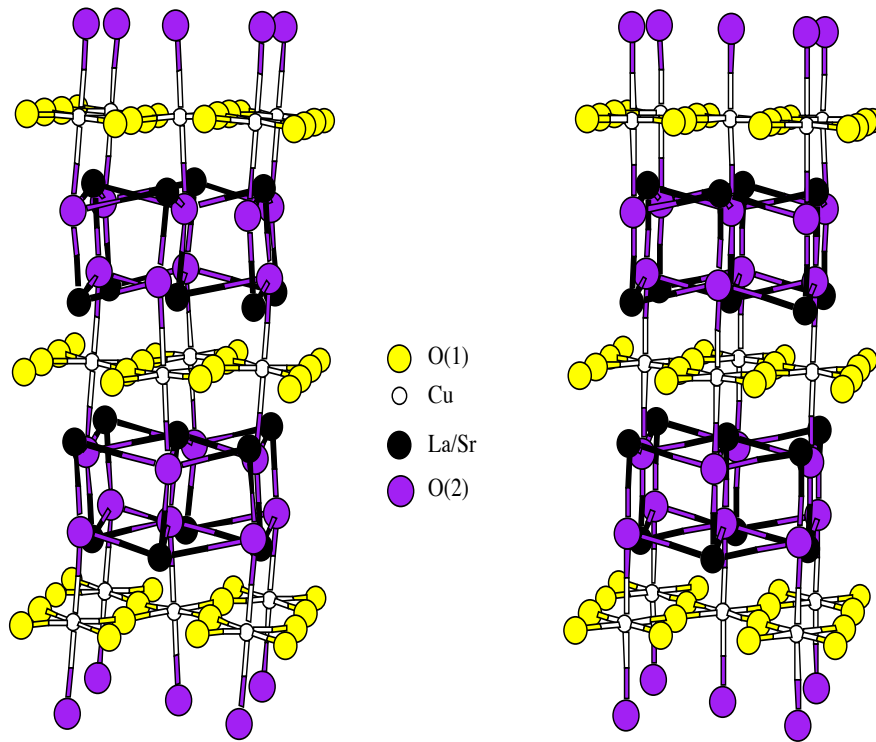


Figure 1.2: Low temperature orthorhombic, LTO, (left) and high temperature tetragonal, HTT, (right) structural modifications of $\text{La}_{2-x}\text{Sr}_x\text{CuO}_4$. In standard $Cmca$ orthorhombic space group representation, the long axis of the unit cell is \hat{b} and \hat{a} is perpendicular to the plane of the paper. In the isomorphic, non-standard $Bmab$ notation, \hat{c} becomes the long axis. The $I4/mmm$ tetragonal space group has the \hat{a} axis along the Cu-O(1) bonds; the $F4/mmm$ space group has an expanded lattice parameter with the \hat{a} axis perpendicular to the paper.

Table 1.1: Lattice parameters and atomic coordinates for the LTO phase of La_2CuO_4 at 10K. Numbers are listed for both space group notations used in this thesis.

<i>Cmca</i>				<i>Bmab</i>			
$a = 5.3346 \text{ \AA}$				$a = 5.3346 \text{ \AA}$			
$b = 13.117 \text{ \AA}$				$b = 5.4148 \text{ \AA}$			
$c = 5.4148 \text{ \AA}$				$c = 13.117 \text{ \AA}$			
	<i>x</i>	<i>y</i>	<i>z</i>		<i>x</i>	<i>y</i>	<i>z</i>
La	0	0.3616	0.0083	La	0	-0.0083	0.3616
Cu	0	0	0	Cu	0	0	0
O(1)	0.25	-0.0084	-0.25	O(1)	0.25	0.25	-0.0084
O(2)	0	0.1837	-0.0404	O(2)	0	0.0404	0.1837

Table 1.2: Lattice parameters and atomic coordinates for the HTT phase of $\text{La}_{1.85}\text{Sr}_{0.15}\text{CuO}_4$ at 300K. Numbers are listed for both space group notations used in this thesis.

<i>I4/mmm</i>				<i>F4/mmm</i>			
$a = 3.7775 \text{ \AA}$				$a = 5.3422 \text{ \AA}$			
$c = 13.2317 \text{ \AA}$				$c = 13.2317 \text{ \AA}$			
	<i>x</i>	<i>y</i>	<i>z</i>		<i>x</i>	<i>y</i>	<i>z</i>
La	0	0	0.3608	La	0	0	0.3608
Cu	0	0	0	Cu	0	0	0
O(1)	0	0.5	0	O(1)	0.25	0.25	0
O(2)	0	0	0.1824	O(2)	0	0	0.1824

the direction of the negative ions, increasing their energy.

In the cuprates, the crystal structure is highly anisotropic. The Cu^{+2} site symmetry is not cubic but tetragonal (symmetry D_{4h}) due to two combined effects: the strongly layered structure, resulting in a tetragonal crystal field at the Cu site together with the occurrence of a strong Jahn Teller (JT) effect.

The tetragonal crystal field is the external, crystal field, acting on the CuO_6 octahedra. This tetragonal field is strong enough to result in a \hat{c} -axis elongated octahedra, consequently lifting most of the remaining electronic degeneracy due to the lowering in symmetry. In this case, tetragonal field results in $x = y < z$, resulting in the energy diagram shown in fig. 1.3, the z related orbitals being lower in energy. That the crystal field is strong enough to cause an elongation of the CuO_6 octahedra can be seen by looking at the isomorphic La_2NiO_4 , whose crystal structure is identical to La_2CuO_4 [39]. There a c -axis elongated octahedra is found, despite the Ni^{+2} ($3d^8$) ion being a non-JT ion, as discussed below. The c -axis elongation in the cuprate, however, is about twice as large than in the nickelate, indicating that the JT effect is in action.

The JT effect [15, 40–42] (or Pseudo Jahn Teller, PJT) is the spontaneous deformation of a molecular system due to the coupling between the electronic degrees of freedom and those of the nuclei motions, in the presence of degenerate (JT) or nearly degenerate (PJT) electronic levels. The interaction between electrons and nuclear displacements mixes the degenerate (or nearly degenerate) electronic states and an overall energy reduction is attained by deforming the molecule (lower symmetry) together with the lifting of the electronic degeneracy (JT) (or enhancement of the electronic splitting, PJT). For nearly degenerate states (PJT), whether a deformation of the nuclear system occurs depends on the relative sizes of the coupling strength and the already existing splitting of the electronic energy levels [42].

All the interactions discussed above lift the electronic degeneracy but preserve the center of mass [38]; e.g., in O_h symmetry the 3-fold degenerate t_{2g} manifold is lowered by 2/3 the amount by which the 2-fold degenerate e_g manifold is raised (see fig. 1.3). Both the tetragonal field and the JT (or PJT) interactions act simultaneously, but can be treated as separate perturbations. As already mentioned the tetragonal crystal field elongates the octahedra and lifts most of the remaining degeneracy. In La_2CuO_4 a further distortion of the CuO_6 occurs due to the JT distortion, since for Cu^{+2} the $3z^2 - r^2$ orbital is fully populated while the $x^2 - y^2$ orbital is half populated, and

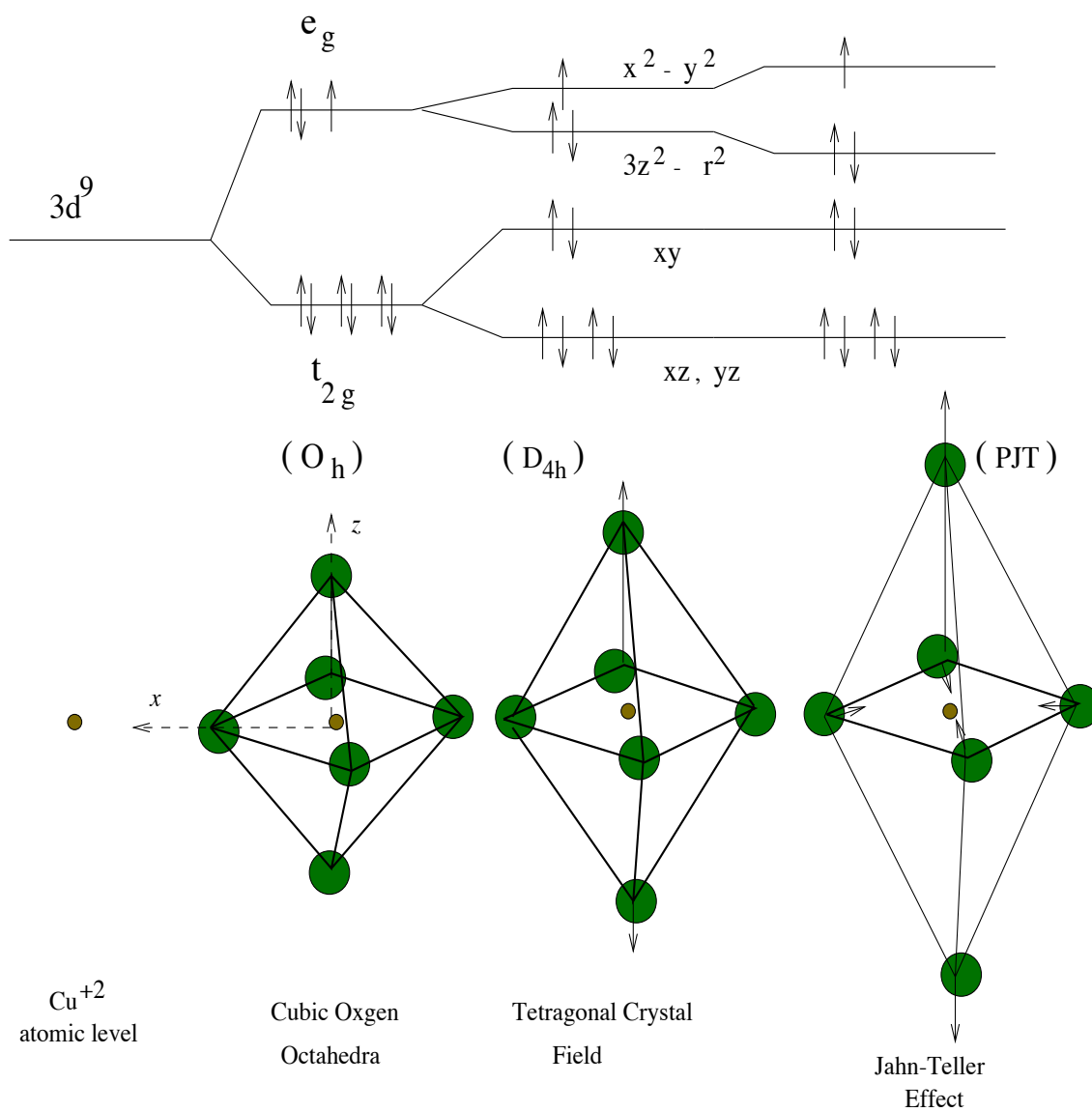


Figure 1.3: The electronic energy levels of a Cu^{2+} ion in a CuO_6 octahedral environment. The effect of the tetragonal crystal field and the Jahn-Teller effect are illustrated.

Table 1.3: Basal and apical distances for CuO_6 and NiO_6 octahedra in La_2CuO_4 and La_2NiO_4 at 300K. In the cuprate the JT (or PJT) effect and the tetragonal crystal field are of similar magnitude.

	La_2CuO_4	La_2NiO_4
Basal	1.904 Å	1.944 Å
Apical	2.427 Å	2.235 Å

then energy gain is obtained by further distorting the octahedra with the resulting enhancement of the splitting. In La_2NiO_4 , Ni^{+2} is a d^8 ion, resulting in equal population of the $3z^2 - r^2$ and $x^2 - y^2$ orbitals (Hund's rule) and then no energy gain is obtained by further distorting the tetragonally distorted NiO_6 octahedra. Table 1.3 lists the basal and apical Cu-O and Ni-O distances at 300K for the pure cuprate and nickelate.

As doped holes are introduced in $\text{La}_{2-x}\text{Sr}_x\text{CuO}_4$, the relative population of the $x^2 - y^2$ and $3z^2 - r^2$ orbitals will change, depending on the symmetry of the orbital into which the holes are doped. The dopant-induced changes in the JT effect should give insights into the orbital character of the doped holes.

1.4 The LTO to HTT structural phase transition and T_c

The proximity of the LTO to HTT structural phase boundary at low temperature to the disappearance of high T_c in $\text{La}_{2-x}\text{Sr}_x\text{CuO}_4$ (see fig. 1.1), together with an apparent reduction in Meissner signal at the structural phase boundary has been originally interpreted by some workers [43] as strong evidence for a detrimental effect of the appearance of the HTT phase on the superconducting properties. Even though the structural deformation associated with the LTO distortion is small, it was argued, the corrugated pattern of the CuO_2 planes with the resulting orthorhombic symmetry could act to enhance T_c . Further studies of the interplay between the structural and superconducting phase boundaries [20, 44–46], however, have shown that bulk superconductivity extends into the HTT phase, with no appreciable effect of the structural transformation on T_c . The most convincing evidence for an accidental proximity of the two boundaries came from pressure experiments [47]. For a given Sr content, pressure stabilizes the HTT phase at a lower temperature, causing the LTO to

HTT phase boundary at low temperature to move from $x \sim 0.21$ at ambient pressure to $x \sim 0.15$ at $P=20$ kbar. The T_c vs. x curves obtained by Yamada and Ido [47] at $P=0$ and 20 kbar, however, were nearly the same, indicating the absence of a significant effect of the structural phase boundary on the superconducting properties. In addition, for superconducting Sr concentrations, T_c was *enhanced* in the pressure induced HTT phase by 2-3°K, as compared to the LTO phase, leading the authors to conclude that the LTO distortion has a negative effect on superconductivity. This last view was recently supported by Dabrowski *et. al* [48] in a systematic study of the effect of $M=(\text{Nd}, \text{Ca}, \text{Sr})$ substitution in $\text{La}_{2-x}\text{M}_x\text{CuO}_4$, concluding that the highest T_c 's are achievable for flat and square CuO_2 planes in the tetragonal structure.

Even-though the LTO to HTT structural phase transition is of the second order type [49] with a *gradual* decrease of the CuO_6 octahedra tilt angle and the related orthorhombic strain to zero, it is still somewhat surprising that T_c vs. x and particularly dT_c/dx show no discontinuity at the structural phase boundary [20]. After all, a change in symmetry has taken place. As already mentioned, for superconductivity to be affected by structural changes, those changes have to occur in scale lengths comparable to the superconducting coherence length (10 – 20 Å). The question that arises: do the LTO *local* distortions of the CuO_2 planes persist in the superconducting, HTT region of the phase diagram? To address this subtle question, it is essential to investigate the *local* structure of the CuO_2 planes in the superconducting, LTO and HTT phases. This investigation is a central part of this thesis.

1.5 Deviations from the conventional model

Evidence in favor of deviations from the conventional model describing the structural properties of $\text{La}_{2-x}\text{Sr}_x\text{CuO}_4$ has been obtained in several, recent work using techniques sensitive to the short-range order (SRO) in the atomic arrangement. In this section I list some of the most remarkable.

The most significant evidence comes from atomic pair distribution function (PDF) analysis of neutron powder diffraction data, in which the Fourier transform of a structure function, $S(Q)$ (Q being the momentum transfer), gives the distribution of interatomic distances. [50–52] The PDF should reveal features of the local structure which are not reflected in the long-range order, like local atomic displacements with SRO only. Peak height-modeling of the PDF in $\text{La}_{2-x}\text{Sr}_x\text{CuO}_4$ across the x and T -induced LTO to HTT phase transitions [50, 51] showed that the amplitudes of

certain peaks failed to reach the values dictated by the appearance of the HTT phase measured by diffraction, but saturated at values consistent with the LTO phase. It was concluded that local LTO domains persisted into the HTT phase and that the appearance of the HTT phase was due to the disordering of the LTO domains over the long range scale measured by diffraction.

The sensitivity of PDF analysis of powder diffraction data to detect local atomic displacements is reduced by the fact that *all* atomic pair correlations contribute to the data, typically resulting in several different bond lengths contributing to the same part of the real space pair distribution. For example, the most significant evidence for peak height saturation occurs for the pair correlations at $\sim 2.7 \text{ \AA}$. [51] At this distance, however, all La-O(2), Sr-O(2) and O(1)-O(1) correlations contribute, making the interpretation of the signal very difficult. The XAFS signal, on the other hand, contains information on *partial* pair correlations (only pairs involving the excited central atom). In addition polarization dependent XAFS can be exploited in anisotropic structures to constrain the contributions even further (see Chapter 2). This results in a XAFS signal which can be interpreted with less ambiguity than the PDF signal.

Additional evidence for disordered local structural distortions in $\text{La}_{2-x}\text{Sr}_x\text{CuO}_4$ comes from x-ray diffuse scattering experiments. [53,54] Strong diffuse scattered intensity was observed in c^* cuts of reciprocal space ($hkl \sim 00l$) in the neighborhood of Bragg peaks, the momentum transfer dependence of the measured intensity implying distortions for the scattering atoms with a remarkable c -axis rms displacement $\langle u_z^2 \rangle^{1/2} \simeq 0.4 \text{ \AA}$. No change in diffuse scattering was observed when scanning the x-ray energy through the Sr K -edge resonance [53], which indicated that the Sr atoms did not contribute to the observed diffuse scattering themselves. It was concluded that the doped holes are liberated from the Sr atoms to yield local, mostly \hat{c} -axis, displacements of atoms due to strong charge-lattice interactions. [53,54] X-ray diffuse scattering, however, cannot determine which are the atoms that are displaced from their average atomic positions. Are these Cu, O(1), O(2) or La? This is a question to which XAFS can provide an answer and is a central part of this thesis.

Sr K -edge XANES experiments [55] were interpreted to conclude that the introduction of Sr under normal preparation conditions leads to the removal of the O(2) apical oxygen neighboring a Sr atom and the related creation of an oxygen defect in a nearby interstitial site. This distortion had implications for the mechanism of

doping, as high T_c superconductivity is induced in oxygen-rich $\text{La}_2\text{CuO}_{4+\delta}$ with excess oxygen residing [56] in a similar interstitial site as that proposed by Tan *et. al* in $\text{La}_{2-x}\text{Sr}_x\text{CuO}_4$, implying a more universal mechanism for doping holes by means of either strontium or oxygen doping. Recent XANES theoretical calculations [57], however, showed that the XANES features attributed by Tan *et. al* to the removal of the apical oxygen to the Sr can be reproduced with the same oxygen configuration as about the La atoms; i.e., a fully occupied apical oxygen site. This controversy exemplifies the need of a quantitative determination of the Sr-induced structural distortions in $\text{La}_{2-x}\text{Sr}_x\text{CuO}_4$, one of the goals of this thesis.

Finally, nuclear quadrupole resonance (NQR) measurements [58] on $\text{La}_{2-x}\text{Sr}_x\text{CuO}_4$ have detected the presence of two inequivalent environments for the Cu atoms. The second, anomalous, Cu site (crystallography shows only one site), whose relative intensity increases with doping, was attributed to a local structural modification of the Cu environment for Cu atoms nearby a Sr dopant atom. [58] This conclusion, however, was later disputed by Hammel *et. al* [59] who found a nearly identical Cu NQR spectra for O-doped $\text{La}_2\text{CuO}_{4+\delta}$. Since Sr and O dopants go to very different sites in the lattice (substitutional and interstitial, respectively) the relation of the Cu second site to a structural anomaly, it was argued, is unlikely and instead an intrinsic, universal, response of the material to the presence of doped holes was suggested. [59] The microscopic origin of the Cu double site detected by NQR is still unknown.

1.6 The phase diagram of $\text{La}_{2-x}\text{Ba}_x\text{CuO}_4$

The $\text{La}_{2-x}\text{Ba}_x\text{CuO}_4$ system shares most of the properties described in the previous section for $\text{La}_{2-x}\text{Sr}_x\text{CuO}_4$ and the phase diagrams of the Ba and Sr-doped systems are very similar (see figs. 1.4 & 1.1). However, two remarkable differences exist between the two, and those are detailed here.

First, a different structural ground state exists in $\text{La}_{2-x}\text{Ba}_x\text{CuO}_4$ for $0.05 \lesssim x \lesssim 0.2$, in which a low temperature tetragonal (LTT) phase is stabilized. [49, 60] Second, in a very narrow range of Ba concentrations around $x = 0.125$, T_c is suppressed dramatically. [61] Whether the appearance of the LTT ground state and the suppression of T_c at $x \approx 0.125$ are related has been the subject of many investigations. [62–67] It is now widely believed that the mere presence of the LTT phase is not enough, by itself, to account for the observed suppression of superconductivity. Major evidence has come from high-resolution x-ray diffraction studies [67] which showed the same

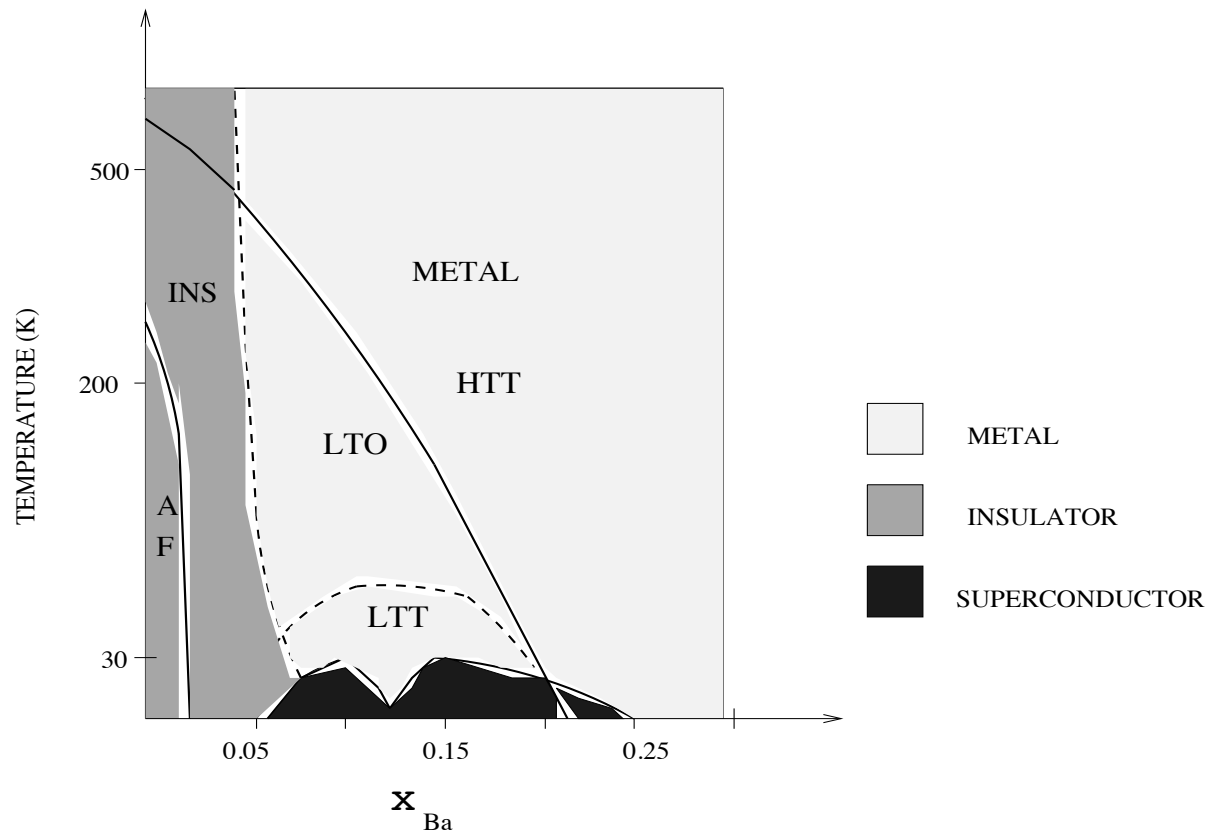


Figure 1.4: Phase diagram of $\text{La}_{2-x}\text{Ba}_x\text{CuO}_4$ in the temperature-doping plane. AF=Antiferromagnet, LTO, HTT and LTT stand for low temperature orthorhombic, high temperature tetragonal and low temperature tetragonal, respectively.

fraction ($\sim 95\%$) of LTT phase present in both $x = 0.125$ and $x = 0.15$ at 10K, even though the former had a $T_c \leq 4\text{K}$ and the later $T_c \sim 25\text{K}$. It was clear that high T_c superconductivity can be achieved even in the presence of the LTT phase.

On the other hand, anomalies in the resistivity [61,62] and the Hall coefficient [62] have been observed *only* for samples with Ba content around $x = 0.125$. Resistivity measurements show metallic behavior ($d\rho/dT > 0$) down to about 60K, where a local minimum and an upturn is observed, with the resistivity behaving in a non-metallic manner ($d\rho/dT < 0$) down to about 10K where superconductivity appears. The Hall effect measurements show a significant reduction ($\sim 50\%$) in the Hall coefficient [62] at about 60K when cooling, the same temperature at which the upturn in resistivity is observed. As shown in fig. 1.4, this is about the same temperature at which the LTT phase appears in $\text{La}_{2-x}\text{Ba}_x\text{CuO}_4$.

The anomalies in the transport properties are consistent with a reduction in the number of free carriers for temperatures below about 60K. This electronic change is believed to be the reason for T_c suppression around $x = 0.125$. Is the electronic change coupled to the structural phase transition? Evidence in favor of coupling is found from experiments in $\text{La}_{2-x}\text{Ba}_{x-y}\text{Sr}_y\text{CuO}_4$ [64, 65] in which the amount of doping is fixed at $x = 0.125$ and the structure is varied by changing y (substituting Ba for Sr in $\text{La}_{2-x}\text{Ba}_x\text{CuO}_4$ stabilizes the LTO phase, as can be deduced from the phase diagram). This experiment shows that the electronic transition resulting in the upturn of the resistivity is mostly suppressed when the LTO phase is stabilized at low temperature for $y \gtrsim 0.075$, and a related increase in T_c is obtained. Additional evidence comes from pressure experiments on $\text{La}_{2-x}\text{Ba}_x\text{CuO}_4$ with $x = 0.125$. [68] The LTO phase is stabilized at low temperature instead of the LTT phase for $P \gtrsim 6$ kbar, with a related increase in T_c from 4K at ambient pressure to about 15K at $P=15$ kbar. This again indicates a coupling between the structural phase transition and electronic change.

Based on the above mentioned results, different mechanisms have been proposed to account for the reduction in the density of free carriers at $x = 0.125$ in the LTT phase. Barisic & Zelenko [63] proposed the formation of a charge density wave (CDW) [69,70] in which charge localization is coupled to the oxygen displacements of the LTT phase (see next section for a description of the LTT phase). Even though such a CDW has not been observed experimentally in $\text{La}_{2-x}\text{Ba}_x\text{CuO}_4$ with $x = 0.125$, the presence of charge (hole) ordering into 1D stripes separated by AF domains in insulating, LTT,

$\text{La}_{1.48}\text{Nd}_{0.4}\text{Sr}_{0.12}\text{CuO}_4$ [71] and $\text{La}_2\text{NiO}_{4.125}$ [72] was deduced from the presence of commensurate lattice displacements observed by neutron scattering. Nd substitution was used in the former study to stabilize the LTT phase without changing the hole content. The static order of holes was observed to disappear at the temperature of the LTT to LTO phase transition, indicating that the LTT pattern of atomic displacements favors charge localization. [71] A similar arrangement of holes and spins was proposed to exist in $\text{La}_{2-x}\text{Ba}_x\text{CuO}_4$ and $\text{La}_{2-x}\text{Sr}_x\text{CuO}_4$, but dynamical in nature [72]. It is possible that a competition between a CDW and a superconducting ground state exist in $\text{La}_{2-x}\text{Ba}_x\text{CuO}_4$ for $x = 0.125$, as the two compete for the same charge carriers at the Fermi surface. The presence of a CDW ground state would explain the decrease in T_c .

Local atomic displacements accompanying the resulting charge ordering of a CDW can be detected by XAFS. The search for such displacements is one main motivation of the XAFS studies on $\text{La}_{2-x}\text{Ba}_x\text{CuO}_4$ performed in this thesis. A direct comparison between $x = 0.125$ and $x = 0.15$ samples should reveal any differences in their structural ground state.

A different mechanism for the suppression of T_c has been proposed by Pickett *et. al* [66] based on band structure calculations. Starting with the HTT structure, it was shown that whereas the LTO distortion has almost no effect on the density of states (DOS) at the Fermi energy (E_F), the LTT distortion causes a reduction by a factor of ~ 2 in the $\text{DOS}(E_F)$, only for $x = 0.125$ (using the rigid band model). [66] The applicability of these results was recently questioned by Norman *et. al* [73], who found a much milder effect of the LTT distortion on the $\text{DOS}(E_F)$ for $x = 0.125$ when using experimental values for the octahedral tilt angle as found by diffraction techniques. This tilt angle is about a factor of ~ 2 smaller than the one used in the work of Pickett *et. al*, where the LTT atomic coordinates were found by energy minimization techniques.

It is evident from this that determining the actual, *local*, LTT-tilt angle of the CuO_6 octahedra is of great importance to assess the possibility of a DOS effect being at the basis of T_c suppression in $\text{La}_{1.875}\text{Ba}_{0.125}\text{CuO}_4$. XAFS can directly measure this tilt angle in $\text{La}_{2-x}\text{Ba}_x\text{CuO}_4$ by means of its sensitivity, via multiple scattering, to three-body correlations in the atomic arrangement (see chapter 2). Accurately measuring this angle is one of the goals of this thesis.

Table 1.4: Lattice parameters and atomic positions for the LTT structure of $\text{La}_{1.875}\text{Ba}_{0.125}\text{CuO}_4$ at 15K.

$P4_2/ncm$			
a=5.3484 Å c=13.235 Å			
	x	y	z
La	0.0053	0.0053	0.3606
Cu	0	0	0
O(1)	0.25	0.25	0.0074
O(1')	0.75	0.25	0
O(2)	-0.0163	-0.0163	0.1821

1.7 The LTT structural modification

The LTT structure, as determined by x-ray and neutron diffraction studies [74, 75] is schematically shown in figure 1.5. In this modification, the CuO_6 octahedra are rotated about $\langle 110 \rangle$ -type axis ($Bmab$ representation); i.e., the tilt axis lies along the Cu-O(1')-Cu bonds. This results in two inequivalent O(1) and O(1') sites, as some of the oxygens in the CuO_2 planes move out of the plane (O(1)) and others remain in the plane (O(1')). As can be seen in figure 1.5, the tilt axis rotates from $\langle 110 \rangle$ at $z = 0$ to $\langle -110 \rangle$ at $z = 0.5$ (z is the height along \hat{c} -axis in lattice units) in going from one CuO_2 plane to another along the \hat{c} -axis. This can be easily seen by observing the change in orientation of the buckled Cu-O(1)-Cu-O(1) lines when going from plane to plane. This is in contrast with the LTO modification in which the tilts are about $\langle 100 \rangle$ -type axis resulting in a unique O(1) site as all the O(1) atoms move out of the CuO_2 planes (see figure 1.2). The space group, lattice parameters and atomic positions in the unit cell for the LTT structure of $x = 0.125$ at 15K are given in table 1.4, based on the neutron diffraction work of Katano *et. al* . [74]

1.8 Evidence for an unusual structural ground state in $\text{La}_{2-x}\text{Ba}_x\text{CuO}_4$

The LTO to LTT phase transition is easily seen in high resolution x-ray diffraction experiments [49, 67], in which the orthorhombic splitting of the a and b -axis starts

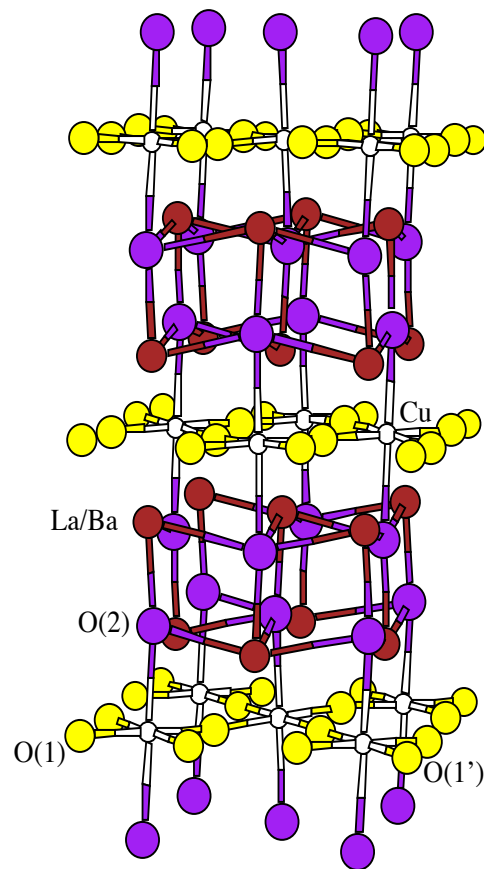


Figure 1.5: Low temperature tetragonal (LTT) structural modification of $\text{La}_{2-x}\text{Ba}_x\text{CuO}_4$. In $P4_2/n\text{cm}$ space group representation the long axis of the unit cell is \hat{c} and \hat{a} is perpendicular to the plane of the paper.

diminishing at a temperature of about 70K to vanish as the sample is cooled below about 40K. The transition is of first order, with the two phases coexisting in a narrow interval of temperature of about ~ 30 K. Even though $\sim 95\%$ of the sample had transformed into the LTT phase, the single Bragg peak of the LTT phase remains quite broad down to 10K [67], the width of the peak being at least twice as big as the one observed for the same fundamental reflection at about 200K in the HTT phase. This anomalous broadening indicates that the LTT phase contains residual strain; either due to the persistence of orthorhombic domains at low temperature or some other mechanism resulting in a significant amount of disorder.

Additional evidence comes from temperature dependent electron microscopy work [76] on $\text{La}_{1.875}\text{Ba}_{0.125}\text{CuO}_4$. In addition to superstructure reflections consistent with the LTT phase, it was found that twins, characteristic of the LTO structure persist in the low temperature LTT phase. Combining imaging and diffraction information, a coexistence of phases was suggested, with the LTT phase mostly present at the twin boundaries and an LTO phase present in the interior of the twin domains.

The nature of the LTT structure in $\text{La}_{2-x}\text{Ba}_x\text{CuO}_4$ is still a matter of controversy. A detailed polarized XAFS study of all three Cu, La and Ba environments in the LTT phase is presented in this thesis, giving a complete picture of the LTT phase from a local perspective.

Chapter 2

XAFS: THEORETICAL CONCEPTS AND DATA ANALYSIS USING THEORETICAL STANDARDS

In this section I describe the basic elements of the XAFS technique, including theory, experiment and analysis. The approach here is to emphasize the concepts involved in understanding the origin of XAFS. A mathematical derivation of the relevant absorption cross section is presented in appendix B. A derivation of the XAFS equation in single scattering (SS) can be found in ref. 77. The contribution of curved wave-effects and multiple scattering is treated in refs. 78–80. The implementation of XAFS theory in the *Ab initio* code FEFF, versions 3-6, can be found in refs. 81–85. FEFF6 was used in this thesis as the theoretical standard for data analysis.

2.1 Theoretical concepts

2.1.1 The origin of XAFS

We consider the interaction of an x-ray photon with an electron bound in a deep atomic core state, $|i\rangle$. The cross section for a photo-induced promotion of the bound electron into a final state $|f\rangle$ in a continuum of energies is given by Fermi's golden rule [86]. For the interaction at hand (see appendix B for a derivation),

$$\sigma(\omega) = 4\pi^2\alpha_{fs}\hbar\omega|\langle f|\vec{r}\cdot\hat{\epsilon}|i\rangle|^2\delta(E_f - E_i - \hbar\omega)\rho(E_f) \quad (2.1)$$

where $\alpha_{fs} = e^2/(\hbar c)$ is the fine-structure constant, $\rho(E_f)$ the density of unoccupied states at the final energy E_f ; $\hat{\epsilon}$ is a unit vector along the linear polarization direction of the photon. The photon incoming energy is $E_\gamma = \hbar\omega$.

Figure 2.1 schematically represents the relevant energy levels. The binding energy of the core electron is represented by E_B : that is the energy required to excite a photoelectron (p.e.) with zero kinetic energy. In a metal that would be the energy difference between the core level and the bottom of the conduction band. Such a

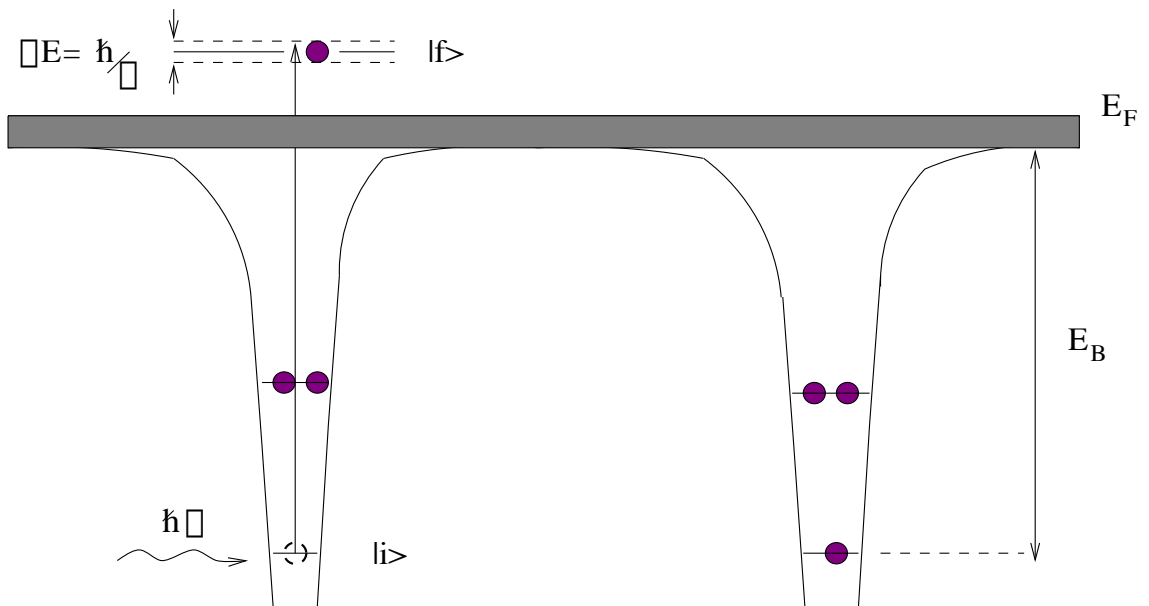


Figure 2.1: Schematic energy diagram indicating the photon-induced transition. E_B is the binding energy of the core electron measured with respect to the bottom of the muffin-tin interstice. Threshold energy for excitation is $E_\gamma = E_B + E_F$ since all states up to E_F are occupied. The final state has a finite lifetime τ and hence is broadened by \hbar/τ .

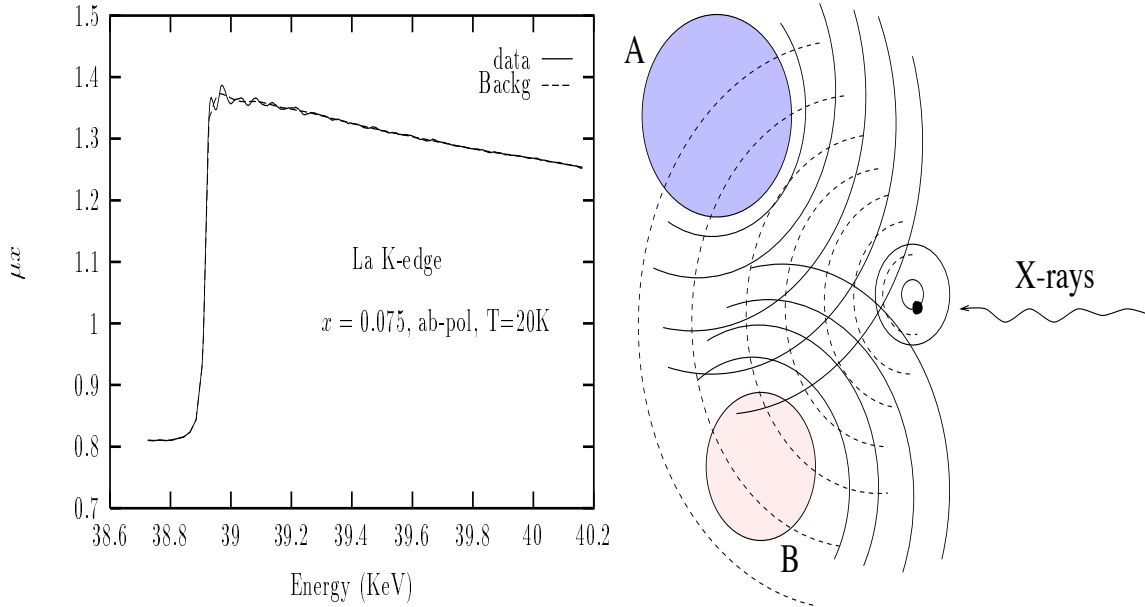


Figure 2.2: Left: X-ray absorption coefficient against photon energy as measured for La K -edge in $\text{La}_{2-x}\text{Sr}_x\text{CuO}_4$. The dashed line simulates the cross section in the absence of neighboring atoms in the solid. Right: Energy-dependent interference between outgoing and scattered parts of the photoelectron wave results in modulation of the absorption cross section, solid line in spectrum at left.

transition ($E_\gamma = E_B$) would be impossible due to Pauli's exclusion principle: all the states up to the Fermi energy E_F are filled, so the minimum kinetic energy for a p.e. in the final state is $\hbar^2 k_F^2 / 2m$. The threshold energy for p.e. excitations is then given by $E_\gamma - E_B = E_{p.e.} \geq E_F$. The p.e. wavenumber k is defined relative to the Fermi level; i.e.,

$$k = \sqrt{2m(E_{p.e.} - E_F)/\hbar}. \quad (2.2)$$

When varying the photon's energy across threshold a jump in the absorption cross section occurs. For an isolated atom, the cross section monotonically varies with photon's energy above threshold. This is simulated in fig. 2.2 by the dashed line superimposed on the actual experimental cross section.

The final state consists of a p.e. together with the presence of the core hole in a deep atomic orbital. Such a configuration is unstable, with a typical lifetime of $\tau \approx 10^{-15} - 10^{-17}$ sec, depending on the absorbing atom and core state. This

finite lifetime of the excited state corresponds to a final state energy broadening of $\Delta E \simeq \hbar/\tau$. For the La K -edge ($1s$ initial state) $\Delta E \sim 20\text{eV}$, [87] the major contribution to broadening of the spectrum shown in fig. 2.2 (inelastic scattering of the p.e. and experimental energy resolution also contribute to the broadening).

When the absorbing atom is surrounded by neighbors, like in a solid, the outgoing photoelectron wave scatters from the potential of the neighboring atoms (see fig. 2.2). Part of this scattered wave interferes with the outgoing wave at the position of the absorbing atom (defined as the origin), modifying the matrix element in eq. 2.1 (the initial state is highly localized at the origin so the matrix element is determined by the value of $|f\rangle$ next to the core level). The interference at the origin between the outgoing and incoming waves changes as the incoming photon's energy increases since the kinetic energy (wavelength) of the p.e. increases (decreases) while the distance between atoms is nearly fixed. The energy dependent modulation of the final state introduces the oscillations in the absorption cross section shown in fig. 2.2 by the solid line. These oscillations (XAFS) contain structural information such as the positions of the scattering atoms and their types and numbers, information that can be retrieved by an appropriate analysis of the isolated fine structure.

2.1.2 The XAFS equation: single scattering

The x-ray absorption coefficient above threshold can be written as

$$\mu(k) = \mu_0(k)(1 + \chi(k)) \quad (2.3)$$

where the energy dependence is translated into p.e. wavenumber by means of eq. 2.2; i.e., $k = 0$ at threshold. For a K -shell initial state, considering only single scattering (SS) events in which the p.e. wave scatters once from a neighboring atom before recombining with its outgoing part, and within the harmonic approximation for lattice vibrations the XAFS modulation is given by [77–80, 82]

$$\chi(k) = \sum_j \chi_j(k) = - \sum_j 3(\hat{\epsilon} \cdot \hat{r}_j)^2 \frac{N_j S_0^2 \mathbf{F}_j(\pi, k, r_j)}{k r_j^2} e^{-2k^2 \sigma_j^2} e^{-2r_j/\lambda(k)} \sin(2kr_j + \delta_j(k, r_j)). \quad (2.4)$$

Most of the ingredients in eq. 2.4 can be explained on a qualitative basis. For the discussion here it is convenient to separate the terms that determine the XAFS amplitude from those that determine its phase; i.e.,

$$\chi(k) = \sum_j \chi_j(k) = \text{Re}[\sum_j A_j(k, r_j) e^{i\phi_j(k, r_j)}], \quad (2.5)$$

where the sum is over all SS centers j . I will focus on $\chi_j(k)$, the partial contribution to the total XAFS from the scatterer at site j , while it is understood that a sum over all scattering sites is needed at the end. Since XAFS has its origin in the interference, at the position of the absorber ($r=0$), between the outgoing wave and the backscattered wave, the XAFS phase ϕ_j is given by the phase difference between these two. The “optical path” phase, $2kr_j$ in the sine term of eq. 2.4, is the phase gained by the p.e. after traveling to the scattering center at r_j and back to the central atom (total distance $2r_j$). Additional phase shifts $\delta_j(k)$ are due to the scattering of the p.e. from the atomic potentials of the absorbing atom and the scattering atom at r_j ; i.e., $\delta_j(k, r_j) = 2\delta_c(k) + \delta_{b,j}(k, r_j)$ where c, b stand for central and backscattering atoms, respectively. The scattering phase at r_j depends not only on k but on the distance, due to the curved wave nature of the p.e.. [80] All this explains the phase term in eq. 2.4, except for the $\sin(\phi(k))$ appearance instead of the $\cos\phi(k)$ dependence that is obtained from the real part of $e^{i\phi(k)}$. This cannot be explained qualitatively but is due to an additional $\pi/2$ phase shift in the asymptotic form ($kr_j \gg 1$) of the outgoing spherical Hankel function at the position of the scatterer, $h_l^+(kr_j)$, with $l = 1$. [78, 88]

A main contribution to the XAFS amplitude is given by the curved-wave, effective backscattering amplitude, $F_j(\pi, k, r_j)$. [80] This is the amplitude of the scattering from the potential of the atom at r_j in an angle $\theta = \pi$; i.e., back towards the absorbing atom. It depends on distance, due to the curved wave nature of the p.e.. [80] The k dependence of F_j is rather complicated [89] but its systematic variation with atomic number Z can be used to distinguish between different types of backscatterers in an unknown structure.

So far it was assumed that coherence in the final state is preserved; i.e., the phase difference between the outgoing and backscattered parts of the p.e. wave, *in the presence of the core hole*, is independent of time. Effects that destroy this final state coherence will destroy the interference process and result in a reduction of the XAFS amplitude. These effects come from the finite lifetimes of the core hole and the p.e., term $e^{-2r_j/\lambda(k)}$ in eq. 2.4, and from the deviation of the interatomic distance from the value r_j due to lattice vibrations, term $e^{-2k^2\sigma_j^2}$ in eq. 2.4.

Finite lifetime effects are phenomenologically described in terms of a mean-free path, $\lambda(k)$. The relevant distance to which we compare this mean free path is $2r_j$, the traveling distance over which coherence has to be preserved. The core hole (c.h.) decays with a lifetime $\tau_{c.h.}$; the p.e. will decay with an independent lifetime, $\tau_{p.e.}$, as it inelastically scatters into a different state. The total lifetime is then $1/\tau = 1/\tau_{c.h.} + 1/\tau_{p.e.}$. Whereas $\tau_{c.h.}$ does not depend on p.e. energy, $\tau_{p.e.}$ depends on k reflecting the energy dependence of the spectrum of excitations available in the media in which the p.e. travels. A finite lifetime results in energy broadening ($\Delta E \sim \hbar/\tau$). In FFFF a complex p.e. wavenumber, $p = p' + ip''$, is introduced to account for energy broadening (losses), i.e., $p = \sqrt{2m(E - V_{\text{int}}(E) + i\Gamma/2)}$, where $V_{\text{int}}(E)$ is a complex, energy dependent interstitial potential and $\Gamma/2$ is the half line width of the core hole. [81,82] The mean free path, $1/\lambda(k) = 1/\lambda_{c.h.}(k) + 1/\lambda_{p.e.}(k)$ is obtained from the imaginary part of the complex wavenumber, $\lambda(p) = 1/p'' = 1/\text{Im}(p)$, after correcting for the different energy references used in the definition of p and k . [81,82] This explains the origin of the mean free path term in eq. 2.4, since with a complex wavenumber the “optical path” phase shift becomes $e^{i2kr_j} = e^{2i\text{Re}(k)r_j} e^{-2r_j\text{Im}(k)}$ which together with the definition $\text{Im}(k) = 1/\lambda(k)$ results in the $e^{-2r_j/\lambda(k)}$ amplitude correction term. Typical value of λ at intermediate p.e. energies is $\sim 10 \text{ \AA}$ [81,90], so χ_j is reduce by $\sim 90\%$ at distances $r_j \sim 10 \text{ \AA}$. This determines the spatial length scale of the XAFS technique and its limitation to probing only the short range order in the atomic arrangement.

The Debye-Waller like term, $e^{-2k^2\sigma_j^2}$ is a result of the loss of coherence due to lattice vibrations (and small static disorder if present) in the harmonic approximation causing deviations from the average interatomic distance and hence altering the “optical path” phase. Since the lifetime of the excited state is so short ($\sim 10^{-15}$ sec) compared to characteristic times for lattice vibrations ($\sim 10^{-13}$ sec), XAFS sees the neighboring atoms “frozen” in their instantaneous positions. The XAFS measurement, however, consists of about 10^8 absorption events at each incoming photon’s energy and hence the instantaneous distances (r_i) will differ from one absorbing atom to another (or the same absorbing atom at a later time), leading to loss of coherence. By considering a “weighted optical phase” term, with the weight given by a Gaussian distribution of distances about r_j (root mean squared (rms) $\sigma_j = \sqrt{\langle (r_i - r_j)^2 \rangle}$),

$$\int_{-\infty}^{+\infty} \frac{1}{\sqrt{2\pi\sigma_j^2}} e^{-(r_i - r_j)^2/2\sigma_j^2} e^{i2kr_i} dr_i \quad (2.6)$$

and by defining $r_i = r_j + \Delta r$,

$$\begin{aligned} & \frac{1}{\sqrt{2\pi\sigma_j^2}} \int_{-\infty}^{+\infty} e^{-(\Delta r)^2/2\sigma_j^2} e^{i2k(r_j+\Delta r)} d(\Delta r) \\ &= e^{i2kr_j} \frac{2}{\sqrt{2\pi\sigma_j^2}} \int_0^{+\infty} e^{-(\Delta r)^2/2\sigma_j^2} \cos(2k\Delta r) d(\Delta r) = e^{i2kr_j} e^{-2k^2\sigma_j^2} \end{aligned} \quad (2.7)$$

where only the real, even in Δr , part of $e^{i2k\Delta r}$ contributes to the first integral in eq. 2.7. The correction to the “optical” phase due to disorder is given by the amplitude correction $e^{-2k^2\sigma_j^2}$. If there are more than one atom of the same type at the same average distance r_j from the absorbing atom, the concept of “shell” is introduced and χ_j becomes the contribution of the j^{th} -shell to the XAFS, with N_j in eq. 2.4 being the number of identical atoms in the shell (coordination number or degeneracy). In this notation, σ_j^2 represents the mean squared deviation in the distribution of distances about the average “shell” distance r_j .

In principle a distribution “weighted” expression has to be obtained for all the terms that depend on r_j in eq. 2.4. However all the other terms beside the “optical phase” slowly vary with r_j (like $1/r_j$ or $1/r_j^2$) and hence the average value of r_j is used for those terms. The Debye-Waller like factor term in eq. 2.4 is responsible for the disappearance of the XAFS oscillations at high k . As k increases the p.e. wavelength decreases and the negative effect that disorder has on the interference process is enhanced.

The term S_0^2 in eq. 2.4 is the passive electrons- amplitude reduction factor. [91] It is a many-body correction which accounts for the changes in the passive electrons wavefunctions (as differ to the photoexcited, active, electron) due to the presence of the core hole. The overlap of the (N-1) passive electrons in the initial and final state, $|\langle\psi^f|\psi^i\rangle|$, with $\psi^{i,f}$ the many body wavefunctions, is reduced leading to a reduction in the strength of the transition associated with the single photoelectron excitation given by the matrix element of eq. 2.1. By definition, $S_0^2 \equiv |\langle\psi^f|\psi^i\rangle|^2$. [91]

The last two terms appearing in eq. 2.4 are the $1/r_j^2$ term and the polarization-dependent factor, $3(\hat{\epsilon} \cdot \hat{r}_j)$. The backscattered wave is proportional, not only to F_j but to the amplitude of the outgoing wave at the position of the scatterer; i.e., $\sim F_j \frac{e^{ikr_j}}{r_j} \frac{e^{ik|r-r_j|}}{|r-r_j|}$, with the outgoing wave originating at $r = 0$ and the backscattered wave originating at $r = r_j$. The relevant quantity for XAFS is the value of the

backscattered wave at the origin, which in complex form is $\sim F_j \frac{e^{i2kr_j}}{r_j^2}$, explaining the origin of the r^{-2} factor.

The polarization term results from the angular dependence of the dipole operator $\hat{r} \cdot \hat{\epsilon}$ in eq. 2.1 together with the angular dependence of the initial state. For K -shell XAFS, the initial state is isotropic ($l = 0$). Since the dipole operator has a $\cos\theta$ dependence (chose the electric field polarization vector, $\hat{\epsilon}$, along \hat{z}), the final state must have a $\cos\theta$ angular dependence ($l = 1, m = 0$) to give a non-zero matrix element in eq. 2.1 (dipole selection rules). The scattering contribution to the final state is then proportional to the amplitude of the outgoing wave at the backscatterer, $\sim \cos\theta_j$, with $\theta_j = \cos^{-1}(\hat{r}_j \cdot \hat{\epsilon})$, resulting in the angular dependence of eq. 2.4 (the square coming from the square of the matrix element in eq. 2.1). [77, 92] For a randomly oriented sample, an angular average has to be done over all possible relative orientations of the polarization vector and the scatterer direction, resulting in

$$\frac{1}{4\pi} \int_0^\pi \int_0^{2\pi} 3\cos^2\theta_j \sin\theta_j d\theta_j d\phi_j = 1 \quad (2.8)$$

(In this thesis partially oriented samples were used requiring a different angular averaging; see appendix B).

2.1.3 Multiple scattering

Multiple scattering (MS) events, in which the p.e. wave scatters from more than one neighboring atom before recombining with the outgoing wave at the origin were neglected in the previous section. For particular atomic configurations, MS contributions can even be larger than SS contributions from atoms at the same (or nearly the same) distance and hence their inclusion is essential for a correct interpretation of XAFS spectra.

Even though tedious algebra is required for a correct account of MS effects [78, 79, 83], a nearly transparent incorporation of MS is realized in FEFF (versions 5 and higher), via the implementation of the Rehr-Albers scattering-matrix algorithm [79] together with an efficient way of enumerating and filtering scattering paths. [84] The polarization dependence of MS paths is incorporated in FEFF6. [85] In FEFF the concept of “path length” is introduced, which is the sum of the lengths of each “leg” involved in the scattering path, r_{tot} . The interatomic distance r_j used in the SS formalism is replaced by an *effective half-path length*, $r_{\text{eff}} = r_{\text{tot}}/2$, for each path j ; the

curved-wave SS amplitude, F_j , is replaced, for an N-leg path, by a special product of (N-1) curved-wave effective scattering matrixes, $F_{\text{eff}}^j \sim F^{(N-1)} \dots F^2 F^1$, with the scattering matrix at site i , F^i , depending in addition to p.e. energy, on the scattering angle $\beta_i = \cos^{-1}(\hat{r}_i \cdot \hat{r}_{i+1})$ (angle between incoming and outgoing legs at site i) as well as on the distance to site $(i-1)$, $|r_i - r_{i-1}|$ due to curved-wave effects. [79] In a similar fashion, the ‘‘optical path’’ phase term, e^{i2kr_j} , is replaced by $e^{ik(\rho_1 + \rho_2 + \dots + \rho_N)}$ where $\rho_i = |r_i - r_{i-1}|$. An effective scattering phase, $\phi^j(k)$ is obtained since the F^i scattering matrixes are complex, and hence $\phi^j(k)$ depends on intersite distances and scattering angles as well.

The XAFS equation can then be written as a sum over scattering paths

$$\chi(k) = \sum_j \frac{N_j S_0^2}{kr_{\text{eff}}^2} |F_{\text{eff}}^j(k)| \sin(2kr_{\text{eff}} + \phi^j(k) + 2\delta_c(k)) e^{-2k^2\sigma_j^2} e^{-2r_{\text{eff}}/\lambda(k)} \quad (2.9)$$

with δ_c the central atom phase shift and N_j the degeneracy of path j . Here $\sigma_j^2 = \langle (r_i - r_{\text{eff}})^2 \rangle_i$, the mean square deviation in half path length with r_i being the instantaneous half path length. Note that the term r_{eff}^2 in the denominator of eq. 2.9 is artificially introduced to resemble the SS equation. A curved-wave emanating from each scattering site results in a product $\rho_1 \rho_2 \dots \rho_N$ in the denominator. The effective scattering amplitude is hence renormalized to result in eq. 2.9 The polarization dependence of MS paths is not included in eq. 2.9. It is properly accounted for in FEFF6 and the correct treatment can be found in refs. 84,85.

2.1.4 Applications of MS XAFS in this thesis

In this thesis MS contributions were exploited in several instances to resolve structural issues which cannot be resolved in SS XAFS. Two of these instances are exemplified in fig. 2.3. In (a) of fig. 2.3 the question at hand was whether the O(2) atom neighboring to Sr was removed completely/partially when Sr is substituted for La in $\text{La}_{2-x}\text{Sr}_x\text{CuO}_4$, as proposed by Tan *et. al.* [55] This type of defect associated with Sr has significant implications for the mechanism of hole-doping in $\text{La}_{2-x}\text{Sr}_x\text{CuO}_4$. As will be discussed later in this thesis, SS XAFS showed a highly disordered Sr-O(2) distance (schematically represented by the ellipsoid in fig. 2.3), with the disorder being nearly temperature-independent indicating its origin in static structural disorder rather than thermal disorder. This lack of temperature dependence made ambiguous

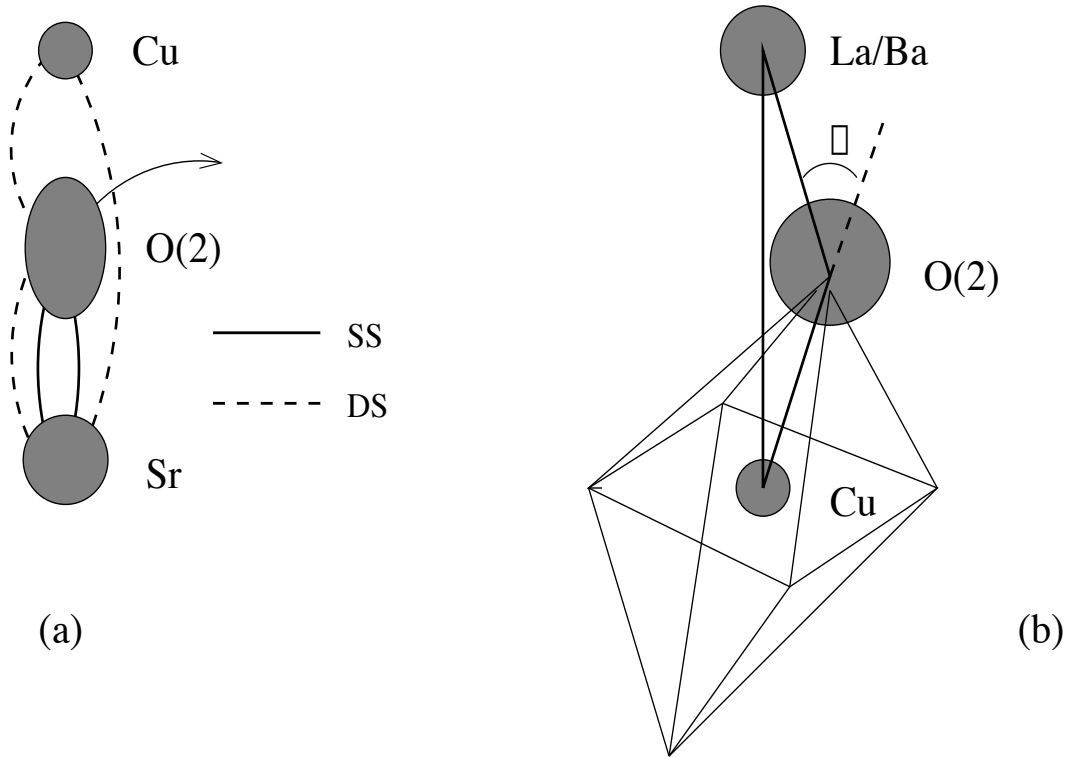


Figure 2.3: Two examples in which MS XAFS is exploited to solve structural issues. (a) Occupancy of highly disordered O(2) atom neighboring Sr, (b) Tilt angle of CuO_6 octahedra in $\text{La}_{2-x}\text{Ba}_x\text{CuO}_4$ with $x = 0.125$.

the separation between N_j and σ_j^2 in eq. 2.4 for SS Sr-O(2). Disorder of the intervening O(2) atom, however, has a small effect on the disorder of nearly collinear MS paths (particularly for O(2) disorder along the path) as the total path length of the MS paths remains nearly unchanged (see appendix C). For simplicity only one double scattering (DS) path is illustrated in fig. 2.3 but its time-reversal DS path, triple scattering (TS) and Sr-Cu SS all contribute to the XAFS at the same distance. The total signal at the Sr-Cu distance then is very sensitive to the *occupancy* of the O(2) site, as the absence of the O(2) atom would change both the phase and amplitude of the total signal at the Sr-Cu distance dramatically. A self-consistent treatment of both SS and MS signals revealed that the O(2) site is fully occupied, as discussed in this thesis and in ref. 21.

MS can be exploited to measure the “buckling” angle, β in fig. 2.3 (b), of a nearly collinear arrangement of atoms [78, 93, 94]. In $\text{La}_{2-x}\text{Ba}_x\text{CuO}_4$ superconductivity is strongly suppressed around $x = 0.125$. [61] Band structure calculations indicate that

a local minimum in the density of states at the Fermi energy could exist for $x = 0.125$, depending on the magnitude of the tilt angle of CuO_6 octahedral units in the structure. [66, 73]. The magnitude of the octahedra's tilt, however, is still a matter of controversy. [73] Changes in tilt angle result in changes in β , shown in fig. 2.3 The sensitivity of XAFS to changes in β arises due to the scattering amplitude at the position of the intervening O(2) atom being strongly peaked in the forward direction and rapidly decreasing with scattering angle, for $0 \leq \beta \lesssim 40$ degrees. [78, 92] For a perfectly collinear arrangement, DS and TS paths involve one and two forward scattering events, respectively. If the angle deviates from collinearity, the effective scattering amplitude, F_{eff}^j , decreases sharply mostly due to the changes in scattering at the intervening atom; the changes in scattering at the end (La/Ba) atoms are small due to the much more flat angular dependence of the scattering amplitude near backscattering angles. [78] The changes in F_{eff}^j are well approximated by a correction factor $\gamma_k + \zeta_k \beta^2$ for $0 \leq \beta \lesssim 20$ degrees. By exploiting this dependence the MS XAFS signal can be parameterized in terms of β and the buckling angle can be measured. A detailed description of the method is presented in appendix A.

2.2 Data analysis: Isolating and interpreting the XAFS signal

The analysis of XAFS data presented in this thesis has been performed by using FEFF6 as the theoretical standard [84, 85] together with the UWXAFS3.0 analysis package. [95] The latter includes the following codes: AUTOBK, which isolates the XAFS signal from the measured absorption coefficient [96]; ATOMS, which generates a list of atomic coordinates in a given cluster size about the absorbing atom based on crystallographic information and calculates some important amplitude corrections [97, 98] and FEFFIT which allows varying the structural parameters in FEFF-generated theoretical standards to best fit the experimental data in r -space, including MS contributions. [99, 100] An overall idea of the steps involved in analyzing XAFS data is presented here. The specialization to the analysis of polarized XAFS data in anisotropic structures is discussed later in this thesis.

2.2.1 Isolating $\chi(k)$

The XAFS signal is defined in eq. 2.3 as the modification of the “isolated” atom absorption coefficient, $\mu_0(k)$, due to scattering of the p.e. from neighboring atoms in

the solid, i.e.,

$$\chi(k) = \frac{(\mu(k) - \mu_0(k))}{\mu_0(k)} \quad (2.10)$$

with k the p.e. wavenumber measured relative to the Fermi level. It is important to note that in this definition $\mu_0(k)$ is the contribution to the absorption of a *given* inner shell electron excitation ($1s$, $2p_{3/2}$, ..., referred as an absorption edge) for a *given* “isolated” absorbing atom (referred as the central atom). The experimentally measured μ , however, contains contributions to the absorption from edges of other atoms beside the central atom together from contributions from other edges in the central atom. These contributions have to be subtracted from the measured μ for a proper normalization of $\chi(k)$. For this purpose, μ is experimentally determined in a wide energy interval (~ 200 eV) below the edge of interest where $\mu_0(k)$ is zero and all the undesired contributions contribute. Since these other contributions are smoothly varying with energy across the edge of interest, they can be subtracted by fitting the “pre-edge” region with a straight line and extrapolating past the edge.

The procedure for isolating $\chi(k)$ used in AUTOBK [96] is based on the distinction between the “frequency” components present in the “isolated” atom contribution to the absorption (referred as background) from those present in $\chi(k)$, the oscillations on top of the background. As can be seen in eq. 2.4, the oscillations in $\chi(k)$, given by the sine term, have “frequencies” which are closely related to twice the interatomic distances, $2r_j$ (the scattering phases, $\delta_j(k)$, depend on k and have a smaller but very significant effect on the “frequency” as well). The non-scattering contribution to μ varies smoothly with k , and hence the background is defined as the contribution to $\mu(k)$ with “frequency” components below those of the XAFS, i.e., below $2r_1$, the “frequency” of the first shell XAFS. The distinction between these two regimes is not as easy to determine as it sounds. On one hand, a Fourier transform (FT) of the expression for $\chi_j(k)$ given in eq. 2.4(with k and $2r_j$ the conjugate variables) will result in a non-trivial line shape due to the overall k dependence, which will result in a given shell contributing to a broad range of “frequencies”. In addition, the background contribution of the “isolated” atom can have some additional oscillatory structure due to, so far neglected, multi-electron excitations in the absorbing atom [91] or the fact that the atom is not really “isolated” but is embedded in the potential of the neighboring atoms. [101] A good background removal should include these effects into $\mu_0(k)$.

To allow for the low frequency oscillatory structure in $\mu_0(k)$ a spline (piecewise polynomial) is used to simulate the background in AUTOBK, with the number of knots in the spline determined by information theory, i.e., equaling the number of independent points in the background region, $N_{bkg} \simeq 2\Delta k R_{bkg}/\pi$. [96, 102] Here Δk is the k -range used in determining $\mu_0(k)$. The criteria for a good background is the one for which the FT of the $\chi(k)$ obtained using eq. 2.10 is minimized with respect to a standard *below* a chosen frequency, R_{bkg} . The parameters of the trial background are adjusted until the difference between $\tilde{\chi}_{\text{trial}}(r)$ and $\tilde{\chi}_{\text{stand}}(r)$ is minimized for $r \leq R_{bkg}$, in a non-linear least squares sense. [96] For some structures, especially those with short first near neighbor distances, the FT of $\chi(k)$ might very well “leak” into the background region and hence minimization with respect to a standard is more appropriate than simply removing all the frequency components below R_{bkg} (if a standard is not used AUTOBK will try to minimize to zero).

In order to choose R_{bkg} for the work presented in this thesis, theoretical standards from FEFF6 are used to simulate the expected low r portion of $\tilde{\chi}(r)$, based on the known average structure of the material under study. FT parameters used for this procedure are the same as those used in the background removal procedure. R_{bkg} is chosen to the value below which the XAFS signal is either small or negligible. This results in typical R_{bkg} values of about half the first neighbor distance (Note that even though the FT conjugate variables are k and $2r$, all the FT performed are mapped from $2r \rightarrow r$ and hence R_{bkg} can be directly compared to r_1 . The FT are not phase-corrected so the value of R_{bkg} is determined from the actual, uncorrected, Fourier transform.) If the FT data “leaks” to very low r , a somewhat arbitrary value of $R_{bkg} \sim 0.8 - 1.0 \text{ \AA}$ is used and the theoretical FEFF6 calculation is used as the standard for background removal.

Due to the degree of arbitrariness in the choice of R_{bkg} extra precautions were taken here to assure that the structural results are independent of the choice of different (reasonable) values of R_{bkg} : these include analyzing $\chi(k)$ data obtained by using slightly different values of R_{bkg} in AUTOBK and fitting (see next section) $\tilde{\chi}(r)$ for frequencies $r \geq R_{bkg} + \pi/(\Delta k)$, i.e., starting fitting the FT data at least one independent point above the background region. [102]

Finally a comment on normalization. Even though AUTOBK allows normalizing $\chi(k)$ by the k -dependent $\mu_0(k)$ as defined in eq. 2.10, a more common practice and

the one used in this thesis is to normalize $\chi(k)$ by the absorption edge step, i.e.,

$$\chi(k) = \frac{(\mu(k) - \mu_0(k))}{\Delta\mu_0(k=0)}. \quad (2.11)$$

Here $\Delta\mu_0(k=0)$ is the difference in absorption immediately below and above the edge (edge step). The reason for not using the energy dependent background is that its energy dependence can be distorted due to a number of systematic experimental errors. One possible source of error is changes in the energy response of the I_0 and/or I_t ion chambers used to detect the intensity of the incident and transmitted beams as the scan progresses. This would result in energy-dependent changes in the measurement of $\mu(k)$ and hence in a distortion of the energy dependence of $\mu_0(k)$ (the *relative* size of $\mu_0(k)$ and $\chi(k)$ is unaffected so the numerator in eq. 2.10 is safe). The edge step is nearly unaffected by energy dependent corrections as the large change in absorption at the edge occurs in a narrow energy interval. Normalizing by the edge step, however, introduces a k -dependent reduction in the amplitude of $\chi(k)$, as the decay of $\mu_0(k)$ with energy is neglected. This error can be corrected since the energy dependence of the X-ray absorption atomic cross section for the central atom can be calculated using the tables of McMaster. [103] The program ATOMS [97,98] calculates this cross section $\mu_0(E)$ for several energies above the edge (E) and regresses a quadratic polynomial in energy $\sum_{i=0}^2 A_i E^i$ to $\ln\mu_0(E)$. The lowest order correction to the amplitude of edge step normalized data is given by the term $e^{A_1 E} = e^{A_1 k^2}$ so it can be approximated by an effective Debye Waller factor correction to $\chi(k)$, $e^{-2k^2\sigma_m^2}$ where $\sigma^2 = -A_1/2$. McMaster corrections are used in this thesis to correct for edge step normalized data.

2.2.2 Fitting $\chi(k)$ using FEFFIT and theoretical standards from FEFF6

As already mentioned, the FT of $\chi(k)$ given in eq. 2.4 will be “peaked” near interatomic positions. Even though the shape of the FT in r -space is much more complicated than isolated “peaks” (due to the overall k -dependence of $\chi_j(k)$ and the overlapping of contributions from different shells due to the limited k range used in the FT), interpreting the data in r -space is of great advantage since the contribution from scattering paths within a certain cluster size from the central atom can be evaluated. Limiting the number of paths that contribute to the signal of interest is important since the number of scattering paths increases exponentially with path

length [84] and the number of variables required in modeling their contribution becomes prohibitive, as discussed below. Interpreting the data in r -space is equivalent (but one step simpler) to doing so in *filtered*, back Fourier transformed k -space.

In this thesis, the program FEFFIT [99,100] is used to construct a *model* $\chi(k)^{\text{th}} = \sum_j \chi_j(k)^{\text{th}}$ using values of $F_j(k)$, $\delta_j(k)$ and $\lambda(k)$ calculated by FEFF6 [84,85]. Only those paths that contribute to the region of r -space, $r_{\min} \leq r \leq r_{\max}$ to be fitted are included in the model. Since the average structures (as determined by diffraction techniques) of the materials under study here are known, the FEFF6 calculation is performed using the average atomic positions as found in those studies. The structural parameters in the model $\chi(k)^{\text{th}}$ (r_j , σ_j^2 , N_j , S_0^2) are allowed to vary (for each path j) in order to minimize, in a least squares sense, the difference (in r -space) between the theoretical model and the experimental data in the r -region of interest, i.e.,

$$\text{Minimize } \left[\sum_{i=1}^N \left| \tilde{\chi}(r_i)^{\text{th}} - \tilde{\chi}(r_i)^{\text{exp}} \right|^2 \right]; r_{\min} \leq r_i \leq r_{\max} \quad (2.12)$$

where the complex form $\tilde{\chi}(r_i)$ is used and the sum is over all N points in the r -space region of interest. As already mentioned, the value of r_{\min} is determined by separating the background region from the structural region by at least one independent point, $r_{\min} \geq R_{\text{bkg}} + \pi/(\Delta k)$. r_{\max} is determined by the radial distance up to which structural information is desired, provided this information can be retrieved with a number of parameters which does not exceed the amount of information in the data. [102]

The number of independent points in a Δr interval of r -space (as opposed to the “mere” points whose spacing relates to the arbitrary sizes of the k grid and FT arrays) is given by [102]

$$N_I = \frac{2\Delta k \Delta r}{\pi} + 2, \quad (2.13)$$

with Δk the k -range used in defining the FT. This relation arises because the spatial resolution in r -space (the minimum separation between points which can be resolved) is dictated by the k -range used in the FT. In physical terms, a larger k -range contains shorter p.e. wavelengths ($\lambda_{\text{p.e.}}$) and hence allows higher spatial resolution. The minimum distance between points in r space that are independent, δr , depends on the k range available in the FT. It can be shown [102] that $\delta r = \pi/\Delta k$. Since both real and imaginary parts of the FT contain information, the number of independent

points in Δr is then $2\Delta r/\delta r = (2\Delta r\Delta k)/\pi$, similar to eq. 2.13. A correct derivation of N_I , including the additional 2 points included in eq. 2.13 can be found in ref. 102.

The number of structural parameters to be fit cannot exceed the amount of information in the data, N_I . This requires implementing constrains between the structural parameters of different paths based on physical grounds. For the anisotropic structures studied in this thesis, the ability to constrain parameters is reduced. This can be compensated, however, by exploiting the polarization dependence of XAFS (see eq. 2.4) to measure the contribution of only a *subset* of scattering paths to the measured signal. Further constrains can be implemented by simultaneously fitting XAFS spectra obtained under two different polarization conditions for paths that contribute to the XAFS in both polarizations, as discussed later in this thesis.

Additional path parameters not listed above are E_0^j , σ_j^3 and σ_j^4 . The last two are the third and fourth order moments of the radial distribution function of shell j about the central atom, $\sigma_j^3 = \langle (r_i - r_j)^3 \rangle_i$ and $\sigma_j^4 = \langle (r_i - r_j)^4 \rangle_i - 3(\sigma_j^2)^2$. [104, 105] This terms are important when the radial distribution of atoms in a shell deviates from Gaussian (eq. 2.6) and contribute both a phase correction, $-\frac{4}{3}k^3\sigma_j^3$, and an amplitude correction, $e^{\frac{2}{3}k^4\sigma_j^4}$ to eq. 2.4. For the materials studied in this thesis at temperatures below about room temperature the contribution of this terms was found to be negligible and then were not included in eq. 2.4.

An overall (same for all paths) ΔE_0 correction is needed to adjust the energy origin ($k = 0$) used in the FEFF6 calculation to that of the experimental data. Experimentally determining the Fermi energy is in many cases accurate only within a few eV, as the onset of p.e. excitations is broadened by lifetime effects and experimental resolution. Typically the onset is chosen to be around the middle of the rising absorption edge. Even in cases where the location of the Fermi level can be determined experimentally (as when the onset corresponds to p.e. transitions into bound states resulting in pre-edge features before the continuum-related excitations of the rising edge [98]), the accuracy of FEFF6 in determining E_F is no better than a few eV. In FEFF6 an electron gas model is used to calculate E_F , where the free electron charge density, ρ_{int} , is found by averaging the charge between the muffin tin radii and the Norman radii, for all atom types. [81, 82] Chemical effects at the valence level, such as charge transfer and hybridization are not properly accounted for in this approximation, since these require a self-consistent calculation of electronic charge densities. Errors in the determination of ρ_{int} propagate into E_F which is determined

within a few eV accuracy.

Chemical effects at the valence level affect the p.e. phase mostly at low k since at higher energies the scattering is mainly from inner core electrons and is not sensitive to the valence state of the atoms. [106] Because of this k dependence, errors in the treatment of chemical effects in FEFF can be roughly compensated by applying a different ΔE_0^j correction to different paths. This can be seen as follows: by changing $E_0 \rightarrow E'_0$ then,

$$k \rightarrow k' = \sqrt{k^2 - \frac{2m}{\hbar^2} \Delta E_0} \quad (2.14)$$

with $\Delta E_0 = E'_0 - E_0$. For $\hbar^2 k^2 / 2m \gg \Delta E_0$, which holds in the XAFS regime ($k \geq 2 \text{ \AA}^{-1}$) for $\Delta E_0 \sim$ (few eV), we have

$$k' = k \left(1 - \frac{2m \Delta E_0}{\hbar^2 k^2}\right)^{\frac{1}{2}} \approx k \left(1 - \frac{m \Delta E_0}{\hbar^2 k^2}\right) \quad (2.15)$$

resulting in a change in phase for path j

$$\Delta \phi_j \approx \frac{-m \Delta E_0^j}{\hbar^2 k} \left[2r_j + \frac{\partial \delta_j}{\partial k}\right] \quad (2.16)$$

which is most important at low k . The difference $\delta_j(k') - \delta_j(k) / (k' - k)$ is replaced by the derivative since typical values of $E_0^j \sim 2$ eV, corresponding to $\Delta k = k' - k \sim 0.05 \text{ \AA}^{-1}$ at $k = 5 \text{ \AA}^{-1}$, while the k grid onto which the phases calculated in FEFF are interpolated has a spacing of 0.05 \AA^{-1} .

Phase corrections of the form given in eq. 2.16 were found to be important to determine interatomic distances in BaZrO_3 with an accuracy of 0.005 \AA . [107] The structure of BaZrO_3 is simple enough (perfect perovskite) but charge transfer and covalency are important. Since only a few parameters are required to model the structure, that leaves room for additional parameters in the form of E_0^j shifts for SS paths (E_0^j for MS paths are related to those of SS paths, see ref. 107) which significantly improves distance determination. For the more complex structures studied in this thesis the number of parameters required is larger and then only an overall E_0 is used, the same for all paths. This limits the accuracy of distance determination in this thesis to $\sim 0.01 \text{ \AA}$.

2.2.3 Evaluating the correctness of a model

Two numbers are calculated by FEFFIT to evaluate the goodness of a fit. These are χ^2 statistic and the fraction of misfit, R . [99, 108] χ^2 statistic is defined as

$$\chi^2 = \frac{N_I}{N} \sum_{i=1}^N \left(\frac{|\tilde{\chi}^{\text{th}}(r_i) - \tilde{\chi}^{\text{exp}}(r_i)|}{\epsilon(r_i)} \right)^2 \quad (2.17)$$

where the sum is over all “mere” pairs of points (both real and imaginary parts of the difference are evaluated at each “mere” point) in the region of r -space being fitted. The number of “mere” points in $[r_{\text{rmin}}, r_{\text{rmax}}]$ is arbitrary as it depends on the grid spacing in k -space and the size of the fast FT array. The prefactor N_I/N in eq. 2.17 is introduced to remove this arbitrariness as the number of independent points, N_I , (eq. 2.13) is independent of k -space grid or array size. [99, 102] The difference of model and data at each point r_i is weighted against the uncertainty *in the difference* (not just the data) at that point, $\epsilon(r_i)$. In FEFFIT a single value of ϵ is used as it is assumed that the uncertainty at point r_i is all due to random noise *in the data*, independent of r_i . The random noise is estimated by the rms value of $\tilde{\chi}^{\text{exp}}(r)$ in the range $[15, 25] \text{ \AA}$, where the XAFS oscillations are assumed to be indistinguishable from the noise (typical p.e. mean free path $\lambda_{\text{p.e.}} \sim 10 - 15 \text{ \AA}$). Systematic errors in the data and the theory are not accounted for in χ^2 as those are extremely hard to evaluate. A related, useful quantity calculated in FEFFIT is *reduced* χ_ν^2 , given by $\chi_\nu^2 = \chi^2/\nu$ with ν being the degrees of freedom in the fit, i.e., $\nu = N_I - N_P$, where N_P is the number of parameters used in the fit.

If the errors are evaluated correctly (i.e., they are mostly random), a good fit should have $\chi_\nu^2 \approx 1 \pm \sqrt{2/\nu}$. [95, 108] Two fits with different N_P (and hence different ν 's) can be compared and if their χ_ν^2 differ by more than $2\sqrt{2(1/\nu_1 + 1/\nu_2)}$ (2 times the fluctuation in the difference) the fit with the lower χ_ν^2 is significantly better.

Typical values of χ_ν^2 found in this thesis, however, are on the order 10-50, indicating that (a) the model is bad, and/or (b) the value of ϵ has been underestimated by not considering systematic contributions to it. In order to check (a) as a possibility, FEFFIT calculates the fraction of misfit, R , given by

$$R = \frac{\sum_{i=1}^N \left| \tilde{\chi}^{\text{th}}(r_i) - \tilde{\chi}^{\text{exp}}(r_i) \right|^2}{\sum_{i=1}^N \left| \tilde{\chi}^{\text{exp}}(r_i) \right|^2}. \quad (2.18)$$

This gives the fractional misfit, i.e., the ratio of total amplitude between theoretical and experimental curves to the total amplitude under the experimental curve. If R is only a few percent, as always found in this thesis for fits that “look” good, option (a) can be ruled out (*provided the structural parameters obtained are reasonable on physical grounds*) and the reason for $\chi_\nu^2 \gg 1$ is the underestimation of ϵ .

If ϵ were known (and that would have meant $\chi_\nu^2 \approx 1$ for a good fit), the uncertainties in the parameters (one standard deviation) are found by the change needed to increase χ^2 by 1, relative to its minimum value, χ_0^2 (or increase χ_ν^2 by $1/\nu$). [99, 108] Since ϵ is underestimated and the fit is good (again, assuming a small R) we can redefine $\epsilon \rightarrow \epsilon\sqrt{\chi_\nu^2}$ so that the definition of a good fit having $\chi_\nu^2 \approx 1$ is recovered. FEFIT finds the uncertainties by the change in the parameters that will result in $\chi^2 = \chi_0^2 + 1$ (assumes a “good” fit) but then rescales them by multiplying by $\sqrt{\chi_\nu^2}$. This procedure would *overestimate* the value of these uncertainties as the fit is required to be good; i.e., $\chi_\nu^2 \approx 1$, while in reality even if most of the “enhanced” χ_ν^2 is due to a bad ϵ a fraction of it could be due to a bad fit, the later effect neglected in the rescaling of uncertainties.

Comparison between different fits by means of χ_ν^2 has to be reinterpreted. Since a “good” fit will have $\chi_\nu^2 \gg 1$, the standard fluctuation in χ_ν^2 has to be renormalized to $\sqrt{2/\nu} \chi_\nu^2$. A fit is significantly better than other if the difference in their χ_ν^2 is larger than about $2\sqrt{2((\chi_{\nu_1}^2)^2/\nu_1 + (\chi_{\nu_2}^2)^2/\nu_2)}$ (2 times the fluctuation of the difference), the fit with the lower χ_ν^2 being better.

An estimation of the relative sizes of random and systematic errors in ϵ is possible. Initially only random contributions were considered, ϵ_{ran} , while the “correct” estimation of ϵ is given by

$$\epsilon^2 \approx \epsilon_{\text{ran}}^2 + \epsilon_{\text{sys}}^2 \approx \epsilon_{\text{ran}}^2 \chi_\nu^2 \implies \epsilon_{\text{sys}} \approx \epsilon_{\text{ran}} \sqrt{\chi_\nu^2 - 1} \approx \epsilon_{\text{ran}} \chi_\nu \quad (2.19)$$

since $\chi_\nu^2 \gg 1$. This indicates that for the data presented in this thesis ($10 \leq \chi_\nu^2 \leq 50$), systematic errors are $\sim 3 - 7$ times bigger than random errors. A pretty severe assumption in deriving eq. 2.19 is that systematic errors are also independent

of r and can be added in quadrature; i.e., they are also normally distributed. This is certainly not the case as systematic errors due to, e.g., a poor background removal will be more significant at low r and errors in the FEFF calculation could perfectly show r -dependence; i.e., could depend on the particular scattering path involved (as an example the use of a uniform interstitial charge density would result in underestimation of charge density along certain paths while it will overestimate it along others).

Chapter 3

EXPERIMENTAL SETUP FOR TRANSMISSION XAFS MEASUREMENTS

The experimental setup used in this thesis to measure the absorption coefficient of a sample as a function of incident photon energy, $\mu(E)$, is schematically shown in fig. 3.1. It consists of a high-brilliance tunable source (synchrotron radiation), a double crystal monochromator for energy selection, a pair of detectors (ion-chambers) to measure the incident and transmitted beam, slits to limit the vertical divergence of the beam (energy resolution) and last but not least the sample. A brief discussion of some of these elements together with the requirements for a successful transmission XAFS measurement, including polarization dependence, is presented here.

3.1 The measurement of $\mu(E)$

The goal of the measurement is to determine $\mu(E)$ with enough accuracy so that the XAFS oscillations can be reliably determined. As the XAFS oscillations are typically only a few percent of the total absorption signal, this requires that $\mu(E)$ be measured with a noise to signal ratio better than about 10^{-3} . The counting statistics required for this level of noise are easily attainable with a synchrotron source in short

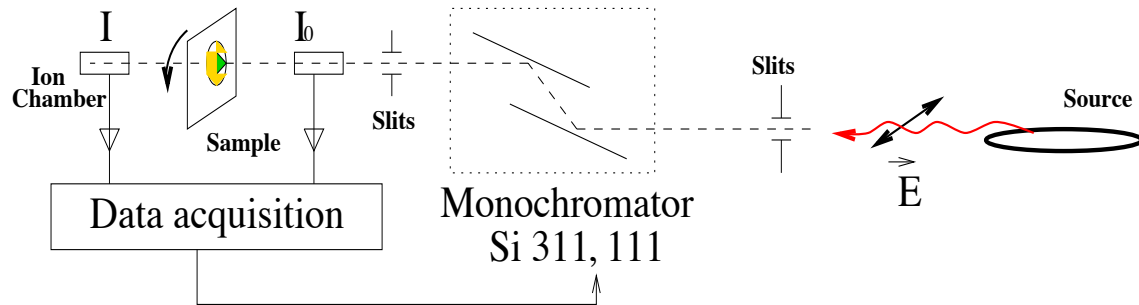


Figure 3.1: Experimental setup for measuring the energy dependent absorption coefficient in transmission geometry.

acquisition times (1 sec. integration time per energy point), where photon counts in the transmission chamber are typically 10^8 - 10^9 photons/sec, resulting in noise to signal ratios in $\mu(E)$ of about $10^{-4} - 10^{-5}$ (XAFS noise to signal ratios of about 10^{-3}) This corresponds to typical currents in the I_t transmission chamber of about $I \approx (\#\text{photons/sec})(E_\gamma/E_{\text{ionization}})(e) \approx 0.5 \text{ nA}$, for $E_\gamma \sim 10 \text{ KeV}$ and $E_{\text{ionization}} \sim 30 \text{ eV}$ (it takes $\sim 30 \text{ eV}$ to produce an electron-ion pair in argon [109]). The electronic noise of the commercial Keithley[©] current amplifiers used here that is associated with such currents is small compared to the pure counting statistical noise. For the case here, then, the major sources of error in the measurement of $\mu(E)$ are other than purely counting statistics. These include, e.g., non-uniform sample's thickness or the presence of higher energy harmonics in the "monochromatic" beam. [110] Minimizing these systematic errors is the key to a successful measurement of $\mu(E)$.

3.2 The double crystal monochromator and vertical slits

Synchrotron radiation extends over a wide range of energies from the infra-red to the hard x-ray region, with its intensity increasing nearly linear with energy up to a critical energy $E_c(eV) = 2218E^3(GeV)/R(m)$ after which it decreases exponentially. [111] At the National Synchrotron Light Source (NSLS) where the measurements were carried out, electrons in the ring are stored at $E = 2.5 \text{ GeV}$ and accelerated in magnetic sectors with radius of curvature $R = 8.17 \text{ m}$, resulting in $E_c = 4.24 \text{ KeV}$. The exponential drop in intensity above E_c results in negligible intensities above 100 KeV. [111] Since a tunable monochromatic beam is needed for the measurement of $\mu(E)$, a monochromator is used. It consists of two parallel, flat Si crystals cut along either (111) (used here for Cu and Sr K -edge measurements) or (311) (used here for La and Ba K -edge measurements) planes. The first crystal is used to select the desired energy, E_γ , by bringing it to an angle θ that satisfies the Bragg condition,

$$2d_{hkl}\sin\theta = \lambda_\gamma = \frac{hc}{E_\gamma}. \quad (3.1)$$

The second crystal being parallel, satisfies the same Bragg condition and reflects the monochromatized beam back into the original incident direction towards the sample (see fig. 3.1). As the measurement proceeds, the Bragg angle is continuously changed and hence the height of the beam changes. This effect is larger for low

energies, as the change in angle required for a given energy change is bigger. The change in angle is related to the change in energy by

$$\Delta\theta = \frac{\Delta E_\gamma}{E_\gamma \cot\theta} \quad (3.2)$$

The lowest energy edge measured in this thesis is Cu K -edge ($E = 8.979\text{KeV}$, $\lambda = 1.38\text{\AA}$) using a Si (111) crystal ($\theta = 12.7^\circ$). For a monochromator about 5 meters away from the sample, the change in beam height over the XAFS measurement ($\Delta E \sim 1500\text{eV}$) is about 0.2 mm at the sample. At the higher energies of the Sr, La and Ba K -edges, this motion is even smaller. As the samples used in this thesis are about 1 cm^2 in size and uniform over at least a few mm, the experiments performed here did not require for the optical table to track the beam position.

As also seen from eq. 3.2, the energy resolution of the monochromatic beam is mostly determined by the vertical divergence of the radiation incident on the monochromator and on the sample (for angular divergences $\leq 10^{-4}$ rad the intrinsic angular width of the diffraction, i.e. the Darwin width can be of comparable size [109]). The purpose of the vertical slits shown in fig. 3.1 is to limit the vertical divergence of the beam (with some loss of photon flux) to improve resolution. Synchrotron radiation is highly collimated with an angular divergence that goes like $\sim 1/\gamma_{e^-}$, where $\gamma_{e^-} = E_{e^-}/mc^2$. At NSLS (2.5 GeV) this corresponds to ~ 0.2 mrad, which results in a vertical beam size of ~ 4 mm at the monochromator position ~ 20 m away from the source. For the experiments here, the pre-mono slits were set at a separation of 1 mm for the Cu and Sr K -edges and at 0.5 mm for the Ba and La K -edges. In fact the finite size of the source (bunch of electrons of size ~ 0.3 mm) also contributes to the angular divergence. With a 1 mm pre-mono slits and 0.3 mm source size the vertical angular spread of radiation entering the monochromator becomes $\delta\theta \sim 1.3 \cdot 10^{-3}/20 \sim 6.5 \cdot 10^{-5}$. With an intrinsic Darwin width of about the same size, the resolution at the Cu K -edge with a Si(111) becomes $\Delta E \sim 2.5$ eV. At the La K -edge with a Si(311) and 0.5 mm pre-mono slits it becomes $\Delta E \sim 16$ eV. For comparison the core-hole lifetime broadening at the Cu and La K -edges are ~ 2 and 20 eV, respectively. [87] The second pair of slits (hutch slits) are adjusted vertically to further improve resolution and determining the horizontal size of the beam. The vertical adjustment is done by taking a short energy scan around the absorption edge and monitoring the sharpness of the observed features for different

slits apertures. A typical hutch slits vertical separation used here is about 1 mm, depending on the experiment. The horizontal dimension of the beam is determined mostly by the sample size and its homogeneity. For some of the samples measured here, a 10-15 % degree of thickness inhomogeneity was found over ~ 1 cm length scale. For those samples, beams of about 2-3 mm horizontal size were used without severely compromising counting statistics.

An important source of systematic errors is the presence of higher energy harmonics in the “monochromatic” beam. For an interplanar spacing d_{hkl} , the Bragg condition is satisfied at θ_1 for λ_1 . Higher order reflections from the same family of planes (reciprocal lattice vectors $2(h,k,l)$, $3(h,k,l)$, etc) are possible at the same angle (provided the structure factor doesn’t vanish) for energies $\lambda_1/2$, $\lambda_1/3$, etc. These higher harmonics have to be eliminated from the “monochromatic” beam as they are less detected in the I_0 chamber and are preferentially detected in the I_t chamber (see next section), resulting in a distortion of the measurement of $\mu(E)$. The structure factor for the second harmonic in Si(111) and Si(311) ($hkl=(222)$ and $hkl=(622)$, respectively) vanish as the only allowed reflections in Si are $h + k + l = 2n$; $n=\text{even}$ and $h + k + l = n$; $n=\text{odd}$. [112] This is in fact one main reason for using this type of crystals. Third, fourth and fifth harmonics, however, are allowed. Care has to be taking to remove higher harmonics from the beam. Since the intrinsic (Darwin) angular width of the higher energy harmonics is narrower than that of the fundamental, by detuning the second crystal a small amount most of the higher harmonics can be rejected while keeping most of the fundamental. For Cu and Sr K -edge measurements, the second crystal was detuned so as to reduce the intensity of the fundamental by 20%. At the Ba and La K -edges, no detuning was applied as the energy of the third harmonic is $\approx 3 \times 40 = 120$ KeV, energy at which the intensity of the synchrotron radiation at NSLS is negligible.

3.3 The ion chambers

The detectors shown in fig. 3.1 are gas ion chambers filled with either pure or a mixture of inert gases (Ar, He, N₂, Kr). Incident x-rays ionize the gas and the electron-ion pairs are collected on the plates of a capacitor (which are ~ 2 cm apart), producing a current proportional to the incident intensity. The accelerating electric field between the collector plates is about 150 V/cm, large enough to avoid pair recombination. Gases are selected so that about 10-15% of the incoming intensity is spent in the

I_0 chamber ($\mu_{I_0}x_0 \sim 0.1 - 0.15$) while about 90% of the transmitted intensity is absorbed in I_t ($\mu_{I_t}x_t \sim 2.5$). [113] Here x_0 and x_t are the lengths of the chambers. For an incident beam on the I_0 chamber with intensity I_{inc} , the I_0 signal is given by

$$I_0 = \Omega(I_0)I_{inc}(1 - e^{-\mu_{I_0}x_0}) \quad (3.3)$$

with $\Omega(I_0)$ the gain in the current amplifier. The intensity after the sample is $I_{inc}e^{-\mu_{I_0}x_0}e^{-\mu_s x_s}$, with $\mu_s \equiv \mu(E)$ (the quantity of interest) and x_s the sample thickness. The intensity detected in the I_t chamber is then

$$I_t = \Omega(I_t)I_{inc}e^{-\mu_{I_0}x_0}e^{-\mu_s x_s}(1 - e^{\mu_{I_t}x_t}) \quad (3.4)$$

Multiplying and dividing eq. 3.4 by $\Omega(I_0)(1 - e^{-\mu_{I_0}x_0})$, I_t can be rewritten as

$$I_t = I_0 e^{-\mu_s x_s} \frac{\Omega(I_t)}{\Omega(I_0)} \frac{(1 - e^{\mu_{I_t}x_t})}{(e^{\mu_{I_0}x_0} - 1)}. \quad (3.5)$$

By taking the natural logarithm of I_0/I_t signals we obtain

$$\ln \left[\frac{I_0}{I_t} \right] = \mu_s x_s + \ln \left[\frac{\Omega(I_0)}{\Omega(I_t)} \right] + \ln \left[\frac{(e^{\mu_{I_0}x_0} - 1)}{(1 - e^{\mu_{I_t}x_t})} \right]. \quad (3.6)$$

There are two additional terms in eq. 3.6 besides the quantity of interest, $\mu_s x_s$. The first is a constant offset containing the ratio of I_0 and I_t gains which is unimportant as it only shifts the $\ln(I_0/I_t)$ spectrum. The second is an energy-dependent offset, since $\mu_{I_{(0,t)}}$ depend on energy. This second term, however, is smoothly varying with energy across the absorption edge of interest (gases have to be chosen so that their characteristic absorption thresholds are outside the energy range of the measurement) so they contribute an energy dependent background that can be subtracted together with the other background contributions by fitting the pre-edge absorption, extrapolating past the edge and subtracting from the data. This procedure assumes that the energy dependence of this second term is the same below and above the edge over the entire energy range of the measurement, which might not be true. Since the subtraction of the extrapolated pre-edge will affect the value of the ‘‘isolated’’ atom absorption $\mu_0(E)x_s$ (see eq. 2.10), an edge step normalization (see eq. 2.11) together with a McMaster correction is used, that do not rely on knowing accurately the energy responses of the detectors (see chapter 2).

Table 3.1: Ion chamber gases used for the different energy edges measured in this thesis. I_0 is the chamber before the sample, I_t the chamber after the sample.

Edge	I_0 (15 cm)	I_t (30 cm)
Cu (8.979 KeV)	N_2 $\mu_{I_0}x_0 \sim 0.1$	50% Ar, 50% N_2 $\mu_{I_t}x_t \sim 2.5$
Sr (16.105 KeV)	30% Ar, 70% N_2 $\mu_{I_0}x_0 \sim 0.14$	20% Kr, 80% N_2 $\mu_{I_t}x_t \sim 2.2$
Ba (37.441 KeV)	30% Kr, 70% N_2	Kr
La (38.925 KeV)	$\mu_{I_0}x_0 \sim 0.15$	$\mu_{I_t}x_t \sim 1$

Table 3.1 summarizes the different gas mixtures used in the experiments described here. The heaviest gas available (Kr) together with the longest chamber (30 cm) resulted in a total $\mu_{I_t}x_t \sim 1$ at the very high energy of the Ba and La K -edges. This was not a problem, however, as the total absorption of the samples at the Ba and La K -edges was only $\mu x \sim 1 - 1.4$ (see chapter 4) resulting in large currents in the I_t chamber.

3.4 Polarization dependent measurements

Synchrotron radiation is 100% linearly polarized in the plane of the orbit (electric field parallel to plane of orbit) while a perpendicular component of the electric field develops as the point of observation moves out of the plane, resulting in a certain amount of circular polarization outside the plane. [111,114] In this thesis the in-plane linear polarization is exploited to measure the XAFS along different orientations of an anisotropic, oriented sample. The samples used here are superconducting powders that are magnetically aligned so that their \hat{c} -axis point along the same direction while they are randomly oriented in the $\hat{a}\hat{b}$ plane (a full description of the sample preparation and characterization is given in chapter 4). The polarized measurements are done by rotating the sample so that either the \hat{c} or $\hat{a}\hat{b}$ orientations lie along the direction of the linearly polarized electric field.

Care has to be taken to ensure that the measurement is done using the properly polarized radiation. This includes (a) that the observation point (the sample) be at the plane of the orbit and (b) the acceptance angle determined by the aperture of

the slits is such that no significant contribution is obtained from the out-of-plane component of polarization.

Satisfying (a) can be achieved by observing that the angular distribution of the total synchrotron radiation's intensity, integrated over all energies and irrespective of polarization is peaked at the plane of the orbit and decreases with the elevation angle from the plane, ψ . For example at $\gamma_e - \psi = 0.5$ the intensity decreases by about $\sim 35\%$. [114] (the in-plane polarization component is peaked in intensity at the plane of the orbit for all energies while the smaller, out of plane component is peaked out of the plane). As the total intensity is peaked at *all* energies in the plane of the orbit ($\psi = 0$), the plane of the orbit can be found by using the monochromatic beam and maximizing the I_0 signal with respect to the height of the pre-mono slits. For this procedure the slits just before I_0 (hutch slits) are either removed or wide open as the height of the optical table is not optimized at this point. In addition the double crystal monochromator is at maximum tuning so that the monochromatic beam is parallel to the plane of the orbit. After centering the pre-mono slits on the plane of orbit, the hutch slits are restored and centered on the beam by adjusting the height of the optical table to maximize I_0 . The sample is then brought into the desired position by independently adjusting the sample table. This procedure guarantees that the observation point can be optically traced back to the center of the plane of the orbit, within a certain angular spread as discussed below.

In order to satisfy (b) above, however, it is necessary to set the aperture of the pre-mono slits so that only the in-plane polarized component contribute to the measured intensity. The angular distribution of both in-plane and out of plane electric field components depends on energy. [114] As already mentioned the pre-mono slits separation used for determining the energy resolution in the experiments here is ≤ 1 mm, resulting in an elevation angle ψ of $0.5 \times 10^{-3}/20 \sim 0.025$ mrad as the slits are 20 m away from the source. At the Cu K -edge ($\sim 9\text{KeV}$), the intensity of the in-plane polarized component, integrated up to $\psi = 0.025$ mrad is $\sim 97\%$ of the total intensity. At the higher energies of Sr, Ba and La K -edges the percentage is even higher [114] and the radiation allowed by the angular aperture of the slits can be considered fully polarized in the plane of the orbit. To ensure that the polarization condition is not changed during the time of the measurement, the height of the beam *before* the pre-mono slits is monitored by means of a position sensitive ion-chamber detector. The overall alignment procedure is repeated if significant changes in beam

height occur; e.g., after a new current is injected in the synchrotron ring.

3.5 *Low temperature measurements*

The experiments performed in this thesis were carried out at temperatures ranging from 10 to 300K, the temperature range in which the phenomena under study (structural phase transitions and superconducting phase transitions) manifest themselves. A closed cycle Displex refrigerator is used for the measurements in which, using helium as a working medium, compressor and expander modules are used to cool a copper cold finger to which the sample cell is attached. The sample cell is a copper cell sealed with kapton windows. The oriented samples are embedded in a thermoplastic resin which itself is in contact with an aluminum frame (see chapter 4). Even though the aluminum frame is in thermal contact with the copper cell, to which it is attached with vacuum grease, helium exchange gas is introduced into the sealed copper cell to guarantee proper thermal contact between the sample and the cell and therefore with the cold finger. A copper radiation shield is placed around both the cold finger and the sample cell, which are then placed under a mechanical vacuum of ≤ 50 mTorr to provide additional thermal insulation. The radiation shield has open slots cut in it allowing the x-rays to pass through; the slots are covered with aluminized mylar. A heating element is located around the cold finger together with a temperature sensor (calibrated diode) so that the temperature of the cold finger is varied and controlled to within 1K by a LakeShore[©] temperature controller.

Enough time is allowed for the sample's temperature to equilibrate. Typically at least 10 minutes elapse from the time the sensing diode reads the desired temperature to the time the measurement starts. Care is taken to readjust the sample's vertical position so as to correct for any noticeable thermal expansion/contraction of the copper cylinder hosting the cold finger. Typically two to three samples can be fitted into the sample cell at a time, reducing considerably the duration of the experiment as cooling the samples down to 10K is time consuming (typically 30 minutes). To accelerate the initial cooling, the cold finger together with the sample cell are cooled down to liquid nitrogen (LN₂) temperature (77K) by placing them in a LN₂ bath prior to turning on the displex and pulling vacuum around them. This helps slowing down the diffusion of helium gas exchange out of the sample cell. The samples are measured with the electric field along one orientation for all temperatures then taken out, rotated by 90° and remeasured with the electric field along the other orientation.

Chapter 4

SAMPLE PREPARATION AND CHARACTERIZATION FOR POLARIZED XAFS MEASUREMENTS

4.1 Magnetically aligned powder

In order to exploit the polarization dependence of the XAFS for structural determination oriented samples are required (see appendix B). In this thesis, \hat{c} -axis magnetically aligned powder was used for that purpose. In what follows, a description of the principles and technicalities behind this method are presented.

As experimentally shown by Farrell *et.al* [115], if a crystal possessing anisotropy in its normal state paramagnetic susceptibility is placed in a magnetic field, it will align so that the direction having the greatest susceptibility lies along the field direction (if diamagnetic then the opposite is the case [116, 117]).

The anisotropy in the normal state susceptibility of $\text{La}_{2-x}\text{Sr}_x\text{CuO}_4$ and $\text{La}_{2-x}\text{Ba}_x\text{CuO}_4$ was measured by Fukuda *et.al* [118]. For magnetic fields above about 10kOe (1T), the \hat{c} -axis susceptibility is larger than the \hat{ab} one by about $\Delta\chi = (\chi_c - \chi_{ab}) \sim 10^{-7}\text{emu/g} \sim 7 \cdot 10^{-7}\text{emu/cm}^3$ (the density of this materials $\rho \sim 7\text{gr/cm}^3$). For a particle of volume $V \sim 1\mu\text{m}^3 = 10^{-12}\text{cm}^3$ in a field $H = 10\text{kOe}$ the magnetic energy difference between \hat{c} and \hat{ab} alignment is then [119, 120] $\Delta E_M = (\Delta E_c - \Delta E_{ab}) = VH^2\Delta\chi/2 \sim 3.5 \cdot 10^{-11}\text{erg}$. Our alignment is done at a temperature $T \sim 120^\circ\text{C}$, which corresponds to a thermal energy $E_T \sim 0.034\text{eV} = 5.4 \cdot 10^{-14}\text{erg} \ll \Delta E_M$ and hence the torque associated with the magnetic energy gain would overcome the thermal disorder and alignment will occur. The caveat here is that a suitable medium for embedding the particles is used so as to minimize friction that would otherwise oppose particle rotation. In addition, each powder particle has to be a single crystal.

The embedding medium used here is a Buehler[©] thermoplastic cement (No. 40-8100). Among the advantages of this product are its very low density ($\rho=1.13\text{gr/cm}^3$), resulting in a small contribution to the total x-ray absorption, and its lost of solid integrity with temperature becoming nearly liquid at about 100°C .

Note that this alignment procedure results in powder aligned along the \hat{c} -axis

but otherwise randomly oriented in the \hat{ab} plane. For samples in which $a \neq b$, the XAFS measurement with in-plane polarization gives the angular average discussed in appendix B.

4.2 The $\text{La}_{2-x}\text{Sr}_x\text{CuO}_4$ system

The ceramic samples used in the polarized $\text{La}_{2-x}\text{Sr}_x\text{CuO}_4$ experiments were made by D. G. Hinks and A. W. Mitchell at Argonne National Laboratory. Samples from the same batch have been characterized thoroughly both in their structural and superconducting properties and the reader is referred to the work of Radaelli *et. al* [20] for their description.

The sintered pellets as obtained had a crystallite size in the range $20 - 50\mu\text{m}$, independent of Sr content [121]. Based on this crystallite size, the sintered pellets were ground by hand using a mortar and pestle and the powder obtained sieved through 400 mesh (opening $38\mu\text{m}$). This procedure was repeated until enough fine powder was obtained ($\approx 100\text{ mg}$). The sieved powder was examined under an optical microscope and a typical particle size of $10\text{-}20\mu\text{m}$ was corroborated. Assuming the grain boundaries are weak links and therefore the polycrystalline sample breaks along them, this procedure should result in the vast majority of the powder particles being single crystal.

The mixing of the appropriate ratio of powder and resin was done on a clean aluminum plate kept at about 110°C on a hot plate. At this temperature the resin is soft enough to allow a good uniform mixture to be obtained in a time period of 10-15 minutes. The mixture is then transferred to the sample cell, a 1.27cm ($0.5''$) diameter hole centered in a $1.8 \times 1.8 \times 0.158\text{ cm}^3$ piece of aluminum (made out of standard aluminum sheet, $1/16''$ thickness) with the help of a wooden Q-tip applicator. The bottom of the sample cell is previously sealed with Kapton tape to contain the liquid mixture. It is important to maintain good thermal contact between the sample cell and the aluminum plate with the mixture during transfer in order to avoid hardening of the mixture. This is achieved by making the two overlap and sliding the mixture over the edge of the plate directly into the cavity. The cavity is filled and the sample cell transferred from the hot plate to a cold surface with the help of tweezers. Extreme care has to be taken to ensure that a uniform thickness sample is obtained. If a convex or concave surface is obtained it can be readily seen by light reflection. In that case the sample cell is put back onto the hot plate and material is removed or added until

a flat surface is obtained. The top surface is then sealed with Kapton tape and the sample is ready for alignment.

It is important to avoid air bubbles trapped inside the cooled mixed sample as well as in between the top kapton tape and the surface of the sample. The former is avoided by pressing down with the help of tweezers on the sides of the sample cell (while on the hot plate) to make good thermal contact and cause any hidden air bubble to rise to the surface. The latter is avoided by pressing down on the kapton tape at the same time it is being rolled to sealed the top surface of the sample. These precautions are essential to avoid having the sample shape changing as it is being heated in the magnet for alignment, as the sample is held *vertically* in the magnetic field.

Samples were prepared for La and Sr *K*-edge XAFS measurements for $x = 0.075, 0.1, 0.125, 0.15, 0.2, 0.25, 0.3, 0.36$. The amount of sample required was calculated using the x-ray absorption atomic cross sections listed in the tables of W. H. McMaster [103]. As an example, we present here such calculation for the $x = 0.15$ sample.

At the La *K*-edge ($E=38926$ eV) the absorption coefficient is given by

$$\begin{aligned}\mu(E) &= \frac{1}{V_{\text{cell}}} \sum_i n_i \sigma_i(E) = \frac{1}{V_{\text{cell}}} (n_{\text{La}} \sigma_{\text{La}} + n_{\text{Sr}} \sigma_{\text{Sr}} + n_{\text{Cu}} \sigma_{\text{Cu}} + n_{\text{O}} \sigma_{\text{O}}) \\ &= \frac{4}{377.6} (1.85 * 6378 + 0.15 * 1500 + 1 * 540 + 4 * 7) = 133.4/\text{cm} \quad (4.1)\end{aligned}$$

since there are four molecular units in the unit cell volume $V_{\text{cell}} = a^2c = 377.6 \text{ \AA}^3$ (F4/*mmm* space group representation). The cross sections are given in units of Barn/atom so the 10^{-24} factors appearing in both the nominator and denominator cancel out ($1\text{Barn}=10^{-24}\text{cm}^2$; $1 \text{ \AA}^3 = 10^{-24} \text{ cm}^3$). The edge step is given by

$$\begin{aligned}\Delta\mu &= \frac{1}{V_{\text{cell}}} n_{\text{La}} (\sigma_{\text{La}}^+ - \sigma_{\text{La}}^-) \\ &= \frac{4 * 1.85}{377.6} (6377.96 - 1173.9) = 102 \text{ cm}^{-1} \quad (4.2)\end{aligned}$$

where $\sigma^{+,-}$ are the absorption coefficients above and below the edge, respectively. At the Sr *K*-edge ($E=16105$ eV) the absorption coefficient is given by

$$\mu = \frac{4}{377.6} (1.85 * 13213 + 0.15 * 15662 + 1 * 6620 + 4 * 38.6) = 355.6 \text{ cm}^{-1} \quad (4.3)$$

and the edge step given by

$$\Delta\mu = \frac{4 * 0.15}{377.6}(15662 - 2376) = 21.1\text{cm}^{-1} \quad (4.4)$$

As shown by Rose and Shapiro [113], optimizing the signal to noise in a transmission experiment with respect to the sample thickness yields an optimal thickness x of $\mu x \sim 2.5$. This can be achieved at the Sr K -edge with a sample thickness $x \sim 70\mu\text{m}$. The resulting edge step at the Sr K -edge is $\Delta\mu x \sim 0.15$.

The same thickness sample results in a total absorption of $\mu x \sim 0.94$ and an edge step $\Delta\mu x \sim 0.71$ at the La K -edge. Besides the optimal thickness mentioned above, it is desirable for concentrated samples to have an edge step $\Delta\mu x < 1.5$ to avoid “thickness effects” [110]. Hence an edge step value of 0.71 at the La K -edge is not very far from optimum. In this way the same thickness samples can be used for both Sr and La K -edge measurements without compromising the quality of the data.

The density of the superconducting sample can be evaluated by

$$\begin{aligned} \rho &= \frac{1}{V_{\text{cell}}} \sum_i n_i M_i \\ &= \frac{4}{377.6 \cdot 10^{-24}} (1.85 * 138.9 + 0.15 * 87.62 + 63.55 + 4 * 16) \times 1.66 \cdot 10^{-24} \\ &= 7\text{gr}/\text{cm}^3 \end{aligned} \quad (4.5)$$

The volume ratio between sample and resin is given by

$$\frac{V_s}{V_r} = \frac{t_s}{t_r} = \frac{73 \cdot 10^{-4}}{0.158 - 73 \cdot 10^{-4}} = 0.046 \quad (4.6)$$

since the thickness of the sample cell is 0.158 cm. The mass ratio is given by

$$\frac{M_s}{M_r} = \frac{V_s \rho_s}{V_r \rho_r} = 0.046 * \frac{7.0}{1.13} = 0.285 \quad (4.7)$$

A sample thickness of $t_s = 70 \cdot 10^{-4}$ cm corresponds to a volume $V_s = \pi R^2 t_s = 8.87 \cdot 10^{-3} \text{cm}^3$ and to $M_s = 0.062$ gr. Since a significant amount of the sample-resin mixture sticks to the aluminum-plate and the Q-tip applicator, the startup mixture contains about 50% more sample-resin than needed, with their ratio given by eq. 4.7. Note that the mixture contains 20 times more resin than sample (by volume). It is essential that the powder particles be well dispersed in the resin, isolated from each other.

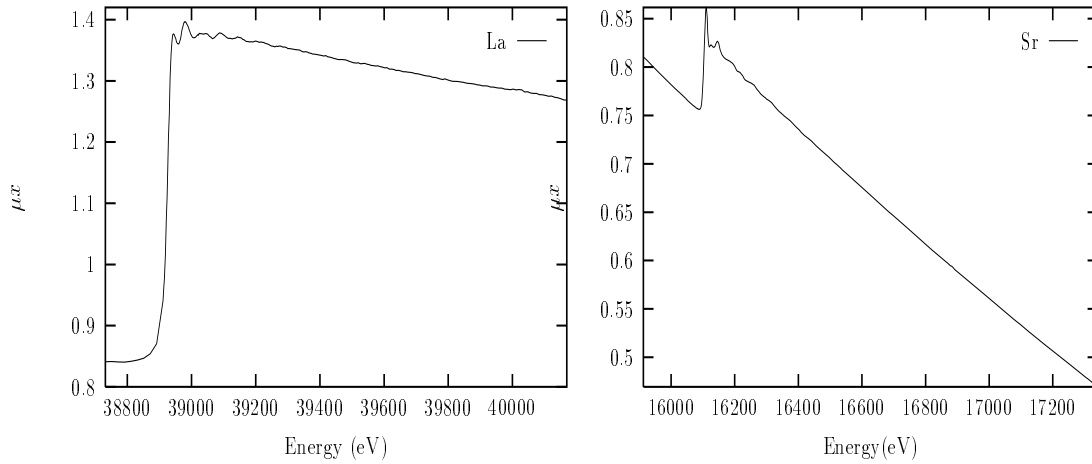


Figure 4.1: La and Sr K -edges in $\text{La}_{1.85}\text{Sr}_{0.15}\text{CuO}_4$ at $T=300\text{K}$, $\hat{a}b$ -polarization; $\Delta\mu x = 0.54, 0.095$, respectively.

The actual thickness of the sample can only be determined *a posteriori* from the measurement of the edge step. Figure 4.1 shows the absorption coefficient obtained for the Sr and La K -edges of $\text{La}_{1.85}\text{Sr}_{0.15}\text{CuO}_4$ at $T=300\text{K}$. The $\hat{a}b$ -polarized spectra are shown, although the edge-step is independent of polarization (see appendix B). The values obtained are somewhat smaller than calculated, the reduction being percentage wise about the same for both edges ($\sim 30\%$), indicating that the actual sample thickness is about $t \sim 50\mu\text{m}$.

Additional information that can be obtained in this case from the ratios of the edge steps is the relative concentrations of Sr and La. From eqs. 4.2& 4.4 we obtain

$$\frac{(\Delta\mu t)|_{\text{Sr}}}{(\Delta\mu t)|_{\text{La}}} = \frac{x_{\text{Sr}}(\sigma_{\text{Sr}}^+ - \sigma_{\text{Sr}}^-)}{x_{\text{La}}(\sigma_{\text{Sr}}^+ - \sigma_{\text{Sr}}^-)} \quad (4.8)$$

since the same sample is used for both edges and hence the thickness of the sample cancels out.

For example, using the values measured for the edge steps in the $x = 0.15$ sample we obtain $(x_{\text{Sr}}/x_{\text{La}})=0.069$, compared to the nominal value of $(0.15/1.85)=0.081$ for this sample. The main source of error in our measurement of this ratio is the assumption of same thickness for both edges' measurements. Even though the same sample was used, the actual measurements were done using different spots on the sample. Sample thickness variation can be easily seen experimentally by placing different parts of the sample in the beam and measuring the variation in edge step. We found a 10-15% variation in thickness to be typical of our samples, limiting the

accuracy with which we can determine the ratio of concentrations to the same percentage. This implies a Sr content for this sample consistent with any value in the range 0.12-0.15. Since the superconducting and structural properties of these High T_c compounds depend strongly on dopant content, the concentration of the dopant has to be independently checked by, e.g., measuring T_c or the lattice parameters of the sample. As already mentioned, those measurements have been done by Radaelli *et.al* [20] on samples from the same batch used here and then the Sr content of our samples is assumed to be the one determined in Radaelli's work.

The alignment of the samples was done in the Materials Science Department of Brookhaven National Laboratory, using one of the superconducting magnets owned by Mas Suenaga's group. The samples were mounted vertically in the sample stage, located at the bottom of a hollowed, stainless steel cylindrical rod. Heating wires and a thermocouple were attached to the sample stage (see figure 4.2). The samples were pre-heated to 120 °C in an oven outside the magnet and then quickly introduced in the magnet with the axis of the cylindrical rod parallel to the magnetic field direction. The magnetic field was set to 8 Tesla which corresponds to a current of $I=76$ Amperes flowing in the Nb-Sn superconducting wire which is maintained at LHe temperature. The samples were re-heated and kept at 120°C inside the magnet for about 2 minutes, to assure the whole sample has reached thermal equilibrium. The samples were then cooled inside the magnet to a temperature of $\sim 40^\circ\text{C}$, cold enough for the resin to solidify and then permanently freezing the particles with their \hat{c} axis aligned in the direction of the field. The cooling of the samples inside the magnet was accelerated by flowing LN2 in the hollowed rod.

4.2.1 Determining degree of alignment with x-ray diffraction

The degree of alignment is checked by powder x-ray diffraction. Figure 4.3 schematically shows the scattering geometry in the diffraction experiment. The magnitude of the momentum transfer is given by

$$\Delta q = \sqrt{(q_i^2 + q_f^2 - 2q_i q_f \cos 2\theta)} = \sqrt{(2q^2(1 - \cos 2\theta))} = \frac{4\pi}{\lambda} \sin \theta \quad (4.9)$$

where the relations $|\vec{q}_i| = |\vec{q}_f| = \frac{2\pi}{\lambda}$ and $\cos 2\theta = 1 - 2\sin^2 \theta$ were used. For a Bragg reflection to occur, the momentum transfer has to equal a reciprocal lattice vector (r.l.v)

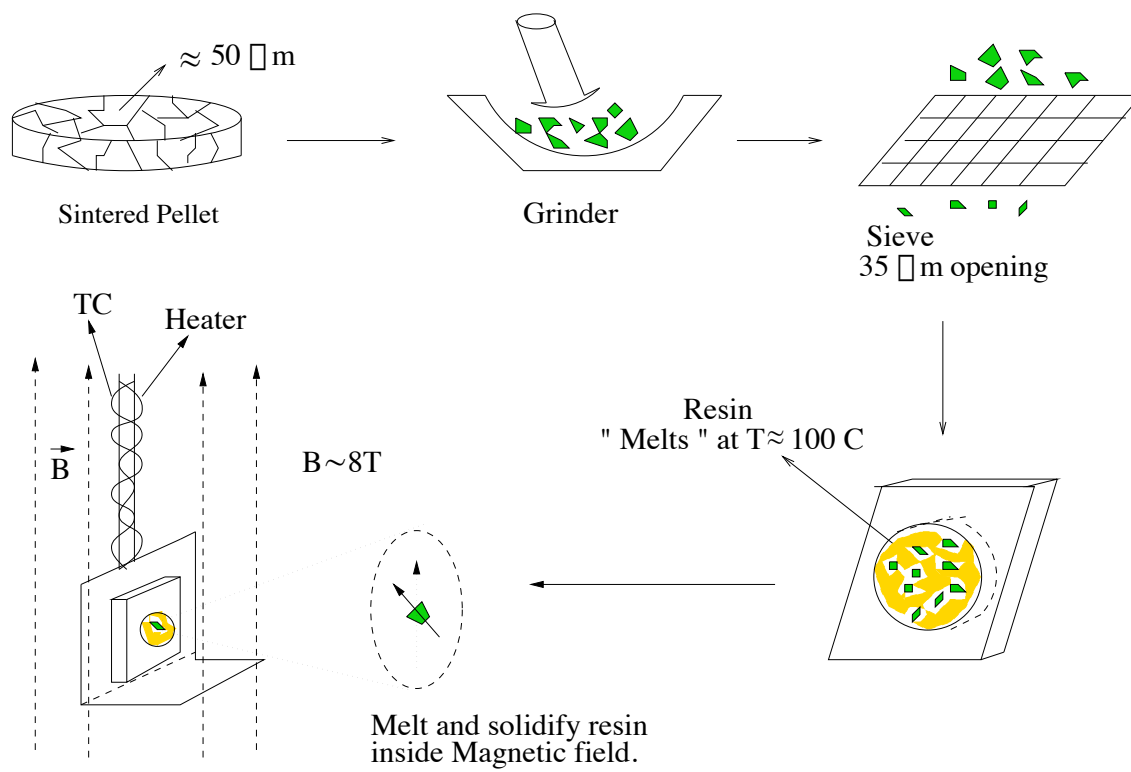


Figure 4.2: Schematic representation of the procedure used to magnetically align $\text{La}_{2-x}\text{Sr}_x\text{CuO}_4$ powder.

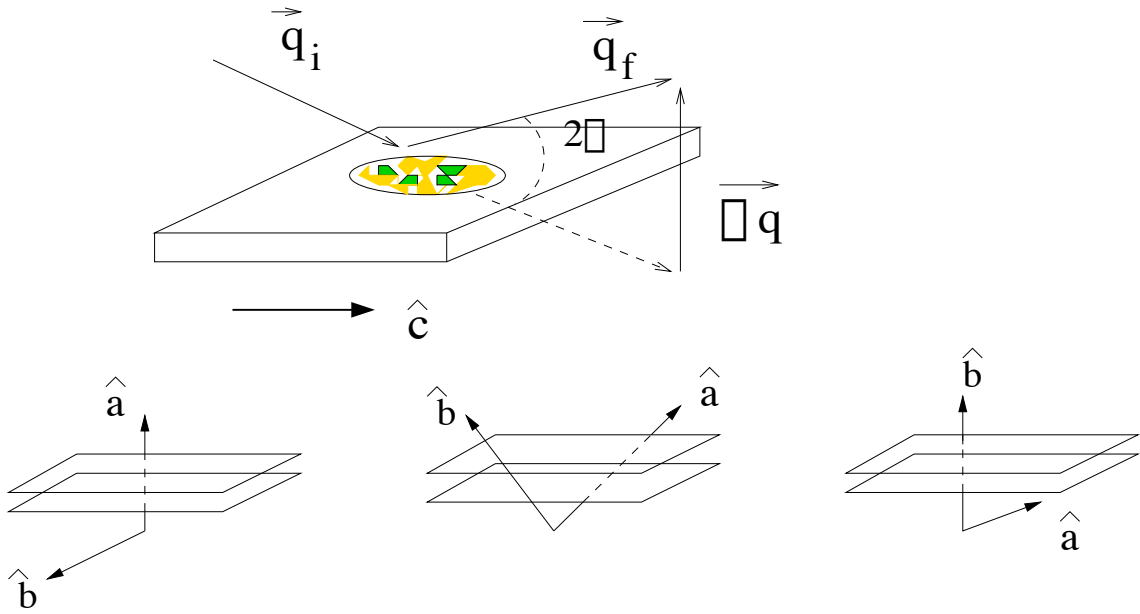


Figure 4.3: Scattering geometry used for checking the degree of magnetic alignment using powder x-ray diffraction.

$$\vec{\Delta}q = \vec{g}_{hkl} = \frac{2\pi}{d_{hkl}} \quad (4.10)$$

which results in the Bragg Law, $2d_{hkl}\sin\theta = \lambda$. Here (h,k,l) are Miller indexes.

If the sample is oriented with the \hat{c} -axis in the plane of the sample cell, $\vec{\Delta}q \perp \hat{c}$ and only planes parallel to the \hat{c} -axis will Bragg diffract, i.e., only allowed $(h, k, 0)$ reflections will appear in the powder diffraction pattern. As shown in figure 4.3, since the orientation of the powder is random about the \hat{c} -axis, some powder will have the right orientation for, e.g., the allowed $(1, 1, 0)$ reflection; others will reflect, e.g., in the $(2, 0, 0)$ channel.

Figure 4.4 shows powder x-ray diffraction patterns for $\text{La}_{1.85}\text{Sr}_{0.15}\text{CuO}_4$ before and after magnetic alignment. The diffraction peaks are labeled within the $I4/mmm$ tetragonal space group. Aluminum peaks coming from the sample cell are denoted “Al”. The oscillatory background appearing mostly at low scattering angles in the aligned spectrum is due to scattering from the amorphous resin/kapton in the oriented sample. (Note: the scattered intensity of an amorphous solid contains an expression of the form $\int_0^\infty 4\pi r^2[\rho(r) - \rho_a]\sin qr/qr dr$, where $4\pi r^2\rho(r)$ is the radial distribution function, ρ_a the average atom density and q the momentum transfer [122]. Therefore

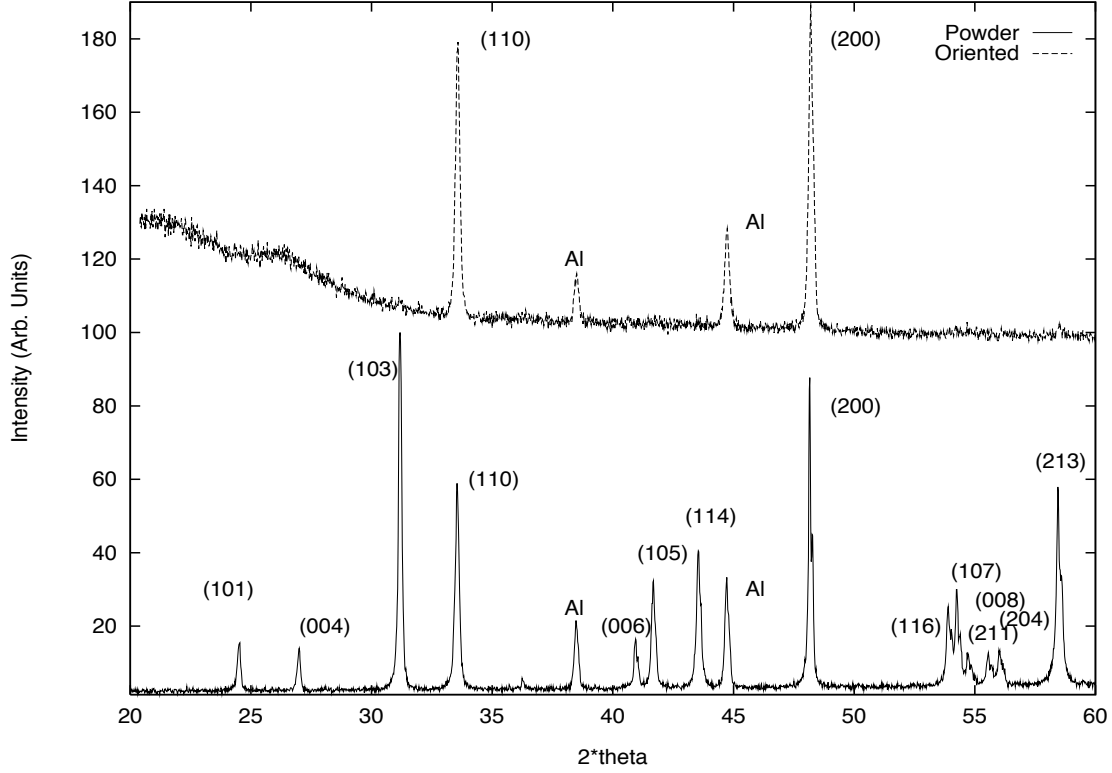


Figure 4.4: X-ray powder diffraction of $\text{La}_{1.85}\text{Sr}_{0.15}\text{CuO}_4$ before and after alignment.

the intensity decreases and oscillates with q , with local maxima positions being related to certain interatomic distances (short range order) being present in the amorphous resin/kapton.)

In order to determine the degree of alignment, let us assume a fraction $(1 - x)$ of the crystallites are perfectly aligned with their \hat{c} -axis along the field direction (random in the \hat{ab} plane) while x are randomly oriented. The intensities of the (103) and (110) reflections obtained in the “aligned” pattern are given by

$$\begin{aligned} I_{110} &= (1 - x)I_{110}^{\text{ali}} + xI_{110}^{\text{ran}} \\ I_{103} &= (1 - x)0 + xI_{103}^{\text{ran}} \end{aligned} \quad (4.11)$$

since for a perfectly \hat{c} -aligned powder the (103) reflection vanishes for the scattering geometry used (see fig. 4). Ratios of peak intensities can be accurately measured from the aligned and random powder patterns (not so absolute intensities which depend, e.g., on the amount of sample in the beam). From eq. 4.11 we obtain

$$\frac{I_{110}}{I_{103}} = \frac{(1 - x)}{x} \frac{I_{110}^{\text{ali}}}{I_{103}^{\text{ran}}} + \frac{I_{110}^{\text{ran}}}{I_{103}^{\text{ran}}} \quad (4.12)$$

For a randomly oriented powder the \hat{c} -axis can point in any direction of the 4π solid angle with equal probability, as does \hat{n}_{110} , a unit vector representing the (110) planes. For \hat{c} -axis oriented powder, however, the \hat{n}_{110} unit vector can only be oriented perpendicular to the field direction and hence spanning a 2π angle. It follows from this that $I_{110}^{\text{ali}} = 2I_{110}^{\text{ran}}$ and then

$$\frac{I_{110}}{I_{103}} = \frac{(2-x) I_{110}^{\text{ran}}}{x I_{103}^{\text{ran}}} \quad (4.13)$$

The ratios are then determined from the measured intensities (areas under the peaks after background subtraction) using the random and aligned diffraction patterns. In this way I obtained $(I_{110}/I_{103}) = 20 \pm 9$, where an average value and a standard deviation are obtained from the different samples checked ($x = 0.1, 0.15, 0.25, 0.3$). In addition, $(I_{110}^{\text{ran}}/I_{103}^{\text{ran}}) = 0.48$ resulting in a value of $x = 0.05 \pm 0.02$. It can be concluded that the degree of alignment of the samples is about 95%.

4.2.2 Electron diffraction study of $La_{1.85}Sr_{0.15}CuO_4$

As part of the sample characterization procedure, I performed an electron diffraction study on the $x = 0.15$ sample as a function of temperature, to determine the temperature at which the LTO to HTT phase transition is completed in this sample. A neutron diffraction study on a sample from the same batch was performed by Radaelli *et.al* [20] but structural data were obtained only at 10K, 70K and 295K. The orthorhombic splitting exists at 70K and is absent at 295K, indicating the phase transition is completed in between those temperatures. The actual temperature of the LTO to HTT phase transition is of importance here since a detailed temperature and polarization dependent XAFS study was performed on the $x = 0.15$ sample to study the nature of the temperature-induced LTO to HTT phase transition.

The electron diffraction experiment was performed using a Philips 430 transmission electron microscope (TEM) at the Materials Science department of the University of Washington. The microscope was operated at 200kV accelerating voltage and a low temperature (liquid N₂) specimen holder was used for measurements in the 100K-300K temperature range. Figure 4.5 shows the schematics of the TEM optics. The fundamentals of electron diffraction in the TEM are not discussed here and can be found elsewhere [123].

As shown in figure 4.5, electrons that are Bragg diffracted in the specimen are focussed by the objective lens and a diffraction pattern is obtained at the back focal

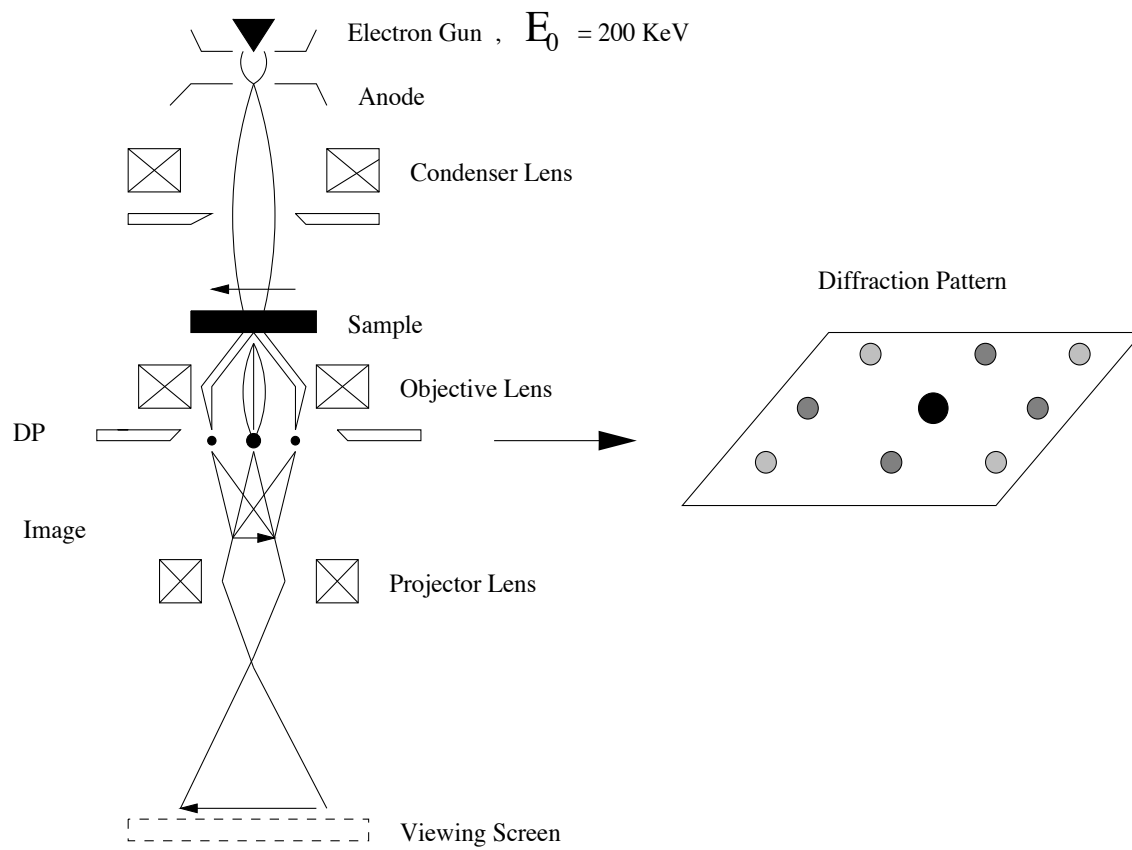


Figure 4.5: Schematic view of the TEM used for the temperature dependent electron diffraction study of $\text{La}_{1.85}\text{Sr}_{0.15}\text{CuO}_4$.

plane of the objective lens. A magnified image of this pattern can be projected onto the viewing screen by means of intermediate and projector lenses. By placing an aperture in the image plane, the region of the sample from which diffraction is obtained can be limited. This is called selected area diffraction (SAD) and the patterns shown here are obtained in this way. An effective camera length L is defined so as the magnification factor for the projected diffraction pattern on the screen is λL . Here λ is the wavelength of the incoming electrons and L is determined by the magnifications introduced by the various imaging lenses in the column. This definition becomes clearer from figure 4.6. Since the microscope optics limit the planes from which diffraction is obtained to only those nearly parallel to the zone axis ($\leq 1 - 2^\circ$) [123],

$$r = L \tan 2\theta \approx L \sin 2\theta = L(\lambda/d_{hkl}) = g_{hkl}(\lambda L) \quad (4.14)$$

where the relations $2d_{hkl}\sin\theta = \lambda$ (Bragg's law) and $g_{hkl} = 1/d_{hkl}$ were used.

Using this relations and the electron diffraction work of Zhu *et. al* [76] on the closely related $\text{La}_{1.88}\text{Ba}_{0.12}\text{CuO}_4$ system, I was able to show that the diffraction patterns shown in figure 4.7 correspond to a $\langle -110 \rangle$ zone axis (Z.A.) (the incident beam is along the zone axis direction) and a full indexing of the patterns, including the superlattice reflections appearing in the LTO phase was obtained. It is the disappearance of the superlattice reflections in the HTT phase that allowed us to determine the phase transition temperature.

Indexing was done within the $Cmca$ orthorhombic space group (No. 64) for the LTO phase ($a=5.3247$, $b=13.197$, $c=5.3486$) and for consistency diffraction spots in the tetragonal HTT phase are indexed using the $\sqrt{2}$ expanded cell ($a=c=5.342$, $b=13.23$). Note that in $Cmca$ notation the b -axis becomes the long axis of the unit cell. The reflections allowed in the HTT phase are referred to as fundamental.

Among all the reflections allowed by the space group, only those planes whose r.l.v are perpendicular to the zone axis will appear in the diffraction pattern (see figure 4.6). For a $\langle -110 \rangle$ Z.A.,

$$(-1, 1, 0) \cdot (h, k, l) = 0 \text{ or } -h + k = 0 \quad (4.15)$$

Table 4.1 lists the first five fundamental reflections (allowed in both HTT and LTO space groups) which satisfy eq. 4.15, together with their respective interplanar spacing and r.l.v. The interplanar spacing in the tetragonal phase is given by

$$\frac{1}{d^2} = \frac{h^2 + l^2}{a^2} + \frac{k^2}{b^2} \quad (4.16)$$

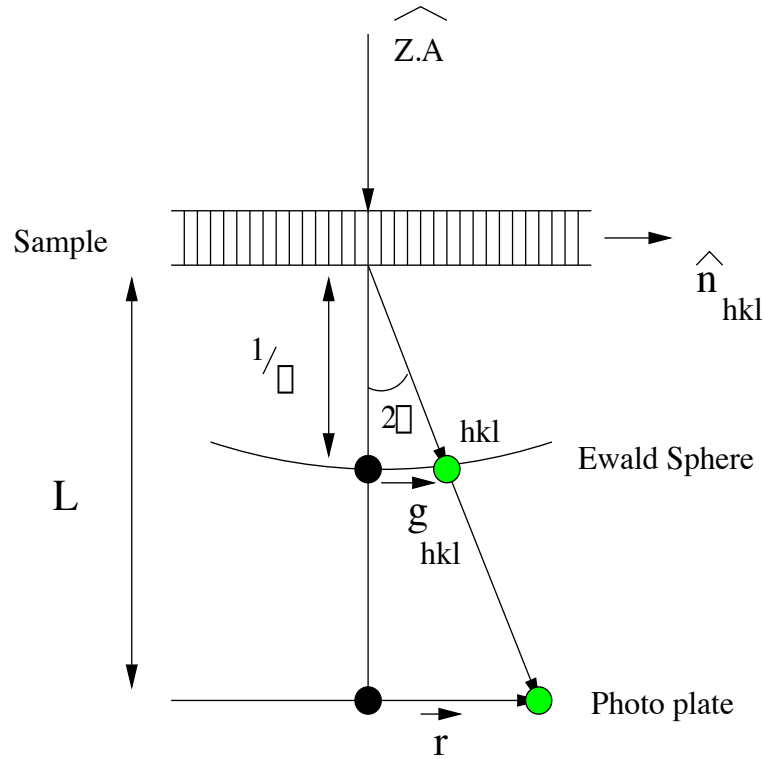


Figure 4.6: Schematic diagram of the formation of a diffraction pattern in the TEM. Note that for 200keV electrons the radius of the reflecting sphere is quite large, $\lambda = 0.0251 \text{ \AA}$; $1/\lambda = 39.84 \text{ \AA}^{-1}$ and then a number of reciprocal lattice points can be quite close to the sphere and appear in the diffraction pattern.

In figure 4.7 the first five magnified r.l.v are labeled $r(1 - 5)$. We want to prove that these five fundamental reflections correspond to the (h, k, l) values listed in table 4.1. Since these magnified vectors are proportional to their true r.l.v (eq. 4.14), the ratios of the distances on the film, $r_i/r_1, i = 2, 3, 4, 5$ has to correspond to the ratios $g_i/g_1, i = 2, 3, 4, 5$ shown in table 4.1, if the indexing is done correctly. In addition, the angles between magnified r.l.v have to match the true angles formed by their true counterpart r.l.v.

Table 4.2 shows the ratios r_i/r_1 as obtained from directly measuring on the film and their comparison to the true ratios obtained from table 4.1.

To reassure that the indexing is done properly, I calculated the angles formed by the above mentioned r.l.v and compared them to the values measured on the film.

Table 4.1: First five fundamental reflections allowed for both LTO and HTT phases for a $\langle -110 \rangle$ Z.A.

(h, k, l)	$d(\text{Å})$	$g = 1/d(\text{Å}^{-1})$
111	3.63	0.275
002	2.67	0.374
220	2.47	0.404
222	1.81	0.551
113	1.68	0.596

Table 4.2: Comparison between experimentally determined ratios of magnified r.l.v with their true ratios for a $\langle -110 \rangle$ Z.A. Here $i = 2, 3, 4, 5$.

r_i/r_1	1.33	1.42	1.97	2.12
g_i/g_1	1.36	1.47	2.00	2.16

The angles are calculated using the expression

$$\cos\theta = \frac{g_i \cdot g_j}{g_i g_j} = \frac{\frac{1}{a^2}h_i h_j + \frac{1}{b^2}k_i k_j + \frac{1}{c^2}l_i l_j}{\sqrt{\left[\left(\frac{h_i^2}{a^2} + \frac{k_i^2}{b^2} + \frac{l_i^2}{c^2}\right)\left(\frac{h_j^2}{a^2} + \frac{k_j^2}{b^2} + \frac{l_j^2}{c^2}\right)\right]}}. \quad (4.17)$$

Table 4.3 compares the angles between the different magnified, experimental r.l.v and their true, theoretical values.

The very good agreement shown in tables 4.2& 4.3 indicates that the indexing is correct.

Now to the superlattice reflections allowed in the LTO orthorhombic phase. These reflections become allowed due to the lowering of crystal symmetry from tetragonal to orthorhombic resulting from the strain relieving appearance of tilts of the CuO_6 octahedra as the temperature is lowered. These tilts result in a doubling of the unit cell.

For a $\langle -110 \rangle$ Z.A., the allowed superstructure reflections satisfy [76] $h + k = 2n$; $n = 0, 1, 2, \dots$ ($Cmca$ notation). Some of these reflections are shown in figure 4.7

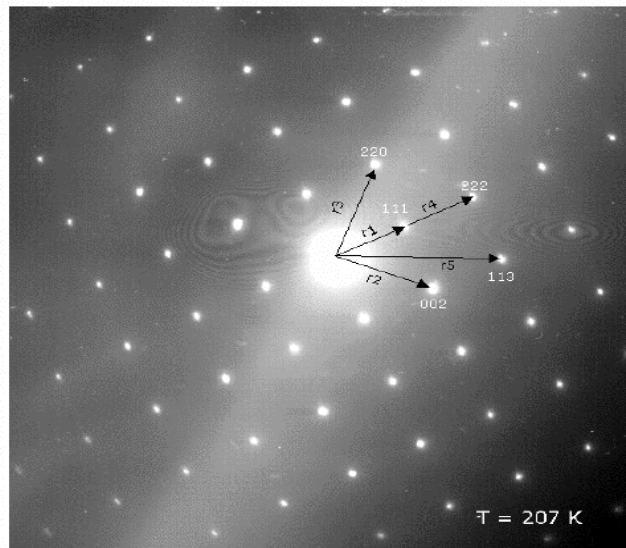
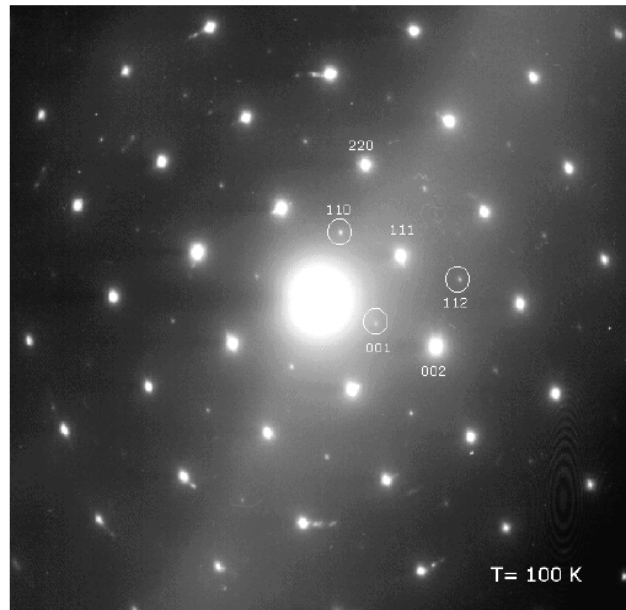


Figure 4.7: Selected area diffraction patterns of $\text{La}_{1.85}\text{Sr}_{0.15}\text{CuO}_4$ in the LTO phase ($T=100\text{K}$) and in the HTT phase ($T=207\text{K}$). Patterns taken at 200kV accelerating voltage and $L=950$ mm nominal camera length. Superstructure reflections in the LTO phase are circled. The lattice parameters in both phases are nearly the same but the magnification used to scan the pictures is different.

Table 4.3: Angles measured between r.l.v and their comparison to the respective theoretical values.

$\angle[(h_i, k_i, l_i), (h_j, k_j, l_j)]$	Experimental ($^\circ$)	Theoretical($^\circ$)
$\angle[(002), (111)]$	48	47.28
$\angle[(220), (111)]$	43	42.69
$\angle[(222), (111)]$	0	0
$\angle[(113), (111)]$	28	27.43

with white circles. Those are (001), (110), (112), (221),

The experimental ratio measured on the film is $r_{112}/r_{111} = 1.5$ while the theoretical ratio $g_{112}/g_{111} = 1.54$ (the orthorhombic modification of eq. 4.16 is used here). The experimental angle, $\angle[(112), (111)] = 20^\circ$ while the theoretical value is 19.0° . Again the good agreement indicates the success of the indexing procedure.

Diffraction patterns at 181K, 198K and 207K are shown in figure 4.8. The completion of the LTO to HTT phase transition, as indicated by the disappearance of the LTO superstructure reflections is found to occur at $T=200\pm 10$ K.

Note that the indexing of the patterns cannot be done based on the knowledge of the nominal camera length and its resulting magnification factor (λL), as the calibration of the microscope could be wrong. The actual camera length can be determined *a posteriori* by plotting r_{hkl} (as directly measured on the negative) vs. $1/d_{hkl}$ (see eq. 4.14). The slope obtained is the magnification factor. The camera length calibration for the patterns shown here is shown in figure 4.9. Noting that $\lambda = 0.0251 \text{ \AA}$, a camera length of $L=841$ mm is obtained, compared to the nominal camera length $L=950$ mm.

4.3 The $La_{2-x}Ba_xCuO_4$ system

Oriented samples for polarized XAFS measurements were prepared for the La, Ba and Cu *K*-edges of $La_{1.875}Ba_{0.125}CuO_4$ and $La_{1.85}Ba_{0.15}CuO_4$. The ceramics were prepared at the Materials Science department of the University of Washington by Fatih Dogan.

Powders of $La_{2-x}Ba_xCuO_4$ were synthesized by the combustion technique to achieve a high grade of chemical homogeneity. Starting compounds, the appropri-

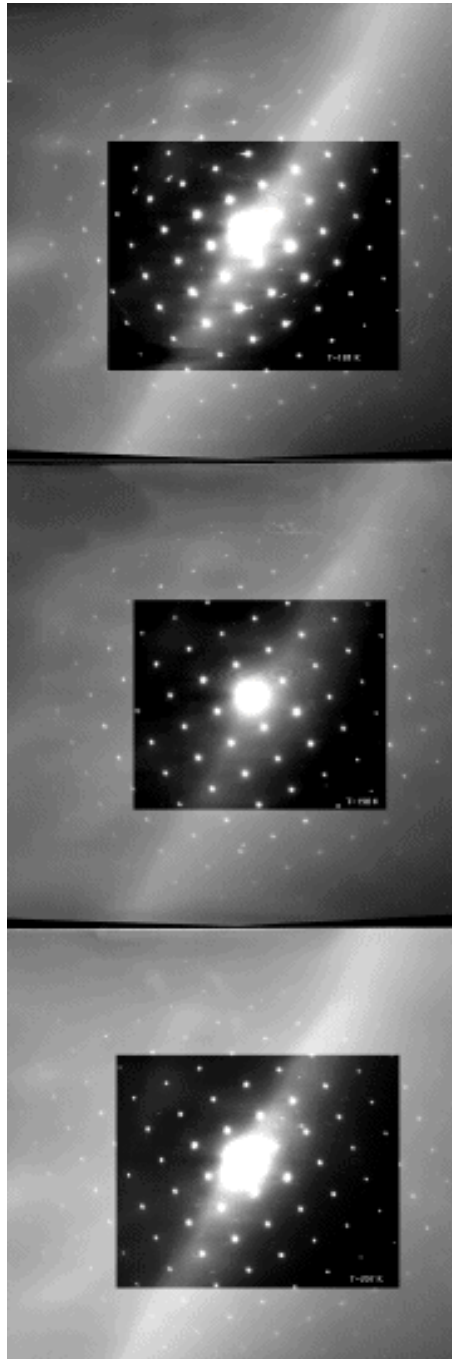


Figure 4.8: Sequence of selected area diffraction patterns at three different temperatures around 200K. From top to bottom: $T=181\text{K}$, 198K , 207K .

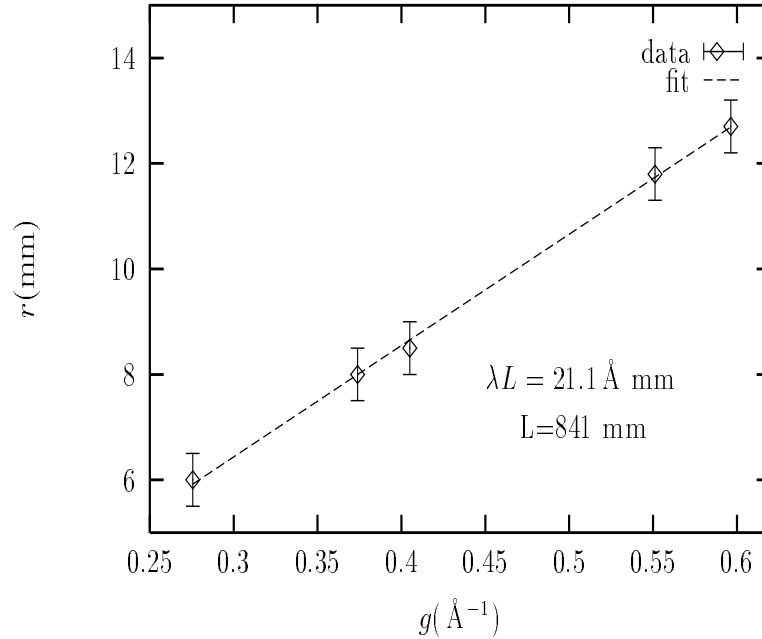


Figure 4.9: Camera length calibration for the patterns shown in figures 4.7& 4.8. The magnified reciprocal lattice vectors were measured directly from the negative.

ate mixtures of La, Ba and Cu nitrates, were dissolved in water along with the appropriate amount of sucrose to obtain a highly concentrated solution. The solution was dried and pyrolyzed on a hot plate. The precursor powders were then calcined at 900°C and pressed into cylindrical pellets (~ 3 grams each). The melting temperature of the powders was 1180°C , as determined by thermogravimetical analysis (TGA). Sintering of the samples took place at 1140°C for 4 days in order to achieve a larger grain size. The sintered samples were slowly cooled with a cooling rate of $1^{\circ}\text{C}/\text{min}$ to room temperature.

A full sample characterization was required for these samples. First, x-ray powder diffraction was performed on ground pellets to confirm (a) the absence of impurity phases and (b) that the lattice parameters obtained agree with previously published values for this system. As lattice parameters depend on Ba content (Ba substitutes for La), they indicate whether incorporation of Ba into the lattice was properly achieved. Second, magnetic measurements were made to determine the superconducting transition temperature, T_c . Since the dependence of T_c on Ba and oxygen content is much stronger than that of the lattice parameters [61, 75, 124], this is a better measurement of the effective hole content of the sample.

4.3.1 Fitting of x-ray powder diffraction patterns

Lattice parameters were obtained by fitting the diffraction patterns with a sum of Lorentzian lines in addition to a straight line to account for the background. Fits were done using the program PHIT. [125] Two Lorentzian lines were used for each Bragg reflection, since both Cu K_{α_1} and K_{α_2} are present in the x-ray beam. The relative intensities of the α_1, α_2 lines were set to their relative content in the beam, $\alpha_2/\alpha_1=0.5$; their widths were set to be the same. The centroids of each Bragg reflection (h,k,l) were related to the lattice parameters and the x-ray wavelengths by

$$\begin{aligned} (2\theta_{hkl})_{\alpha_1} &= 2\sin^{-1}\left(\frac{\lambda_{\alpha_1}}{2}\sqrt{\frac{h^2}{a^2} + \frac{k^2}{b^2} + \frac{l^2}{c^2}}\right) + \text{offset} \\ (2\theta_{hkl})_{\alpha_2} &= 2\sin^{-1}\left(\frac{\lambda_{\alpha_2}}{2}\sqrt{\frac{h^2}{a^2} + \frac{k^2}{b^2} + \frac{l^2}{c^2}}\right) + \text{offset}. \end{aligned} \quad (4.18)$$

In this way a unique set of lattice parameters a, b, c is fit that optimizes the overall diffraction pattern.

The values $\lambda_{\alpha_1} = 1.5406 \text{ \AA}$ and $\lambda_{\alpha_2} = 1.54439 \text{ \AA}$ were used. An overall offset was used for the peak positions, to account for a possible systematic error in peak position introduced if the sample surface's height is not located at the center of rotation of the 2θ detector (the error introduced is larger at small scattering angles so in principle a 2θ -dependent offset is needed). Both $x = 0.125$ and $x = 0.15$ samples are tetragonal at room temperature [61, 75, 126] with the $I4/mmm$ space group (in this notation the c -axis is the long axis of the unit cell; $a = b$). The allowed (h, k, l) reflections are those shown in figure 4.10. A theoretical diffraction pattern using the lattice parameters reported by Jorgensen *et. al* for a $x = 0.15$ sample is also shown [126]. Aluminum peaks from the sample holder are labeled "Al" and were left out of the fit.

As shown in figure 4.10 no impurity phases are present in the pattern as all the diffraction peaks correspond to allowed reflections within the $I4/mmm$ space group. Table 4.4 contains the lattice parameters obtained in the fits. For comparison, values found in previous investigations by A. Moodenbaugh [61], E. Takayama [75] (x-ray diffraction) and J. Jorgensen [126] (Neutron diffraction) are also shown.

From table 4.4, the agreement in lattice parameters with previous work is quite good. However, as already mentioned, a more robust test of the Ba and oxygen content of the samples is a measurement of T_c .

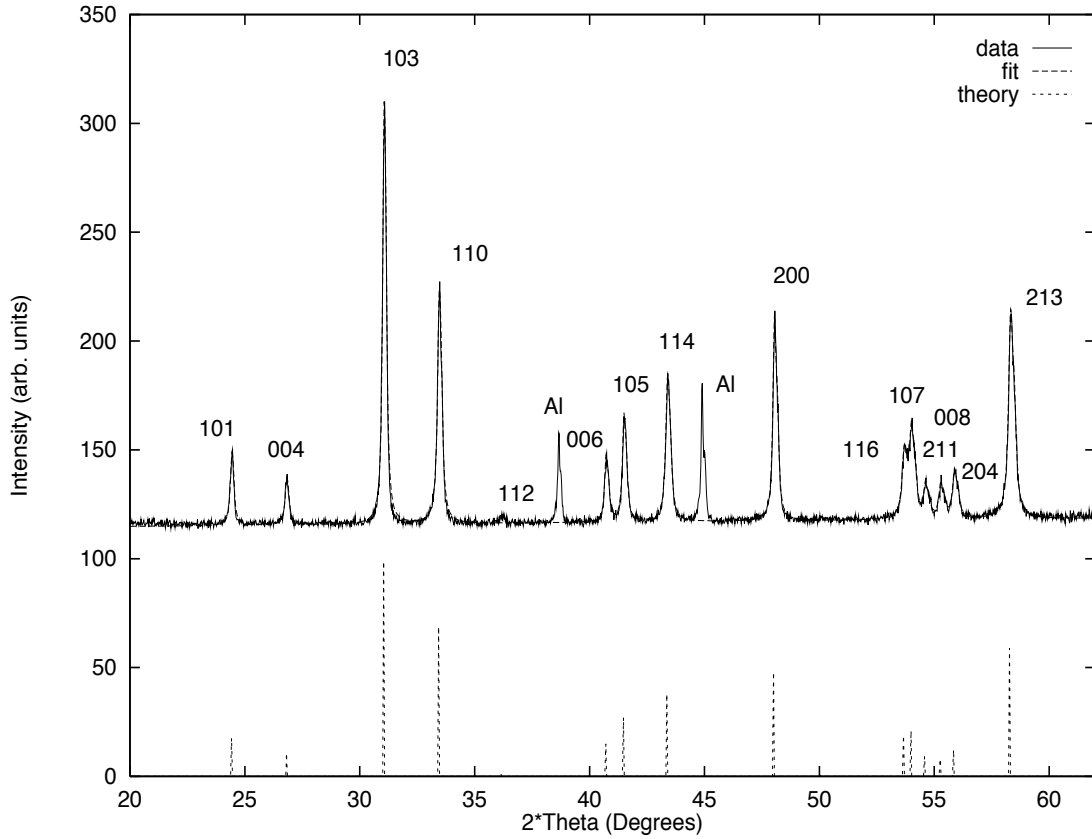


Figure 4.10: Powder diffraction pattern for $\text{La}_{1.85}\text{Ba}_{0.15}\text{CuO}_4$ at 300K together with the fit obtained by varying the lattice parameters. A theoretical powder pattern is also shown.

Table 4.4: Lattice parameters for the $I4/mmm$ tetragonal phase of $\text{La}_{2-x}\text{Ba}_x\text{CuO}_4$ as obtained by fitting the powder x-ray diffraction patterns. Results from other groups are shown for comparison.

	$x = 0.125$	$x = 0.15$
This work	$a = 3.791(1) \text{ \AA}$ $c = 13.289(5) \text{ \AA}$	$a = 3.784(1) \text{ \AA}$ $c = 13.283(5) \text{ \AA}$
Moodenbaugh	$a = 3.790(1) \text{ \AA}$ $c = 13.29(1) \text{ \AA}$	$a = 3.785(1) \text{ \AA}$ $c = 13.30(1) \text{ \AA}$
Jorgensen		$a = 3.7873(1) \text{ \AA}$ $c = 13.2883(3) \text{ \AA}$

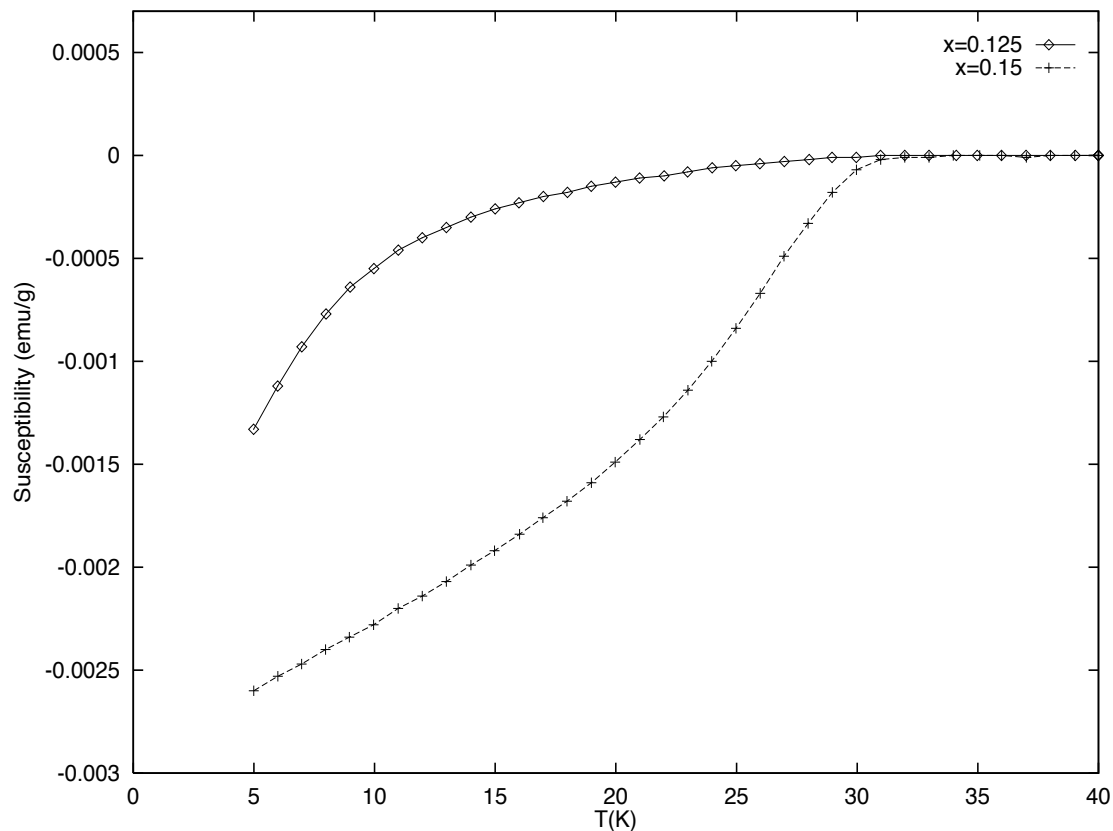


Figure 4.11: Zero field cooled magnetic susceptibility measurements on fine powder ($\sim 10\mu\text{m}$) of $\text{La}_{2-x}\text{Ba}_x\text{CuO}_4$.

4.3.2 Magnetic measurements of superconducting transition temperatures

Superconducting transition temperatures were measured by Arnie Moodenbaugh at the Materials Science department of Brookhaven National Laboratory by measuring DC magnetic susceptibility using a Quantum Design MPMS[©] SQUID magnetometer. On the order of 10 mg of fine powder ($\sim 10\mu\text{m}$ size) was fixed in a glue binder before the measurement. After samples were cooled in zero field (ZFC) a nominal DC $H=1$ Gauss field was applied and measurements were obtained on heating, typically in 1°C increments. Immediately after ZFC measurements, samples were measured on cooling in the same field (FC).

Figure 4.11 shows ZFC data for both $x = 0.125$ and $x = 0.15$ samples. FC data are within 5% (always smaller diamagnetic response) of those obtained for ZFC and are not plotted separately. The Meissner fraction (field-cooled diamagnetic fraction) always underestimates the superconducting phase fraction, due to flux pinning, flux

Table 4.5: Bulk onset values for T_c (as defined in the text) obtained from magnetic susceptibility measurements on our samples and their comparison to previous work.

	$x = 0.125$	$x = 0.15$
This work	10(1)K	30(1)K
Moodenbaugh	7(2)K	30(1)K
Takayama	5(1)K	30(1)K
Billinge	≤ 5 K	27(1)K
Rial	10(2)K	28(1) K

trapping and penetration length effects. The shielding fraction (zero-field cooled diamagnetic fraction) always overestimates the superconducting fraction due to screening of voids and non-superconducting regions of the sample [20, 45].

For very fine powder, especially one with a large fraction of single crystallites as is the case here, ZFC and FC measurements result in very similar results due to the lack of complex topology in the majority of the sample, i.e., flux pinning is a small factor.

As can be seen in figure 4.11, both samples show a diamagnetic response at about 30K (highest onset), where the signal first deviates from its normal state value. This broad onset has also been observed by other workers [61, 67, 75] and is attributed to a small fraction (few %) of the sample becoming superconductor. The bulk onset is defined here as the temperature at which the normal-state extrapolated susceptibility intercepts the extrapolated steepest slope of the transition. For our samples, the bulk onsets are 10 ± 1 K and 30 ± 1 K for $x = 0.125, 0.15$, respectively. Since T_c values reported in the literature depend on their definition (midpoint, onset, etc), I compare bulk onset values, as defined here, to those obtained in previous work by Moodenbaugh [124], Takayama [75], Billinge [67] and C. Rial [127]. This comparison is summarized in table 4.5.

The values obtained for our samples are in quite good agreement with previous work. The transition temperature obtained for the $x = 0.125$ sample, however, is somewhat higher than the lowest values attainable for fully oxygenated samples, $T_c \leq 5$ K. Thorough studies by Takayama *et. al* [75] and Moodenbaugh *et. al* [124] on the dependence of T_c on oxygen content show that for samples with Ba content

around $x = 0.125$, T_c *increases* when the oxygen content is reduced, whereas for Ba content around $x = 0.15$ it *decreases*. Based on these studies, a $T_c=30(1)$ K for the $x = 0.15$ sample indicates full oxygenation ($\delta \sim 0$ in $\text{La}_{2-x}\text{Ba}_x\text{CuO}_{4-\delta}$) while for the $x = 0.125$ sample with $T_c=10(1)$ K, an oxygen deficiency $\delta \leq 0.005$ cannot be ruled out. The minor effect that such oxygen reduction has on the structural properties of this sample is discussed in the work of Takayama *et. al.*

The possibility of our nominal $x = 0.125$ sample being fully oxygenated but having a slightly different Ba content was considered (e.g., $T_c \sim 10$ K for $x \sim 0.11$), but found less likely due to the increased disagreement between the lattice parameters measured here and those corresponding to the presumably different Ba content.

To conclude this section, M/H curves for both samples as obtained from the SQUID measurements as a function of applied H field at a fixed temperature are shown in figure 4.12. The apparent superconducting volume fraction is given by the slope of these curves at low magnetic fields. At higher magnetic fields, $H \geq H_{c1}(T)$ with $H_{c1}(T)$ the lower critical field of a type II superconductor, this volume fraction decreases as vortex lines penetrate the sample. This is more clearly seen for the $x = 0.125$ sample measured at $T=2$ K, close to T_c (figure 4.11), where $H_{c1}(2K) \leq 20G$. For the $x = 0.15$ sample, $H_{c1}(5K) \leq 30G$. For comparison, the effective $H_{c1}(4K)$ at the polycrystalline grain boundaries of sintered pellets of $\text{La}_{2-x}\text{Sr}_x\text{CuO}_4$ was found by Nagano *et. al* to be in the range 1-10G. It is expected that the less complex topology of a fine powder will result in higher values of $H_{c1}(T)$.

For a powder sample of density ρ , the ideal diamagnetic response for a 100% superconducting volume is given by

$$\chi_{\text{ideal}} = \frac{M}{H} = \frac{-1}{4\pi\rho}(\text{emu/g}) = -1.1 \times 10^{-2} \text{emu/g} \quad (4.19)$$

since $\rho = 7.06 \text{gr/cm}^3$ for the two samples studied here. The apparent superconducting fractions obtained from the slopes at low field in figure 4.12 are $(M/H)_{0.125} = -8.0(3) \times 10^{-4} \text{ emu/g}$ and $(M/H)_{0.15} = -1.1(2) \times 10^{-3} \text{ emu/g}$, giving a $\sim 10\%$ apparent volume superconducting fraction. This low fraction by no means implies that the samples are not good superconductors; they are due to the powder crystallite size being on the order of the penetration depth of the magnetic field, $\lambda(T)$. Similar values of apparent superconducting volume fractions were measured by Nagano *et. al* in $\text{La}_{2-x}\text{Sr}_x\text{CuO}_4$, using powder of 1-4 μm size [45]. There, $\lambda(0) \sim 1 - 2\mu\text{m}$. Even though the powder used here is slightly larger ($\sim 10\mu\text{m}$), the lower T_c 's of

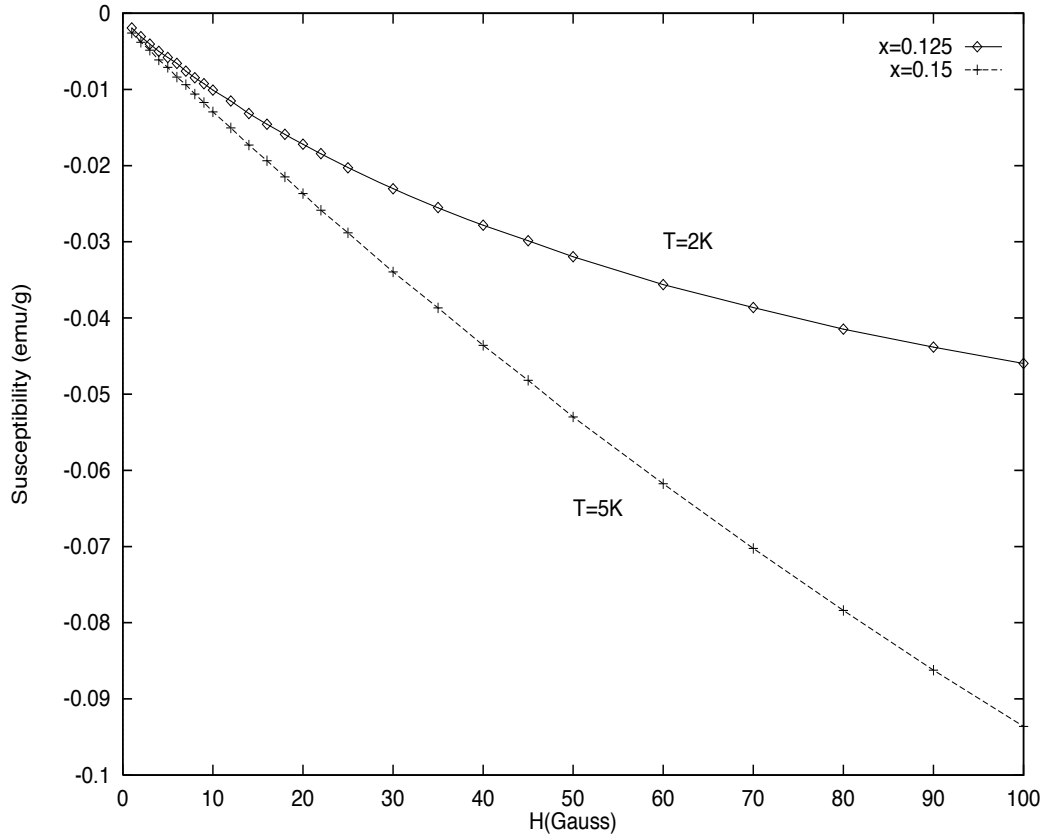


Figure 4.12: M/H curves on the $\text{La}_{2-x}\text{Ba}_x\text{CuO}_4$ system used to estimate the superconducting volume fraction of the samples.

the $\text{La}_{2-x}\text{Ba}_x\text{CuO}_4$ system would result in larger penetration depths. In addition, since the penetration depth is inversely proportional to the square root of the carrier concentration [45] (the larger the carrier density the larger the supercurrent density and hence the cancellation of the penetrating field is achieved over a shorter distance from the surface) a larger Ba content (higher hole carriers content) will result in a shorter penetration length and then a larger apparent SC volume fraction. This is indeed observed in our samples, as the apparent SC volume fraction of the $x = 0.15$ sample is larger than the $x = 0.125$ one.

4.3.3 Obtaining very fine powder in $\text{La}_{2-x}\text{Ba}_x\text{CuO}_4$

In what follows the sample preparation for alignment is described. Only the differences from the procedure described above for $\text{La}_{2-x}\text{Sr}_x\text{CuO}_4$ are discussed.

One major problem of the $\text{La}_{2-x}\text{Ba}_x\text{CuO}_4$ system is the absence of significant

grain growth during sintering. Whereas grain sizes of $\sim 10 - 50\mu\text{m}$ can be easily achieved in $\text{La}_{2-x}\text{Sr}_x\text{CuO}_4$ at sintering temperatures $\sim 100^\circ\text{C}$ below the melting point in ~ 24 hours [20, 45], the largest grain size we could obtain in $\text{La}_{2-x}\text{Ba}_x\text{CuO}_4$ after sintering for 4 days at $\sim 40^\circ\text{C}$ below the melting point was $\sim 2 - 5\mu\text{m}$ (see figure 4.13). Similar small grain sizes were reported before for this system under similar sintering conditions. [61, 67]

For the magnetic alignment procedure to succeed each powder particle has to be a single crystal. Due to the small polycrystalline grain size of the sintered pellets, a new procedure was developed that assures that only very fine powder ($\leq 5\mu\text{m}$) is obtained. The sintered pellets were ground in a porcelain mortar. The resulting powder was added to a beaker containing dehydrated alcohol. A well dispersed powder was obtained in the liquid by stirring the mixture on a magnetic stirring plate for 5 minutes. After the stirring is stopped, the heavy particles will precipitate to the bottom of the beaker while the light ones (smaller) will be distributed along the height of the beaker, forming a gradient according to their mass. However, it will even take some time for the upper layer of the solution to contain only the desired particle size. This time was found by extracting a small sample from the upper layer (with the help of a syringe) at different time intervals and examining the particle size under an optical microscope. It was found that about 2 minutes was enough for the upper layer to be composed of particles $\sim 1 - 2\mu\text{m}$ size.

After separation of the upper layer, both solutions containing fine and coarse powders were dried on a hot plate at $\sim 120^\circ\text{C}$. The dried coarse powder was reground and the procedure repeated about 10 times (~ 10 mg of fine powder can be obtained in each interaction; a “mass production” plan was used using 10 beakers, 2 hot plates and 2 magnetic stirring plates). X-ray powder diffraction was retaken on leftover powders to ensure no structural changes had occurred during the procedure.

In addition to each powder particle being a single crystal, care has to be taken to ensure these particles don't form agglomerates, as that will result in misalignment since the rotation of each of the agglomerated particles in the field will be correlated. Agglomeration occurs via weak electrostatic interactions due to charge accumulation on the surface of the particles (these ceramics are bad conductors). The smaller the particles, the larger their surface to volume ratio and this effect becomes more important. Since the powder has to be dispersed into the resin for alignment, chances are that this mixing would break those weak bonds and the particles will be isolated.

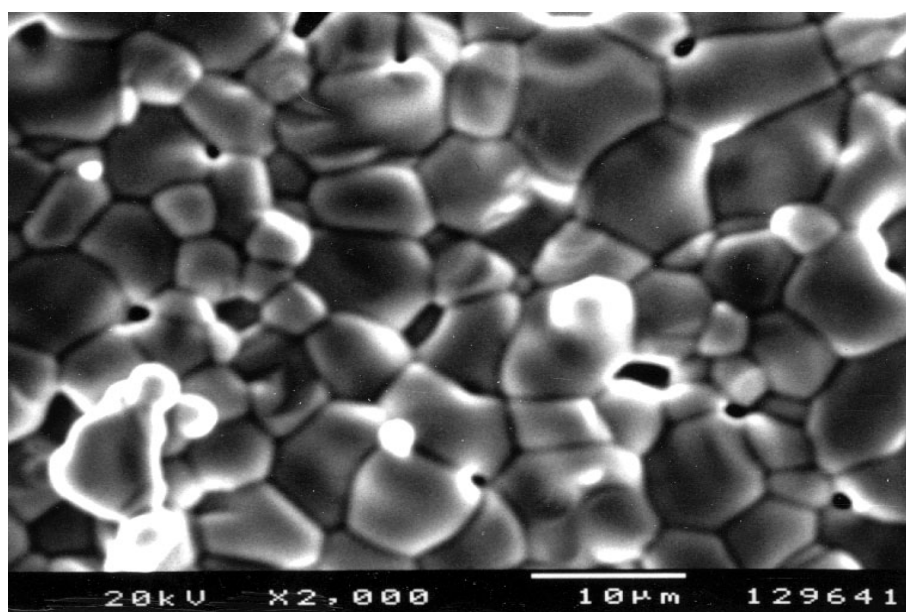


Figure 4.13: Scanning electron microscopy (SEM) photograph of a sintered pellet's surface of $\text{La}_{1.875}\text{Ba}_{0.125}\text{CuO}_4$ after annealing for 4 days at 1140°C . The scale bar indicates that a typical grain size is $\sim 2 - 5\mu\text{m}$.

Table 4.6: Calculation of the desired sample thickness for La, Ba and Cu K -edges of $\text{La}_{1.875}\text{Ba}_{0.125}\text{CuO}_4$.

	$\mu(\text{cm}^{-1})$	$\Delta\mu(\text{cm}^{-1})$	$x_{sc}(\mu\text{m})$	μx_{sc}	$\Delta\mu x_{sc}$
La (38925 eV)	139	102.4	97.6	1.36	1
Ba (37442 eV)	40.2	6.99	350	1.4	0.24
Cu (8979 eV)	1599	277.8	15.6	2.5	0.43

To reassure that isolated particles would be obtained at the end, I thoroughly mixed the fine powder with graphite powder ($\leq 1 - 2\mu\text{m}$ size) prior to mixing with the resin. This should help breaking the bonding forces as graphite conducts away the static charge. The ratio of graphite to powder used is 25% by volume, somewhat larger than the 15% critical volume fraction for percolation in a random 3-dimensional medium. [128]

The importance of the procedure developed here is readily seen in figure 4.14, where the degree of alignment is compared for a sample prepared using powder that has been sieved through 400 mesh ($\sim 10 - 20\mu\text{m}$ grain size) and that obtained by using the new procedure described above. Whereas a $\lesssim 70\%$ degree of alignment is obtained for the sieved powder, the new procedure results in a $\gtrsim 97\%$ degree of alignment.

Samples were prepared for the $\text{La}_{2-x}\text{Ba}_x\text{CuO}_4$ system for all La, Ba and Cu K -edges. Table 4.6 lists the calculated total absorption cross section μ , the change in absorption across the edge, $\Delta\mu$, the desired superconducting sample thickness, x_{sc} , and the corresponding total absorption and edge step, μ and $\Delta\mu x$, for the three edges in $\text{La}_{1.875}\text{Ba}_{0.125}\text{CuO}_4$.

As can be seen in table 4.6, different sample thicknesses are needed for the different edges, e.g., one absorption length at the Ba K -edge is about 3.5 times larger than that at the La K -edge and about 40 times that at the Cu K -edge. Hence a different sample thickness was prepared for each edge experiment.

For the Ba samples the large absorption length requires a significant fraction of the volume of the sample cell to be filled with the superconducting sample, resulting in a resin to sample volume ratio of about 4. This could compromise the quality of the sample, as the superconducting powder has to be well dispersed into the resin. As

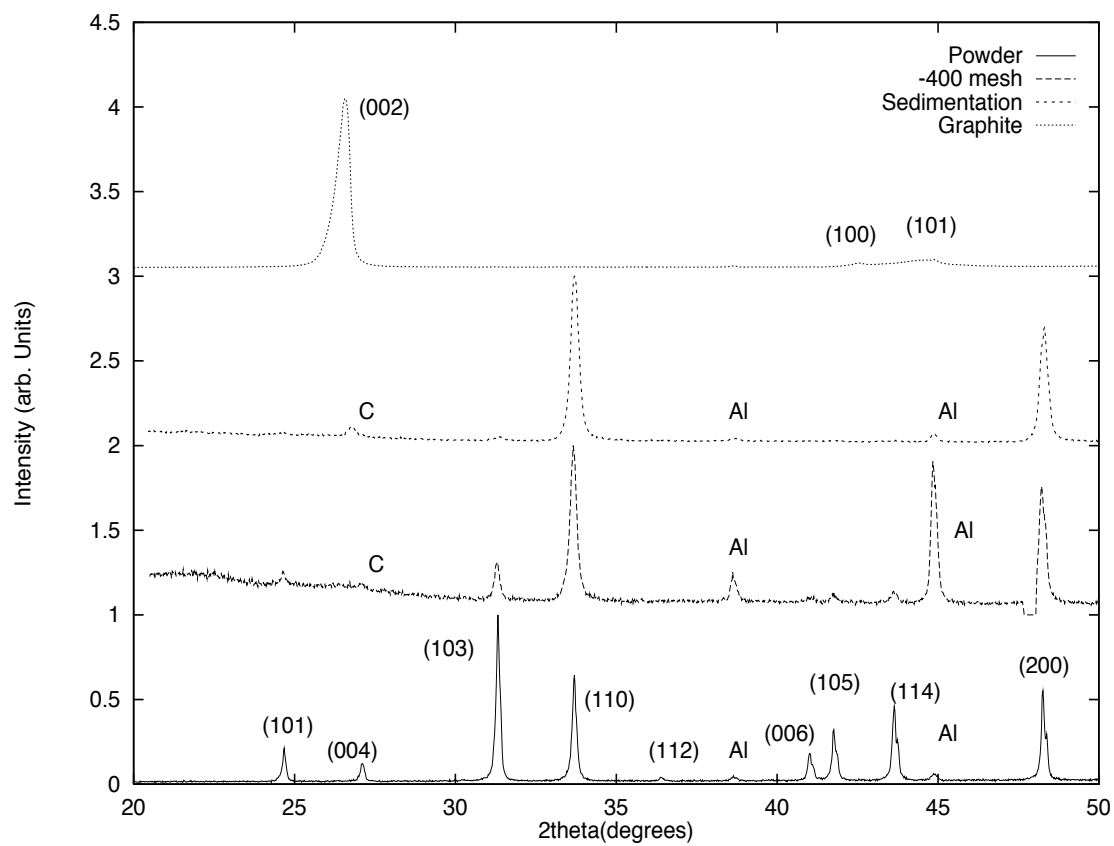


Figure 4.14: X-ray diffraction from an aligned -400 mesh sieved sample compared to a sedimented one for $\text{La}_{1.875}\text{Ba}_{0.125}\text{CuO}_4$. The random powder pattern is also shown together with a pattern obtained from pure graphite powder. Graphite peaks in the sample are labeled “C”; aluminum peaks from the sample holder are labeled “Al”.

mentioned above, the $\text{La}_{2-x}\text{Sr}_x\text{CuO}_4$ samples had a resin to superconductor volume ratio of 20. To increase this ratio, a sample cell with a ~ 3 times larger thickness was made for the Ba K -edge samples (1/6 ") resulting in a resin to sample volume ratio of about 11. This was enough to achieve a very well dispersed mixture. Even though this sample cell could have been made even thicker to further optimize the sample thickness for the Ba measurement, constraints in available space in the cryostat and vacuum system used for the low temperature measurements prevented me from doing so. The sample thickness listed in table 4.6 for the Ba measurement is optimized within this constraint and should be good enough for a successful experiment.

Figure 4.15 shows absorption coefficient measurements for the three different edges. Good agreement was obtained between the measured and desired sample thicknesses.

4.4 Why not single crystals?

The use of single crystals is plagued with a series of experimental difficulties. One of these is the occurrence of strong Bragg scattering for particular photon energies (wavelengths) at which the Bragg condition is satisfied by some set of diffracting planes in the sample ($2d\sin\theta_B=n\lambda$). This will introduce glitches in the measured absorption coefficient as intensity is being taken away or into the detection chamber. Since Bragg peaks have a very sharp angular distribution ($\sim 0.1^\circ$) a sample rotation of about 1° would destroy the Bragg condition and the Bragg peak will move to a different energy (wavelength) position in the spectrum. Since $\lambda \sim 1/E$, the Bragg peak will reappear at $\Delta E = E\Delta\theta/(\tan\theta_B)$. For example, at 10 KeV and for $\theta_B \sim 45^\circ$, $\Delta E \sim 170\text{eV}$.

The effect of such a small rotation on the amplitude of the XAFS signal is relatively small; as shown in appendix B, for K -edges $\chi \sim (\hat{\epsilon} \cdot \hat{r}_j)^2$ and hence $\Delta\chi/\chi = 2\tan\theta_j\Delta\theta$ which is of the order of 3% for a 1° change assuming $\theta_j \sim 45^\circ$, the angle between the electric field vector and the direction of the scatterer at \vec{r}_j . In this way, it is typically possible to obtain a Bragg-peak-free absorption spectrum over a small energy region (100-200 eV) which usually allows measuring high quality XANES (x-ray absorption near edge structure) data on single crystals [98]. An XAFS measurement, however, comprises an energy interval of about 1000-1500 eV and getting a clean spectrum over such a large energy range is nearly impossible with a stationary sample.

Single crystals of the $\text{La}_{2-x}(\text{Sr},\text{Ba})_x\text{CuO}_4$ family grow with the \hat{c} -axis perpendic-

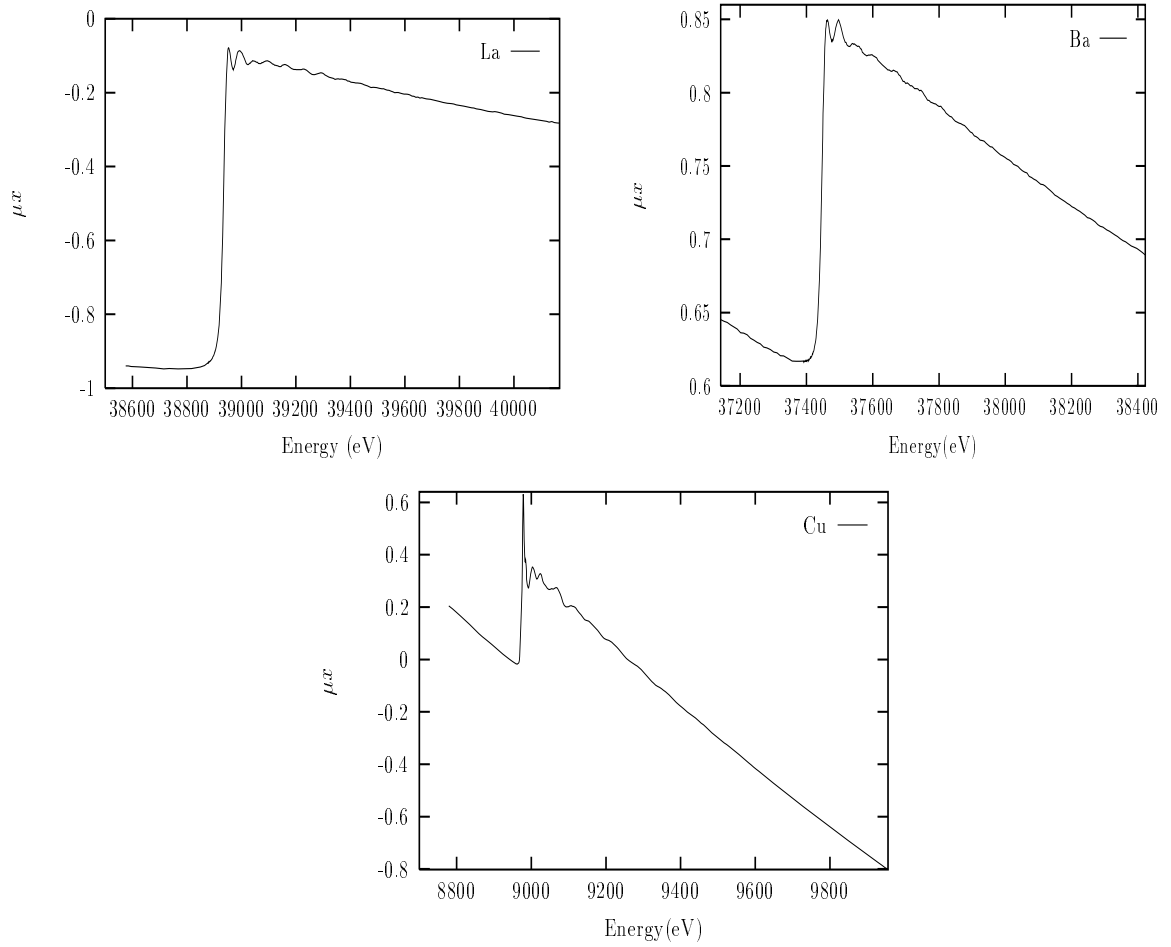


Figure 4.15: La, Ba and Cu K -edges of $\text{La}_{1.875}\text{Ba}_{0.125}\text{CuO}_4$ at $T=270\text{K}$, \hat{c} -polarization; $\Delta\mu_x = 0.86, 0.25, 0.4$, respectively.

ular to the face. It is then impossible to measure pure \hat{c} polarized XAFS; a mixture of \hat{c} and \hat{a} or \hat{b} XAFS is obtained instead. Since pure \hat{a} and \hat{b} polarizations can be measured, the \hat{c} XAFS can be obtained from the mixture by accounting for the angle-dependent weight of each component. This procedure, however, could be an additional source of systematic errors that we tried to avoid when planning an experiment.

Single crystals are usually too thick for a transmission geometry and require to be measured in fluorescence, an additional drawback. Modifying their thickness *a-posteriori* is a dangerous procedure as it might damage the crystal and introduce additional domains. The sample size (face) typically obtained for uniform, single-phase, mono-domain crystals is typically $\sim 1 \text{ mm}^2$ requiring the use of even smaller beams and then compromising the counting statistics.

Chapter 5

XAFS MEASUREMENTS OF $\text{La}_{2-x}\text{Sr}_x\text{CuO}_4$: ANALYSIS AND RESULTS

In this chapter, La K -edge polarized XAFS results on the local structural changes at the *dopant* (x) and *temperature* (T) induced LTO to HTT structural phase transitions are presented. Insight is gained into the nature of these phase transitions by combining information from XAFS and diffraction. It is found that the Sr-induced transition has displacive and disorder components while the temperature induced transition is purely of disorder character. Sr K -edge polarized XAFS results also presented here reveal the presence of strong lattice distortions around the dopant atoms that shed light into the role played by the Sr atoms in determining the structural and electronic properties of these cuprates. In particular, the neighboring apical oxygen to Sr is split into two sites showing that the hole donated by Sr is a polaron.

5.1 *The nature of the Sr-induced LTO to HTT structural phase transition*

5.1.1 *Experimental results*

As shown in the phase diagram of fig. 1.1, the addition of Sr to $\text{La}_{2-x}\text{Sr}_x\text{CuO}_4$ at low temperature induces a structural phase transition from orthorhombic LTO to tetragonal HTT at $x \sim 0.21$. [20] As already mentioned and shown in fig. 5.1, the LTO structure is mainly characterized by the presence of a coherent tilt pattern of the CuO_6 octahedra resulting in the lowering of symmetry and the doubling of the unit cell, as compared to the higher symmetry HTT structure. The phase transition was, till our measurements, understood as a purely displacive one, in which adding Sr introduces holes into planar Cu-O antibonding orbitals leading to a reduction of the Cu-O planar bond length and a related reduction in lattice mismatch between LaO and CuO_2 layers, resulting in the gradual decrease with Sr of the tilt angle of the CuO_6 octahedra to zero. As can be seen in fig. 5.1, the atomic displacements of the lower symmetry LTO structure result in changes in interatomic distances which

can be detected by XAFS.

From an XAFS point of view, the most suitable site to study the phase transition is the one whose interatomic distances show the largest changes with Sr content. Since the CuO_6 octahedra tilt about the Cu sites in a nearly rigid manner [20], the Cu-O distances remain almost unchanged in going from the LTO to HTT phase (e.g., the Cu-O(1) planar distance decreases by $\lesssim 0.02 \text{ \AA}$ in going from $x = 0.075$ to $x = 0.36$ at 10K). A single scattering (SS) XAFS study at the Cu K -edge would then be almost insensitive to the occurrence of the phase transition. Since the tilt angles involved are quite small ($\leq 5^\circ$), the changes expected in multiple scattering (MS) Cu K -edge XAFS at the phase transition are also small. In spite of this lack of sensitivity most of the XAFS work performed on the $\text{La}_{2-x}\text{Sr}_x\text{CuO}_4$ system up to date has been on the Cu K -edge, the reason being the simplicity of its local atomic environment. [129–132]

On the other hand, the La/Sr local environment is the most sensitive to the distortions induced by the structural phase transition, with changes in splitting of planar La-O(2) distances as large as 0.5 \AA (see fig. 5.1). This is mostly due to the tilt-induced in-plane atomic displacements of the O(2) oxygens at the apexes of the CuO_6 octahedra ($\lesssim 0.2 \text{ \AA}$) resulting in one short, two intermediate and one long La-O(2) planar distances. (Actually a small $\lesssim 0.04 \text{ \AA}$ correlated displacement of the La atoms contributes to the splitting as well [20]) Although ideal due to the large changes in distances involved, the complexity of the La/Sr near neighbor environment makes it a hard XAFS probe and the reason for not being studied until now. The La/Sr immediate environment in the LTO phase is composed of nine oxygens at six different distances, which, e.g., for the $x = 0.075$ sample at $T = 10\text{K}$ are in the range $[2.3, 3.0] \text{ \AA}$ (see fig. 5.1). The number of independent points (see eq. 2.13) in this r -region of interest for a typical k range $[3-14] \text{ \AA}^{-1}$ used here is $N_I \sim (2\Delta k \Delta r / \pi) \sim 5$, smaller than the number of parameters needed to successfully model the oxygen environment to the La atoms.

This drawback, however, is overcome here by the use of *oriented* samples. Because of the layered structure of these cuprates, by having the polarization vector of the x-rays along the long axis of the unit cell (\hat{b} in the $Cmca$ representation, \hat{c} in $Bmab$), the contribution to the XAFS of the nearly in-plane La-O(2) bonds is negligible (see eq. 2.4) and then only three oxygen distances contribute to the nearest neighboring XAFS (La-O(2) apical and two La-O(1) distances to the O(1) oxygens in the CuO_2 planes). The remaining in-plane La-O(2) distances can be found by analyzing the

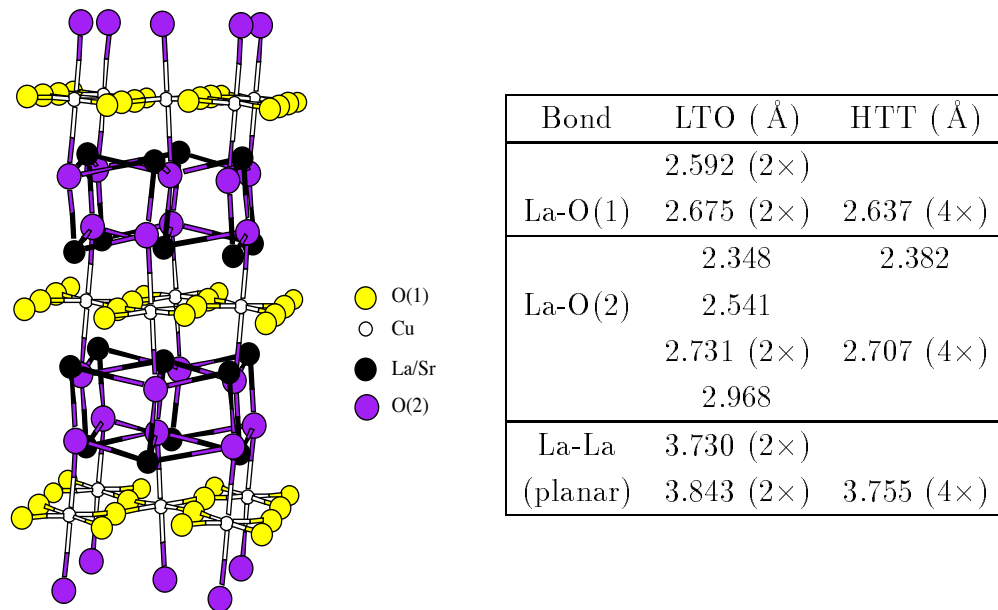


Figure 5.1: Schematic representation of the LTO structure. In the $Cmca$ representation, the vertical axis is the b axis and the a axis is perpendicular to the plane of the paper. The La-O and planar La-La interatomic distances are shown for $x = 0.075$ (LTO) and $x = 0.36$ (HTT) as obtained from neutron diffraction. [20] Degeneracies are shown in parenthesis.

XAFS for the in-plane polarization and setting the La-O(1) distances to the values found in the fitting of the long-axis polarization. (Since the La-O(1) bonds form a $\approx (44-48)^\circ$ angle with the long axis, they contribute to the XAFS in both polarizations)

A complete description of the sample preparation for the polarized measurements and their characterization can be found in chapter 4. For the x -induced phase transition at low temperature, La K -edge measurements were taken for $x = 0.075, 0.15, 0.2, 0.25, 0.3, 0.36$ at 10-20K. Measurements were done in transmission at beam line X-11A of the National Synchrotron Light Source using a Si(311) double crystal monochromator. Details on the experimental setup are given in chapter 3. The polarized XAFS spectra were measured by rotating the oriented samples relative to the polarization vector of the synchrotron radiation.

The experimental XAFS is analyzed using the UWXAFS3.0[©] analysis package [95] together with theoretical standards from FEFF6[©] [84,85] as described with some detail in chapter 2. Here only details relevant to the system under study are presented. Background removal is performed using the program AUTOBK [96] by minimizing, with respect to a FEFF6 standard, the low- r portion of the Fourier transformed $\tilde{\chi}(r)$ for frequencies below r_{bkg} . The standard is a FEFF6 calculation of $\chi(k)$ of the average structure as found in the neutron diffraction studies [20]. As an example, figure 5.2 shows absorption data for $x = 0.2$, \hat{b} -polarization (long axis) at T=20K, together with the background function obtained by AUTOBK. The parameters used in the background removal are shown in table 5.1. Typically at least two energy scans are measured for each Sr content, polarization condition and temperature to evaluate the level of statistical noise. Figure 5.3 shows reproducibility scans for $x = 0.2$ at 20K in both polarization conditions. $k\chi(k)$ data is shown, where the k -weighting is applied to emphasize the high- k portion of the spectra where, due to the Debye-Waller attenuation factor $e^{-2k^2\sigma^2}$ in eq. 2.4, the XAFS signal becomes weaker and the noise level is clearly seen.

The fitting of the data is performed in r -space by adjusting the structural parameters of the FEFF6 theoretical standard obtained using the atomic coordinates of the average structure found in the neutron diffraction work of Radaelli *et. al.* The polarization dependence of the XAFS spectra can be calculated by FEFF6. [84] For the \hat{b} (long axis) polarization, an electric field linearly polarized along the \hat{b} -axis of the cell is used in the calculation. Since the samples are randomly oriented about the \hat{b} -axis, a circularly polarized electric field lying in the $\hat{a}\hat{c}$ plane is used for the in-

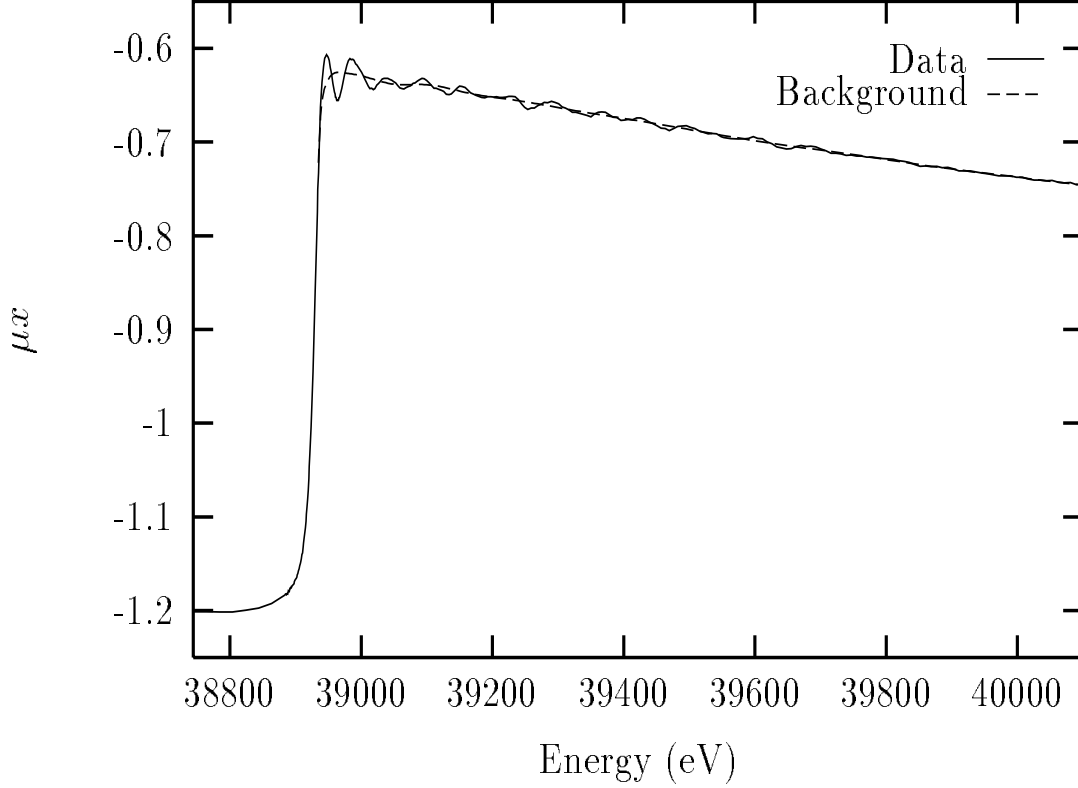


Figure 5.2: La K edge in $\text{La}_{1.8}\text{Sr}_{0.2}\text{CuO}_4$ at $T=20\text{K}$, \hat{b} -polarization

Table 5.1: Parameters used for the background removal shown in fig. 5.2. Fourier components are minimized with respect to the FEFF6 standard in the region $[0, r_{\text{bkg}}]$. The amplitude of the standard is scaled to that of the data in the region $[r_{\text{bkg}}, r^{1\text{st}}]$. Fourier transform k -weight, range and Hanning window sill widths are also shown.

E_0 (KeV)	r_{bkg} (\AA)	$r^{1\text{st}}$ (\AA)	k_{min} (\AA^{-1})	k_{max} (\AA^{-1})	kw	dk (\AA^{-1})
38.925	1.6	2.3	0.25	18	1	0.5

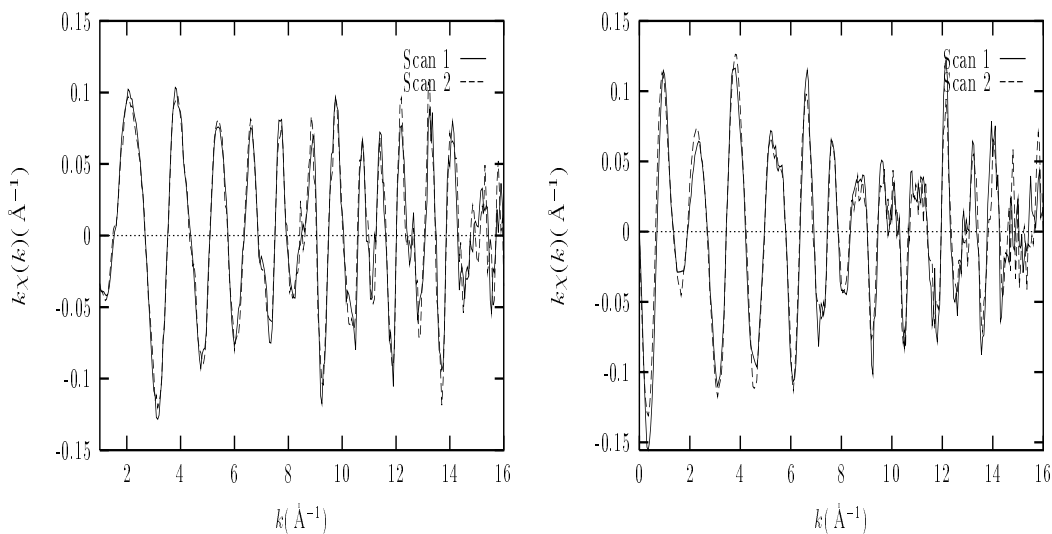


Figure 5.3: $k\chi(k)$ reproducibility data for $\text{La}_{1.8}\text{Sr}_{0.2}\text{CuO}_4$ at $T=20\text{K}$. Left: \hat{b} -polarization; right: in-plane, $\hat{a}\hat{c}$ -polarization

plane polarized theoretical XAFS. This results in the appropriate angular averaging as discussed in appendix B.

Since the samples used in this work are from the same batch as those used in the diffraction work mentioned above, discrepancies due to sample preparation are avoided when comparing local structure results to those obtained for the average structure.

Table 5.2 & 5.3 list all the theoretical photoelectron paths that were found to contribute significantly to the experimental XAFS in the $r = [1.8, 5.2]$ region of r -space. Table 5.2 lists SS contributions while table 5.3 lists nearly collinear MS paths together with SS paths of nearly the same length. Only nearly collinear MS paths were used in the fit as other MS contributions (e.g., triangular paths) are negligible for this open structure. (MS triangular paths did not make the 4% curved wave criteria of importance in the FEFF6 calculation [84]) The distances in table 5.2 & 5.3 correspond to the average structure of the $x = 0.075$ sample at 10K (LTO phase), as found in ref. 20 but a corresponding FEFF6 calculation was performed for every value of x analyzed here. Also shown in the table: the effective half path length, r_{eff} , the path degeneracy and the polarization in which their contribution is significant. For MS paths the number of scattering events is also shown (i.e., double or triple scattering). Paths that contribute to both polarizations are listed once, but it is understood

that the appropriately weighted path as found in the polarization-dependent FEFF6 calculation is used in modeling the XAFS of each polarization. The suffix *c* indicates the position of the absorbing atom along the path.

A very important feature of FEFFIT [99, 100] exploited here is its ability to *simultaneously* refine several experimental data sets, allowing a parameter that affects more than one data set to be commonly refined so that the value that best fits (in a non-linear least squares sense) *all* the data sets that share this parameter is found. Here, the two data sets corresponding to the two different polarization conditions for a given *x* are refined *simultaneously*. As shown in table 5.2 & 5.3, many of the scattering paths contribute to both \hat{b} and \hat{ac} polarized XAFS. Since the structural parameters (r_j, σ_j^2) of these paths do not depend on polarization, the parameters for these paths can be constrained to be the same for both data sets. (The effect of polarization on the amplitude of the path is included in the FEFF6 calculation; for SS it is the term $3(\hat{e} \cdot \hat{r}_j)^2$ in eq. 2.4, averaged over all possible relative orientations of \hat{e} and \hat{r}_j , as described in appendix B) By implementing this constraints the number of parameters needed in modeling the data (relative to the number of independent points) decreases dramatically since the amount of information essentially doubles.

Despite this improved condition it is imperative to impose additional constraints in order not to overwhelm the information content of the data. This is not straightforward to do here, however, because of the very large anisotropy of the structure together with the presence of the structural phase transition. These result in non trivial relations between different distances as a function of Sr content; some distances decrease whereas some others increase and the rate of change with Sr depends on orientation. The aim here, then, is to accurately determine in a “nearly” model-independent way the structural parameters of the distances that are affected the most by the phase transition, with only minor reasonable assumptions. This distances are planar La-O(2), planar La-La and La-O(1), whose splittings of $\Delta r \sim 0.43, 0.11, 0.083 \text{ \AA}$ (for $x = 0.075$) were found by diffraction to vanish at the boundary of the Sr induced transition. Along these lines, the following constraints were applied: (1) a single σ^2 is refined for all La-O(2) nearest neighbors; a single σ^2 is refined for both La-O(1) near neighbor bonds, (2) a linear “expansion” relation is assumed for the SS La-Cu paths in the LTO phase; i.e., the correction in distance is proportional to the average half path length so a single “expansion” coefficient is varied. A single σ^2 is refined for all SS La-Cu paths, (3) a single σ^2 is refined for all SS La-La paths, (4) a lin-

Table 5.2: Theoretical SS photoelectron paths that were found to significantly contribute to the experimental XAFS signal in $r = [1.8, 5.2]$. Values correspond to $x = 0.075$ at 10K.

Path	r_{eff} (AA)	Degeneracy	Polarization
La _c -O(2)-La _c	2.348	($\times 1$)	\hat{b}
La _c -O(2)-La _c	2.541	($\times 1$)	\hat{ac}
La _c -O(1)-La _c	2.592	($\times 2$)	\hat{b}, \hat{ac}
La _c -O(1)-La _c	2.675	($\times 2$)	\hat{b}, \hat{ac}
La _c -O(2)-La _c	2.731	($\times 2$)	\hat{ac}
La _c -O(2)-La _c	2.968	($\times 1$)	\hat{ac}
La _c -Cu-La _c	3.22	($\times 1$)	\hat{b}, \hat{ac}
La _c -Cu-La _c	3.23	($\times 2$)	\hat{b}, \hat{ac}
La _c -Cu-La _c	3.286	($\times 1$)	\hat{b}, \hat{ac}
La _c -La-La _c	3.658	($\times 1$)	\hat{b}
La _c -La-La _c	3.73	($\times 2$)	\hat{ac}
La _c -La-La _c	3.84	($\times 2$)	\hat{ac}
La _c -La-La _c	3.957	($\times 2$)	\hat{b}, \hat{ac}
La _c -La-La _c	3.974	($\times 2$)	\hat{b}, \hat{ac}
La _c -O(2)-La _c	4.367	($\times 2$)	\hat{ac}
La _c -O(2)-La _c	4.535	($\times 2$)	\hat{ac}
La _c -O(1)-La _c	4.565	($\times 4$)	\hat{ac}
La _c -O(1)-La _c	4.62	($\times 2$)	\hat{ac}
La _c -O(1)-La _c	4.698	($\times 2$)	\hat{ac}

Table 5.3: Theoretical MS photoelectron paths (and SS paths of nearly the same length) that were found to significantly contribute to the experimental XAFS signal in $r = [1.8, 5.2]$. Values correspond to $x = 0.075$ at 10K.

Path	r_{eff} (Å)	Degeneracy	Type	Polarization
La _c -Cu-La _c	4.754	(×1)	SS	\hat{b}
La _c -Cu-O(2)-La _c	4.762	(×2)	DS	\hat{b}
La _c -O(2)-Cu-O(2)-La _c	4.77	(×1)	TS	\hat{b}
La _c -La-La _c	5.264	(×4)	SS	\hat{b}, \hat{ac}
La _c -La-O(1)-La _c	5.265	(×8)	DS	\hat{b}, \hat{ac}
La _c -O(1)-La-O(1)-La _c	5.267	(×4)	TS	\hat{b}, \hat{ac}
La _c -La-La _c	5.327	(×2)	SS	\hat{ac}
La _c -La-La _c	5.382	(×2)	SS	\hat{ac}
La _c -La-O(2)-La _c	5.394	(×4)	DS	\hat{ac}
La _c -La-O(2)-La _c	5.446	(×4)	DS	\hat{ac}
La _c -O(2)-La-O(2)-La _c	5.462	(×2)	TS	\hat{ac}

ear “expansion” relation is assumed for all SS La-O paths at $r \sim 4.5 \text{ \AA}$ in the LTO phase; a single σ^2 is refined for these paths, (5) a single σ^2 is refined for each group of nearly collinear focusing MS paths, constrained to be the same as that of the SS path of nearly the same length (see appendix C); a linear expansion relation is assumed within each group of MS paths in the LTO phase.

Despite all this constraints being reasonable on a physical basis, a few of these are questionable. For example, the treatment of the highly disordered SS La-O fourth shell with a linear expansion model and a single σ^2 requires that the structural information derived for those distances is to be interpreted within the assumed model. What is relevant here, however, is that the structural parameters of the distances of interest (those that are affected the most by the phase transition) are not affected by the somewhat questionable constraints, as corroborated for the analysis performed here.

Coordination numbers were set to the values dictated by the average structure and full oxygen occupancy is assumed since even for the $x = 0.36$ sample the oxygen’s vacancy concentration was found to be less than 1%. [20] The treatment of Sr

substitution in the lattice deserves attention. Two theoretical FEFF6 calculations were performed for each value of x and polarization: one for which all La/Sr sites are populated by La atoms; the other for which all La/Sr sites are populated by Sr atoms (except of course the central atom). Because of both the La/Sr atoms being third shell to the absorbing atom and the strong layered structure of this cuprates, replacing La by Sr has a small effect on the potentials of the first and second shell atoms and therefore on their XAFS phases and backscattering amplitudes calculated by FEFF6. This can be seen in fig. 5.4 where the backscattering amplitudes ($F(k)$) and phases (ϕ_b) are shown for La-O(2) apical ($r = 2.348 \text{ \AA}$) and La-Cu ($r = 3.23 \text{ \AA}$) SS paths for all La neighbors or all Sr neighbors.

The above mentioned result justifies neglecting the effect of substitution on the first and second shell scattering paths. As Sr substitutes for La in the lattice (as corroborated by the Sr K -edge analysis presented later in this thesis), the scattering paths involving La or Sr backscatterers were weighted by their relative concentrations $(1 - x/2)$ or $x/2$, respectively. This is done in FEFFIT by using an “effective” $S_{0\text{eff}}^2$ for these paths, i.e., $S_{0\text{eff}}^2(\text{La}, \text{Sr}) = S_0^2 * [(1 - x/2), x/2]$. Initially the relative concentrations $x/2$ were allowed to vary. Since the fitted values for all samples were always in agreement with the nominal Sr content but the uncertainties in their values were quite large due to the small Sr signal (e.g., $x/2 = 0.069 \pm 0.05$ for the $x = 0.15$ sample and $x/2 = 0.19 \pm 0.04$ for the $x = 0.36$ sample, in agreement with random substitution), the nominal values of x were used and set in the fits. The structural parameters of the La-Sr paths were constrained to be the same as those of the La-La paths of the same length. A common S_0^2 value was refined for both polarization conditions and was found to be independent of x , in agreement with the expectation that the overlap of passive electrons in the central atom with and without a core hole should be dependent on only the central atom and not on Sr substitution in the third shell. [90,91] An overall ΔE_0 correction was allowed for each data set (each polarization condition) to adjust the energy reference of the data to that of the FEFF6 calculation.

Typical fits obtained in the manner described above are presented in figs. [5.5-5.8] for $x = 0.075$ and $x = 0.2$ samples in both polarization conditions. Both the amplitude and the real part of the complex Fourier transforms are shown. Fourier transform parameters and fitting region of r -space are indicated in table 5.4.

The main results of the fits are summarized in figs. 5.9 & 5.10 and table 5.5. As

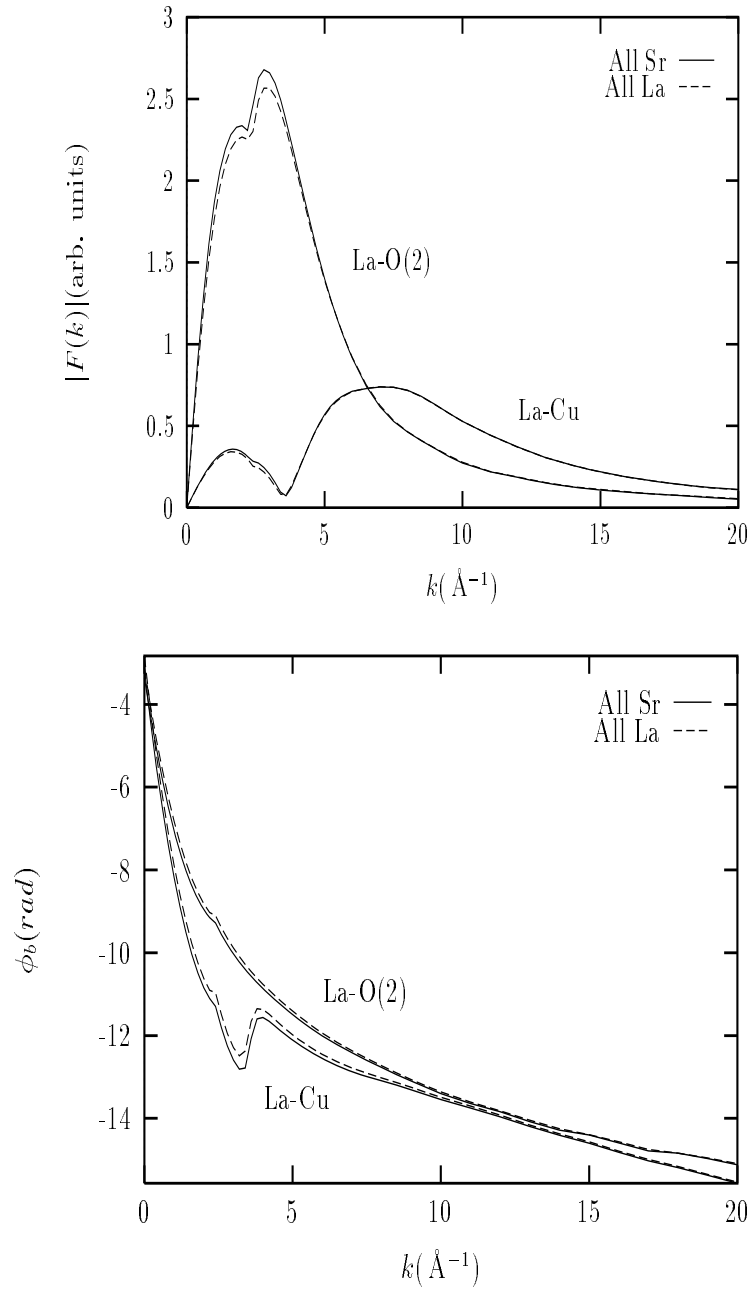


Figure 5.4: FEFF6 Backscattering amplitudes and phases for La-O(2) and La-Cu SS paths for all La atoms in the La/Sr sites vs. all Sr atoms (except of course the La central atom) in $\text{La}_{2-x}\text{Sr}_x\text{CuO}_4$. Calculation corresponds to $x = 0.075$ and \hat{b} polarization.

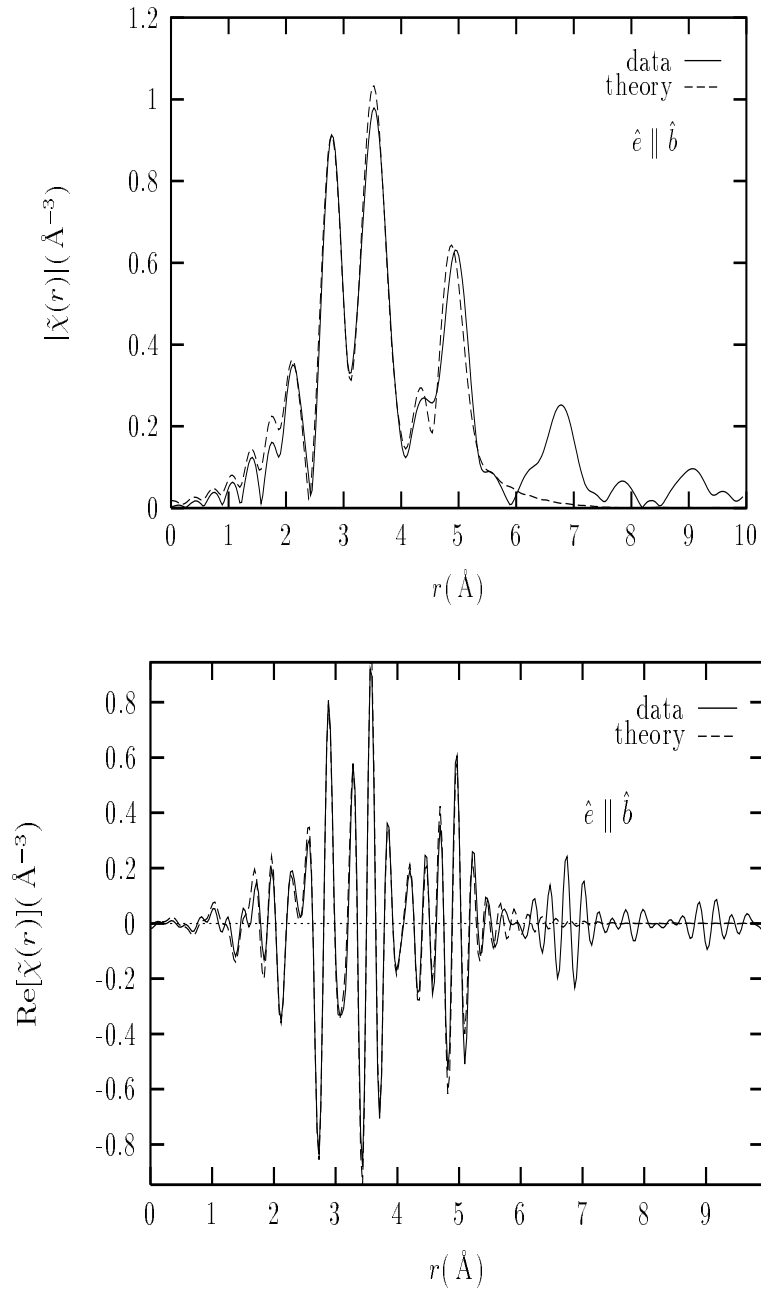


Figure 5.5: Fit results for the $x = 0.075$ sample at 20 K. The magnitude (top) and the real part (bottom) of the complex Fourier transform are shown for $\hat{e} \parallel \hat{b}$

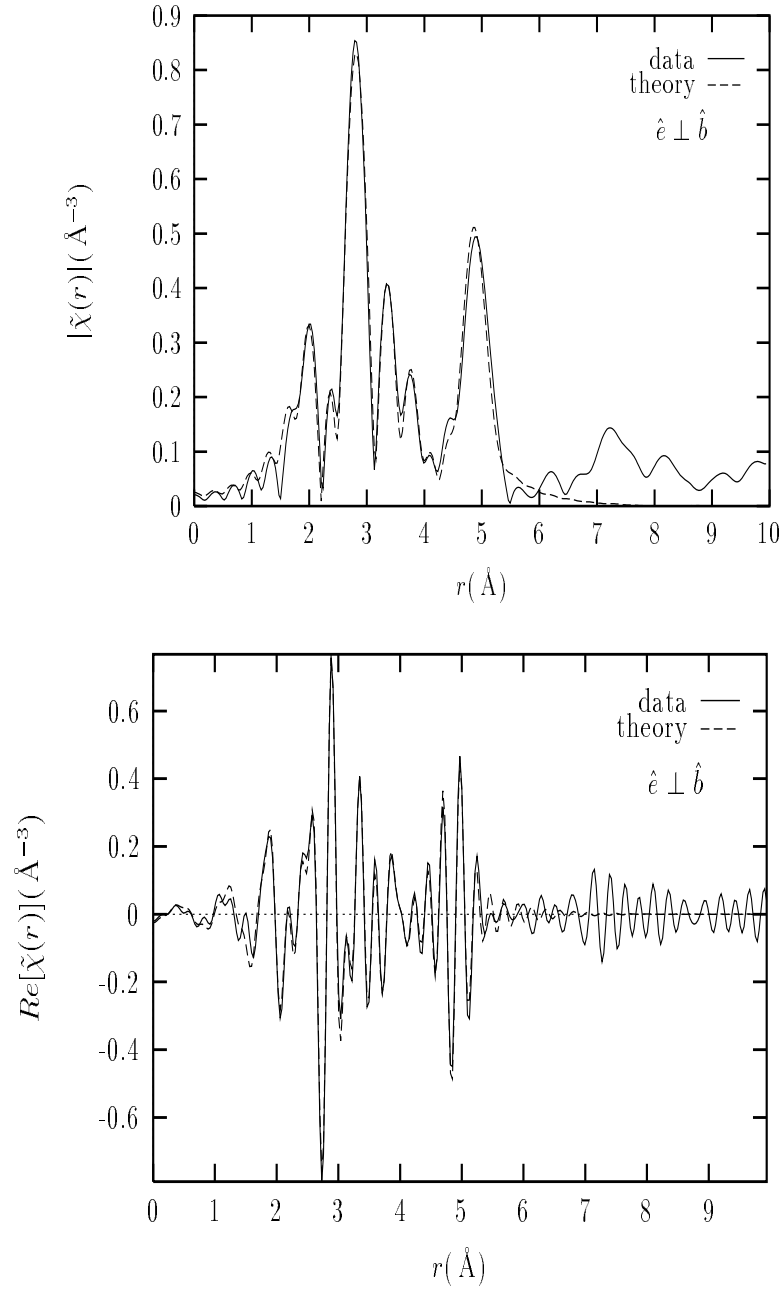


Figure 5.6: Fit results for the $x = 0.075$ sample at 20 K. The magnitude (top) and the real part (bottom) of the complex Fourier transform are shown for $\hat{e} \perp \hat{b}$

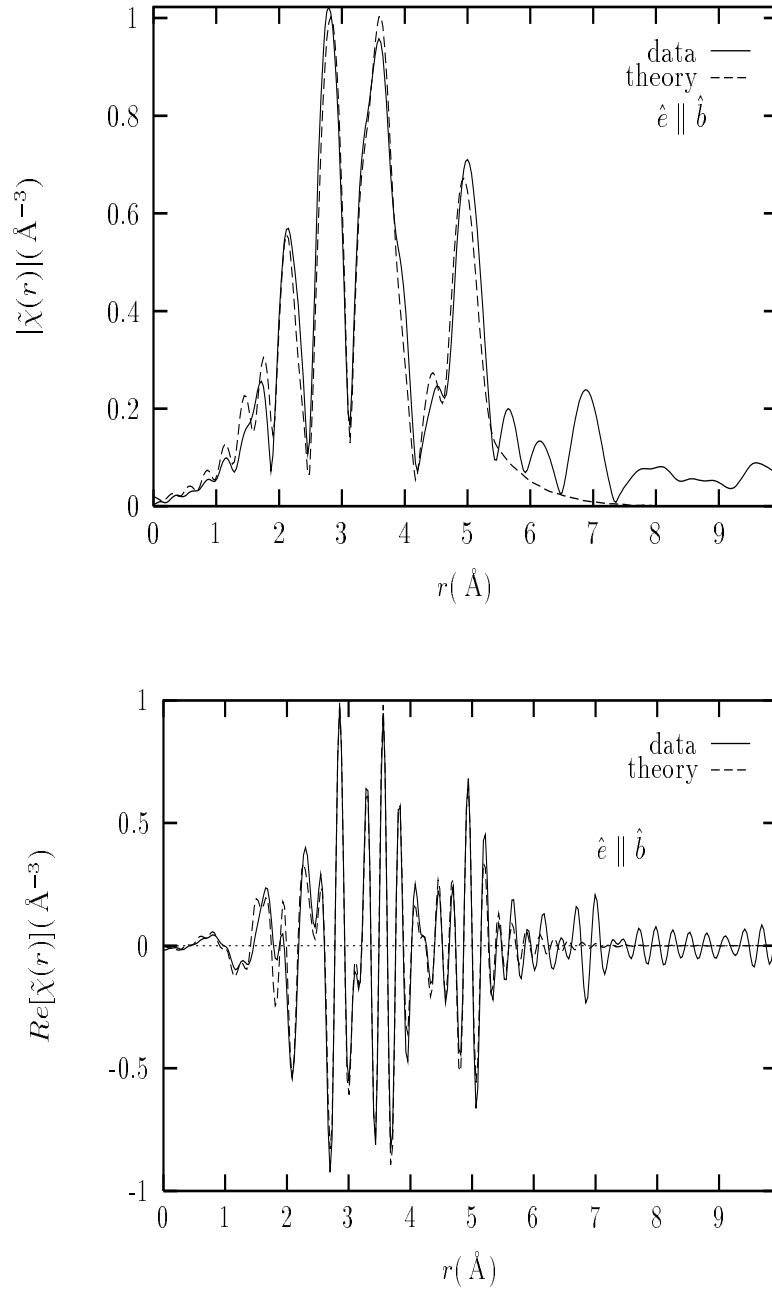


Figure 5.7: Fit results for the $x = 0.20$ sample at 20 K. The magnitude (top) and the real part (bottom) of the complex Fourier transform are shown for $\hat{e} \parallel \hat{b}$

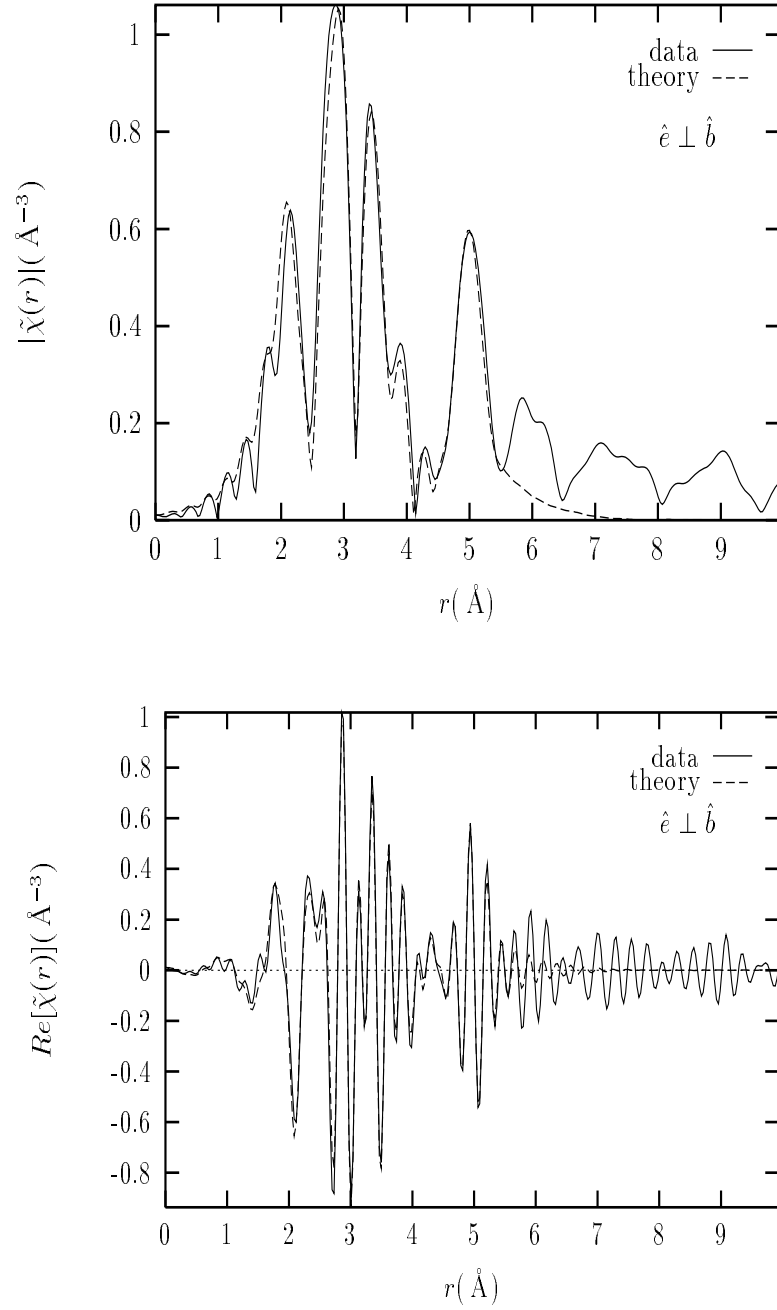


Figure 5.8: Fit results for the $x = 0.20$ sample at 20 K. The magnitude (top) and the real part (bottom) of the complex Fourier transform are shown for $\hat{e} \perp \hat{b}$

Table 5.4: Fourier transform parameters and fitting region of r -space for the fits shown in figs. [5.5- 5.8]. Hanning window sills width (dk) and k -weight (kw) also shown.

$k_{\min}(\text{\AA}^{-1})$	$k_{\max}(\text{\AA}^{-1})$	$dk(\text{\AA}^{-1})$	kw	$r_{\min}(\text{\AA})$	$r_{\max}(\text{\AA})$
3.0	14.0	1.5	2	1.8	5.2

can be seen in figs. 5.9 & 5.10, whereas the La-O and planar La-La distances merge into a single distance in the average HTT tetragonal phase, XAFS shows that, locally, they remain split. The La-O and planar La-La distances agree within experimental uncertainties with their average values up to $x \approx 0.15$, consistent with a gradual reduction of the tilt angle of the CuO_6 octahedra as indicated by the diffraction studies. [20, 33] However, as the phase boundary is approached ($x \approx 0.21$ at low temperature [20]), the magnitude of the tilt of the CuO_6 octahedra stops decreasing locally, as seen from the smaller but persistent local splitting of distances in the $x = 0.25, 0.3, 0.36$ samples. This shows that the local structure about the La atoms retains orthorhombicity even in the average tetragonal phase, and implies that the tilt angle of the CuO_6 octahedra does not vanish at the LTO \rightarrow HTT phase boundary.

Figure 5.11 shows fits to the $x = 0.3$ sample using the LTO model, whose results are shown in figs. 5.9 - 5.10 and table 5.5, together with a fit using the average HTT structure, the results of which are shown in table 5.6. It is important to note that in the ‘‘HTT’’ fit the local symmetry is constrained to that of the HTT phase (e.g., a single distance for La-O(2) planar, La-O(1) and La-La planar) but otherwise the distances and their disorder are allowed to vary. The ‘‘HTT’’ fit is significantly worse than the LTO fit, as seen by the ~ 2 times larger χ^2_ν of the former, even if the ‘‘HTT’’ model has a larger number of degrees of freedom ν . The reduced χ^2_ν of the two models relate as $(\chi^2_\nu(\text{HTT}) \sim \chi^2_\nu(\text{LTO})(1 + 5\sqrt{2/\nu})$ so they are ~ 5 standard deviations apart, as detailed in chapter 2). Not less important than the statistical significance of the worse fit is the physical meaning of the derived parameters. As seen in table 5.6 the ‘‘HTT’’ fit results in unphysically large σ^2 's to compensate for the additional structural disorder present in the data (distances *are* locally split) but not included in the ‘‘HTT’’ model. In addition the best fit value of the planar La-O(2) single distance in the ‘‘HTT’’ model is $2.64 \pm 0.03 \text{\AA}$ as compared to the 2.71\AA distance

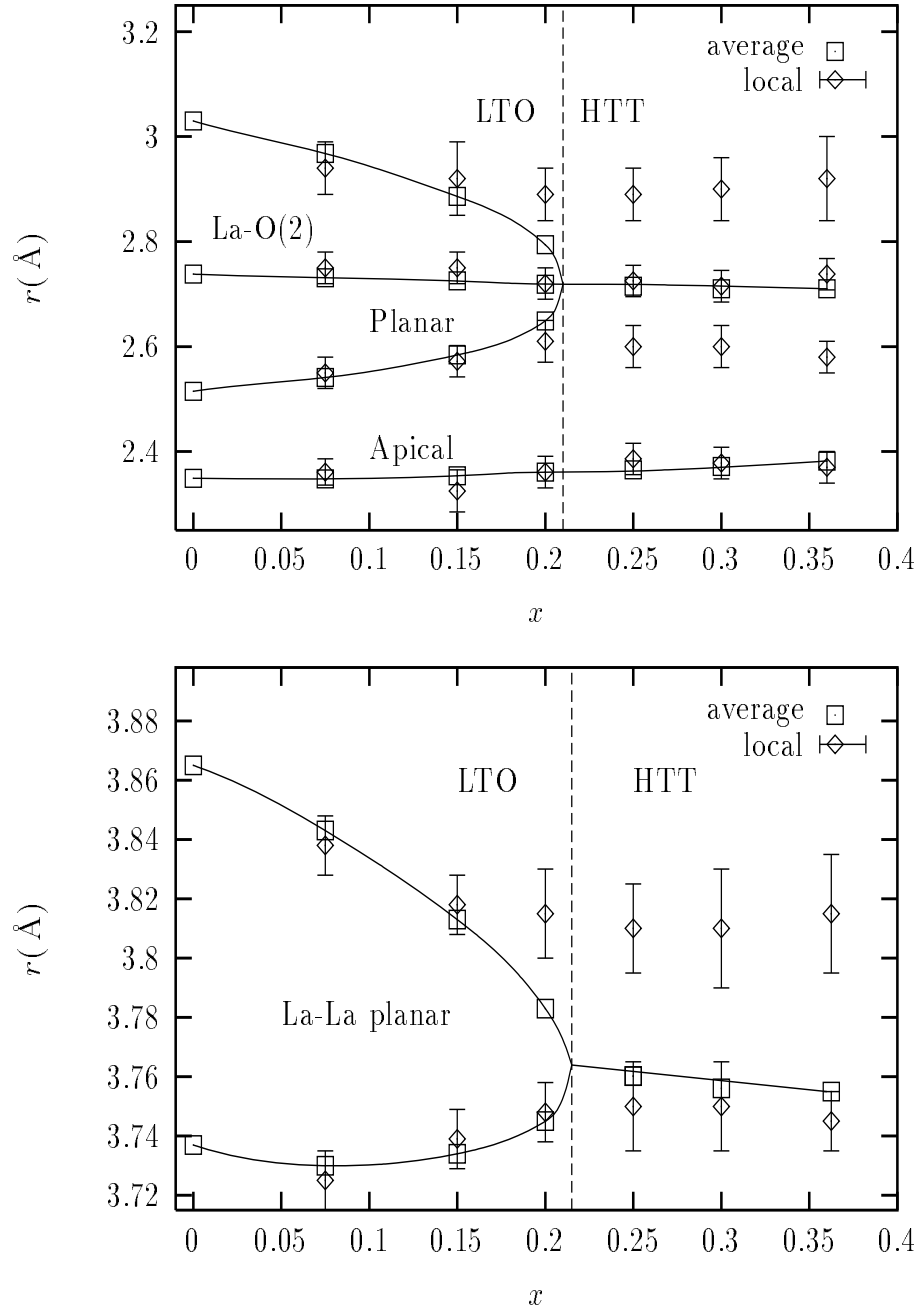


Figure 5.9: Fit results as obtained in the analysis of La K -edge polarized XAFS data as function of x at $T=20\text{K}$. La-O(2) (top) and La-La in plane (bottom) distances are shown. The average structure distances as determined by neutron diffraction [20] in the same samples are also shown for comparison. The position of the phase boundary is indicated by the vertical line.

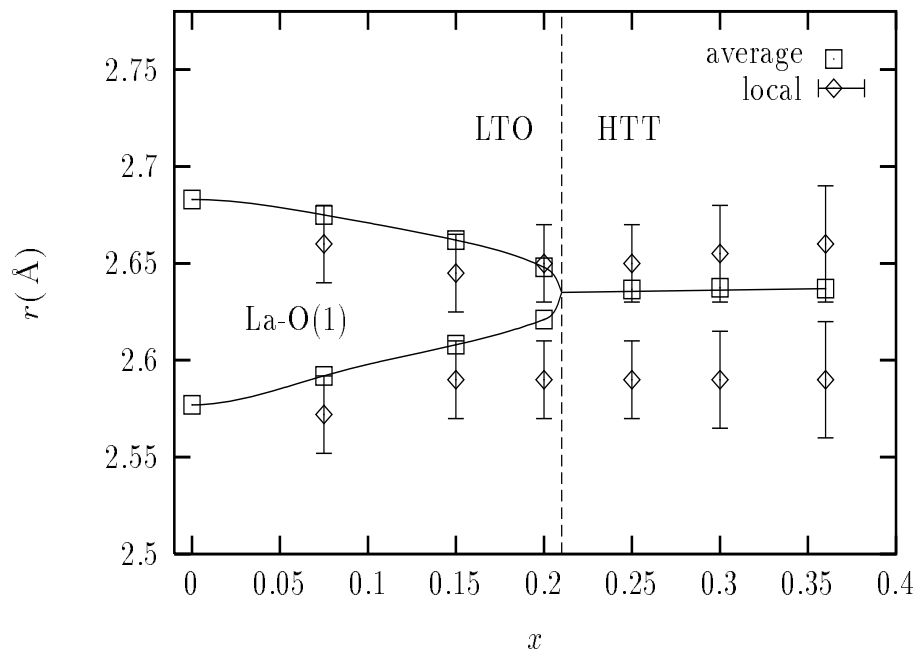


Figure 5.10: Fit results as obtained in the analysis of La K -edge polarized XAFS data as function of x at $T=20\text{K}$. La-O(1) distances are shown. The average structure distances as determined by neutron diffraction [20] in the same samples are also shown for comparison. The position of the phase boundary is indicated by the vertical line.

Table 5.5: XAFS Debye-Waller factors (in \AA^2) as obtained from La K -edge polarized XAFS as function of x at $T=20\text{K}$. Fit quality factors, χ_ν^2 and R , are shown for the different values of x . $S_0^2 = 0.95 \pm 0.06$ and $\sigma_{mm}^2 = 0.00011 \text{\AA}^2$ is the McMaster correction used for all fits. The degrees of freedom, ν , in the fits are $\nu = (N_I - N_P) = (52 - 23) = 29$. Paths are indicated by the atom at end of path.

	$x = 0.075$	$x = 0.15$	$x = 0.2$	$x = 0.25$	$x = 0.3$	$x = 0.36$
O(1)	0.0018(10)	0.002(1)	0.0022(10)	0.002(1)	0.002(1)	0.0025(15)
O(2)	0.0020(15)	0.0025(10)	0.0020(10)	0.0030(15)	0.004(2)	0.004(2)
Cu	0.0019(3)	0.0020(4)	0.0019(4)	0.0021(5)	0.002(3)	0.0019(5)
La	0.0024(2)	0.0019(5)	0.0020(5)	0.0026(5)	0.0025(6)	0.0022(10)
O _{4th}	0.003(2)	0.0050(25)	0.0050(30)	0.0070(40)	0.0045(30)	0.005(3)
Cu _{MS}	0.004(1)	0.0035(10)	0.005(1)	0.0069(30)	0.0060(25)	0.0062(30)
La _{MS}	0.0021(3)	0.0022(5)	0.0019(6)	0.0024(10)	0.0023(10)	0.0030(15)
χ_ν^2	11	10	12	11	14	16
R	0.015	0.016	0.02	0.022	0.018	0.019

Table 5.6: Relevant XAFS Debye-Waller factors and fit quality factors for the “HTT” fit of the $x = 0.3$ sample shown in fig. 5.11. The degrees of freedom in the “HTT” fit are $\nu = (N_I - N_P) = (52 - 17) = 35$.

	La-O(1)	La-O(2)	La-La
$\sigma^2(\text{\AA}^2)$	0.004(1)	0.017(6)	0.003(1)
χ^2_ν	32.7		
R	0.029		

of the average structure. This unphysical contraction is another way to compensate for the wrong model. If this contraction were real and the local symmetry was indeed tetragonal as in the average structure, the resulting lattice parameter measured by XAFS would be in marked disagreement with the value measured by diffraction. On the other hand, for a local symmetry that is lower than the one of the average structure (as found here), it is thinkable that the long range order average structure measured by diffraction can be regained if disorder in the atomic arrangement is present, as discussed below.

The La-O(2) planar distances obtained for the $x = 0.3$ sample with the LTO model are $r = 2.60, 2.715, 2.90 \text{ \AA}$ (fig. 5.9) while a distance $r = 2.64 \text{ \AA}$ is found in the worse “HTT” fit. The additional mean squared structural disorder not accounted for in the HTT model is then

$$\begin{aligned} \sigma_{\text{HTT}}^2 &= \langle (r_{\text{LTO}} - r_{\text{HTT}})^2 \rangle = & (5.1) \\ &= \frac{(2.6 - 2.64)^2 + 2 \times (2.715 - 2.64)^2 + (2.9 - 2.64)^2}{4} = 0.02 \text{ \AA}^2 \end{aligned}$$

As seen in tables 5.6 & 5.5, the difference in σ^2 obtained for the La-O(2) distances in the two models is $\Delta\sigma^2 = 0.017 - 0.004 = 0.013 \pm 0.006 \text{ \AA}^2$. This is close to the value in eq. 5.1, when accounting for the fact that a single distance and σ^2 can only partially compensate for the actual atomic distribution. It should be mentioned here that any attempts to improve the “HTT” fit by adding higher order cumulants (anharmonicity) to the fit using a single distance were unsuccessful. The same arguments made above also explain the smaller but significant increase in the σ^2 's of La-O(1) and La-La planar obtained in the “HTT” fit, as seen in tables 5.6 & 5.5.

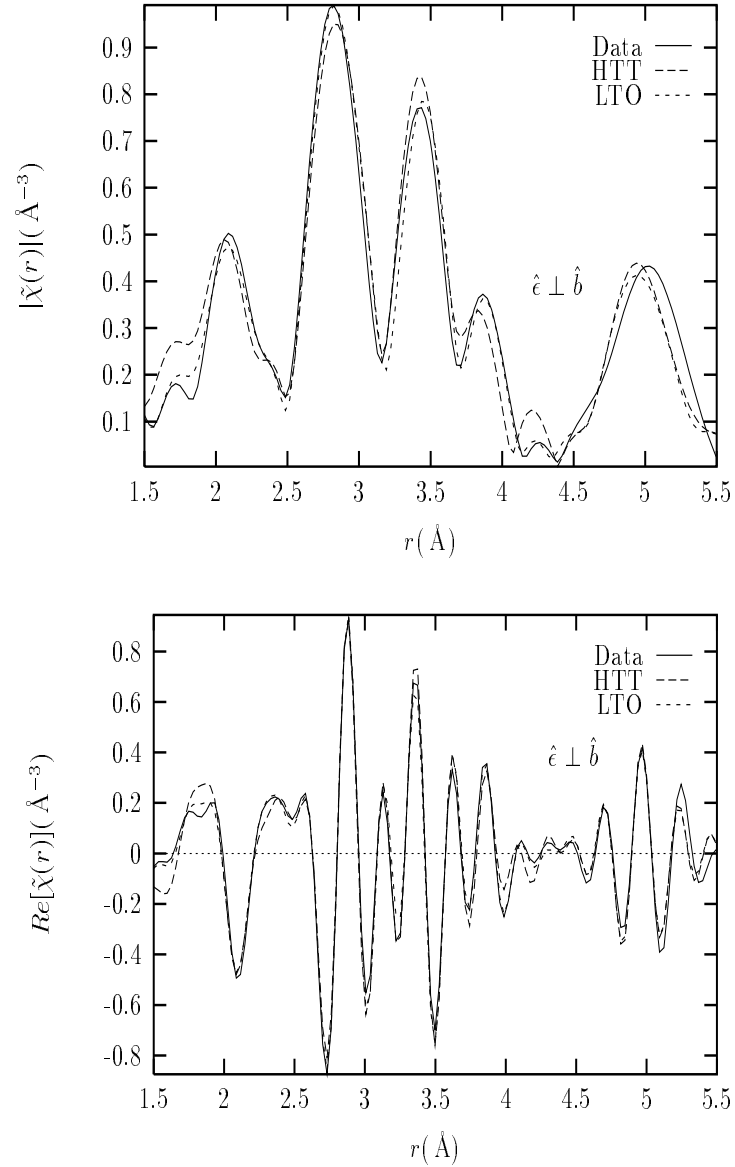


Figure 5.11: Fit results for the $x = 0.3$ sample, $\hat{\epsilon} \perp \hat{b}$ by using LTO and HTT models. The HTT model resulted in a significantly worse fit together with unphysical values for the structural parameters, as shown in table 5.6 and discussed in the text. Magnitude (top) and real part (bottom) of the complex Fourier transform are shown, the region of r -space fitted is emphasized for clarity.

5.1.2 Discussion

The XAFS results can be combined with the diffraction results to infer about the nature of the Sr-induced phase transition. At low Sr content, the local structure is the same as the average structure, i.e., the short range order is the same as the long range order in the atomic arrangement. As the Sr content is increased, a gradual reduction in orthorhombic strain is observed, consistent with the gradual decrease in tilt angle of the CuO_6 octahedra measured by diffraction. This is clearly seen for the La-O(2), La-O(1) and La-La in-plane distances, whose splittings show a significant decrease up to about $x \sim 0.15$ (fig. 5.9). It is interesting to note that the La-O(2) and La-La in-plane distances show a correlated pattern of displacements, in agreement with the correlated displacements observed by diffraction. [20] The phase transition up to $x \sim 0.15$ is clearly shown by XAFS to be of the displacive type, in agreement with diffraction.

At higher Sr content, however, some of the atomic positions measured by XAFS start to deviate from the values measured by diffraction, the deviation being already significant for the $x = 0.2$ sample. The *local* tilt angle of the CuO_6 octahedra saturates at the $x \sim 0.15$ value and fails to vanish at the phase boundary ($x \sim 0.21$), despite the fact that the long range order is certainly changing and the *average* tilt angle decreases to zero at $x \sim 0.21$. The only way to account for the disagreement between the measured short range and long range order is the presence of disorder in the atomic arrangement. In order to regain the average, HTT tetragonal structure above $x \sim 0.21$ over the long range scale measured by diffraction, the structure must be composed of local LTO domains with orthorhombic symmetry in which the CuO_6 octahedra tilts are ordered, but the domains become disordered with one another as the tetragonal phase is approached. XAFS can directly measure and quantify disorder in the atomic arrangement *only* if the correlation length of octahedra tilts, ζ_{tilt} , is smaller than the photoelectron mean free path, $\lambda(k)$, at photoelectron energies corresponding to the XAFS regime, i.e., 20-1000 eV. As mentioned in chapter 2, $\lambda(k)$ is determined by both core-hole lifetime and inelastic scattering of the photoelectron, and typically $\lambda \approx 5 - 10 \text{ \AA}$. However, even if not “visible” for XAFS, disorder must be present if the local structure differs from the average structure.

For the case here, the correlation length of local octahedral tilts (domain size) is larger than $\lambda(k)$, at least up to $x = 0.25$, as can be seen from the nearly constant χ^2_ν of the fits using the local LTO model together with the absence of any significant increase

with x of the σ^2 's in table 5.5. A possible indication for disorder becoming noticeable in an XAFS length scale at the highest Sr concentrations is the small increase in χ_ν^2 and some of the σ^2 's in table 5.5 for the $x = 0.3, 0.36$ samples. These increases, however, are within the uncertainties and therefore caution should be exercised in assigning any physical meaning to them.

It should be noted that since XAFS is such a fast probe (core-hole lifetime $\sim 10^{-15}$ sec much shorter than lattice relaxation times $\sim 10^{-13}$ sec) it cannot distinguish between static and dynamic disorder. The Sr-induced disorder at low temperature, however, is most likely quasi-static, as the potential barrier to activate dynamical fluctuations of the CuO_6 octahedra is estimated at about $10 \text{ meV} \sim 120 \text{ K}$. [66] Evidence in support of Sr-induced static disorder is found from the Sr K -edge XAFS measurements performed in this thesis, as discussed later in this chapter.

The presence of structural disorder in phase transitions previously thought to be of purely displacive character has been reported in many recent investigations [19, 50, 133–138] and a review of the current understanding of the role of local distortions and disorder in structural phase transitions, particularly in perovskite ferroelectric crystals, can be found in the work of Stern and Yacoby in refs. 139, 140.

In terms of the structural phase transition here, it is clear that Sr induced reduction of the lattice mismatch between LaO and CuO_2 layers can only be *partially* responsible for the appearance of the HTT phase above $x \sim 0.21$, as the orthorhombic strain persists in the HTT phase. Disorder in the atomic arrangement becomes significant above about $x \sim 0.15$ and its appearance results in the long range HTT order measured by diffraction techniques. The effect of the appearance of disorder on the superconducting properties can be evaluated by comparing the LTO domain size to the superconducting coherence length, $\zeta_{\text{sc}} \sim 10 - 20 \text{ \AA}$. [17, 18] As already mentioned, the size of the domains cannot be obtained from the XAFS measurement unless disorder is directly observed, which was not the case here at least up to $x = 0.25$. Only a lower limit for the domain size can be obtained from the XAFS measurement, of about $\lambda(k) \sim 5 - 10 \text{ \AA}$. In addition, the correlation length of LTO tilts must be short enough so that it doesn't result in a sharp enough Bragg peak to be observed in the diffraction experiments. This gives an upper limit to the domain size of several tens of angstroms. If $\zeta_{\text{tilt}} > \zeta_{\text{sc}}$, the effect of disorder on the superconducting properties will be small. This could explain, e.g., the absence of any apparent effect of the structural phase boundary ($x \sim 0.21$) on T_c , including dT_c/dx . On the

other hand, if $\zeta_{sc} \leq \zeta_{\text{tilt}}$, structural disorder is expected to affect the superconducting properties. For example, electronic structure calculations by Pickett *et. al* [141] on LTO $\text{La}_{2-x}\text{Sr}_x\text{CuO}_4$ doped with divalent Ba atoms show a significant contribution of O(2)-derived O $2p_z$ orbitals to the total density of states at the Fermi level for $x = 0.15$ (the largest contribution comes from Cu and O(1)-derived in-plane hybrids of O $2p_{x,y}$ and Cu $3d_{x^2-y^2}$ orbitals). It is argued [141] that the O(2) $2p_z$ contribution is strongly enhanced in the doped system due to the reduced electrostatic interaction between the O(2) atoms and the divalent Ba^{+2} , Sr^{+2} (as opposed to La^{+3}). These results are in agreement with O K -edge XANES measurements [25] showing that doped holes in $\text{La}_{2-x}\text{Sr}_x\text{CuO}_4$ indeed assume some O(2) $2p_z$ character. The observed structural disorder of the O(2) and O(1) atoms for $x > 0.15$ will then have an impact on the electronic structure at the Fermi level and therefore on the superconducting properties, provided $\zeta_{sc} \leq \zeta_{\text{tilt}}$. In this regime, it is thinkable that the structural disorder observed here for $x > 0.15$ could partially contribute to the suppression of T_c in the overdoped regime ($0.15 < x \leq 0.25$, see fig. 1.1).

In order to discriminate between these regimes, it is of importance to experimentally determine the actual domain size. This can be done by techniques which are sensitive to the *intermediate* range order ($10 \text{ \AA} \leq r \leq 30 \text{ \AA}$) in the atomic arrangement, such as PDF analysis of neutron diffraction. [52]

5.2 The nature of the temperature-induced LTO to HTT structural phase transition

5.2.1 Experimental results

As shown in the phase diagram of fig. 1.1, a temperature induced LTO \rightarrow HTT structural phase transition takes place in $\text{La}_{2-x}\text{Sr}_x\text{CuO}_4$ for $x \lesssim 0.21$, which for the $x = 0.15$ sample is completed at about $T=200\text{K}$. The present understanding of the transition is based on a strain relieving mechanism of the lattice mismatch of the CuO_2 and LaO layers, due to the different thermal expansion of the La-O and Cu-O bonds. This results in a gradual reduction of the orthorhombic splitting and the CuO_6 octahedra tilt angle, to become zero at the phase boundary, very much in the same way as described for the Sr induced transition [20]. The aim here is to study the temperature dependence of the local structure across this phase transition with XAFS.

Since the neutron diffraction data [20] on the samples used here was reported

only at 10, 70 and 300K, electron diffraction was used here to verify the location of the phase boundary. As detailed in chapter 4, the phase boundary for the $x = 0.15$ sample was found at $T=200\pm 10$ K, as determined from the disappearance of the superstructure reflections associated with the LTO phase. For the investigation of the temperature-induced phase transition, La K -edge polarized measurements were taken at $T=20, 40, 145, 210$ and 285 K. Figure 5.12 shows $k\chi(k)$ data for all temperatures and their corresponding Fourier transforms. The effect of increased thermal disorder as temperature increases is evident by the damping of the XAFS signal at high values of k ($e^{-2k^2\sigma^2(T)}$ term in eq. 2.4).

The analysis procedure is the same as described in the previous section. Both polarizations at each temperature were analyzed *simultaneously*. For temperatures in the LTO phase an LTO model was used; for those in the HTT phase both HTT and LTO models were refined and compared. Since no significant improvement was found by having a different σ^2 for the La-O(1) and La-O(2) first shell distances, a single value was refined for all La-O first shell bonds. Due to the increase in thermal disorder with temperature and the corresponding damping of the XAFS signal, the usable k -range is reduced from $[3,14] \text{ \AA}^{-1}$ at 20, 40 and 145K to about $[3,10-12] \text{ \AA}^{-1}$ at 210, 285K.

Figures. 5.13- 5.15 show fit results for $T=20$ K and $T=285$ K. Quality fit factors are summarized in table 5.7 Fit results are shown in figs. 5.16- 5.19. It is important to note that the temperature dependence of the different σ^2 's shown in fig. 5.18 was *not* required in the fittings to follow an Einstein model of lattice vibrations in order not to impose biased constraints on the temperature dependence of the local structure in the presence of a structural phase transition. The Einstein-like behavior observed in fig. 5.18 is the natural behavior of the local structure, as found by the minimization procedure. As can be clearly seen from figs. 5.16- 5.19, the only changes observed in the La-O distances are increases in thermal disorder about their equilibrium values at $T=20$ K. For the La-La planar distances and other distances along the \hat{b} -axis (La-La apical and La-Cu apical) a non-negligible thermal expansion is observed. The \hat{b} -axis lattice constant as measured by XAFS ($[\text{La-La}] + 2*[\text{La-Cu}]$) is compared to the values measured by diffraction and good agreement is found, as shown in fig. 5.19.

Figure 5.20 shows fits to the $T=285$ K data using both the LTO and HTT models. In the HTT model a local tetragonal structure was imposed (e.g. no splitting in La-O(1), La-O(2), planar La-La distances) but otherwise the structural parameters

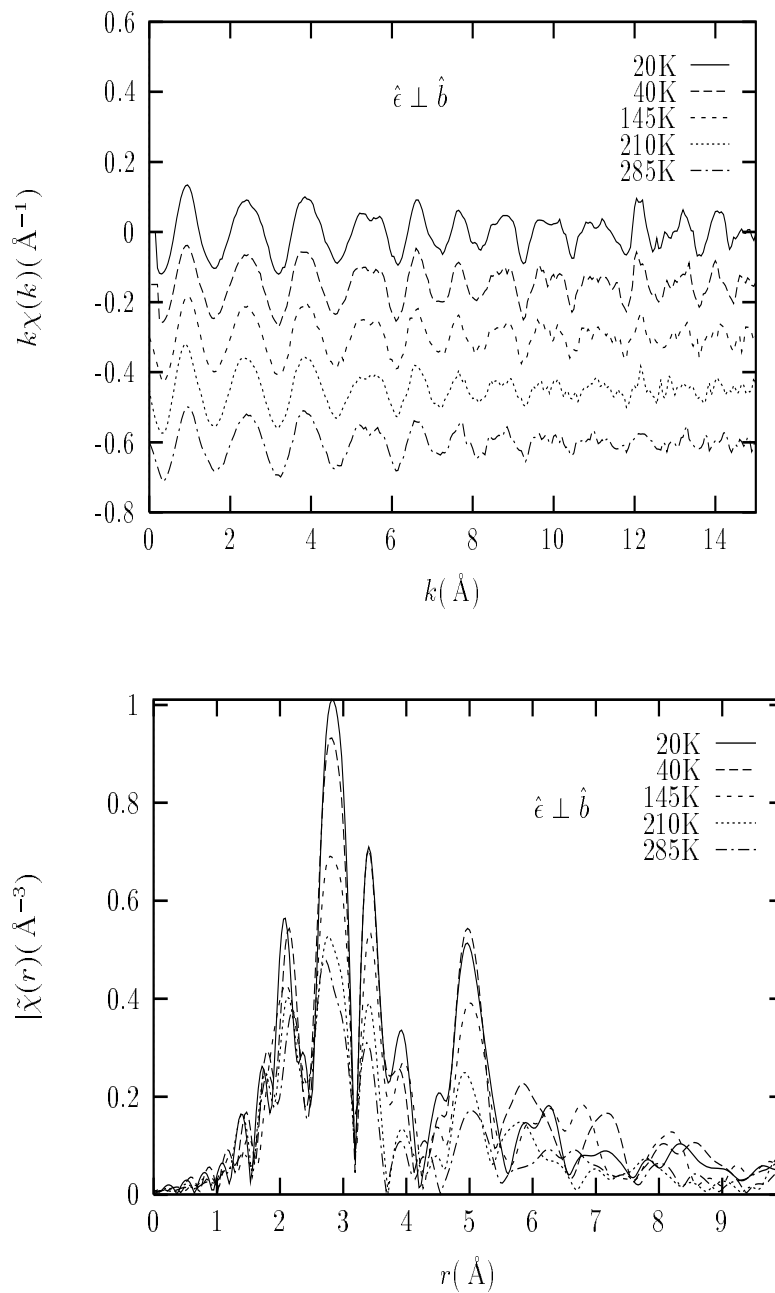


Figure 5.12: Temperature dependence of La K -edge data for $x = 0.15$ at $T=20$, 20, 145, 210 and 285K. Top: $k\chi(k)$; bottom: magnitude of the complex Fourier transform. Fourier transforms done using $k = [3, 14]$ and $kw = 2$ for all temperatures. The damping of the XAFS signal due to the increased thermal disorder is evident.

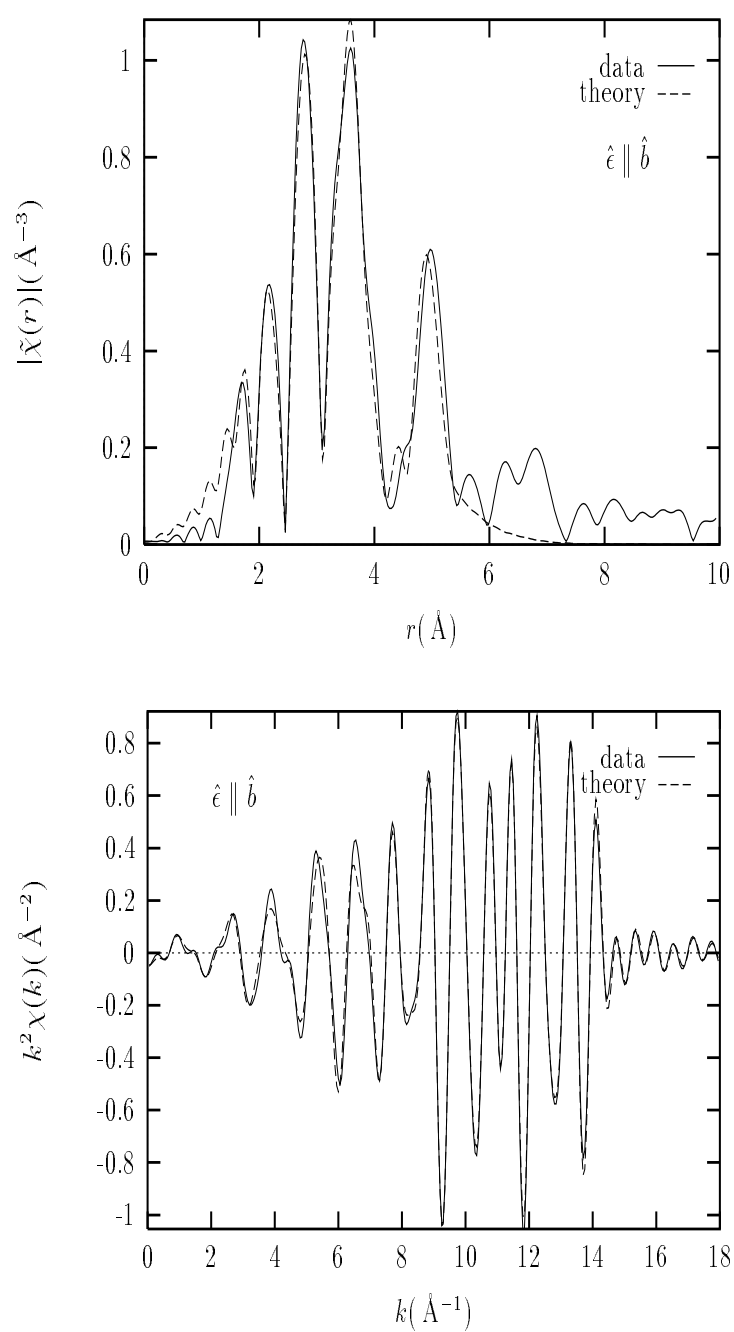


Figure 5.13: La K -edge fit results for $x = 0.15$, $\hat{\epsilon} \parallel \hat{b}$ at $T=20\text{K}$. Top: Magnitude of the complex Fourier transform; bottom: back Fourier transform of the fitted region of r -space.

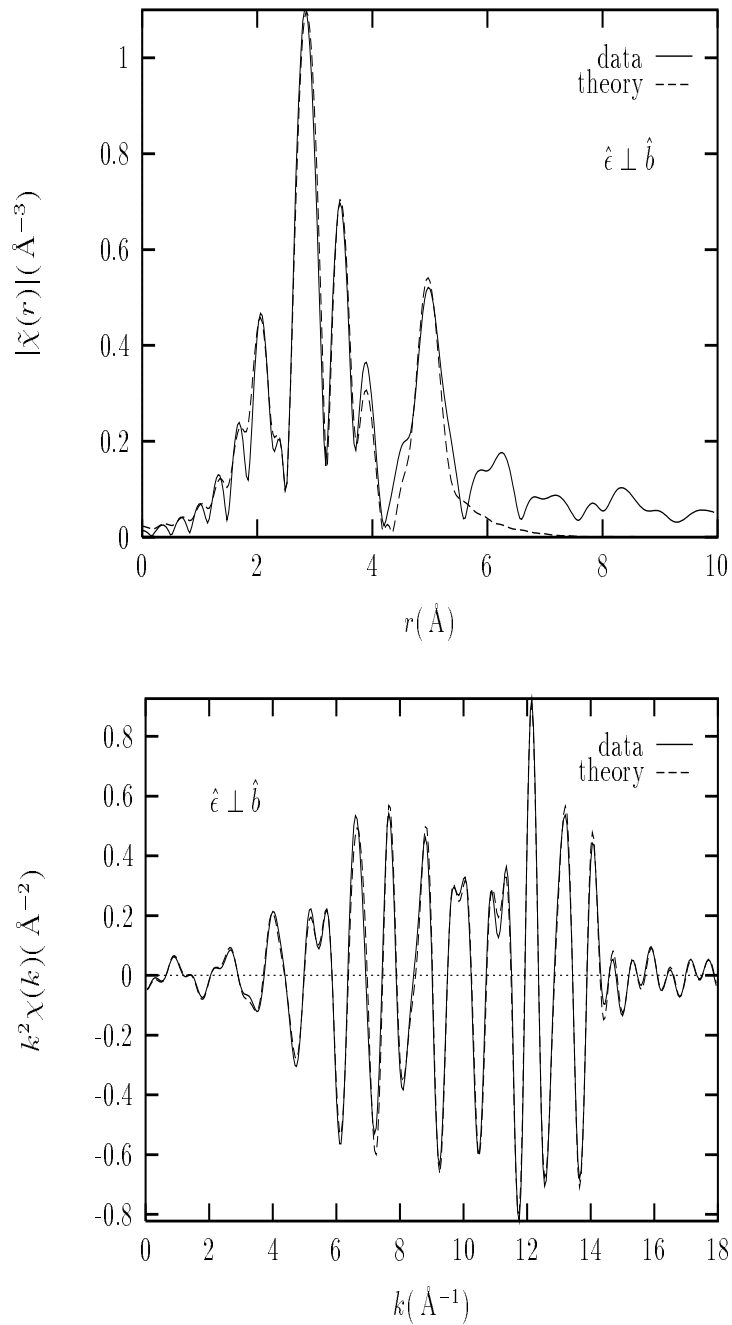


Figure 5.14: La K -edge fit results for $x = 0.15$, $\hat{e} \perp \hat{b}$ at $T=20\text{K}$. Top: Magnitude of the complex Fourier transform; bottom: back Fourier transform of the fitted region of r -space.

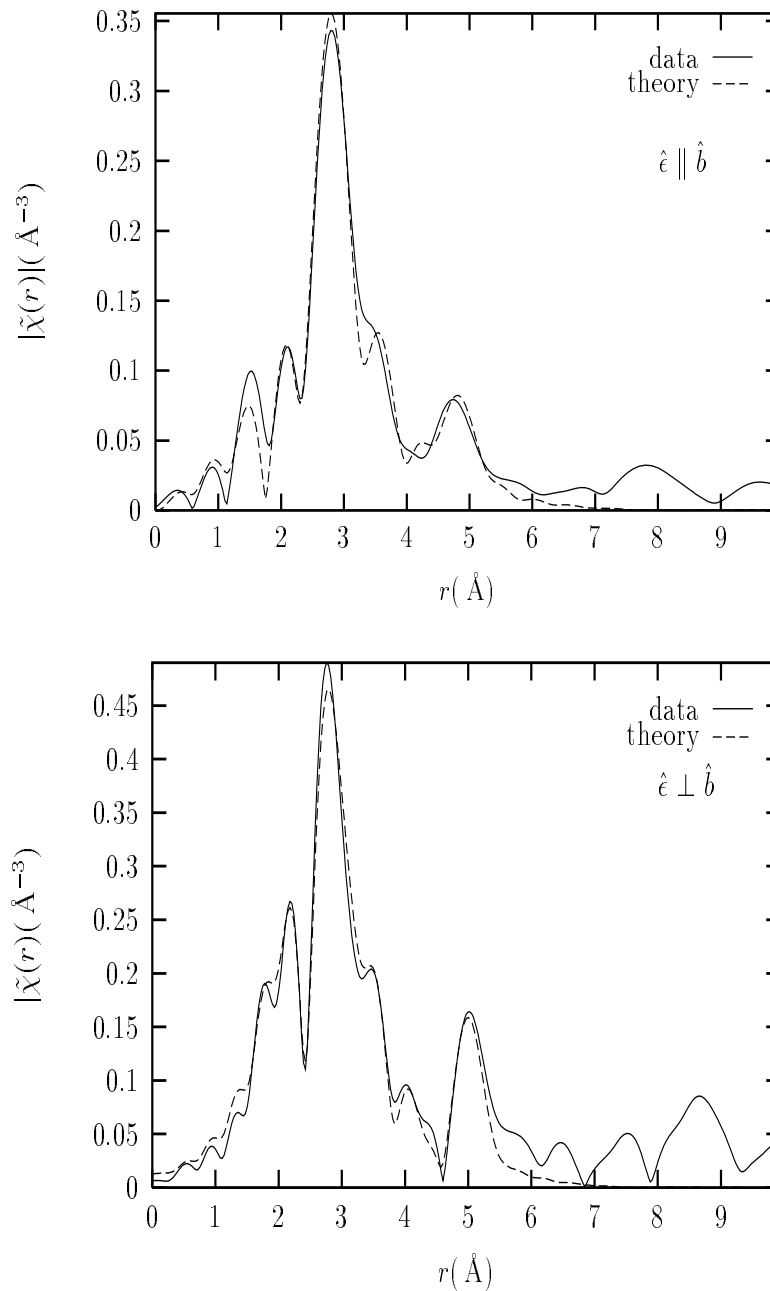


Figure 5.15: La K -edge fit results for $x = 0.15$ at $T=285\text{K}$. Magnitude of the complex Fourier transform shown. Top: $\hat{\epsilon} \parallel \hat{b}$; bottom: $\hat{\epsilon} \perp \hat{b}$. k -range of Fourier transform $k = [3, 10]$ and $k = [3, 12]$ for top and bottom, respectively.

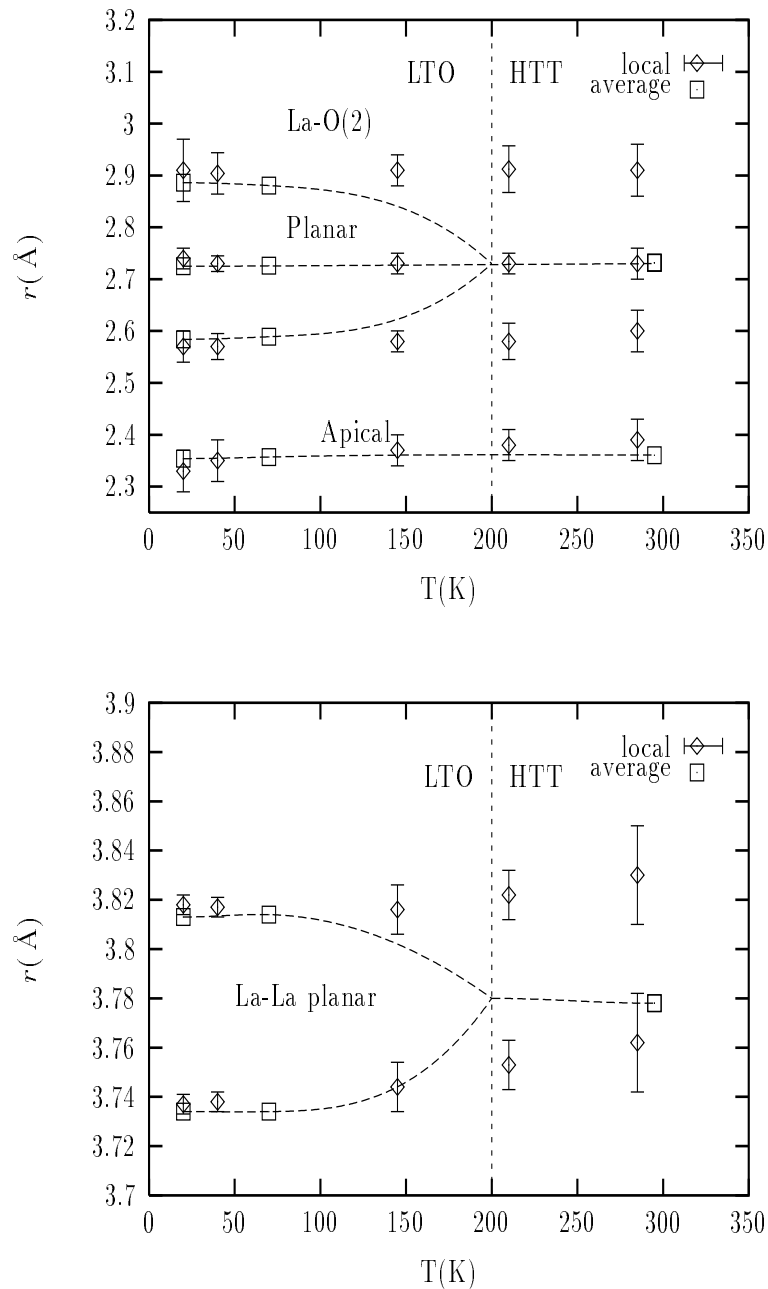


Figure 5.16: Fit results for $x = 0.15$ at temperatures below and above the structural phase transition. Diffraction results also shown for comparison. Top: La-O(2) distances; bottom: La-La planar distances. Lines through diffraction values are guide to the eye. The location of the phase boundary indicated by the vertical line.

Table 5.7: Fit quality factors, χ^2_ν and R , together with the k -ranges used in the fits. The number of independent points is reduced from $N_I = 52$ at $T=20\text{K}$ to $N_I = 39$ at 285K . The number of parameters used is 22. The degrees of freedom are $\nu = 30$ and $\nu = 17$ at $T=20\text{K}$ and $T=285\text{K}$, respectively.

	20K	40K	145K	210K	285K
χ^2_ν	10.5	12	9	12.3	13.7
R	0.016	0.017	0.015	0.018	0.019
Δk	[3,14]	[3,14]	[3,14]	[3,12]	[3,11]

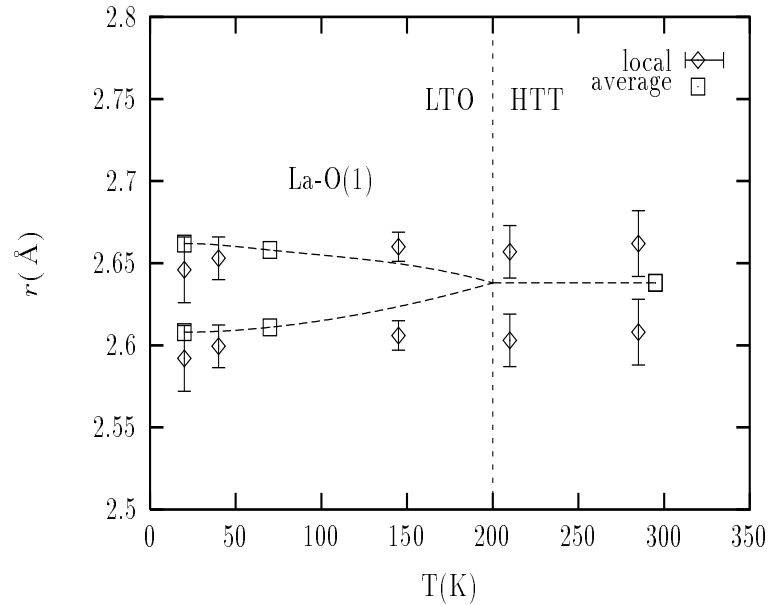


Figure 5.17: Fit results for the La-O(1) distances in $x = 0.15$ at temperatures below and above the structural phase transition. Diffraction results also shown for comparison. Lines through diffraction values are guide to the eye. The location of the phase boundary indicated by the vertical line.

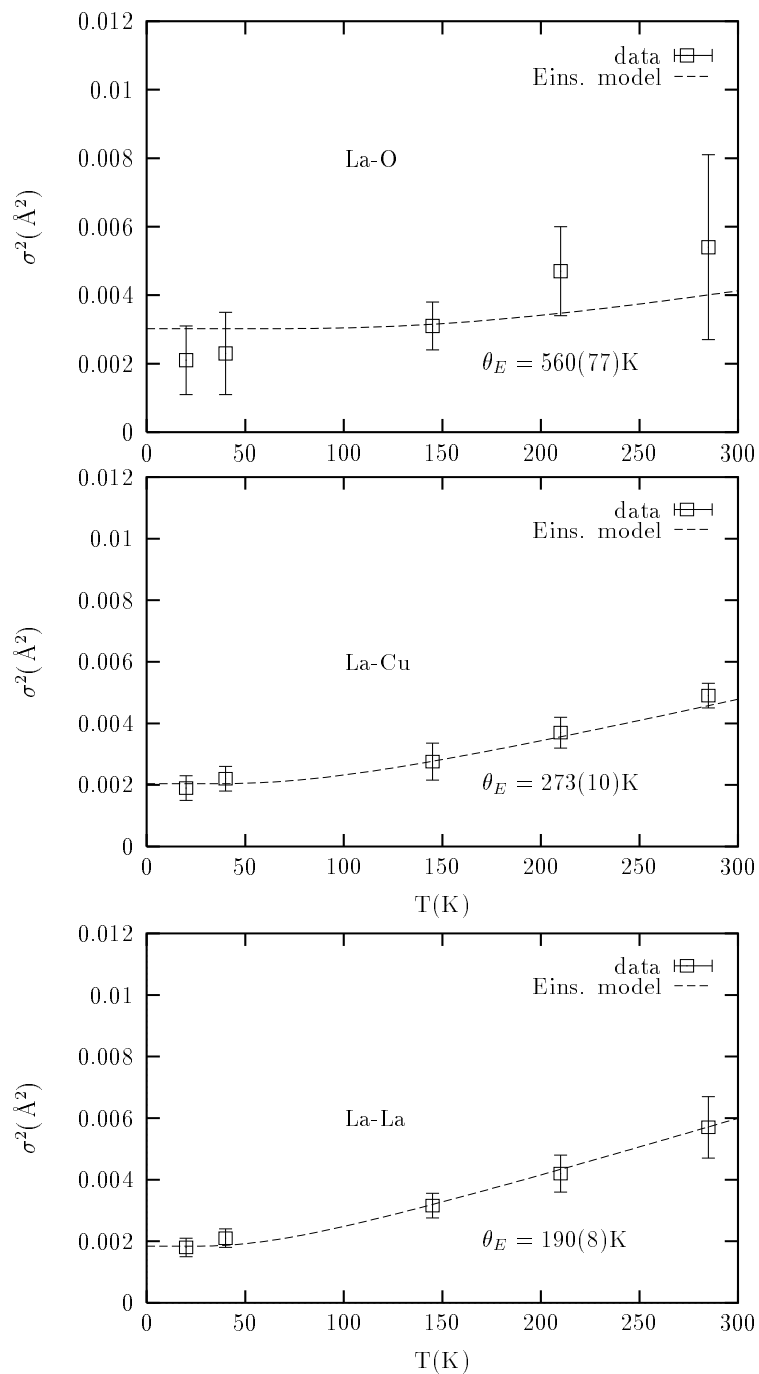


Figure 5.18: Fit results for Debye-Waller factors as obtained for $x = 0.15$ at temperatures below and above the structural phase transition. Fits to Einstein models also shown with their respective Einstein temperatures.

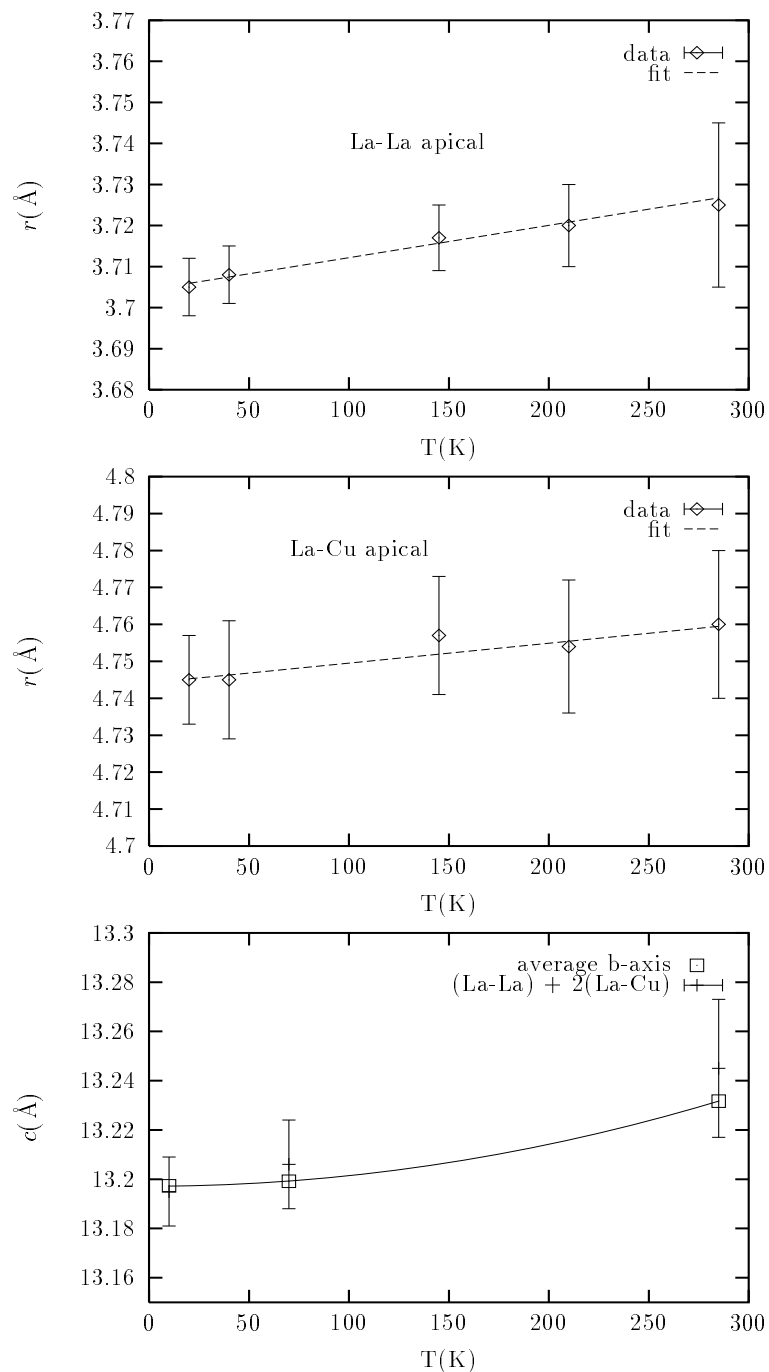


Figure 5.19: Fit results for La-La apical and La-Cu along \hat{b} axis as obtained for $x = 0.15$. The local \hat{b} lattice constant is obtained as $[\text{La-La}] + 2[\text{La-Cu}]$ and compared to the diffraction value. Solid line in lower figure is a guide to the eye.

Table 5.8: Fit quality factors, χ_ν^2 and R together with relevant σ^2 values obtained for $x = 0.15$ at 285K using the HTT model shown in fig. 5.20. The HTT model results in a significantly worse fit and unphysically large σ^2 's to compensate for unaccounted structural disorder. The degrees of freedom in the HTT fit at 285K are $\nu = (N_I - N_P) = (39 - 16) = 23$.

	La-O	La-La
$\sigma^2(\text{\AA}^2)$	0.018(4)	0.008(2)
χ_ν^2	39	
R	0.031	

were allowed to vary to best fit the data. As is clearly seen in fig. 5.20 and from the fit quality factors shown in table 5.8, the HTT model is not only significantly worse, but it results in the unphysically large σ^2 of the oxygen atoms. This is to compensate for the existence of the local splitting in La-O, as shown in fig. 5.16 & 5.17. A smaller but significant increase in La-La disorder is also observed for the same reason.

5.2.2 Discussion

It is interesting to compare the x -induced phase transition to the T -induced one. The different character of these two is clearly seen by comparing the behavior of the La-La planar distances in both cases, as shown in fig. 5.21. Whereas a clear displacive component is observed for the x -induced transition, as indicated by the initial reduction in the measured splitting of distances, a temperature *independent* splitting is observed for the T -induced transition in the whole temperature range measured here. This, combined with the temperature independent splitting of distances observed for the La-O(2) and La-O(1) distances (fig. 5.16 & 5.17), indicates that the magnitude of the tilt angle of the CuO_6 octahedra remains constant as a function of temperature and that the T -induced phase transition measured by diffraction techniques is due to the loss of coherence in the ordering of tilts over the length scale measured by diffraction techniques, i.e., the T -induced transition is purely of disorder character.

This result is in good agreement with the work of Egami and Sendyka [50, 51] using Pair Distribution Function (PDF) analysis of neutron scattering data, in which they concluded that the CuO_6 octahedra do not change their tilt angle in the whole

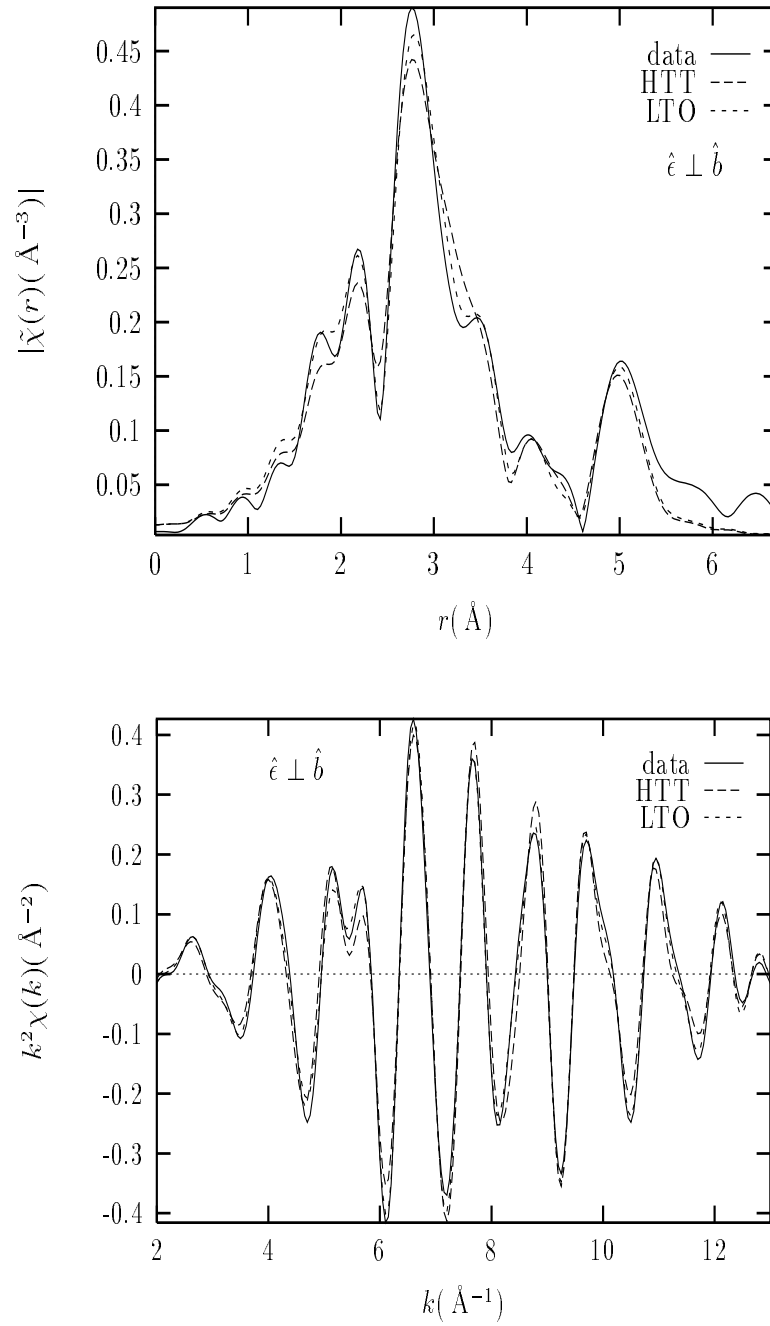


Figure 5.20: Fit results for $x = 0.15$ at 285K using both LTO and HTT models. LTO \rightarrow HTT phase boundary is at $T=200\pm 10$ K Top: magnitude of the complex Fourier transform; bottom: back Fourier transform of the fitted region of r -space. Data corresponds to $\hat{e} \perp \hat{b}$ polarization.

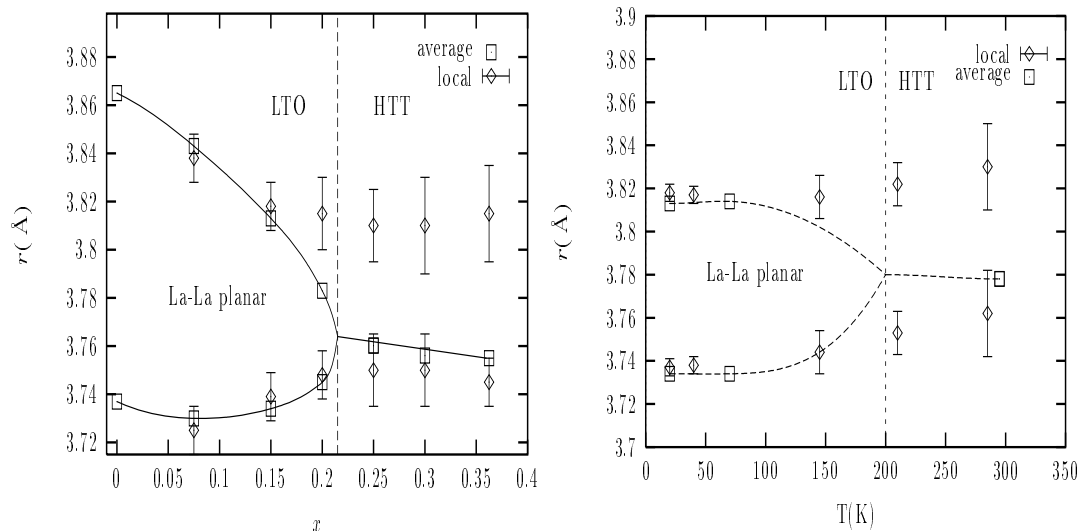


Figure 5.21: In plane La-La distances as obtained in La K -edge analysis as a function of x (left) and for $x = 0.15$ as a function of temperature (right). The x -induced transition has both displacive and disorder components while the T -induced transition is purely of disorder character.

temperature range measured here but rather become disordered relative to each other to give rise to the HTT average structure. A similar mechanism has been proposed to occur in $\text{La}_{2-x}\text{Ba}_x\text{CuO}_4$. [133] The structural ground state of the $\text{La}_{2-x}\text{Ba}_x\text{CuO}_4$ system is the LTT phase described in chapter 1 (fig. 1.5) in which the CuO_6 octahedra tilt about $\langle 101 \rangle$ directions instead of about the $\langle 100 \rangle$ ($Cmca$ notation) directions of the LTO phase. As shown in the phase diagram of fig. 1.4, a sequence of temperature induced transitions $\text{LTT} \rightarrow \text{LTO} \rightarrow \text{HTT}$ occurs in this system. PDF analysis of neutron scattering data on this system by Billinge *et. al* [133], however, showed that as opposed to the predictions of the crystal structure models, the CuO_6 octahedra do not change their tilt direction at the $\text{LTT} \rightarrow \text{LTO}$ phase boundary and that the long range structure can be obtained from coherent spatial superpositions of $\approx 10 \text{ \AA}$ sized local LTT variants. The size of the local variants was obtained from the information on intermediate range order in the PDF. These results are in partial agreement with energy surface calculations of Pickett *et. al* [66] on $\text{La}_{2-x}\text{Ba}_x\text{CuO}_4$ which show that the LTT distortion leads to the greatest gain in energy whereas the HTT structure corresponds to a local *maximum* of the energy surface. As the LTO distortion is slightly above the LTT one in energy ($\sim 200\text{K}$), at high temperature the system is

expected to fluctuate between the eight minima of the LTT and LTO structures [66], resulting in the average zero tilt angle measured by diffraction techniques in the HTT phase, despite the HTT phase being a local maximum of the energy surface.

A similar mechanism could explain the results obtained here on $\text{La}_{2-x}\text{Sr}_x\text{CuO}_4$. Since XAFS is so fast, it will be insensitive to the lattice dynamics of the CuO_6 octahedra *provided* the correlation length of tilts is larger than the p.e. mean free path, as discussed in the previous section.

Based on PDF analysis of the $\text{La}_{2-x}\text{Sr}_x\text{CuO}_4$ system, Egami *et. al* [50] proposed that the tilts in $\text{La}_{2-x}\text{Sr}_x\text{CuO}_4$ might be about $\langle 101 \rangle$ direction and disordered to give the average LTO structure, instead of about $\langle 100 \rangle$ (*Cmca* notation) as found in the diffraction studies of the LTO phase. [20] The main argument in favor of $\langle 101 \rangle$ -like tilts is that a La ion can get close to two O(2) ions instead of only one, as occurs in the LTO distortion. Since the LaO planes are highly ionic [37], this would presumably result in a more stable configuration. This possibility is schematically represented in fig. 5.22.

To check for this possibility, I constructed a hypothetical LTT distortion of the local structure so that the average over the two equivalent local configurations shown in fig. 5.22 would result in the atomic coordinates measured by diffraction for the LTO phase. This required, e.g., LTT tilts slightly larger than the LTO tilts measured by diffraction, so that the projections of the $\langle 101 \rangle$ O(2) displacements of the LTT distortion along the $\langle 100 \rangle$ direction result in the O(2) displacements measured by diffraction. In addition, the presence of orthorhombic strain as found by diffraction was also accounted for in generating the LTT distortion.

Two main differences exist between these two tilting patterns: In a $\langle 101 \rangle$ -type tilt two of the O(1) oxygens in the basal plane of the Cu-O octahedra remain in the plane, whereas the other two move above and below the plane splitting the La-O(1) distances in three different distances instead of the two occurring in the $\langle 100 \rangle$ tilts. For the magnitude of the tilt angles at hand, however, the differences in splitting are of about 0.04 \AA (see table 5.9), which in our fittings cannot be distinguished from an increase in thermal disorder of about 0.0004 \AA^2 in the La-O(1) distances. The more significant difference, however, appears in the in-plane La-O(2) distances. For the $x = 0.075$ sample, e.g., by tilting about $\langle 101 \rangle$ the in-plane La-O(2) distances will be grouped in *two* sets of distances (with differences within each group not bigger than 0.04 \AA , due to the orthorhombic splitting) while tilts about $\langle 100 \rangle$ result in *three*

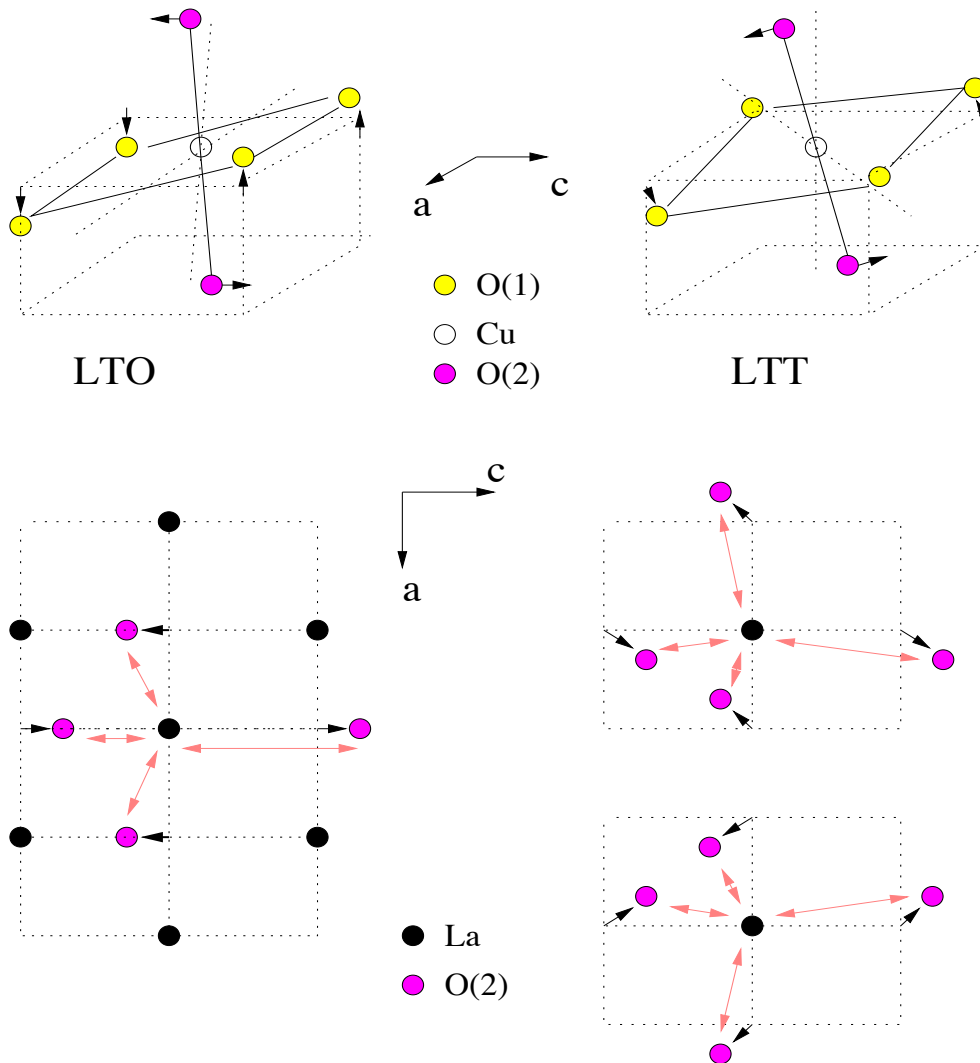


Figure 5.22: Atomic displacements associated with LTO and LTT types of tilts. The LTO tilts result in three different sets of La-O(2) planar distances while they are grouped in two sets of distances in the LTT tilts. The small correlated displacements of the La atoms are not shown. Dynamical fluctuations between the two equivalent LTT configurations will result in the average LTO tilts. Fluctuations between four equivalent LTT configurations will result in the HTT phase.

Table 5.9: Nearest neighbor La-O distances (degeneracies shown in parenthesis) for $\langle 100 \rangle$ and $\langle 101 \rangle$ tilt configurations for the $x=0.075$ sample at 20K.

Bond	$\langle 100 \rangle$	$\langle 101 \rangle$
La-O(1) (Å)	2.592 (2×)	2.542
	2.675 (2×)	2.632 (2×)
		2.725
La-O(2) (Å)	2.348	2.353
	2.541	2.550
	2.731 (2×)	2.574
	2.968	2.910
		2.950

different sets of distances, as shown in table 5.9. When the La-O(2) distances are *set* to the values consistent with the $\langle 101 \rangle$ tilt, the quality of fit is 100% worse than the one obtained by setting the La-O(2) distances to the $\langle 100 \rangle$ tilt configuration. In addition, a $\sigma^2 = 0.06(4) \text{ \AA}^2$ is obtained for the La-O(2) distances in the $\langle 101 \rangle$ tilt model. This σ^2 is at least four times bigger than the value obtained in the diffraction studies (in the extreme case of completely anticorrelated motion of La and O(2) atoms, see appendix C), confirming that the wrong model is being used in the fitting.

It is then concluded that the data are not consistent with a $\langle 101 \rangle$ tilt configuration of the Cu-O octahedra and that only the $\langle 100 \rangle$ tilts are present locally, in agreement with the results of the diffraction studies of the LTO phase [20, 33, 34]. Temperature-induced dynamical disorder leading to the average HTT phase must then occur through fluctuations between equivalent LTO minima. It is important to notice that such a hopping between equivalent minima of the energy surface is consistent with the large and highly anisotropic “thermal” ellipsoids obtained in the structural refinements of neutron diffraction data [33], especially for the O(2) atoms, the anisotropy being larger at high temperatures. For the O(1) atoms, the unaccounted structural disorder in the refinements of the HTT phase is larger in the \hat{b} direction than in the in-plane $\hat{a}\hat{c}$ direction since the O(1) atoms will fluctuate in the direction perpendicular to the CuO_2 planes. The anisotropy in the O(1) “thermal” ellipsoids refined for the HTT phase result in larger displacements along the \hat{b} -axis,

with the anisotropy increasing by $\sim 40\%$ in going from $T=20\text{K}$ to $T=295\text{K}$ for an $x = 0.13$ sample. [33] For the O(2) atoms the octahedra fluctuations described above will result in large unaccounted disorder in the HTT refinements mostly in the $\hat{a}c$ direction as the O(2) atoms at the apexes of the CuO_6 octahedra will dynamically wobble in the LaO planes. The “thermal” ellipsoids refined for the O(2) atoms are indeed elongated in the $\hat{a}c$ direction and correspond to “thermal” rms in-plane displacements of $\sim 0.14\text{\AA}$ in the HTT phase. [33] This large “thermal” disorder is of about the right size to compensate for the observed rms structural disorder unaccounted for in the HTT refinements, as shown in fig. 5.16.

Recent new evidence for dynamical fluctuations of the CuO_6 octahedra with temperature in $\text{La}_2\text{CuO}_{4+\delta}$ comes from elastic energy loss measurements by Cordero *et. al* [142] in which an intense relaxation process is observed at $\sim 150\text{K}$ for $\delta \sim 0$. The energy loss peak shifts to higher temperatures for higher vibration frequencies, consistent with a thermally activated process which was attributed to hopping of a fraction of the CuO_6 octahedra between nearly equivalent configurations. [142] Additional evidence in favor of dynamical disorder at the basis of the LTO to HTT structural phase transition comes from a re-interpretation of ^{151}Eu Mössbauer data on $\text{La}_{1.83-x}\text{Eu}_{0.17}\text{Sr}_x\text{CuO}_4$. [143, 144] Since the Mössbauer technique measures local structural changes with a characteristic time scale of $\sim 10^{-8}$ sec, much slower than XAFS, the two techniques can be combined to learn about structural dynamics. As shown in ref. 144, a dynamical picture for the CuO_6 octahedra tilts is mandatory to reconcile the XAFS and the Mössbauer results.

5.3 Sr induced distortions in $\text{La}_{2-x}\text{Sr}_x\text{CuO}_4$

5.3.1 Experimental results

Polarized Sr K -edge measurements were performed on the same samples used in the La K -edge measurements described above. For these measurements, the harmonic content of the beam was minimized by detuning the second crystal of the Si(111) double crystal monochromator so that the intensity of the fundamental is reduced by about $\sim 20\%$, as explained in chapter 3. Measurements were carried out at low temperatures (10-300K) in the way described previously for samples with $x = 0.075, 0.1, 0.125, 0.15, 0.2, 0.25, 0.36$. Typical absorption data at the Sr K -edge is shown in fig. 5.23 for $x = 0.1$, $T=17\text{K}$, $\hat{e} \perp \hat{b}$ after pre-edge subtraction and edge

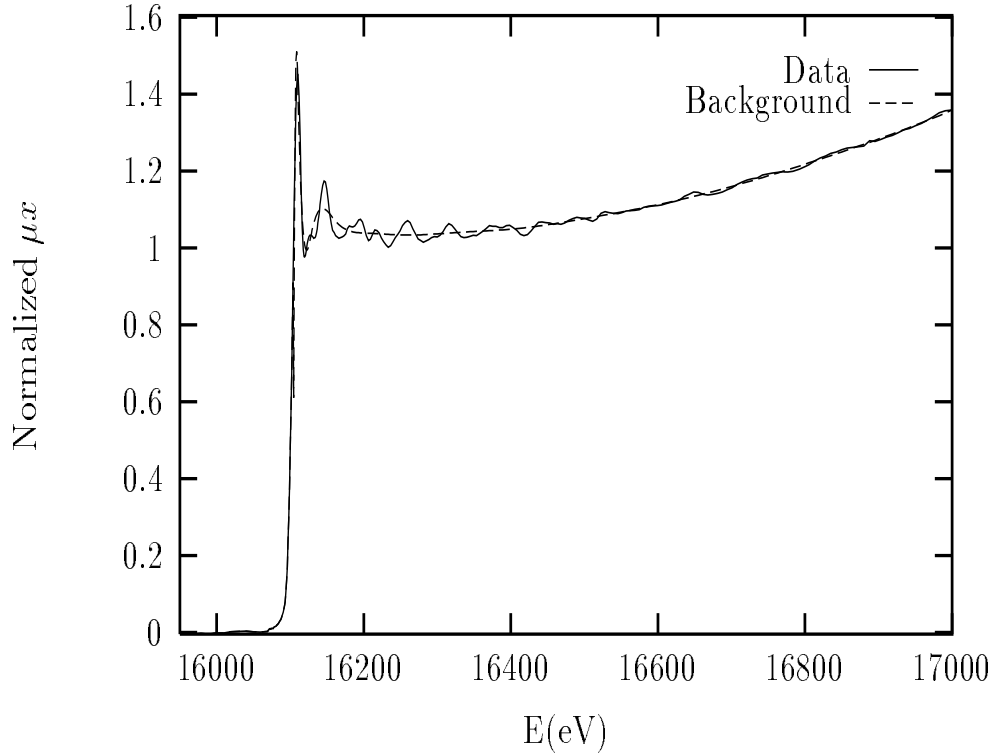


Figure 5.23: Sr K edge in $\text{La}_{1.9}\text{Sr}_{0.1}\text{CuO}_4$ at $T=17\text{K}$, $\hat{a}c$ -polarization

step normalization. The background function as obtained by AUTOBK with the parameters shown in table 5.10 is also included. Reproducibility scans for the $x = 0.1$ sample at 17K are shown in fig. 5.24.

The same procedure used in modeling the atomic environment about the La atoms, as described above, was used in the analysis of the Sr K -edge data. As diffraction determines that Sr substitutes for La in the lattice [20], FEFF6 calculations were performed for a Sr central atom substituted at the La site. The effect of random substitution is modeled in the same way as described for the La K -edge analysis, i.e., FEFF6 calculations are performed for all La/Sr neighboring sites occupied by either La or Sr and the theoretical paths weighted in the fit by the relative concentration of Sr. If Sr indeed substitutes for La in the lattice, without major additional structural distortions, their XAFS should be similar. Of course some differences are expected due to two main reasons: the central atom phase shift and the core-hole lifetime. Figure 5.25 shows a comparison between the total mean free path, $\lambda(k)$, calculated by FEFF6 for both Sr and La central atoms. As inelastic losses of the p.e. in

Table 5.10: Parameters used for the background removal shown in fig. 5.23. Fourier components are minimized with respect to the FEFF6 standard in the region $[0, r_{\text{bkg}}]$. The amplitude of the standard is scaled to that of the data in the region $[r_{\text{bkg}}, r^{\text{1st}}]$. Fourier transform k -weight, range and Hanning window sill widths are also shown.

E_0 (KeV)	r_{bkg} (Å)	r^{1st} (Å)	k_{min} (Å ⁻¹)	k_{max} (Å ⁻¹)	kw	dk (Å ⁻¹)
16.105	1.5	2.3	0.1	18	1	0.5

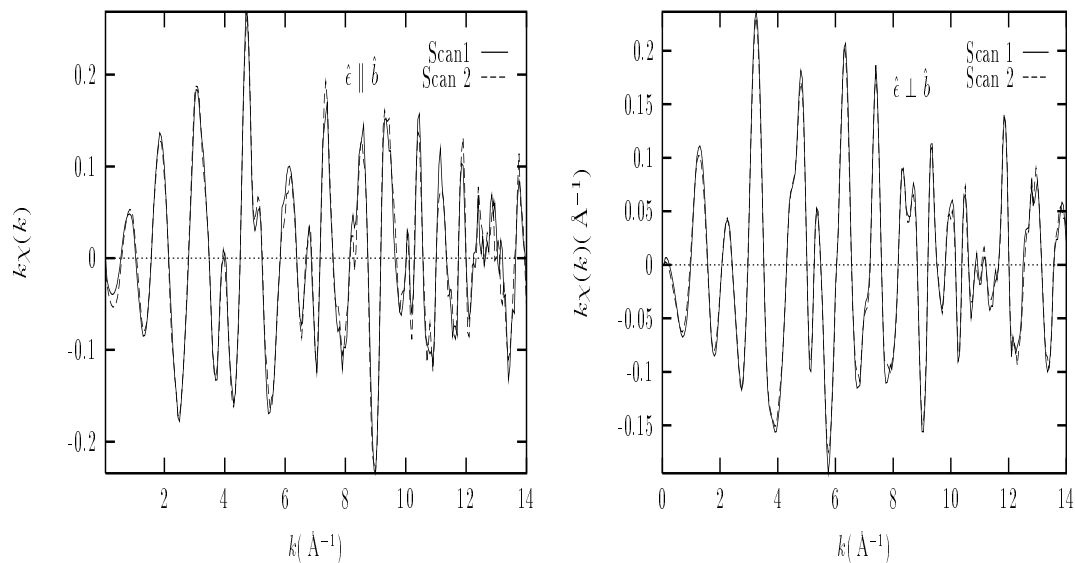


Figure 5.24: $k\chi(k)$ reproducibility data for $\text{La}_{1.9}\text{Sr}_{0.1}\text{CuO}_4$ at $T=17\text{K}$. Left: \hat{b} -polarization; right: in-plane, $\hat{a}\hat{c}$ -polarization

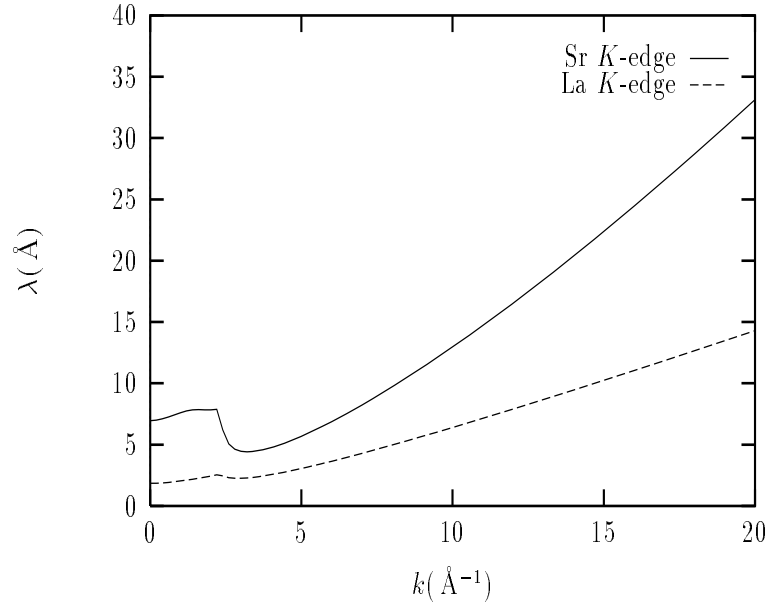


Figure 5.25: Theoretical total p.e. mean free path as calculated by FEFF6 for both Sr and La K -edge XAFS in $\text{La}_{2-x}\text{Sr}_x\text{CuO}_4$. Calculation is done using the average atomic positions corresponding to $x = 0.075$ at 10K. [20]

the interstitial region are expected to be nearly the same in both cases, the major difference comes from the longer lifetime of the Sr core hole resulting in a longer mean free path. The final state energy broadening is smaller in the Sr case and therefore the amplitude of the Sr XAFS is expected to be larger than the La one. Because of this difference, three additional SS paths that did not significantly contribute to the La XAFS were needed in the modeling of the Sr \hat{b} polarized XAFS. These paths are listed in table 5.11.

Initially fits were performed for the more dilute samples $x = 0.075, 0.1$, as these should better reflect the effect of an isolated Sr atom in the lattice without significant interactions with distortions induced by other Sr atoms. In addition, the reports on observations of strong diffuse scattering [53] and Sr-induced apical O(2) removal [55] were based on experiments on samples with these particular Sr contents. The low x results are then reported first and their concentration dependence, when present, will be emphasized.

In order to check if the Sr atoms substitute for La in the lattice and for the presence of Sr-induced distortions, a more general model was used that allowed the

Table 5.11: Additional paths required in fitting the Sr K -edge XAFS in the $r = [1.8, 5.2]$ region of r -space. The corresponding theoretical paths listed in tables 5.2 & 5.3 for a Sr central atom were also used. Values correspond to $x = 0.075$ at 10K.

Path	r_{eff} (AA)	Degeneracy	Type	Polarization
Sr _c -O(2)-Sr _c	5.010	($\times 2$)	SS	\hat{b}
Sr _c -O(1)-Sr _c	5.028	($\times 2$)	SS	\hat{b}
Sr _c -O(1)-Sr _c	5.205	($\times 2$)	SS	\hat{b}

angle that some SS paths form with the \hat{b} axis to vary, as explained below. For powder oriented only in the \hat{b} direction and random in the \hat{ac} plane, the following holds for the XAFS of a SS path i at an angle θ_i with the \hat{b} axis:

$$\begin{aligned}\chi_b^{(i)}(k) &= 3\cos^2\theta_i \chi_{\text{ran}}^{(i)}(k) \\ \chi_{ac}^{(i)}(k) &= 3\frac{\sin^2\theta_i}{2} \chi_{\text{ran}}^{(i)}(k)\end{aligned}\tag{5.2}$$

with $\chi_b(k)$, $\chi_{ac}(k)$ being the measured XAFS with the electric field parallel to the \hat{b} and \hat{ac} orientations, respectively, and $\chi_{\text{ran}}(k)$ the XAFS signal of a completely unoriented powder (see appendix B for a derivation). Therefore, initially the FEFF6 calculation was performed to calculate the random XAFS $\chi_{\text{ran}}(k)$ using the average atomic positions found by diffraction [20] and the two polarized XAFS data were fitted *simultaneously* by weighting their respective amplitudes as given in eq. 5.2 and varying θ_i , in addition to varying the structural parameters as described above. This procedure was applied to fit the data up to $r \approx 4 \text{ \AA}$ where only O, Cu and La/Sr SS paths contribute to the XAFS (see table 5.2). Due to the limited amount of information in the first shell region of r -space, $r = [2.3-3] \text{ \AA}$ coupled to the complexity of the first shell environment, only three angles were refined in that region (Sr-O(1) and in-plane Sr-O(2)) while two additional constraints were imposed at this stage: the Sr-O(2) in-plane distances at $r \sim 2.73 \text{ \AA}$ were set to their average structure values and the same σ^2 was refined for the Sr-O(1) and Sr-O(2) distances. These constraints were later removed, as explained below. The angle determination together with the refined interatomic distances should provide a well defined answer for the position of the Sr atoms.

This initial SS analysis confirmed that Sr indeed substitutes for La in the lattice. For example, for the $x = 0.1$ sample at 17K the angles the two pairs of Sr-O(1) short and long distances form with the \hat{b} -axis are $\theta^{(s)} = 44.1 \pm 6.1^\circ$ and $\theta^{(l)} = 41.9 \pm 6.2^\circ$, respectively, consistent with the values $\theta^{(s,l)} = 47.8, 44.2^\circ$ found in the diffraction studies. For the in-plane Sr-O(2) distances, the single common angle varied for all three bonds was found at $\theta(O(2)) = 78.8 \pm 8^\circ$, consistent with the values 76.6, 77.6, 78.6° found by diffraction. [20] In addition, the Sr-Cu and Sr-La distances agree with their average values, as discussed below. Therefore, for subsequent fits, *polarized* FEFF6 calculations were used in the refinements with the angles corresponding to their average structure values.

A $k = [3, 14] \text{ \AA}^{-1}$ data range was used in the analysis of the $r = [1.8, 5.2] \text{ \AA}^{-1}$ region of r -space (which now includes MS paths), resulting in $N_I = 52$ and $N_P = 25$, as two more additional parameteres (a distance and a σ^2) were added, as compared to the La case, for the three additional paths in table 5.11. Sr K -edge data and fits for the $x = 0.1$ sample at T=17K in both orientations are shown in figs. 5.26 & 5.27

As expected for substitution at the La site, the Sr K -edge XAFS and the La K -edge XAFS have a lot of similarities, as seen by comparing the Fourier transforms of both data. The overall amplitude of the Sr XAFS is larger, due to core hole lifetime effects discussed above. Whereas the signal above $r \sim 3 \text{ \AA}$ is very similar for both edges (corresponding mostly to the Cu and La heavy atoms), a clear difference exists in the low r -region of the spectra, associated with the first neighboring oxygen environment.

The main results of the fits are summarized in the following sections.

5.3.2 On Sr substitution at the La site

The Sr-Cu and Sr-La distances and σ^2 's up to the fifth shell are, within 0.01 \AA and 0.001 \AA^2 , respectively, the same as those found in the La K -edge analysis for La-Cu and La-La and in agreement with the distances found by diffraction for the average structure. This result confirms that Sr indeed substitutes for La in the lattice and is consistent with the Sr⁺² and La⁺³ ions having nearly the same size. The fact that the Sr atoms are not themselves displaced from the average lattice positions is in agreement with the observation of no change in diffuse scattering when scanning the x-ray energy through the Sr K -edge resonance, as observed by Isaacs *et. al.* [53] The Cu and La atoms around Sr being at the average lattice positions rules out

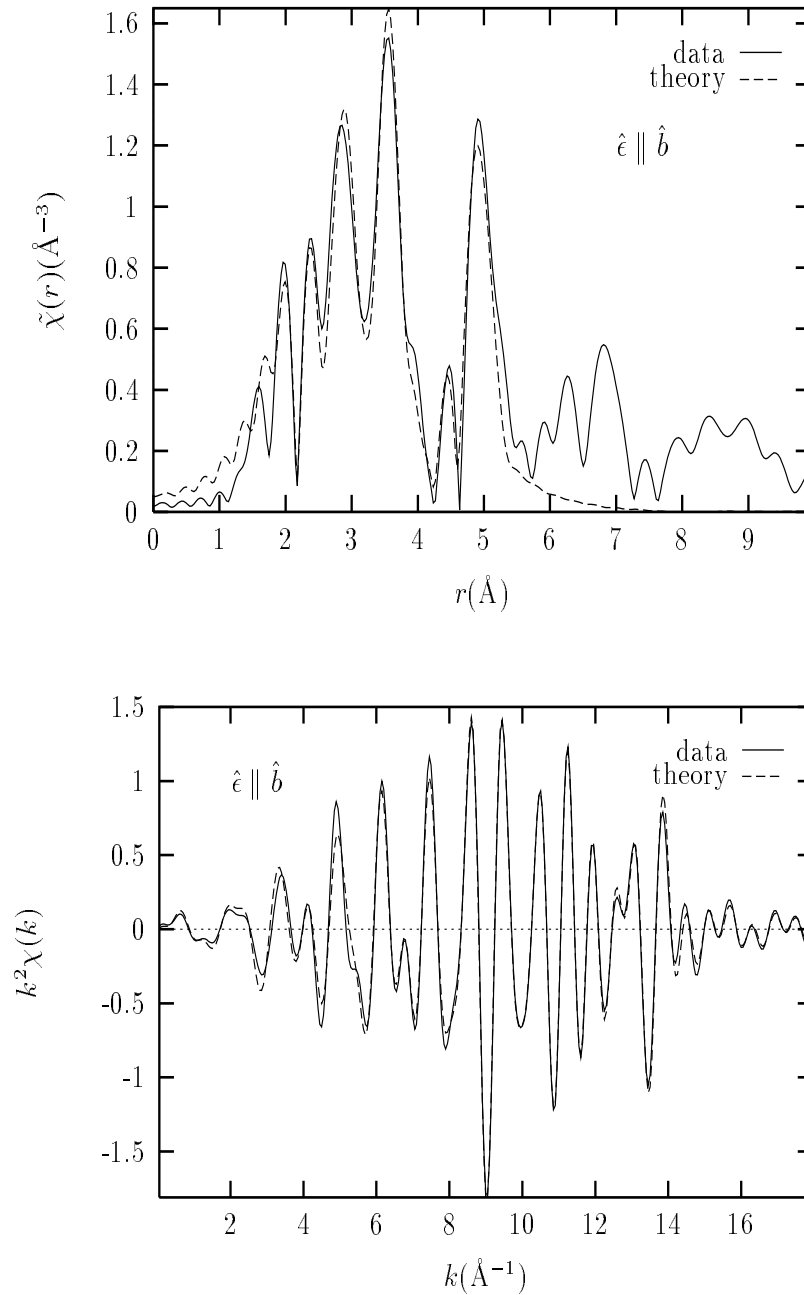


Figure 5.26: Sr K -edge fit results for $x = 0.1$, $\hat{\epsilon} \parallel \hat{b}$ at $T=17\text{K}$. Top: Magnitude of the complex Fourier transform; bottom: back Fourier transform of the fitted region of r -space.

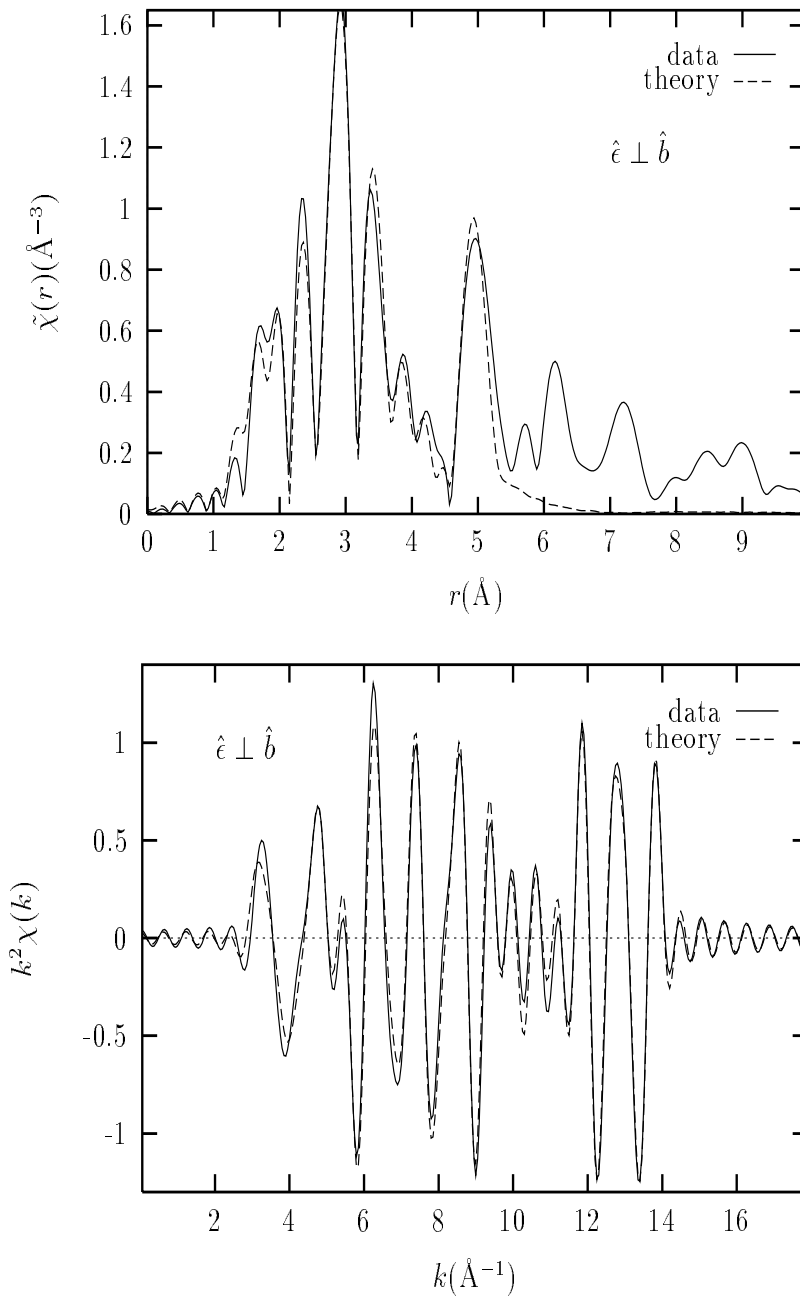


Figure 5.27: Sr K -edge fit results for $x = 0.1$, $\hat{\epsilon} \perp \hat{b}$ at $T=17\text{K}$. Top: Magnitude of the complex Fourier transform; bottom: back Fourier transform of the fitted region of r -space.

the possibility of them contributing to the observed diffuse scattering, leaving the Sr-induced oxygen distortions, as discussed below, the most likely origin for the observed diffuse scattering.

5.3.3 On the nature of the Sr-O(1) distortions

Whereas the La-O(1) distances ($r = 2.591 \text{ \AA}$ and $r = 2.675 \text{ \AA}$ for $x = 0.1$ at 10K) were found to be in agreement with the diffraction results, at least up to about $x = 0.15$ (see fig. 5.10), the short and long Sr-O(1) distances are found to be $r_s = 2.542(10) \text{ \AA}$ and $r_l = 2.734(12) \text{ \AA}$, respectively. This increased splitting is the reason for the double peak structure observed in $\tilde{\chi}(r)$, \hat{b} -polarization, at low r (1.8-2.6 \AA) (fig. 5.26) as the signal there is due to scattering contributions from four O(1) atoms and one apical O(2) atom, the latter having a small contribution as will be discussed below (the low r contribution to the $\hat{a}c$ polarization includes in-plane O(2) contributions in addition to the O(1) oxygens). The presence of the increased splitting will result in a “beat” in k -space in the first shell signal of the \hat{b} -polarized XAFS. This can be seen by adding two sine waves with the same amplitude A (each distance is double degenerate) but slightly different frequencies Δr ,

$$\begin{aligned} A(\sin 2kr + \sin[2k(r + \Delta r)]) &= & (5.3) \\ A(\sin 2kr + (\sin 2kr \cos 2k\Delta r + \cos 2kr \sin 2k\Delta r)) &\approx \\ A\sin 2kr[1 + \cos 2k\Delta r] & \end{aligned}$$

resulting in a modulated oscillation with a minimum (“beat”) at $2k\Delta r = \pi$. For the splitting of Sr-O(1) distances obtained here, $\Delta r = 0.192 \pm 0.015$, the “beat” would appear at $k = \pi/(2\Delta r) = 8.2 \text{ \AA}^{-1}$. The first shell oxygen signal in the \hat{b} polarization was obtained by subtracting from the data, in r -space (real and imaginary parts), the contribution of the Sr-Cu SS signal ($r \sim 3.2 \text{ \AA}$) as obtained in the best fit (to account for the leakage of the Sr-Cu signal into the first shell region) and back Fourier transforming the $r = [1.8, 2.8] \text{ \AA}$ region to k -space. The result of this procedure is shown in fig. 5.28 together with the \hat{b} -polarized FEFF6 calculation of the first shell signal using the average structure values for the distances corresponding to $x = 0.1$ (theory). Debye Waller factors equal to those found in the fits for the oxygen atoms were added to the theory for the comparison. The “beat” at $\sim 8 \text{ \AA}^{-1}$ is observed in

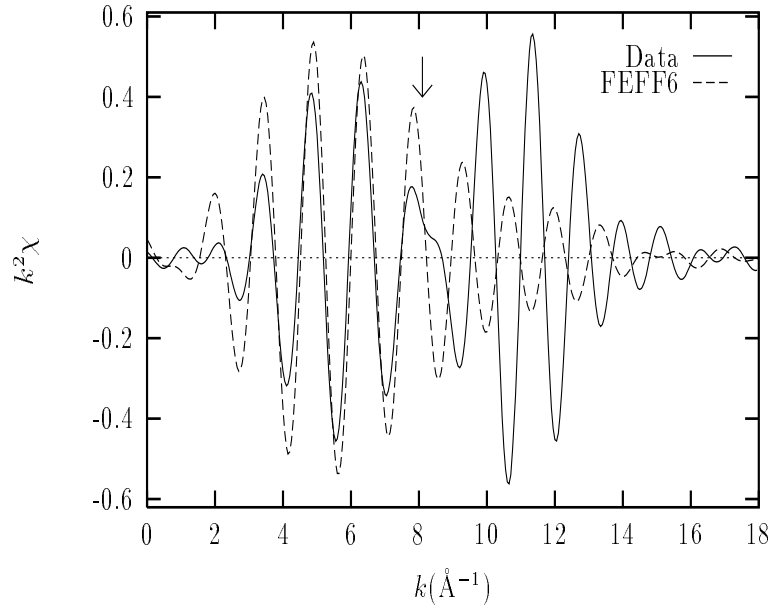


Figure 5.28: Isolated oxygen first shell signal obtained by Fourier filtering the $x = 0.1$, \hat{b} -polarized $\tilde{\chi}(r)$ in the region $r = [1.8, 2.8] \text{ \AA}$ and its comparison to the FEFF6 calculation using the average structure distances (theory). Debye Waller factors equal to those found in the fits were added to the theory for the comparison.

the data and absent in the theory, in agreement with the measured splitting of the Sr-O(1) distances.

Whereas the longer Sr-O(1) distance showed no significant dependence on Sr content, the shorter Sr-O(1) distance exhibits a small concentration dependence, as shown in fig. 5.29. In order to accommodate the changes in Sr-O(1) distances while the Sr-Cu distances remain unaltered, the Cu-O(1) bonds in the basal plane of the CuO_6 octahedra involving these O(1) oxygens must become distorted compared to the average structure. These distortions are *not* associated with a *rigid* tilt of the CuO_6 octahedra involved since that would have caused a related distortion of the O(2) oxygens forming the apex of the CuO_6 octahedra and nearly coplanar with the Sr, which was not the case. The in-plane O(2) oxygen positions and their concentration dependence are also shown in fig. 5.29.

5.3.4 Implications of the Sr-O(1) distortions

Based on the nature of the O(1) distortions (two oxygens get closer to Sr while two others get farther away from it) it is likely that charge redistribution effects around the dopant atoms are responsible for the distortions and not a size effect (a uniform expansion/contraction of distances is not observed). The polaronic nature of these distortions indicate that the hole doped by the Sr atom is liberated from the dopant atoms and is redistributed in the oxygen neighbors (and probably Cu's since they are highly hybridized with oxygens in the plane), resulting in different equilibrium positions of the O(1) atoms around the dopant site. Since the normal state of $\text{La}_{2-x}\text{Sr}_x\text{CuO}_4$ displays metallic behavior in the $\hat{a}c$ orientation, even if a significant fraction of the hole's wave function is localized around the impurity, it must be extended enough to result in the measured conductivity. The small changes detected in the short Sr-O(1) distance with x could reflect changes in the hole occupation of the O(1) $2p_{x,y}$ -Cu $3d_{x^2-y^2}$ hybrids, even though it is not obvious why similar changes are not observed in the longer Sr-O(1) distance. It should be mentioned that when a La atom is replaced for a Sr atom the inversion symmetry about the CuO_2 plane is broken and hence the O(1) sites closer and further away from Sr are not equivalent any more.

Recently, distortions in $\sim 16\%$ of the Cu-O(1) bonds were reported from Cu K -edge XAFS analysis on a $x = 0.15$ sample [131]. Those distortions were attributed to the coexistence of LTO and LTT-like stripes at low temperatures. Even though the changes needed in the Cu-O(1) distances to accommodate the distortions in the Sr-O(1) distances found here are not as big as those reported by Bianconi *et. al* , it is estimated that Sr induces distortions in about 10% of the Cu-O(1) bonds at the given concentrations. This, together with the lack of evidence in our analysis for a change in tilt *direction* of the CuO_6 octahedra (the Sr-O(2) distances found are not consistent with LTT-like tilts), opens a new mechanism to interpret the results of Bianconi *et. al* [131] as localized distortions in the basal plane of the CuO_6 octahedra neighboring the Sr atoms only.

The O(1) distortions can be viewed as an increased local buckling of the CuO_6 plane around the Sr atoms. This type of distortion could have profound implications for the disappearance of AF long range order of the Cu^{+2} moments in the CuO_2 planes as Sr is doped into the system. [24] In addition, the observation that the correlation length of the 2D AF short range order that persists for $x \gtrsim 0.03$ decreases

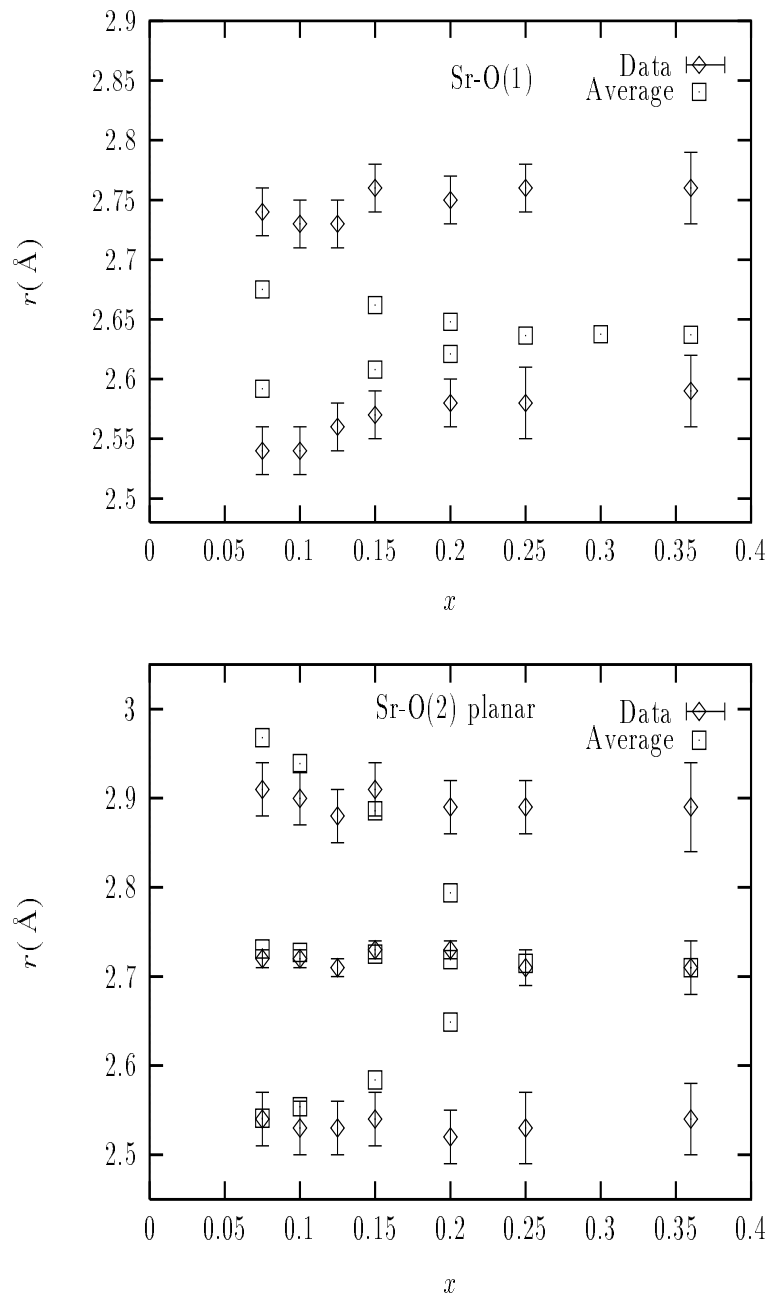


Figure 5.29: Sr-O(1) and planar Sr-O(2) distances as obtained from Sr K -edge fits at $T \sim 20K$. The local distortions of the Sr-O(1) distances are not associated with a rigid tilt of the CuO_6 octahedra involved, as seen by the absence of correlated displacements of the planar O(2) oxygens.

nearly linearly with the average separation between holes (assuming they are doped predominantly into the CuO_2 planes) [24] could indicate that the AF exchange interaction could not only be affected by hole doping into the CuO bonds [28] but also by the related local structural distortion observed here.

The “enhanced” LTO distortion of the CuO_2 planes next to Sr atoms probably contributes to the stabilization of the LTO phase as the structural ground state of $\text{La}_{2-x}\text{Sr}_x\text{CuO}_4$. The calculations of Pickett *et. al* [66] found the LTT phase to be slightly more stable than the LTO phase (by ~ 15 meV per primitive unit cell). The ground state of the $\text{La}_{2-x}\text{Sr}_x\text{CuO}_4$ system is, however, the LTO phase. Even though the calculations were done using unit cell parameters corresponding to $\text{La}_{2-x}\text{Ba}_x\text{CuO}_4$ and a volume effect could be the reason of not accurately describing the situation in the $\text{La}_{2-x}\text{Sr}_x\text{CuO}_4$ system, it is possible that the stabilization energy associated with the Sr distortions and not included in the calculation could drive the LTO phase more stable than the LTT one. [66]

In terms of the Sr-induced LTO to HTT phase transition at low T, it is interesting to note that the local La-O(2) distances in fig. 5.9 saturate at about the values found for the Sr-O(2) distances (fig. 5.29). It is possible that for $x \gtrsim 0.15$ the concentration of Sr is high enough for the distorted, highly stable, LTO domains around the Sr atoms to constrain neighboring cells in the configuration measured around the majority La atoms. How these LTO domains disorder to result in the HTT long range order measured by diffraction is not evident from these results. Probably the answer lies in the intermediate short range order arrangement of atoms about the Sr atoms, as already mentioned.

5.3.5 The O(2) apical oxygen to Sr: experimental results

Since the Sr-O(2) apical SS signal at $r \sim 2.35 \text{ \AA}$ is small, it was not possible to unambiguously separate the effect of O(2) occupancy from that of disorder on the amplitude of the SS path. As already mentioned, it is of interest to determine the O(2) apical occupancy as it was suggested in the work of Tan *et. al* [55] that the O(2) apical to Sr is removed upon Sr doping. To solve this question, the Sr-O(2)-Cu MS signal at $r \sim 4.76 \text{ \AA}$ along the \hat{b} -axis was exploited. Since these MS paths are nearly collinear, they are not so sensitive to the disorder of the focusing atom (O(2)) (see appendix C) but their phase and amplitude are extremely sensitive to the presence of the intervening O(2) focusing atom. [78] Figure 5.30 shows \hat{b} -polarized FFFF6

Table 5.12: Fit results to \hat{b} polarized data in the region $r = [3.8, 4.8]$ where Sr-O(2)-Cu MS paths contribute to the XAFS. Fits were done with and without the presence of the O(2) apical oxygen for $x = 0.075, 0.1$ at 10K. Δr is the change in distance relative to the average structure value of the Sr-Cu SS path; $r = 4.754 \text{ \AA}$.

Model	χ^2_ν	$\Delta r(\text{ \AA})$	$\sigma^2(\text{ \AA}^2)$
With O(2)	5.4	-0.007 ± 0.013	0.0048(20)
Without O(2)	8.1	0.084 ± 0.022	0.0019 (20)

calculation of the Sr-O(2)-Cu MS paths as compared to the calculation when the O(2) intervening atom is removed. The three SS oxygen paths at $r \sim 5 \text{ \AA}$ shown in table 5.11 are also included in the plot in both cases, even though their contribution is small compared to that of the MS paths. Atomic positions correspond to their average values for $x = 0.1$ at 10K. [20] Significant differences exist in both amplitude and phases.

After setting all other parameters to their best fit values, fits were performed for the \hat{b} -polarized data in the region of r -space that includes the MS paths of interest, $r = [3.8, 4.8]$. Comparisons were made between fits obtained when the apical O(2) is in place (MS contributes, model 1) with the one obtained when the O(2) atom is absent as proposed in the literature [55] (only Sr-Cu SS contributes, model 2). Table 5.12 summarizes the comparison. When O(2) is present a factor of ~ 1.5 improvement in χ^2_ν is obtained. The statistical significance of this improvement is questionable, as $N_I \sim 7$ and $N_P = 2$ resulting in $(1 + \sqrt{2/\nu}) \sim 1.6$ and hence the two fits are barely one standard deviation apart. What is more important, however, is the physical parameters obtained. The smaller σ^2 needed for the theory in model 2 compensates for the smaller amplitude of this model as shown in fig. 5.30. The very large, unphysical change in distance (relative to the average structure values of $x = 0.1$ at 10K) is about the right size to partially compensate for the total phase change between the two models (fig. 5.30). This results indicate that the O(2) apical is present in the lattice.

As already mentioned, the nearly collinear MS paths are not so sensitive to the disorder of the intervening O(2) atom. In order to obtain this information and to check that indeed the O(2) site is fully occupied, the structural parameters of the Sr-

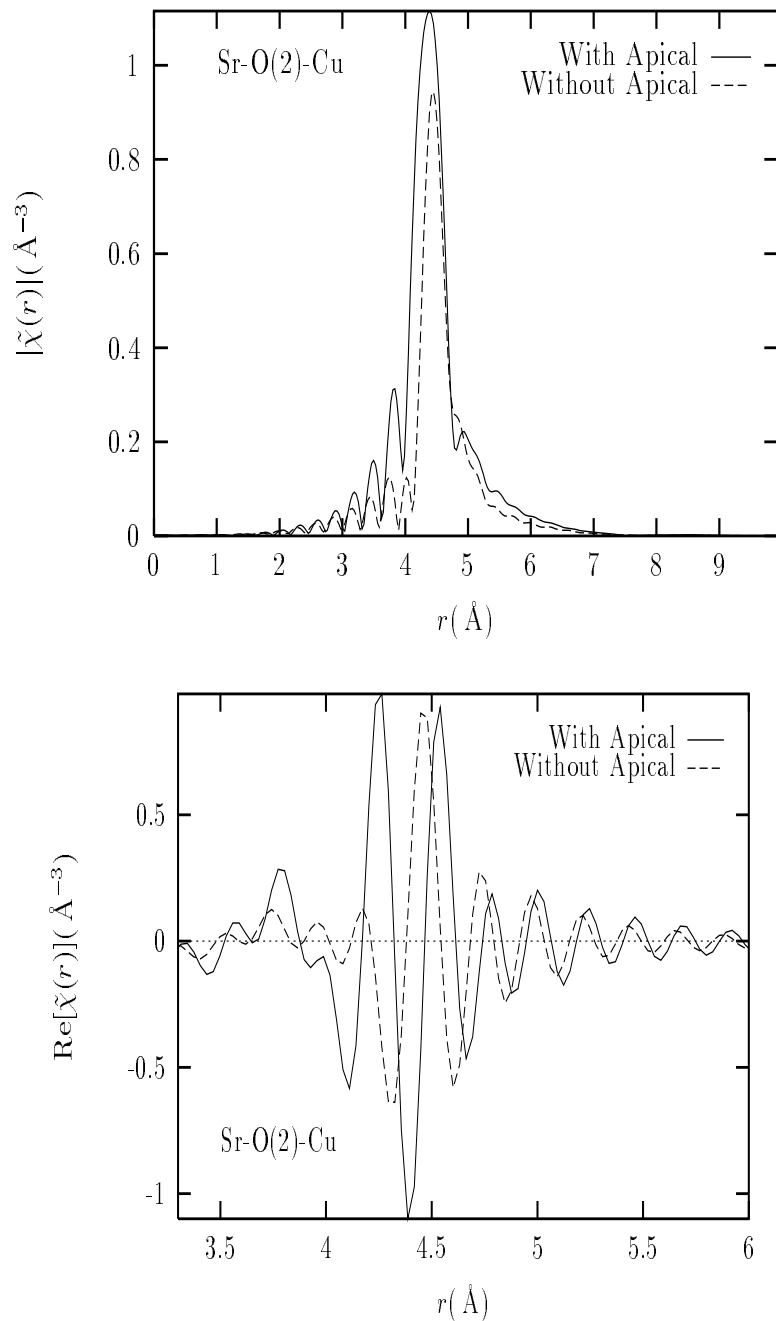


Figure 5.30: FEFF6 calculation of the Sr-O(2)-Cu MS paths at $r \sim 4.76 \text{\AA}$ with and without the O(2) apical oxygen. Three SS oxygen paths at $r \sim 5 \text{\AA}$ listed in table 5.11 are also included in both cases. Magnitude (top) and real part (bottom) of the Fourier transform are shown. Atomic positions used correspond to $x = 0.1$ at 10K.

O(2) SS path and the Sr-O(2)-Cu MS paths were refined in a self-consistent manner to determine the O(2) apical occupancy, position and disorder. For this purpose, the amplitude of the Sr-O(2) SS path and the Sr-O(2)-Cu DS and TS paths was multiplied (via an “effective” S_0^2 in FEFFIT) by a variable, weighting coefficient, z , that was refined by fitting the two regions of r -space simultaneously (note that z is not exactly the same as the occupancy of the O(2) atom but a probability weight of the actual theoretical path being used in the fit; this is equivalent to a linear interpolation between the two extremes: no apical versus full occupancy).

A value of $z = 0.92 \pm 0.2$ was found in the fit, corroborating that the O(2) apical to Sr is fully occupied (within uncertainties). Initially a Gaussian disorder was assumed and found for the Sr-O(2) apical bond to be $\sigma^2 = 0.02 \pm 0.01 \text{ \AA}^2$, compared to a $\sigma^2 = 0.002(1) \text{ \AA}^2$ found for La-O(2) (table 5.5). A Sr-O(2) distance $r = 2.49 \pm 0.1 \text{ \AA}$ was obtained instead of the $r = 2.35 \text{ \AA}$ found for La-O(2) apical (fig. 5.9) and in the diffraction studies. [20] The large uncertainties arise because a Gaussian disorder is a bad model for the Sr-O(2) apical bond, as discussed below. The distance and σ^2 obtained for the Sr-O(2)-Cu MS paths, however, are within 0.01 \AA and 0.001 \AA^2 , respectively, the same as for La-O(2)-Cu as obtained from the La XAFS, and in agreement with the average structure, indicating the the displacement of the O(2) apical oxygen is mostly along the \hat{b} axis and hence does not affect the total path length of the MS paths, as schematically represented in fig. 5.31.

A striking feature is the order of magnitude greater disorder of the O(2) atom compared to that of the surrounding Cu and Sr atoms in fig. 5.31. This is quite unusual since for a constant potential between O(2) and its neighbors one would expect a fluctuating force from the large σ^2 which would increase the σ^2 between the Sr and Cu atoms. A possible explanation is that the potential sensed by the O(2) atom is not constant but is fluctuating depending on the hole occupation at the Cu site. This fluctuation causes the O(2) to fluctuate between inequivalent equilibrium sites, and thus does not displace the Cu and Sr atoms. Because XAFS cannot distinguish between a *dynamic* fluctuation and a *static* distribution of sites, an alternative explanation would be the existence of inequivalent Sr sites with different static O(2) equilibrium positions.

To test this assumption the O(2) apical signal was isolated from the data by subtracting, from the data in r -space (real and imaginary parts), the contribution of all other paths as obtained in the best fit and back Fourier transforming to k -space the

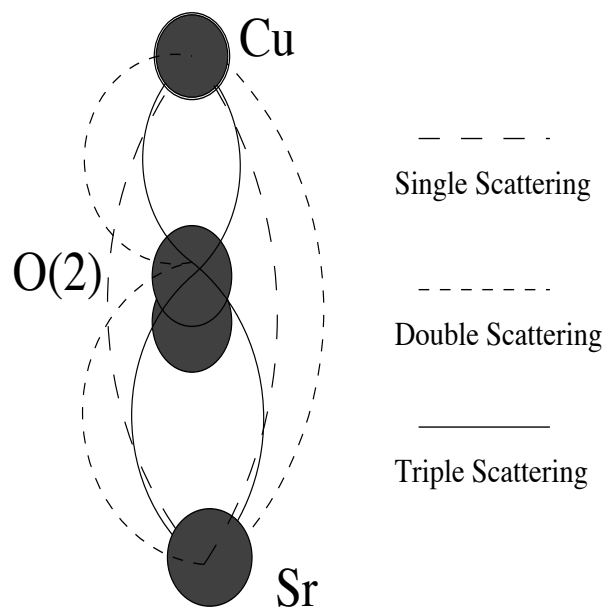


Figure 5.31: Schematic representation of the SS and MS paths used to accurately determine the occupancy of the O(2) apical oxygen to Sr.

$r = [1.8, 2.4] \text{ \AA}$ region of r -space. A comparison of the fitted O(2) apical contribution to the isolated signal showed that a single distance and a σ^2 were not enough, at low x , to fit the O(2) apical XAFS, as shown in fig. 5.32. On the other hand, by fitting the isolated signal with a two-site model, a factor of $\sim (10, 5)$ improvement was obtained for $x = 0.075, 0.1$, respectively, even though the degrees of freedom were reduced by two additional parameters (a splitting and the relative occupancy of the two sites). A significant concentration dependence was found for the O(2) signal, with the improvement in χ_r^2 obtained in the two site model *decreasing* with x to become a factor of ~ 2 at $x = 0.2$ (see fig. 5.32) and negligible at the highest Sr content of $x = 0.36$.

Figure 5.33 summarizes the results obtained by fitting the O(2) signal with a single distance and a σ^2 . Figure 5.34 summarizes the results of the two site model. A single σ^2 was refined for both sites in the two site model and found at $\sigma^2 = 0.0020(15) \text{ \AA}^2$, the uncertainty including the small, random, variation with x . Obviously a correlation exists between the changes observed in σ^2 obtained in the single site model with the changes in relative occupation of the double site model. The splitting of the two site model, however, is independent of Sr content.

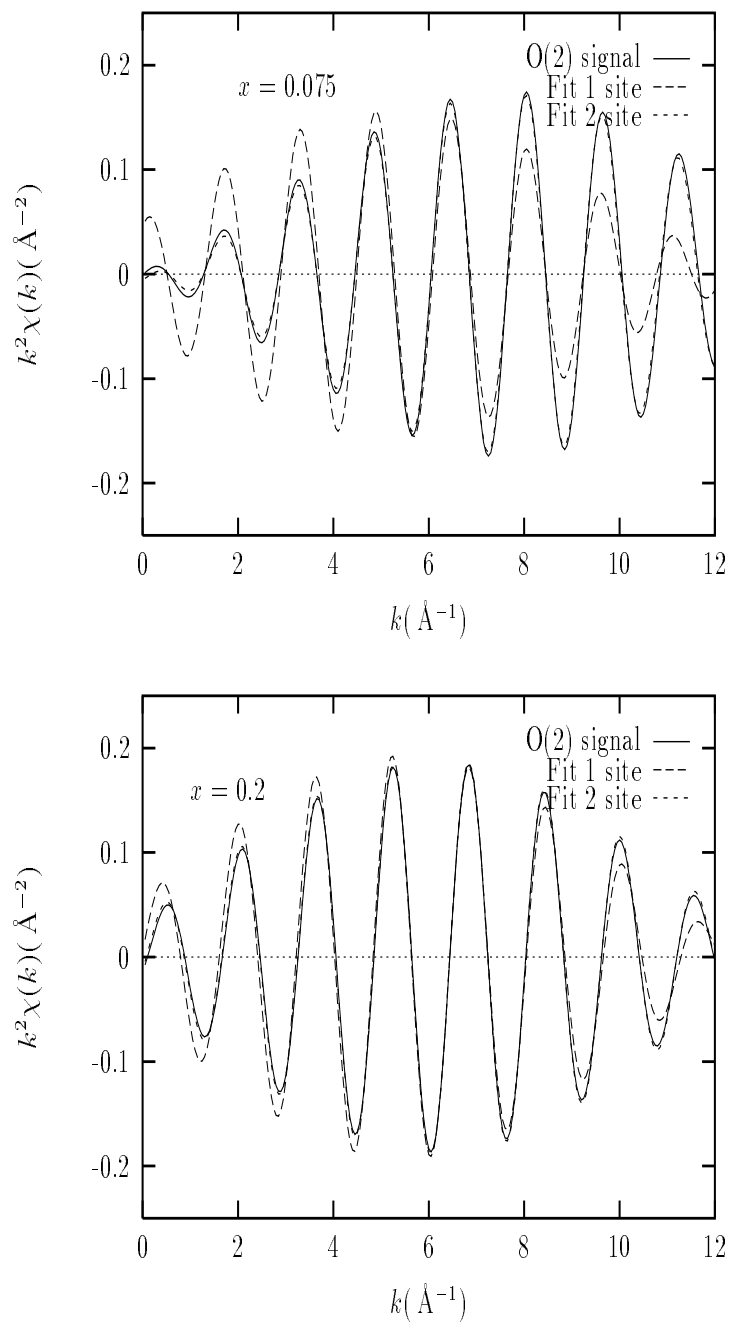


Figure 5.32: Fits to the isolated O(2) signal with single site and double site models. The improvement of the double site model decreases with x , in agreement with the changes in site occupancy shown in fig. 5.34

It is important to note that in addition to these two models, a third model was considered in which anharmonicity was added to the single site potential. This however, resulted in no improvement to the fit, as expected due to the large broadening of the single site model.

To further test this model the temperature dependence of the $x = 0.1$ sample at $T=120\text{K}$, 300K was studied. Whereas the mean-squared disorder in all other distances can be described by harmonic Einstein oscillators, the big σ^2 of the Sr-O(2) bond obtained in the single site model does not show any appreciable temperature dependence. A harmonic potential would have led, at 300K , to a $\sigma^2 \sim$ ten times larger than the measured value. This is inconsistent with a single site, harmonic potential for the O(2) but consistent with the two site model whose overall disorder arises predominantly from the nearly temperature independent splitting of the two sites.

5.3.6 The O(2) apical oxygen to Sr: discussion

Whereas a split apical oxygen site has been observed in several High T_c compounds [145–147], the discovery of such a lattice anomaly *only* at a dopant site is different (no evidence was found for a double site O(2) configuration about the La atoms). This result indicates that hole doping induced by Sr coexists with local lattice distortions, i.e., the Sr hole is a polaron, which could define a more active role for Sr in the mechanism of high T_c superconductivity.

The implications of the O(2) apical distortion are many. In terms of the diffuse scattering intensity observed along c^* cuts (b^* in the notation here) of reciprocal space [53, 54] at low Sr content, the XAFS results clearly indicate that at low x only the O(2) apical and O(1) oxygens *around the Sr atoms* are significantly displaced from their average lattice sites. In addition, the local displacements of these oxygens are mostly along the \hat{b} -axis and therefore they are the most likely origin for the observed diffuse scattering. For example, for $x = 0.075$ the O(2) apical distribution can be described with an effective \hat{b} -axis displacement (relative to the average structure position) of $\Delta r \approx (2.55 - 2.35) \times 0.63 + (2.25 - 2.35) \times 0.37 \approx 0.09 \text{ \AA}$ (each site weighted by its population) and an additional rms broadening of $(\Delta/2) = 0.15$ (Δ the distance between sites $\approx 0.3 \text{ \AA}$) resulting in a \hat{b} -axis rms deviation from the average structure $\langle u_b^2 \rangle^{1/2} \simeq 0.17 \text{ \AA}$. This is a significant contribution to the $\langle u_b^2 \rangle^{1/2} \simeq 0.4 \text{ \AA}$ rms displacement estimated in the diffuse scattering studies. [53] Additional contribu-

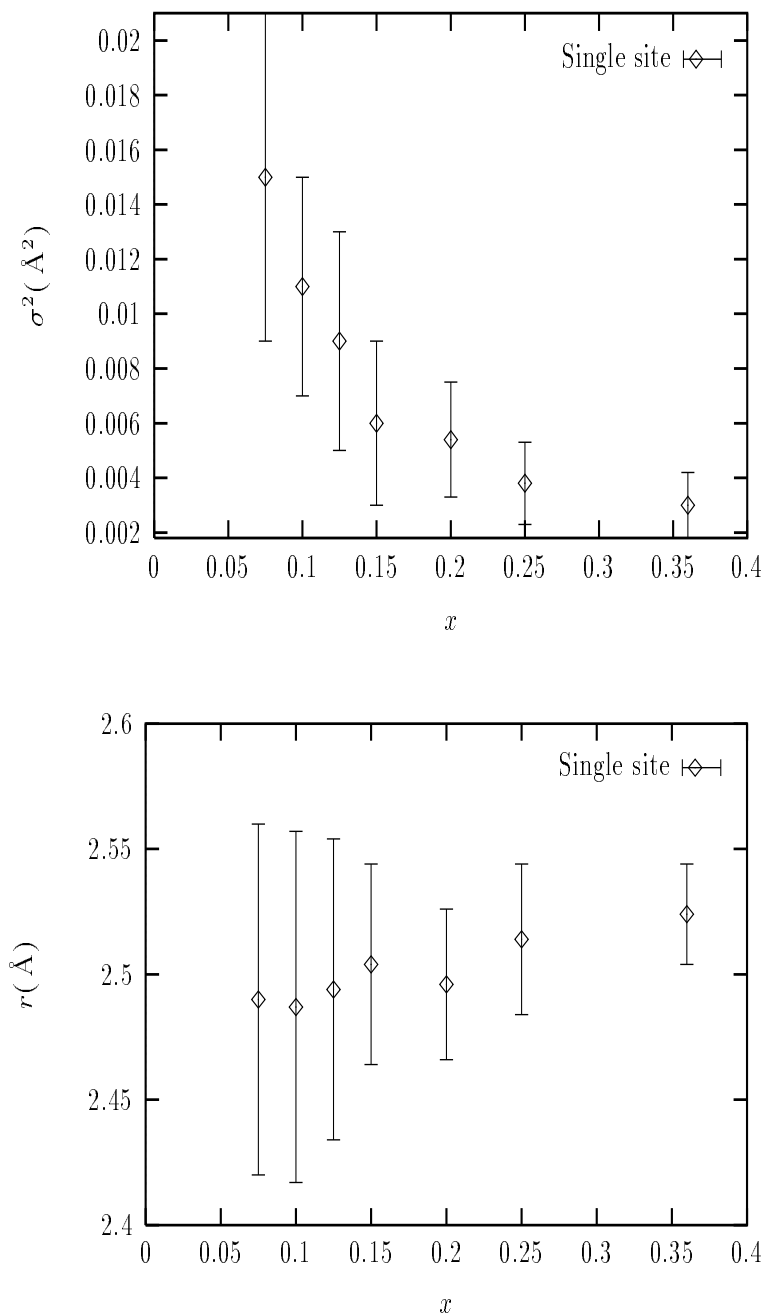


Figure 5.33: Fit results to the isolated O(2) apical signal with a single site model. The mean square-disorder (top) and the site distance (bottom) are shown as a function of Sr content.

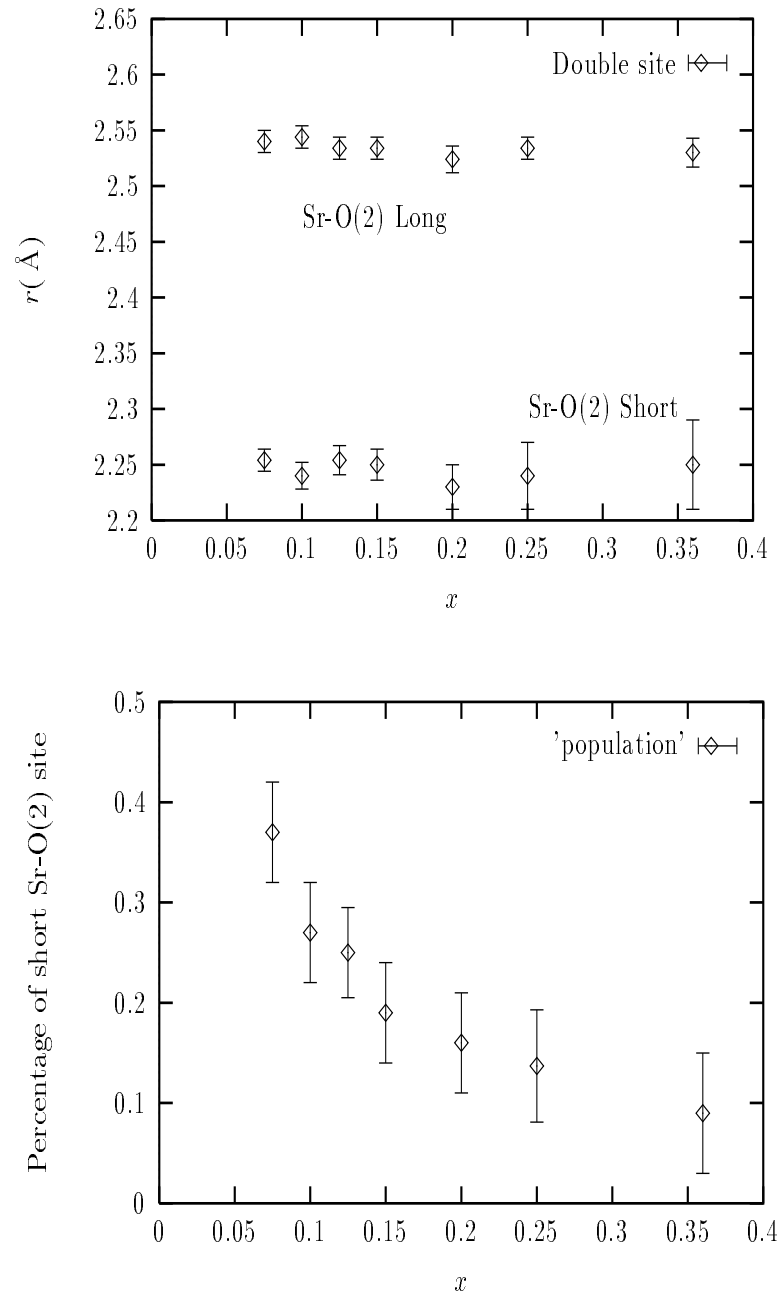


Figure 5.34: Fit results to the isolated O(2) apical signal with a double site model. The distances of the two sites (top) and the percentage population of the short Sr-O(2) distance site (bottom) are shown as a function of Sr content.

tions are expected from the O(1) atoms. The question remains whether the observed distortions here can account for the *magnitude* and the symmetry of the observed diffuse scattering. Preliminary calculations [148] show that the oxygen distortions found here give the right order of magnitude for the observed diffuse scattering, but more accurate calculations are needed to answer this question quantitatively.

The continuous decrease in the normal state \hat{b} -axis resistivity with Sr doping, with the associated change from “insulating” to “metallic” \hat{b} -axis behavior at about $x \sim 0.2 - 0.25$ [30–32] could be related to the observed O(2) apical distortion. Electronic structure calculations [141] show a significant contribution of O(2) derived O $2p_z$ orbitals (hybridized with Cu $3d_{3z^2-r^2}$) to the total density of states at the Fermi level. Since the coupling between planes along the \hat{b} -axis is mediated by the O(2) atoms, the role of these orbitals in \hat{b} axis conductivity is essential. The importance of these orbitals for the transport properties increases with Sr, as XANES measurements show [25] that the *ratio* of dopant-induced O(2) $2p_z$ to O(1) $2p_{x,y}$ holes increases with doping. The increase in O(2) $2p_z$ character of the doped holes with Sr can qualitatively explain, by itself, the decrease in resistivity with doping along the \hat{b} axis. It is unavoidable, however, not to try to correlate the changes in occupation of the two O(2) apical sites observed here with the observed changes in hole population. At low x the \hat{b} -axis exhibits “insulating” behavior, indicating that the fraction of holes with O(2) $2p_z$ character are highly localized around the dopant atoms. “Metallic” behavior is observed in the \hat{ac} plane even for $x \sim 0.075$, indicating the hole component in the O(1) $2p_{x,y}$ -Cu $3d_{x^2-y^2}$ hybrids is more delocalized. A static polaronic distortion of the lattice is expected as a result of charge localization. It is tempting to associate the two site apical distortion as being a lattice response to the presence of two type of holes, the larger distortion ($2.55 - 2.35 \sim 0.2 \text{ \AA}$) corresponding to the highly localized O(2) $2p_z$ hole and the smaller one ($2.35 - 2.25 \sim 0.1 \text{ \AA}$) corresponding to the more delocalized, O(1) $2p_{x,y}$ holes. As Sr content increases and the O(2) $2p_z$ (O(1) $2p_{x,y}$) orbital character of the hole increases (decreases), so does the population of the correspondent site increases (decreases).

It is suggested by Victor Polinger [149] that the two different sites could result from hole induced *enhanced Jahn-Teller (EJT)* and *anti Jahn-Teller (AJT)* effects at the Cu site neighboring the Sr, resulting from the Cu $3d_{x^2-y^2}$ and Cu $3d_{3z^2-r^2}$ orbital character of the doped holes. As shown in fig. 1.3 of the introduction, the JT elongation of the CuO_6 octahedra in pure La_2CuO_4 (Cu $3d^9$) results from the

different occupations of the $x^2 - y^2$ and $3z^2 - r^2$ orbitals. If a hole with $3z^2 - r^2$ character is added, the elongation is no longer favorable and an AJT effect results in a contraction of the Cu-O(2) distance (elongation of the Sr-O(2) distance). By comparison to La_2NiO_4 for which the Ni ions are not JT ions, a $\sim 0.2 \text{ \AA}$ contraction is expected (see table 1.3), in agreement with the longer Sr-O(2) distance obtained here. If a hole with $x^2 - y^2$ character is introduced, it is suggested by fig. 1.3 that an even larger JT elongation of the CuO_6 octahedra (EJT) will occur. An estimation of this effect as calculated by Polinger *et. al* [149] is in good agreement with the observed shorter Sr-O(2) distance, providing an appealing explanation for the origin of the two sites, even though a complete understanding of the x dependence of the two site population is lacking at present.

Finally, concomitant with the \hat{b} -axis distortion of the O(2) apical oxygen, correlated displacements of neighboring, coplanar O(2) and La atoms were found. Figure 5.35 summarizes the pattern of displacements induced by the presence of Sr. The Sr-O(2) oxygen distances at $r = 4.37 \text{ \AA}$ and $r = 4.53 \text{ \AA}$ are changed from their average structure values by $-0.14 \pm 0.02 \text{ \AA}$ and $-0.11 \pm 0.03 \text{ \AA}$, respectively. The Sr-La distances at $r = 3.95 \text{ \AA}$ and 3.97 \AA show small changes of $0.03 \pm 0.01 \text{ \AA}$ and $-0.023 \pm 0.01 \text{ \AA}$, respectively. Since for these size of atomic displacements only the change in radial distance is obtained and not the direction of the displacements, the arrows in fig. 5.35 are intended as an approximate representation of the actual atomic displacements.

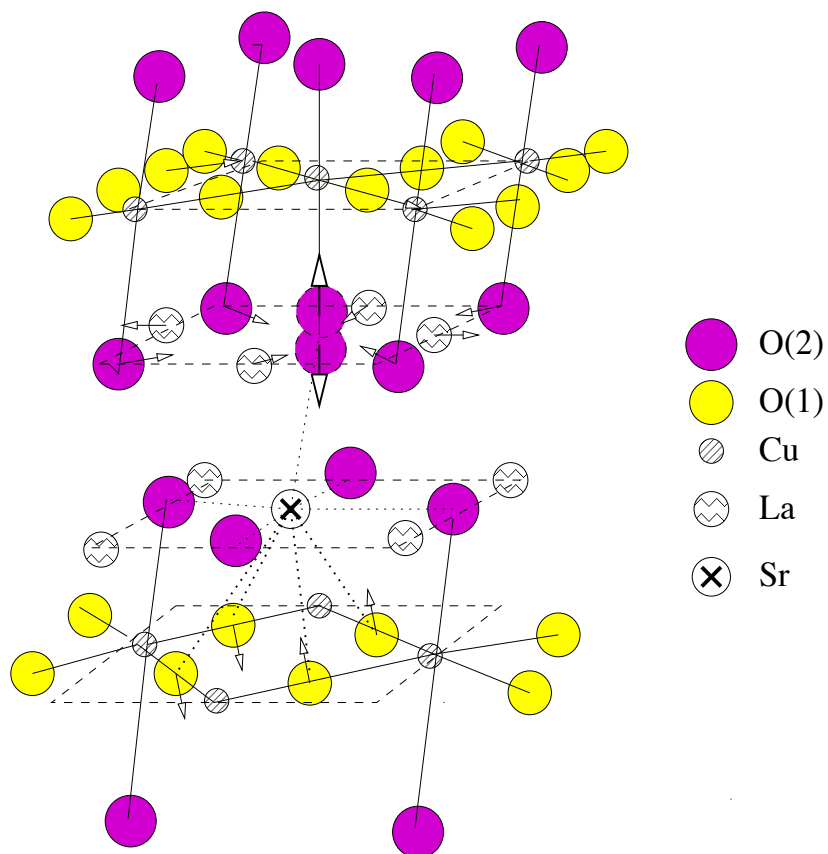


Figure 5.35: Schematic representation of the pattern of atomic displacements induced by Sr substitution in $\text{La}_{2-x}\text{Sr}_x\text{CuO}_4$ as determined by Sr K -edge XAFS. The arrows are intended as an approximate representation of the orientation of the actual atomic displacements.

Chapter 6

XAFS MEASUREMENTS OF $\text{La}_{2-x}\text{Ba}_x\text{CuO}_4$: ANALYSIS AND RESULTS

In this chapter the local structural ground state of $\text{La}_{2-x}\text{Ba}_x\text{CuO}_4$ is determined by La, Ba and Cu K -edge polarized XAFS for $x = 0.125, 0.15$ at $T=10\text{K}$. The combined data reveal a disordered low temperature tetragonal (LTT) ground state, with Ba-induced disorder extending as far as 5 \AA and resulting in a different tilt configuration of the CuO_6 octahedra near the dopant sites. The very different distortions around Ba as compared to those found for Sr in $\text{La}_{2-x}\text{Sr}_x\text{CuO}_4$, are most likely the microscopic origin for the occurrence of the LTT phase in the former. The *local* tilt angle of the CuO_6 octahedra, $\sqrt{\langle\theta^2\rangle}$, averaged over all Cu sites is found to be $\approx 2\langle\theta\rangle$, with $\langle\theta\rangle$ being the tilt angle measured by diffraction techniques based on the long range order, average atomic positions. This result, together with no significant differences in the local atomic displacements of $x = 0.125$ and $x = 0.15$ samples, put strong constraints on models based on charge density wave formation and instead could favor a density of states effect being at the basis of T_c suppression for $x = 0.125$.

6.1 La K -edge measurements

6.1.1 Experimental results

In contrast to the $\text{La}_{2-x}\text{Sr}_x\text{CuO}_4$ system, the $\text{La}_{2-x}\text{Ba}_x\text{CuO}_4$ system undergoes an additional phase transformation when cooling below about $\sim 60\text{K}$ to a low temperature tetragonal (LTT) phase, as shown in fig. 1.4. Since high T_c superconductivity coexists with this new structural modification, it is of interest to determine whether superconductivity is affected by the appearance of the new structural ground state; in particular whether an interplay between the structural modification and superconductivity is at the basis of T_c suppression at $x = 0.125$. A review of some current ideas regarding this interplay together with experimental evidence in favor of an “anomalous” LTT ground state are given in chapter 1. It is then desired to obtain as much

detail as possible about the nature of the LTT structural ground state, especially in the short length scales relevant to superconductivity.

Some details about the LTT structure are given in chapter 1. The space group is $P4_2/nm$ and lattice parameters and atomic positions as determined by neutron diffraction [74] are given in table 1.4. In this notation, the long axis of the unit cell coincides with the \hat{c} -axis. Since neutron diffraction was not performed on the actual samples used here and some variations are reported in the literature for the average structure of fully oxygenated samples [74, 75] (variations in interatomic distances $\leq 0.03 \text{ \AA}$), the XAFS results are compared to two different average structure studies. [74, 75] As discussed before, the superconducting transition temperature T_c obtained for the $x = 0.125$ sample is consistent with an oxygen deficiency $\delta \leq 0.005$ (in $\text{La}_{2-x}\text{Ba}_x\text{CuO}_{4-\delta}$). The structural changes associated with such a small oxygen deficiency were studied by Takayama *et. al* [75], and result in changes in interatomic distances $\leq 0.005 \text{ \AA}$. XAFS results are then compared to diffraction results of fully oxygenated samples.

Figure 6.1 shows the LTT structure together with some near neighboring interatomic distances. The different tilt *direction* of the CuO_6 octahedra in the LTT phase (tilts are about $\langle 110 \rangle$, $Bmab$ representation; i.e. about the direction of the Cu-O(1')-Cu bonds) results in the very different arrangement of La-O(1), La-O(2) and La-La distances shown in fig. 6.1, as compared to the LTO distances shown in fig. 5.1. In terms of XAFS, the La site is therefore the most sensitive to the change in tilt *direction* of the CuO_6 octahedra. Since the tilts are centered on the Cu atoms, Cu XAFS is nearly insensitive to changes in tilt direction, even in MS since the magnitude of the tilt angles involved is rather small ($\leq 3 - 4^\circ$) and about the same in LTO and LTT ground states. Therefore, ascribing changes in local distances obtained from Cu XAFS to changes in tilt *direction* of the CuO_6 octahedra, as it is done sometimes in the literature [131], is speculative unless the suggested distortions can be confirmed from La XAFS.

Polarized XAFS results at the La K -edge of $\text{La}_{2-x}\text{Ba}_x\text{CuO}_4$ with $x = 0.125, 0.15$ at $T=10\text{K}$ are described here. Measurements were done in transmission using a Si(311) double crystal monochromator and details about the experimental setup, including sample preparation and characterization are given in chapters 3& 4. Polarized measurements were taken by rotating the \hat{c} -axis magnetically aligned powder relative to the electric field vector of the synchrotron radiation.

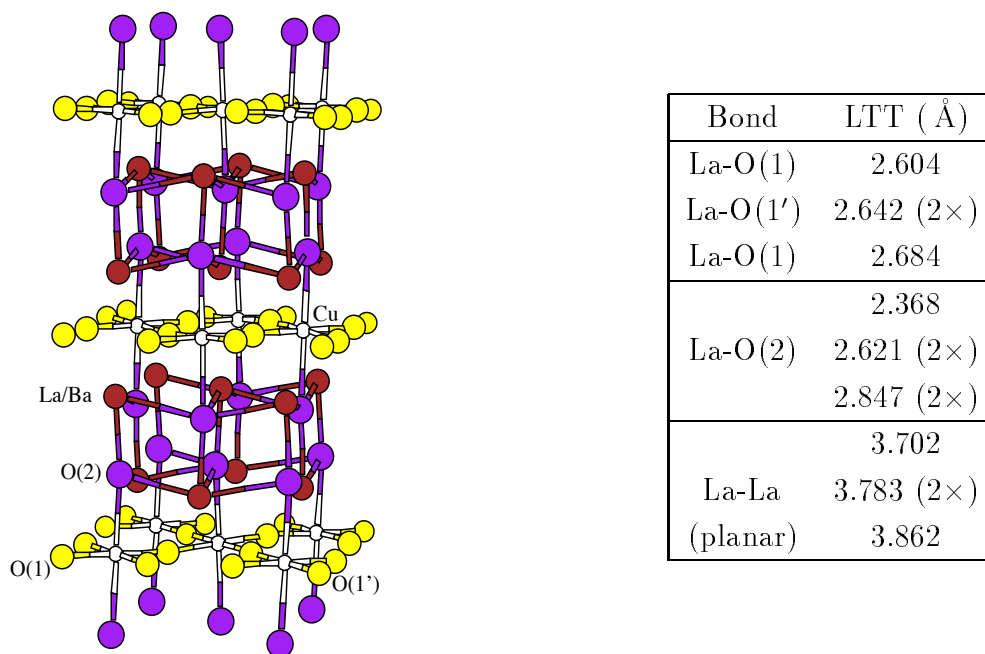


Figure 6.1: Schematic representation of the LTT structure. In the $P4_2/nm$ representation, the vertical axis is the \hat{c} axis and the a axis is perpendicular to the plane of the paper. The La-O and planar La-La interatomic distances are shown for $x = 0.125$ as obtained from neutron diffraction at $T=15\text{K}$. [74] Degeneracies are shown in parenthesis.

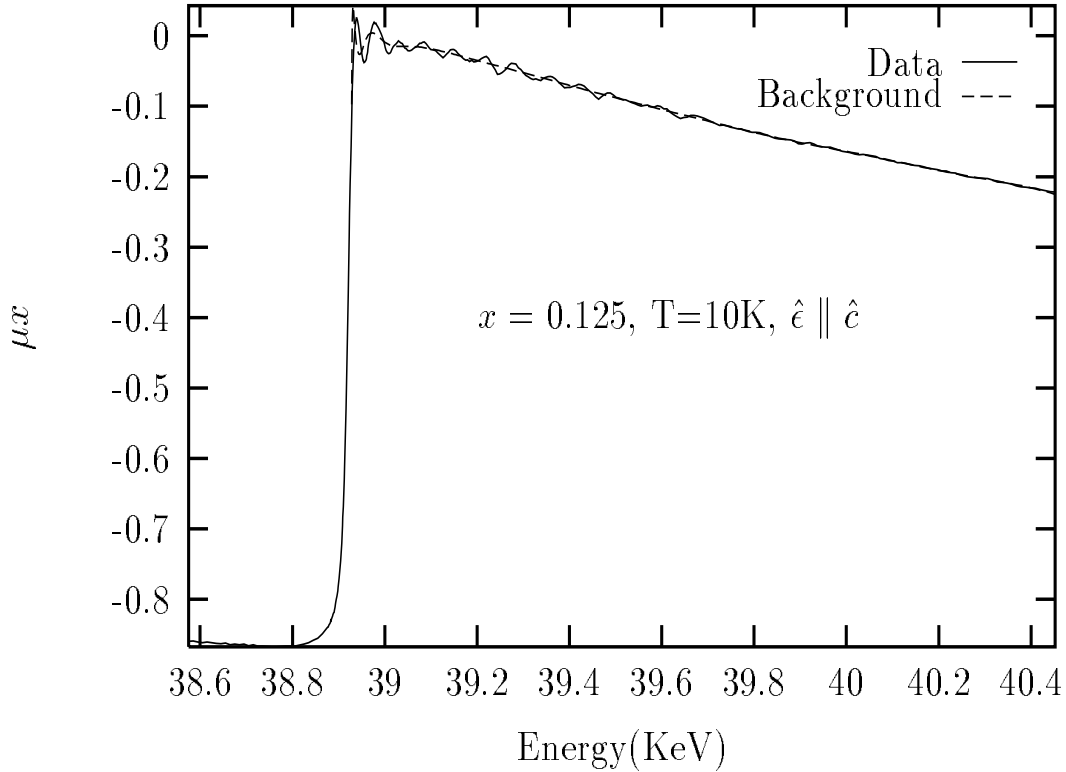


Figure 6.2: La K edge in $\text{La}_{1.875}\text{Ba}_{0.125}\text{CuO}_4$ at $T=10\text{K}$, $\hat{e} \parallel \hat{c}$ -polarization

The data analysis is performed in the same way described for the $\text{La}_{2-x}\text{Sr}_x\text{CuO}_4$ system. Figure 6.2 shows La K -edge data on the $x = 0.125$ sample at $T=10\text{K}$ with $\hat{e} \parallel \hat{c}$. The “embedded” atom background function as determined by AUTOBK with the parameters shown in table 6.1 is also shown. Figure 6.3 shows reproducibility scans for $x = 0.125$ in both polarization conditions.

FEFF6 calculations were performed using the atomic coordinates of the average structure for $x = 0.125$ at $T=15\text{K}$ as determined in the neutron diffraction work of Katano *et. al.* [74] Since the small differences in lattice parameters of $x = 0.125$ and $x = 0.15$ samples result in changes in the average interatomic distances of $\leq 0.005 \text{ \AA}$ [75], the same theoretical standards were used in the analysis of the $x = 0.15$ data. FEFF6 calculations were performed for the different polarization conditions and the data is analyzed by fitting the two polarizations *simultaneously* and constraining the structural parameters of the scattering paths that contribute to both polarizations to be the same, as described for the $\text{La}_{2-x}\text{Sr}_x\text{CuO}_4$ system.

Table 6.2 lists the SS scattering paths that were found to contribute significantly

Table 6.1: Parameters used for the background removal shown in fig. 6.2. Fourier components are minimized in the region $[0, r_{\text{bkg}}]$. Fourier transform k -weight, range and Hanning window sill widths are also shown.

E_0 (KeV)	r_{bkg} (\AA)	k_{min} (\AA^{-1})	k_{max} (\AA^{-1})	kw	dk (\AA^{-1})
38.925	1.4	0.5	18	1	0.2

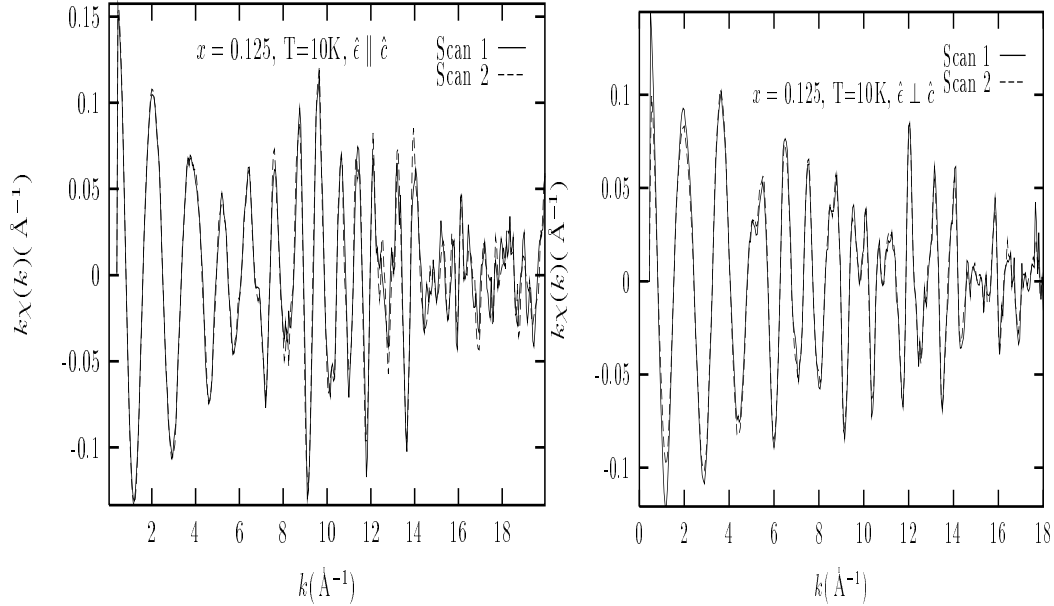


Figure 6.3: $k\chi(k)$ reproducibility data for $\text{La}_{1.875}\text{Ba}_{0.125}\text{CuO}_4$ at $T=10\text{K}$. Left: \hat{c} -polarization; right: in-plane, $\hat{a}\hat{a}$ -polarization

to the La K -edge XAFS in the $r = [1.7, 5.3]$ fitted region of r -space, together with the half path length, r_{eff} , the path degeneracy and the polarization in which they contribute to the XAFS. The c subscript indicates the position of the absorbing atom along the scattering path. Table 6.3 contains equivalent information for MS paths (DS, TS) together with the SS paths of nearly the same length. Only nearly collinear MS paths were found to significantly contribute to the XAFS in the r -space region of interest.

The modeling of the data was done using similar constraints to the ones described for the $\text{La}_{2-x}\text{Sr}_x\text{CuO}_4$ system and hence only deviations from that model are described here. Initially the three different distances corresponding to La-O(1) and La-O(1') were varied independently but constrained to be the same in both polarizations (the polarization dependence of the path's amplitude is included in the theory). Due to the small splitting in these distances, varying the three distances independently resulted in large correlations between the short and long distances and their σ^2 value. This is expected, since the small, symmetric splitting can be well approximated by an effective average distance together with an increase in σ^2 of $\sim 1.610^{-3} \text{ \AA}^2$ (in other words the "beating" in k -space due to a $\sim 0.04 \text{ \AA}$ splitting will be at $k \sim 39 \text{ \AA}^{-1}$, far outside the k -space region analyzed, and hence a σ^2 can compensate for the decay of the envelope quite well, see eq. 5.3). Since the tilt-induced motion of the O(1) atoms above and below the CuO_2 planes results in a nearly equal contraction/expansion of the La-O(1) distances relative to the La-O(1') one (within 0.004 \AA), the La-O(1') distance was varied together with half the splitting of the La-O(1) distances Δ , i.e., $La - O(1)_{\text{short}} = La - O(1') - \Delta$ and $La - O(1)_{\text{long}} = La - O(1') + \Delta$. The magnitude of this splitting is an indirect measurement of the magnitude of the tilt angle. Initially a different σ^2 was varied for La-[O(1),O(1')] and La-O(2) bonds. Their values were found the same (within uncertainties) ($0.0049 \pm 0.02 \text{ \AA}^2$ and $0.0052 \pm 0.0015 \text{ \AA}^2$, respectively) with the large uncertainty in the σ^2 of the La-[O(1),O(1')] bonds due to the correlation with Δ mentioned above. Therefore a single σ^2 was refined for all La-O SS bonds, breaking the correlations in addition to resulting in an improved χ^2_{ν} .

Random substitution of Ba at the La/Ba site was treated in the same way as described for the $\text{La}_{2-x}\text{Sr}_x\text{CuO}_4$ system. The concentration of Ba could not be determined from the fits as the Ba and La atoms have nearly the same backscattering amplitudes ($Z=56,57$, respectively) coupled to the small Ba signal. The scattering paths involving La/Ba backscatterers were weighted by their relative *nominal* con-

Table 6.2: Theoretical SS photoelectron paths found to significantly contribute to the experimental XAFS signal in $r = [1.7, 5.3]$. Values for interatomic distances correspond to the average structure of $x = 0.125$ at 15K. [74]

Path	r_{eff} (AA)	Degeneracy	Polarization
La _c -O(2)-La _c	2.368	($\times 1$)	\hat{c}
La _c -O(1)-La _c	2.604	($\times 1$)	\widehat{aa}, \hat{c}
La _c -O(2)-La _c	2.621	($\times 2$)	\widehat{aa}
La _c -O(1')-La _c	2.642	($\times 2$)	\hat{c}, \widehat{aa}
La _c -O(1)-La _c	2.684	($\times 1$)	\widehat{aa}, \hat{c}
La _c -O(2)-La _c	2.847	($\times 2$)	\widehat{aa}
La _c -Cu-La _c	3.226	($\times 2$)	\hat{c}, \widehat{aa}
La _c -Cu-La _c	3.273	($\times 2$)	\hat{c}, \widehat{aa}
La _c -La-La _c	3.691	($\times 1$)	\hat{c}
La _c -La-La _c	3.702	($\times 1$)	\widehat{aa}
La _c -La-La _c	3.783	($\times 2$)	\widehat{aa}
La _c -La-La _c	3.862	($\times 1$)	\widehat{aa}
La _c -La-La _c	3.965	($\times 4$)	\hat{c}, \widehat{aa}
La _c -O(2)-La _c	4.389	($\times 1$)	\widehat{aa}
La _c -O(2)-La _c	4.46	($\times 2$)	\widehat{aa}
La _c -O(2)-La _c	4.53	($\times 1$)	\widehat{aa}
La _c -O(1)-La _c	4.559	($\times 2$)	\widehat{aa}
La _c -O(1')-La _c	4.581	($\times 2$)	\widehat{aa}
La _c -O(1')-La _c	4.646	($\times 2$)	\widehat{aa}
La _c -O(1)-La _c	4.670	($\times 2$)	\widehat{aa}
La _c -O(2)-La _c	4.996	($\times 2$)	\hat{c}
La _c -O(2)-La _c	5.059	($\times 2$)	\hat{c}
La _c -O(1')-La _c	5.134	($\times 2$)	\hat{c}

Table 6.3: Theoretical MS photoelectron paths (and SS paths of nearly the same length) that were found to significantly contribute to the experimental XAFS signal in $r = [1.7, 5.3]$. Values for the interatomic distances correspond to $x = 0.125$ at 15K. [74]

Path	r_{eff} (AA)	Degeneracy	Type	Polarization
La _c -Cu-La _c	4.773	($\times 1$)	SS	\hat{c}
La _c -Cu-O(2)-La _c	4.777	($\times 2$)	DS	\hat{c}
La _c -O(2)-Cu-O(2)-La _c	4.781	($\times 1$)	TS	\hat{c}
La _c -La-La _c	5.284	($\times 4$)	SS	\hat{c}, \widehat{aa}
La _c -La-O(1')-La _c	5.284	($\times 4$)	DS	\hat{c}, \widehat{aa}
La _c -O(1')-La-O(1')-La _c	5.285	($\times 2$)	TS	\hat{c}, \widehat{aa}
La _c -La-O(1)-La _c	5.286	($\times 4$)	DS	\hat{c}, \widehat{aa}
La _c -O(1)-La-O(1)-La _c	5.288	($\times 2$)	TS	$\widehat{hatc}, \widehat{aa}$
La _c -La-La _c	5.348	($\times 4$)	SS	\widehat{aa}
La _c -La-O(2)-La _c	5.408	($\times 8$)	DS	\widehat{aa}
La _c -O(2)-La _c -O(2)-La _c	5.468	($\times 4$)	TS	\widehat{aa}
La _c -O(2)-La-O(2)-La _c	5.468	($\times 4$)	TS	\widehat{aa}

Table 6.4: Fourier transform parameters and fitting region of r -space for the fits shown in figs. [6.4- 6.7]. Hanning window sills width (dk) and k -weight (kw) also shown.

$k_{\min}(\text{\AA}^{-1})$	$k_{\max}(\text{\AA}^{-1})$	$dk(\text{\AA}^{-1})$	kw	$r_{\min}(\text{\AA})$	$r_{\max}(\text{\AA})$
3.0	15.0	1.5	2	1.7	5.3

centrations, i.e., $y = (1-x)/2$ and $x/2$. Fit results for both $x = 0.125$ and $x = 0.15$ at $T=10\text{K}$ in both polarizations are shown in figs. [6.4- 6.7]. Fourier transform parameters used in the fits are shown in table 6.4. The results of the fits are summarized in tables 6.5& 6.6. The value of $S_0^2 = 0.93 \pm 0.06$ found in the fits is consistent with the value obtained in the La K -edge fits of the $\text{La}_{2-x}\text{Sr}_x\text{CuO}_4$ system, as expected (see table 5.5). The overall agreement with the average atomic positions found in the diffraction studies is quite good. Some interesting observations, however, can be made.

As already mentioned, the splitting in La-O(1) and planar La-O(2) distances is related to the magnitude of the tilt angle. The splitting in La-O(1) distances obtained is $\Delta = 0.049 \pm 0.014 \text{\AA}$, as compared to the values of 0.04\AA and 0.054\AA found by Katano [74] and Takayama [75], respectively. For the planar La-O(2), a splitting of $\Delta = 0.257 \pm 0.015$ is found compared to the values of 0.226\AA and 0.237\AA of the diffraction studies. Even though the La-O(2) splitting is slightly larger than the diffraction value it can not be assigned to an increase in *rigid* tilt since a correspondent increase in La-O(1) splitting is not observed.

6.1.2 Discussion

Most notable are the larger σ^2 values obtained for SS La-O and MS La-O(2)-Cu paths (table 6.6) as compared to their values in $\text{La}_{2-x}\text{Sr}_x\text{CuO}_4$ (table 5.5). Since a similar vibrational zero point motion is expected in $\text{La}_{2-x}\text{Ba}_x\text{CuO}_4$ and $\text{La}_{2-x}\text{Sr}_x\text{CuO}_4$ due to their similar interatomic distances (as seen from the majority La atoms), this is most likely an indication that static disorder is present in the structure, mostly affecting the oxygen atoms as the σ^2 's obtained for SS La-La and SS La-Cu compare well to their values in $\text{La}_{2-x}\text{Sr}_x\text{CuO}_4$. The presence of microscopic static disorder in $\text{La}_{2-x}\text{Ba}_x\text{CuO}_4$ could account for the lower and broader superconducting transition

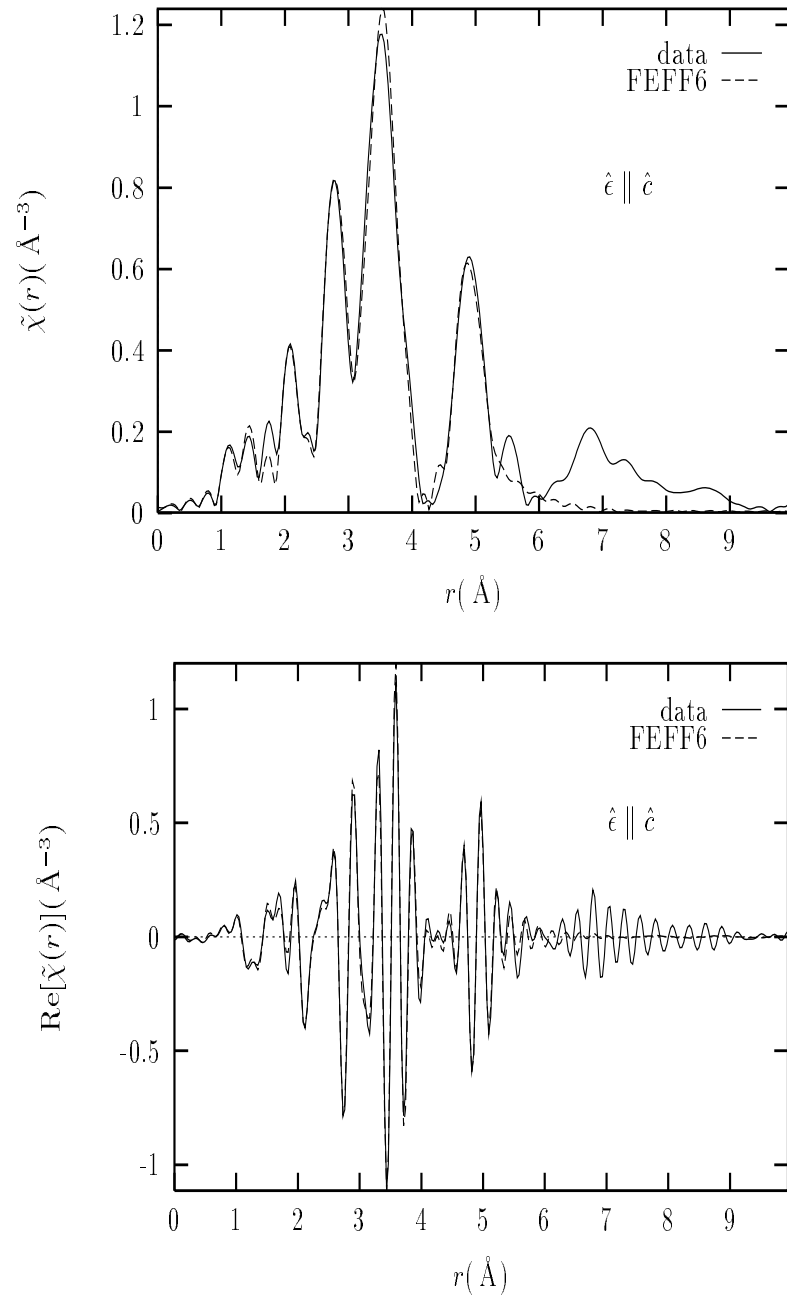


Figure 6.4: Fit results for the $x = 0.125$ sample at $T=10$ K. The magnitude (top) and the real part (bottom) of the complex Fourier transform are shown for $\hat{e} \parallel \hat{c}$

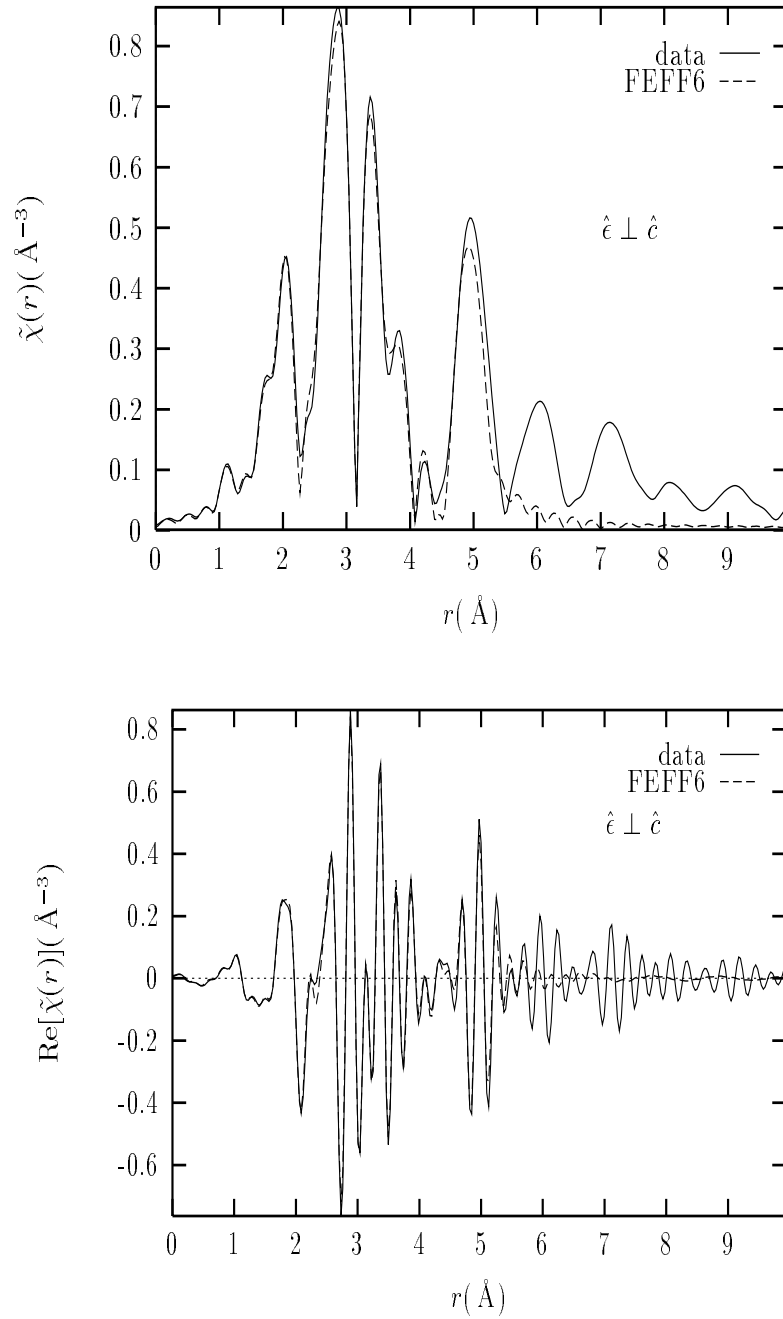


Figure 6.5: Fit results for the $x = 0.125$ sample at $T=10$ K. The magnitude (top) and the real part (bottom) of the complex Fourier transform are shown for $\hat{e} \perp \hat{c}$

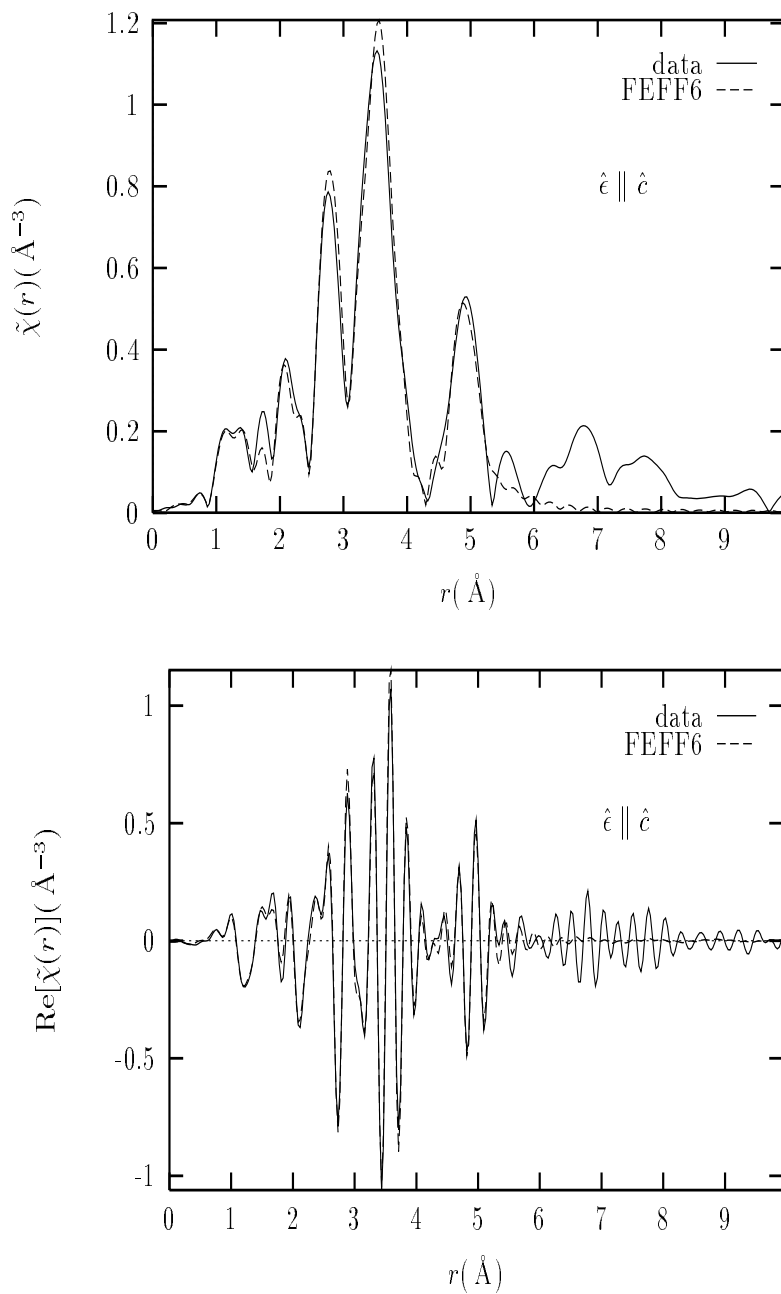


Figure 6.6: Fit results for the $x = 0.15$ sample at $T=10$ K. The magnitude (top) and the real part (bottom) of the complex Fourier transform are shown for $\hat{e} \parallel \hat{c}$

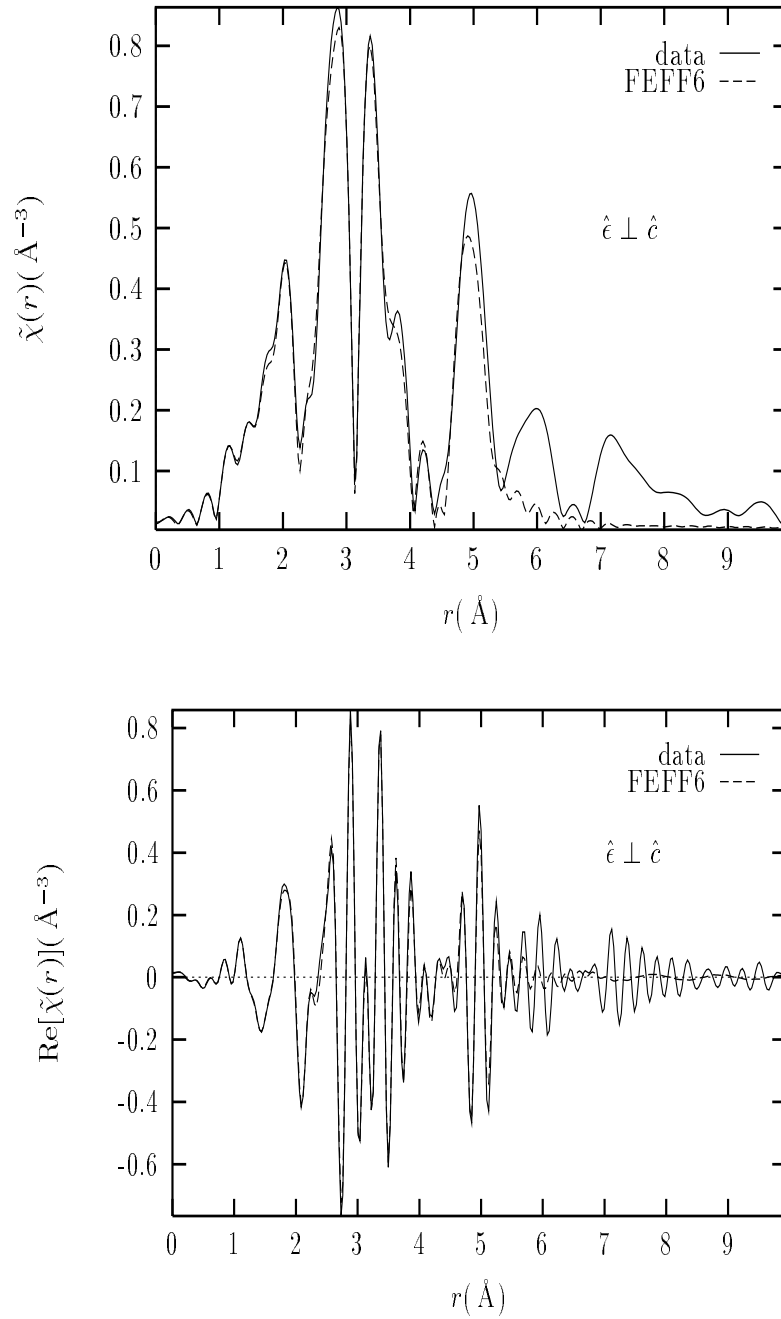


Figure 6.7: Fit results for the $x = 0.15$ sample at $T=10$ K. The magnitude (top) and the real part (bottom) of the complex Fourier transform are shown for $\hat{e} \perp \hat{c}$

Table 6.5: Fit results for interatomic distances in $x = 0.125, 0.15$ samples at $T=10\text{K}$ as obtained from La K -edge polarized XAFS. Neutron diffraction results from two different groups [74, 75] on fully oxygenated $x = 0.125$ samples are listed for comparison (see text for average structure dependence on x and oxygenation). χ^2_ν and R quality of fit factors also shown. $S^2_0 = 0.93 \pm 0.06$ and $\sigma^2_{mm} = 0.00011 \text{ \AA}^2$ is the McMaster correction used. The degrees of freedom in the fits, $\nu = (N_I - N_P) = (59 - 25) = 34$. Paths are indicated by atom at end of path.

	Katano	Takayama	$x = 0.125$	$x = 0.15$
O(2) apical	2.368	2.3697	2.353(14)	2.357(15)
O(1) short	2.604	2.587	2.573(12)	2.574(11)
O(1') middle	2.642	2.639	2.624(8)	2.625(10)
O(1) long	2.684	2.695	2.673(12)	2.676(12)
O(2) planar	2.621	2.616	2.615(10)	2.626(10)
O(2) planar	2.847	2.853	2.872(12)	2.873(13)
Cu short	3.226	3.229	3.235(3)	3.234(3)
Cu long	3.273	3.263	3.282(3)	3.281(3)
La apical	3.691	3.683	3.682(5)	3.701(6)
La planar	3.702	3.723	3.746(10)	3.746(12)
La planar	3.783	3.781	3.776(5)	3.762(8)
La planar	3.862	3.838	3.866(10)	3.833(13)
La	3.965	3.969	3.975(4)	3.966(5)
Cu _{MS}	4.773	4.775	4.767(15)	4.748(17)
χ^2_ν			10.4	11.6
R			0.012	0.014

Table 6.6: XAFS Debye-Waller factors (in \AA^2) as obtained from La K -edge XAFS on $\text{La}_{2-x}\text{Ba}_x\text{CuO}_4$ with $x = 0.125, 0.15$. Paths are indicated by atom at the end of scattering path.

	$x = 0.125$	$x = 0.15$
O	0.0053(11)	0.0054(9)
Cu	0.0019(3)	0.00194(2)
La	0.0023(2)	0.0024(2)
0_{4th}	0.0036(20)	0.0037(20)
Cu_{MS}	0.0078(20)	0.0081(22)
La_{MS}	0.0030(5)	0.0034(6)

temperatures of this system as compared to the closely related $\text{La}_{2-x}\text{Sr}_x\text{CuO}_4$.

The presence of disorder in the La-O(2)-Cu distance can be directly seen in the data, by comparing to the La K -edge measurement on the Sr-doped system. Figure 6.8 shows the real part of $\tilde{\chi}(r)$ for La K -edge, \hat{c} -polarized data, for Sr-doped ($x = 0.075$) and Ba-doped ($x = 0.125$) samples at $T=(20\text{K}, 10\text{K})$, respectively. Even though the two systems crystallize in different phases at low temperature, their structures, *as seen from the La K -edge, c -polarized XAFS* are very similar, partly because the *magnitude* of the CuO_6 octahedra tilt angle is nearly the same in both LTO and LTT structures [20, 74] (as already mentioned, most of the differences between LTO and LTT are seen in the \hat{ab} polarized XAFS). Fig. 6.8 also shows \hat{c} -polarized, La K -edge FEFF6 calculations corresponding to the average structures of the two samples that are compared. The FEFF6 calculation is done using the actual lattice parameters and atomic coordinates for the relevant concentrations. All paths below $r_{\text{eff}} = 5.3 \text{\AA}$ which have significant amplitude are included in the theoretical plots, which have no corrections for thermal or static disorder (differences in the theoretical plots are due to differences in LTO and LTT phases in addition to the slightly different lattice parameters; Ba-doped has a longer c -axis). It is evident that the XAFS signal at about $r \sim 4.5 \text{\AA}$ is strongly suppressed in the Ba-doped sample, where the main contribution to the signal comes from the La-O(2)-Cu MS paths.

As will be shown from Ba K -edge XAFS results, Ba induces big local atomic displacements in neighboring oxygen atoms and beyond, which can account for most

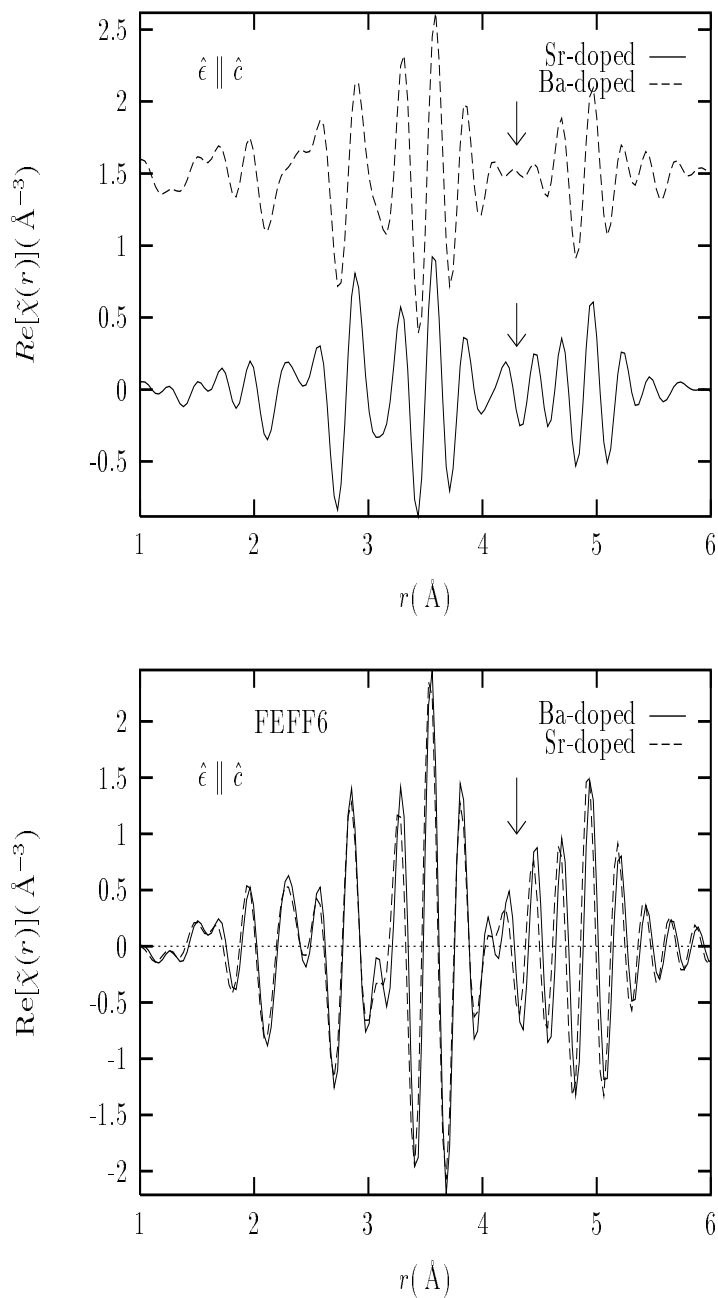


Figure 6.8: Real part of the complex Fourier transforms of Sr-doped ($x = 0.075$, $T=20\text{K}$) and Ba-doped ($x = 0.125$, $T=10\text{K}$) La K -edge, \hat{c} -polarized XAFS data (top) and their respective FEFF6 calculations (bottom) using the relevant average structures found by diffraction. The FEFF6 calculations are not corrected for thermal or static disorder. The larger than expected disorder in the La-O(2)-Cu MS signal of the Ba-doped sample is evident.

of the observed static disorder, including the one observed in the La-O(2)-Cu signal. Other deviations from the average structure include a systematically shorter La-O(2) apical distance and a discrepancy in a planar La-La distance. Beside comparing local and average atomic positions, it is also of interest here to determine differences between the two different values of x . The only measurable differences outside uncertainties are an elongation with x of the apical La-La distance and a shortening of a planar La-La distance with x . Part of these changes are expected due to the elongation (contraction) of the \hat{c} ($\hat{a}a$) axis with Ba. [75] A shortening of the La-Cu_{MS} distance with x is observed, but the uncertainty is too large to conclude. Even though the σ^2 's for both values of x are within uncertainties of each other, systematically larger σ^2 values are observed for the $x = 0.15$ sample. A more complete discussion of these results is postponed until after the Ba K -edge results on the same samples are presented in the next section.

6.2 Ba K -edge measurements

6.2.1 Experimental results

Measurements at the Ba K -edge were performed on samples from the same batch used in the La K -edge measurements. Samples of different thickness were prepared in order to optimize the signal of interest, as discussed in chapter 4. The same Si(311) double crystal monochromator used for the La measurements was used here. Figure 6.9 shows Ba K -edge ($E=37441$ eV) absorption data for the $x = 0.125$ sample at 10K in both polarization conditions. The data have been normalized by the edge step. The background function obtained with the parameters shown in table 6.7 is also shown. Figure 6.10 shows reproducibility scans for both samples.

As already discussed, if Ba substitutes for La in the lattice without distortions in the neighboring atomic environment, the La and Ba K -edge XAFS should be very similar. For the case at hand the core-hole lifetime is nearly the same for both central atoms as is the central atom phase shift, so a direct comparison can be made. This is done in fig. 6.11 where the XAFS of the La and Ba K -edges are compared in both polarizations. Both $x = 0.125$ and $x = 0.15$ are included in the plots. Whereas the two different concentrations are nearly the same in both edges, the two central atoms show very different XAFS, a strong indication that Ba induces major distortions in its atomic environment.

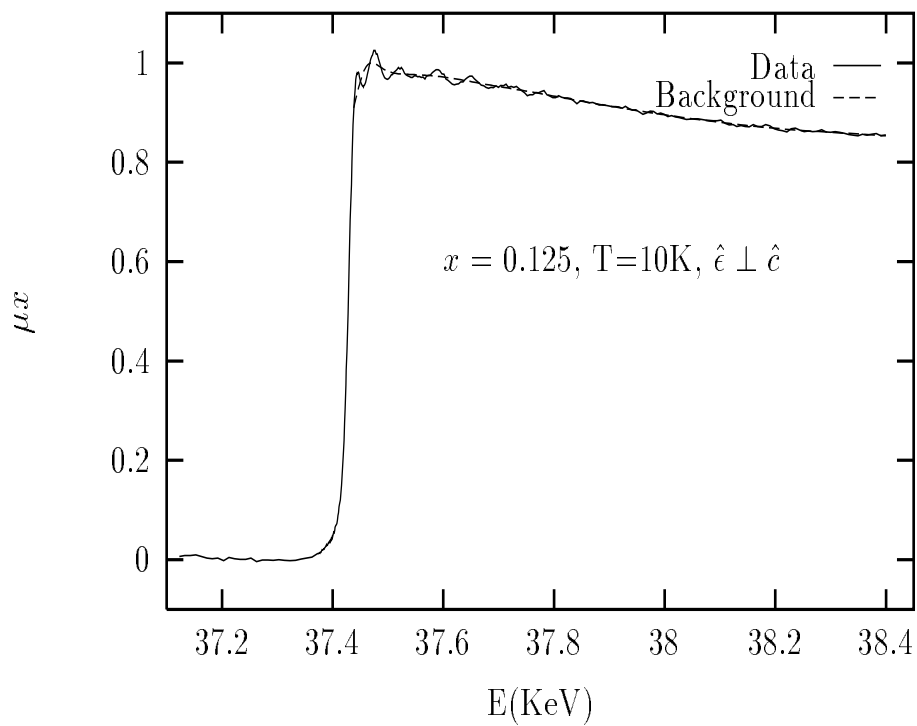
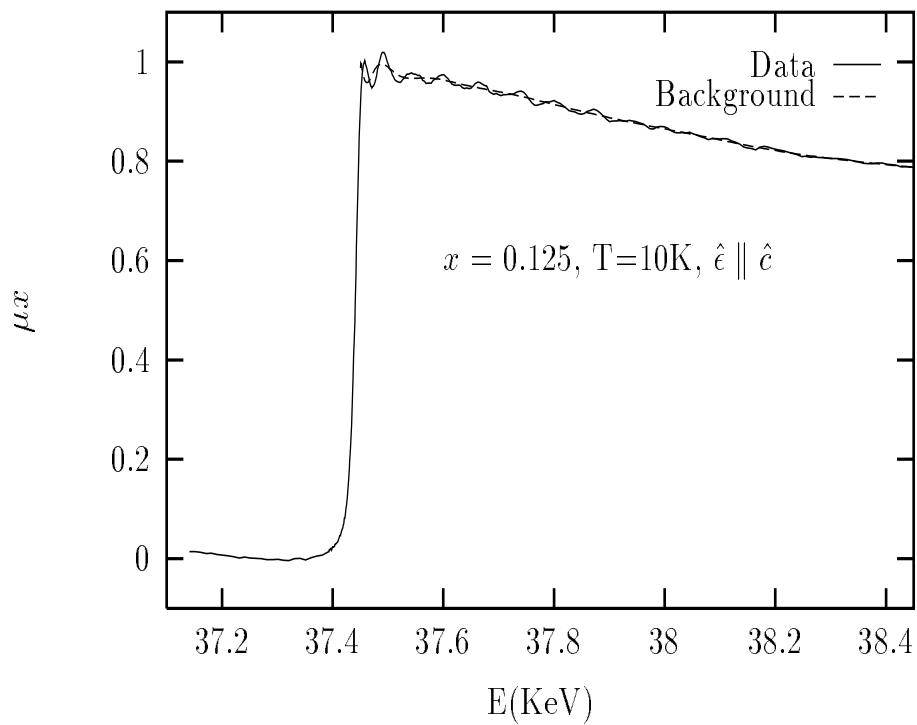


Figure 6.9: Ba K -edge absorption data in $\text{La}_{2-x}\text{Ba}_x\text{CuO}_4$ for $x = 0.125$ at $T = 10\text{K}$. Both polarization conditions are shown, together with the background function obtained with the parameters in table 6.7.

Table 6.7: Parameters used for the background removal shown in fig. 6.9. Fourier components are minimized in the region $[0, r_{\text{bkg}}]$. Fourier transform k -weight, range and Hanning window sill widths are also shown.

E_0 (KeV)	r_{bkg} (Å)	k_{min} (Å ⁻¹)	k_{max} (Å ⁻¹)	kw	dk (Å ⁻¹)
37.440	1.5	0.5	16.5	1	0.2

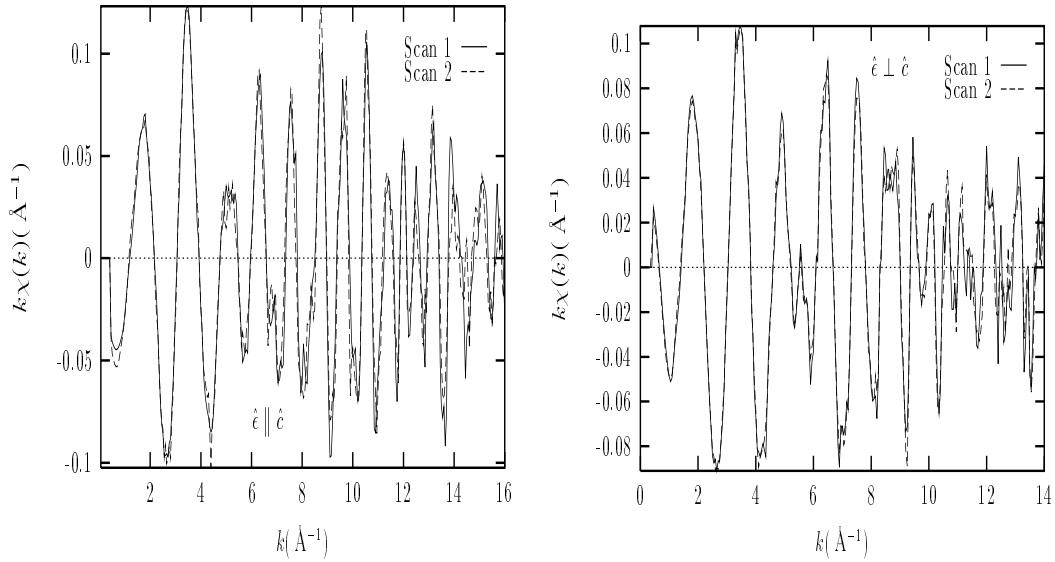


Figure 6.10: $k\chi(k)$ reproducibility data for $x = 0.125, 0.15$ in $\text{La}_{2-x}\text{Ba}_x\text{CuO}_4$ at $T=10\text{K}$. Left: $x = 0.125$, \hat{c} -polarization; right: $x = 0.15$, in-plane, $\widehat{a}a$ -polarization

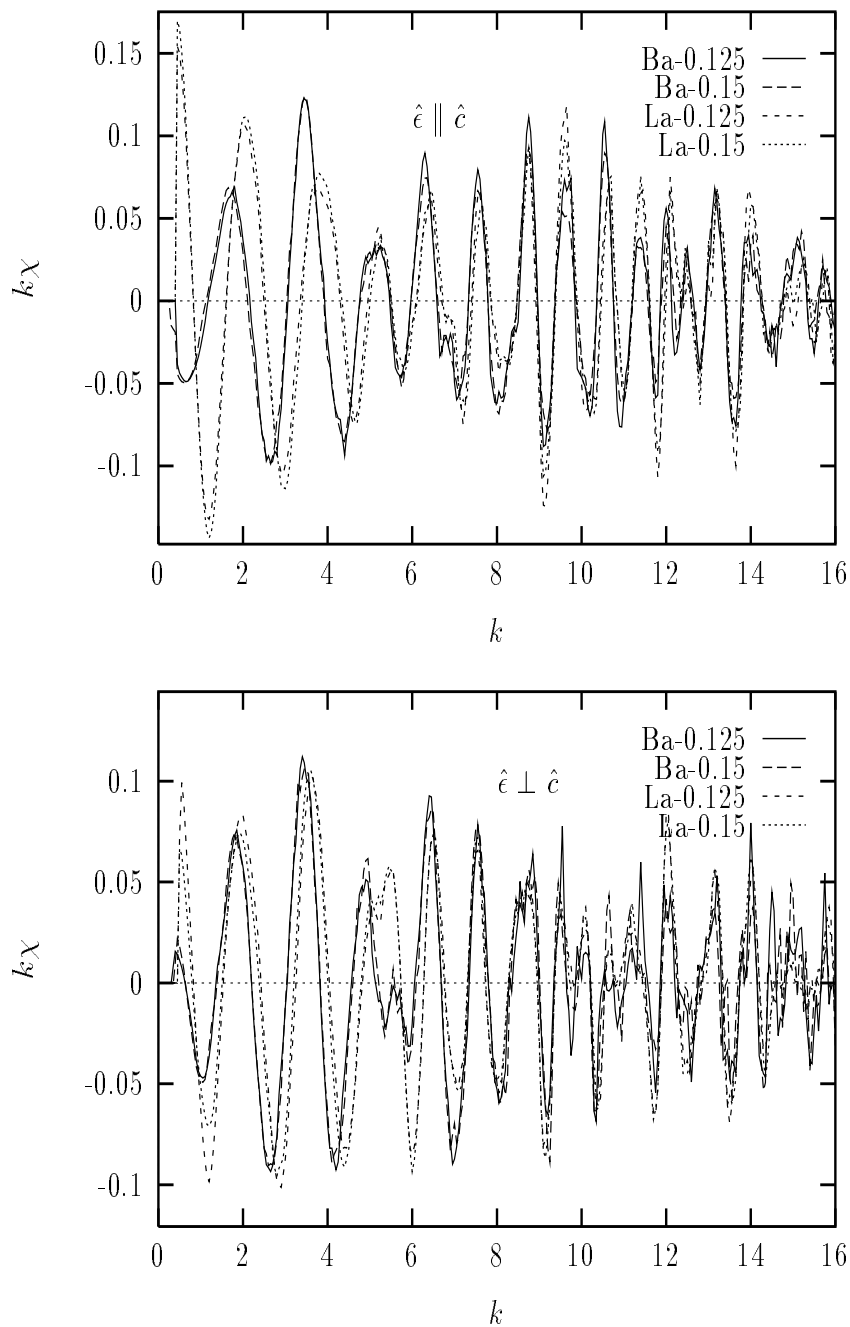


Figure 6.11: Comparison between La and Ba K -edge $\chi(k)$ in $\text{La}_{2-x}\text{Ba}_x\text{CuO}_4$ with $x = 0.125, 0.15$ at $T=10\text{K}$. Whereas no noticeable differences exist between the two different concentrations, major differences exist between La and Ba central atoms, indicating the presence of lattice distortions around the later.

The two polarized XAFS spectra are refined simultaneously, as described above. Initially the same LTT model used in fitting the La K -edge data was used in the fittings here. This resulted in extremely poor fits as the model did not have enough freedom to reproduce the data. Two major constraints of the LTT model turned out to be unrealistic for describing the Ba environment: the nearly equal shortening and elongation of the Ba-O(1) distances relative to the Ba-O(1') one and the existence of only two, double degenerate, Ba-O(2) planar distances. As Ba^{+2} has a formal ionic radius of $r_{\text{Ba}} = 1.35 \text{ \AA}$ compared to the $r = 1.15 \text{ \AA}$ of La^{+3} , it is expected that substituting Ba at the La site will result in local expansion of the lattice around the dopant. For example, the Ba-O interatomic distance in purely ionic BaO is $r = 2.77 \text{ \AA}$ [150], much larger than the La-O(1), La-O(1') distances found in the La K -edge studies. Whereas simple arguments based on ionic radii are not necessarily valid (coordination numbers, structural geometry, charge transfer and partial covalency, all contribute to deviations from the simple picture), those can give a first hint on the nature of the expected distortions.

Based on this argument, the local structure was subsequently fitted with an LTO model; not because of its closeness to the expected local structure but because the distribution of distances in the LTO model is expected to have more freedom to successfully describe the Ba distortions. For this purpose, the LTO atomic positions of the $x = 0.125$ sample at $T=115\text{K}$, as found in the diffraction studies [74] were used for the FEFF6 calculation. Using this model as the initial guess, great improvements were obtained in the fit of the near neighboring oxygen atoms. For the longer distances the FEFF6 theoretical standards of the LTT model were used. Fits obtained this way are shown in figs. [6.12- 6.15]. Structural parameters obtained for both samples are summarized in table [6.8& 6.9].

6.2.2 Discussion

As shown in table 6.8, a large expansion of interatomic distances is observed around the dopant. For example, the Ba-O(2) apical distance is expanded by $\Delta r \sim 0.17 \text{ \AA}$ and a weighted average of the Ba-O(1) distances results in $\Delta r \sim 0.15 \text{ \AA}$. This is consistent with the $\sim 0.2 \text{ \AA}$ difference in ionic radii between Ba^{+2} and La^{+3} . The strain field associated with the larger Ba^{+2} ion extends far beyond the first shell oxygen atoms. Due to the large anisotropy of the structure together with the expectation that some of the Ba-induced displacements will be correlated (e.g., the somewhat rigidity of

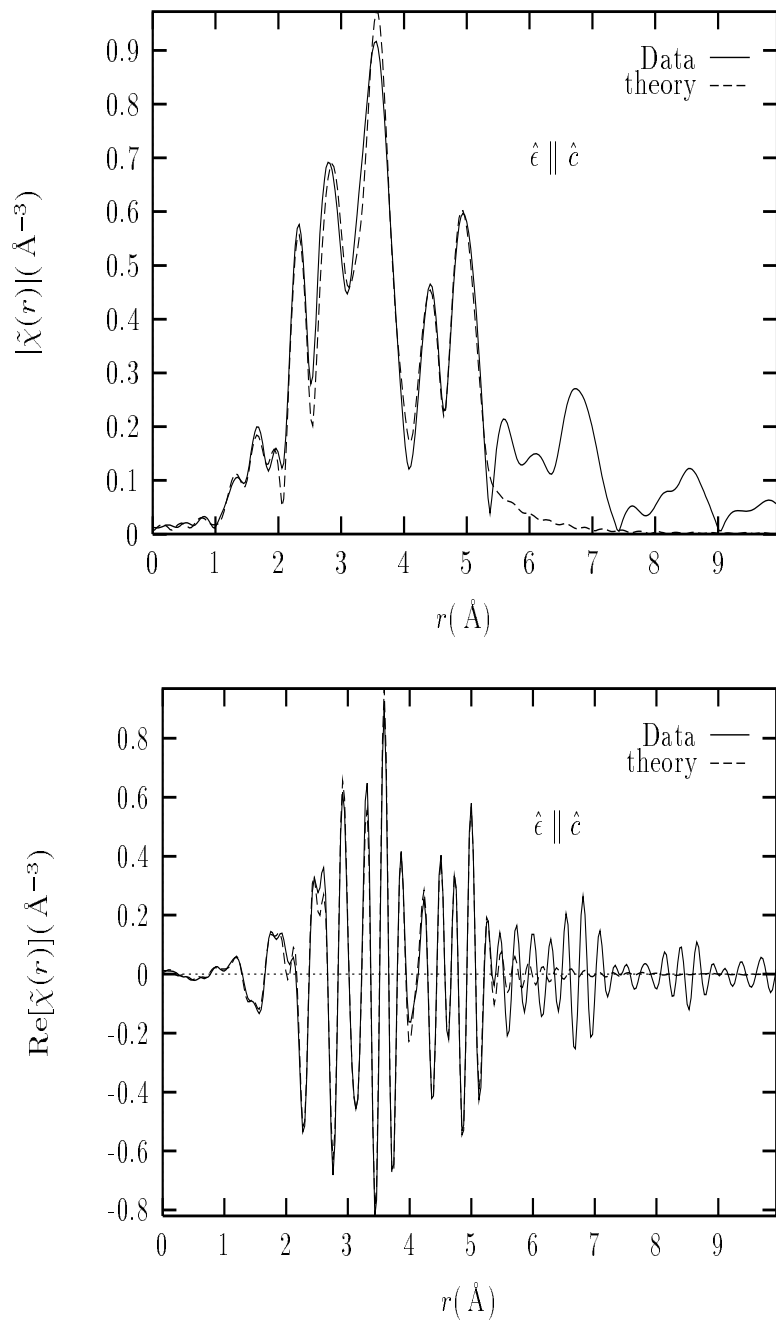


Figure 6.12: Fit results for the $x = 0.125$ sample at $T=10$ K. The magnitude (top) and the real part (bottom) of the complex Fourier transform are shown for $\hat{c} \parallel \hat{c}$

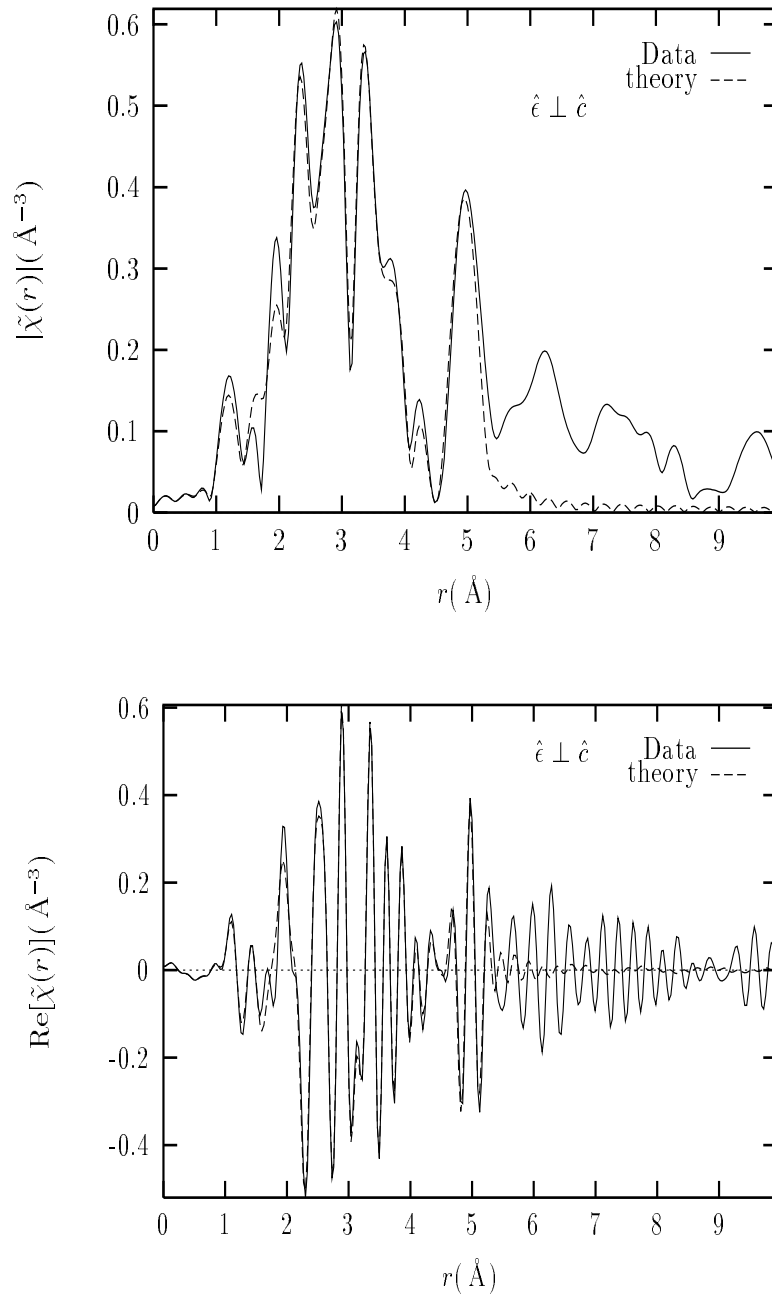


Figure 6.13: Fit results for the $x = 0.125$ sample at $T=10$ K. The magnitude (top) and the real part (bottom) of the complex Fourier transform are shown for $\hat{e} \perp \hat{c}$

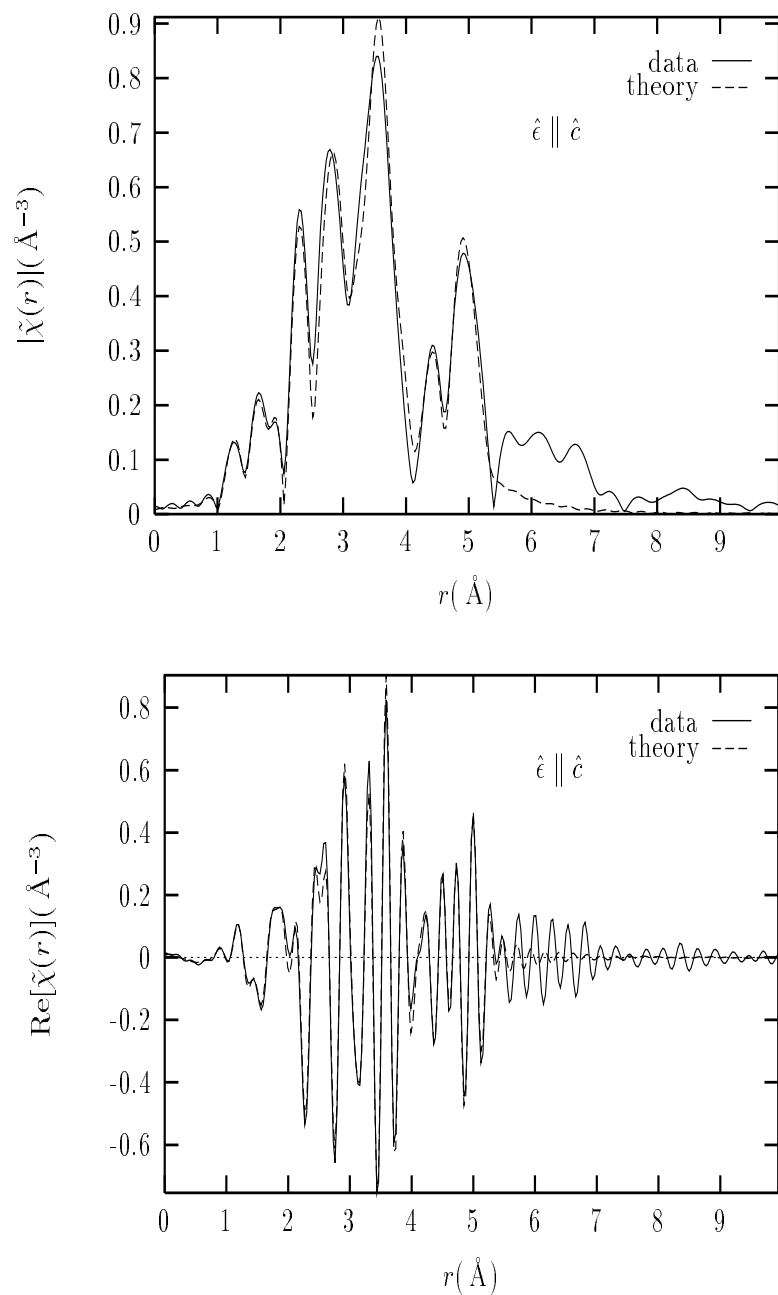


Figure 6.14: Fit results for the $x = 0.15$ sample at $T=10$ K. The magnitude (top) and the real part (bottom) of the complex Fourier transform are shown for $\hat{e} \parallel \hat{e}$

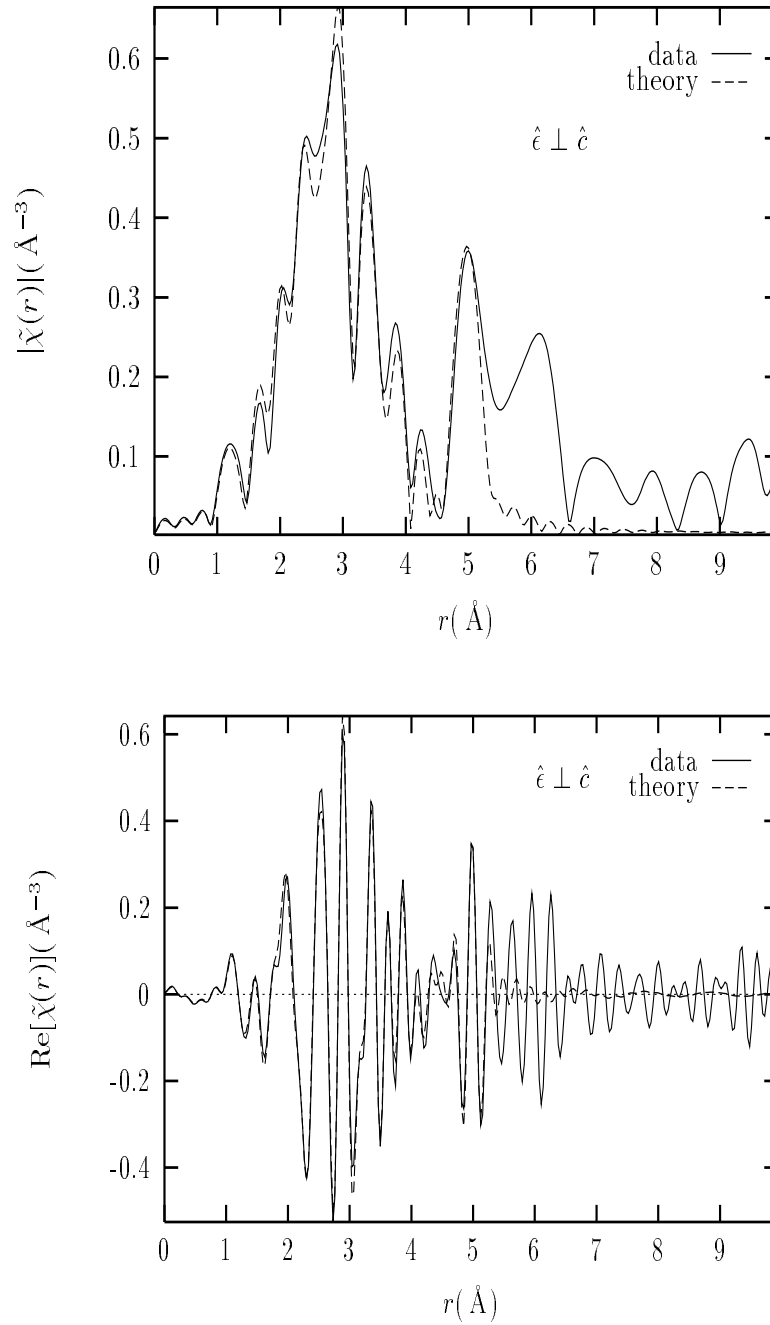


Figure 6.15: Fit results for the $x = 0.15$ sample at $T=10$ K. The magnitude (top) and the real part (bottom) of the complex Fourier transform are shown for $\hat{e} \perp \hat{c}$

Table 6.8: Fit results for interatomic distances (in Å) for $x = 0.125, 0.15$ samples at $T=10\text{K}$ as obtained from Ba K -edge polarized XAFS. Degeneracies are shown in parenthesis. χ^2_ν and R quality of fit factors also shown. $S_0^2 = 1.02 \pm 0.09$ and $\sigma_{mm}^2 = 0.00012 \text{ \AA}^2$ is the McMaster correction used. The degrees of freedom in the fits, $\nu = (N_I - N_P) = (54 - 24) = 30$. Paths are indicated by atom at end of path.

	$x = 0.125$	$x = 0.15$
O(2) apical	2.540(13)	2.526(10)
O(1) ($\times 2$)	2.779(15)	2.748(15)
O(1) ($\times 2$)	2.797(15)	2.819(15)
O(2) planar ($\times 1$)	2.622(20)	2.648(20)
O(2) planar ($\times 2$)	2.871(10)	2.884(10)
O(2) planar ($\times 1$)	2.920(30)	2.895(30)
Cu ($\times 2$)	3.275(5)	3.267(5)
Cu ($\times 2$)	3.323(5)	3.314(5)
La apical ($\times 1$)	3.717(6)	3.722(7)
La planar ($\times 1$)	3.780(10)	3.782(10)
La planar ($\times 2$)	3.783(10)	3.783(8)
La planar ($\times 1$)	3.910(10)	3.903(8)
La ($\times 4$)	3.990(5)	3.981(5)
Cu _{MS}	4.790(10)	4.779(10)
χ^2_ν	13.1	12.2
R	0.029	0.024

Table 6.9: XAFS Debye-Waller factors (in \AA^2) as obtained from Ba K -edge XAFS on $\text{La}_{2-x}\text{Ba}_x\text{CuO}_4$ with $x = 0.125, 0.15$. Paths are indicated by atom at the end of scattering path.

	$x = 0.125$	$x = 0.15$
O	0.0045(12)	0.0044(13)
Cu	0.0034(3)	0.0036(3)
La	0.0035(2)	0.0037(2)
Cu_{MS}	0.0023(5)	0.0041(9)
La_{MS}	0.0041(13)	0.0044(15)

the CuO_6 octahedra could result in correlated motions of O(1) and O(2) atoms; in addition correlated displacements of nearly coplanar La and O(2) atoms are expected due to ionic forces), the strain field is not expected to be isotropic. This is clearly seen from the results; e.g., some Ba-O(2) planar distances are in close agreement with their La-O(2) values. Despite the observed deviations from isotropic displacements, a somewhat reasonable approximation to the strain field can be obtained by weighted averages of the displacements within different shells of atoms. This is shown in fig. 6.16, where the magnitude of the local atomic displacements versus distance from the Ba central atom is shown, after a weighted average within each shell is performed. The averaged displacements were fitted with functional forms $A/r^{3,4}$, and the coefficients obtained in the fits are included in the plot with the hope that someone with a better understanding of elastic theory than the writer would make use of the information. [151]

First, attention is directed to the Ba-O(2) apical distortion. Since Ba substitutes for La in the lattice, diffraction techniques yield an average La/Ba-O(2) apical distance. Appropriately weighting the La-O(2) and Ba-O(2) distances measured by La and Ba K -edge XAFS by their relative concentrations yields

$$\left(1 - \frac{x}{2}\right)(La - O(2)) + \left(\frac{x}{2}\right)(Ba - O(2)) = \begin{cases} 2.364(14)(\text{\AA}) & x = 0.125, \\ 2.369(14)(\text{\AA}) & x = 0.15 \end{cases} \quad (6.1)$$

in very good agreement with the $2.368(1)\text{\AA}$ value measured by diffraction. [74,75]

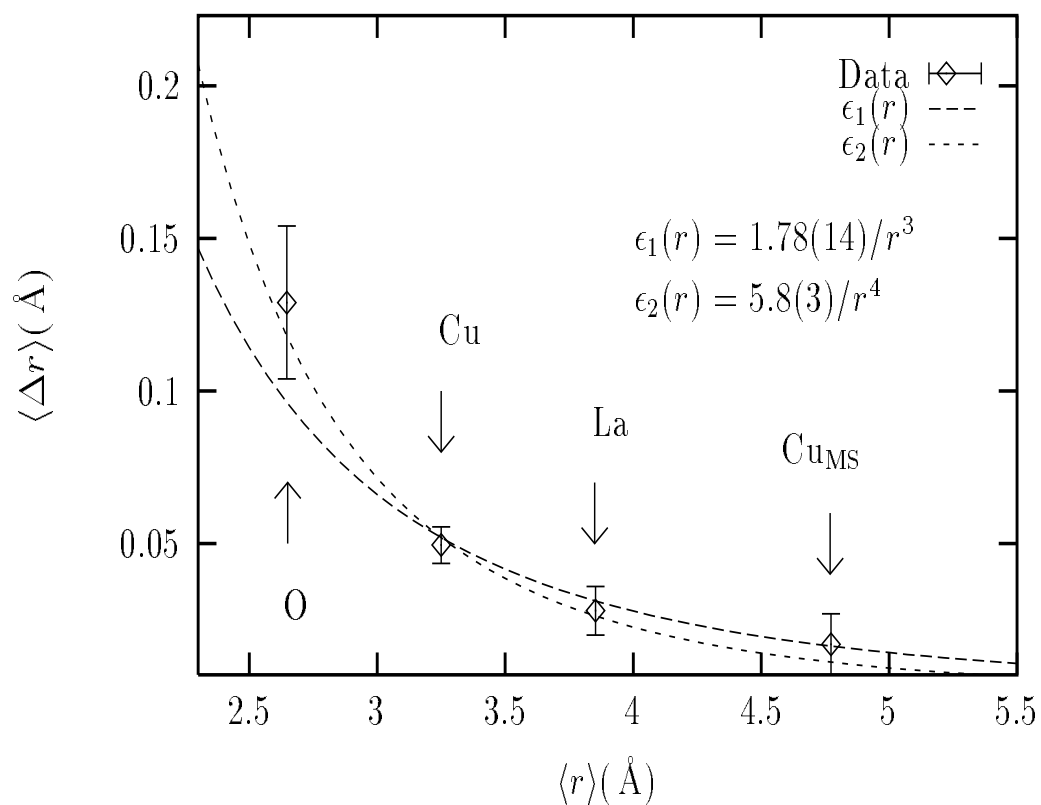


Figure 6.16: Magnitude of the local atomic displacements induced by Ba substitution as function of distance from Ba. Displacements are weighted-averaged within each shell and are plotted versus the weighted-averaged shell distances. Fits to $A/(r^{3,4})$ functional forms are shown.

The four O(1) atoms in the CuO₂ planes are all displaced outward from the Ba atoms, with a weighted-average displacement of $\sim 0.15 \text{ \AA}$. Since in this structure another La/Ba site exists with mirror symmetry about the CuO₂ planes (see fig. 6.1), this expansion results in a *contraction* of La-O(1) distances of about the same size (only nearby a Ba). Assuming random substitution, the probability of having the two La/Ba sites occupied by La is $P_{La,La} = (0.9375)^2 = 0.879$ while the probability of having one site being La and the other Ba is $P_{La,Ba} = 2(0.9375)(0.0625) = 0.1172$. A La XAFS measurements would give a weighted average of La environments with and without a neighboring Ba. This could explain the systematically shorter La-[O(1),O(1')] distances obtained from the La *K*-edge XAFS, as $La - O(1) = 0.879 \times x + 0.1172 \times (2.64 - 0.15) = 2.624 \Rightarrow x \sim 2.65 \text{ \AA}$, in better agreement with the diffraction value (weighted averages of O(1) distances were used). Diffraction will be insensitive to the distortions in La-O(1) distances *next* to a Ba atom as they are random with no periodic component; its effect will be partially accommodated by the refined disorder of the O(1) atoms. Since the La *K*-edge data was modeled with the constraint of a local LTT structure without accounting for the 11.72% contribution of the Ba distortions above mentioned, a bigger than expected σ^2 was obtained for the La-O distances to partially accommodate the bad model. Assuming the vibrational zero point motion is the same as that obtained in La_{2-x}Sr_xCuO₄ ($\sigma^2 = 0.002 \text{ \AA}^2$), the additional static disorder not included in the model results in a total disorder for the La-O(1) distances of $\sigma^2 = 0.879 \times 0.002 + 0.1172 \times [(2.64 - 2.49)^2 + 0.002] = 0.0046 \text{ \AA}^2$, which accounts for most of the increased disorder observed in the La-O distances (see table 6.6). Since the CuO₆ octahedra are coupled by the vertexes, this is only a lower estimate of the unaccounted for static disorder in the La XAFS, as coupled distortions of O(1) atoms in the neighboring cells are expected.

It is important to notice that the large distortion of the O(1) atoms results in an increased *local* buckling of the CuO₂ planes *nearby* Ba atoms. Since Ba is randomly substituted in the lattice, this *extra* buckling will also be random with components along both $\pm \hat{c}$. Since the correspondent distortions of the O(1) atoms are also random, they will not contribute to the intensity of Bragg peaks and therefore will be unnoticed in standard diffraction experiments. Since the average buckling angle is determined by diffraction from the average, periodic, O(1) atomic positions, the random local displacements of O(1) atoms next to Ba average out to zero over long range and therefore they don't contribute to the measurement of buckling as obtained in the

diffraction experiments. Since neighboring CuO_6 octahedra are coupled by their vertexes, it is possible that the large O(1) displacements next to Ba along $\pm\hat{c}$ will induce correlated displacements along $\mp\hat{c}$ in O(1) atoms of neighboring octahedra. These correlations will extend only over short range as standard diffraction techniques measure an average structure (LTT) inconsistent with octahedra tilts about $\langle 100 \rangle$.

It is interesting that the local distortion of the O(1) atoms resembles the LTO-like distortion: the O(1) atoms are displaced as *if* the CuO_6 octahedra next to Ba *were* rotated about $\langle 100 \rangle$ type of axis, especially if the distortion propagates into the neighboring cells. The *actual* “tilts” next to Ba are, however, different from LTO since the O(1) atoms are *all* displaced in the same direction and the displacements of the O(2) atoms forming the apexes of the CuO_6 octahedra involved only partly resemble the LTO type of tilts, as discussed below.

As seen in table 6.8, the distribution of O(2) planar displacements around Ba differs significantly from its average structure counterpart, shown in table 6.5. It is clear that a *rigid* tilt of all the CuO_6 octahedra involving the O(1) and O(2) atoms neighboring Ba is inconsistent with the observed Ba-O(2) distances. Since the four O(1) atoms are displaced in the same direction, rigid tilts will result in two short ($\sim 2.6 \text{ \AA}$) and two intermediate ($\sim 2.73 \text{ \AA}$) distances, which is not the case. The O(2) displacements will be limited by the large size of the Ba^{+2} ion coupled to the energetics of the lattice: ionic interactions between La and O(2) atoms and constraints imposed by the long range LTT order in the tilt pattern of the CuO_6 octahedra. More than one pattern of O(2) displacements in different *directions* will be consistent with the measured Ba-O(2) radial distances. However, by realizing that O(2) motions are highly correlated with neighboring La motions due to the strong ionic interaction in the LaO planes, a more clear picture emerges when accounting for the observed changes in Ba-La planar distances.

Figure 6.17 shows the O(2) displacements together with the correlated La/Ba displacements for all LTO, LTT, $Pccn$ and HTT phases. The $Pccn$ phase is orthorhombic but with a reduced orthorhombic strain as compared to the LTO one [49]. (The presence of a $Pccn$ phase in at least a fraction of the sample’s volume has been held, by some authors, responsible for the broad diffraction peaks of the LTT phase [49] or as a mediator for the hypothetical spatial variation of tilt direction of the CuO_6 octahedra across the twin boundaries deduced from the electron microscopy experiments. [76]) The arrows in fig. 6.17 are not drawn to scale; the magnitude of the O(2)

and La/Ba displacements are $\lesssim 0.2 \text{ \AA}, 0.04 \text{ \AA}$, respectively, relative to the undistorted HTT phase. Despite the La/Ba displacements being small, their correlated motions with the O(2) ions via ionic interactions play an essential role in stabilizing the different phases. [66]

As shown in fig. 6.17, the correlated displacements of the La/Ba atoms in the LTT phase result in one short ($\sim 3.71 \text{ \AA}$), two intermediate ($\sim 3.78 \text{ \AA}$) and one long ($\sim 3.85 \text{ \AA}$) La/Ba-La/Ba planar distances. Whereas the Ba-La intermediate distances were found in the Ba *K*-edge study to be in agreement with their average values (table 6.8), the short Ba-La planar distance is elongated by about $\sim 0.07 \text{ \AA}$. This elongation is much larger than expected from the elastic field around the Ba^{+2} ions (see fig. 6.16) and is probably due to a correlated motion of the La ion in response to the O(2) displacement. This is illustrated in fig. 6.18 where a schematic representation of a *possible* pattern of O(2) and La planar displacements consistent with the data is shown. Disagreement between local displacements and ideal LTT displacements are indicated by the presence of two arrows: solid (approximate local displacements) and dashed (ideal LTT displacements). A single solid arrow indicates no conflict. The Ba *K*-edge measurement provides direct information on the unit cell containing the Ba atoms; deviations from ideal LTT positions in neighboring cells are deduced from the pattern of correlated O(2) and La ions and are *hypothetical*. Line A in the figure indicates the direction *along* which the CuO_6 octahedra tilt in the ideal LTT phase (buckled O(1) pattern); e.g. reversing the tilt direction along this line is expected to be costly in elastic energy. Line B is the direction *about* which the octahedra tilt (unbuckled O(1) pattern); e.g. adding a tilt component along this line is expected to be less costly in elastic energy.

Combining the facts that only one short Ba-O(2) distance is observed together with no observation of a short Ba-La distance (table 6.8), it is imperative that at least one of the O(2) atoms (number 2 in the figure) significantly deviates from the ideal LTT position. Since all the O(1) atoms below Ba are displaced outwards from Ba, the semi-rigidity of one CuO_6 octahedra can be preserved and still result in agreement with the observed distances. This is achieved by displacing one O(2) ion (number 1 in the figure) towards Ba, resembling the ionic displacement of the LTO phase (fig. 6.17). The motions of ions number 1 and 2 in the figure will result in correlated motions of the La ions number 5 and 9 due to the new distribution of O(2) ions. It is emphasized that the displacement of O(2) number 2 is not associated with a

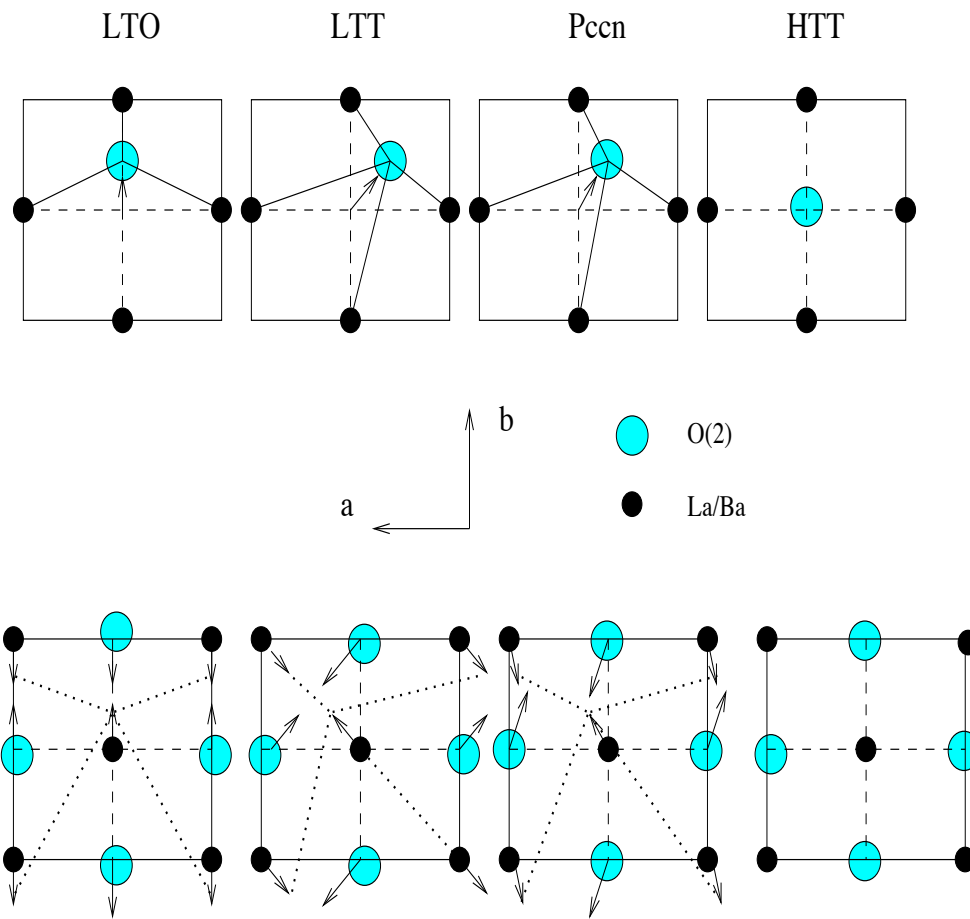


Figure 6.17: Schematic representation of the O(2) and correlated La/Ba atomic displacements in all LTO, LTT, *Pccn* and HTT phase. The arrows are not drawn to scale; the O(2) displacements (relative to the undistorted HTT phase) being much larger than the La/Ba ones.

rigid tilt but instead results in the Cu-O(2) apical bond of this octahedron deviating from perpendicularity to its basal plane, due to the O(1) distortions mentioned above. The O(2) distortions will most likely propagate into neighboring cells (e.g. La number 9) but those displacements are not observable in the measurements and therefore are given on a *hypothetical* basis only. The Ba-O(2) and Ba-La distribution of distances resulting from the displacements are indicated by the dashed and solid lines in fig. 6.18, respectively.

Since the Ba-La apical distance is longer than the average distance measured by diffraction, a resulting expansion in the La-La apical distance with x , as measured at the La K -edge, is expected. On the other hand since Ba pushes the Cu atom at 4.77 Å (along the \hat{c} -axis) outwards, a contraction of the La-Cu_{MS} distance is expected with x . This is indeed qualitatively observed in the La K -edge results (the subscript *MS* indicates the atom is an end atom for both SS and nearly collinear MS paths).

It is found that the four Cu atoms neighboring a Ba are displaced outwards (relative to Ba) with their radial distances increasing by about ~ 0.05 Å. As seen in fig. 6.1, these Cu atoms act as end atoms for several La-Cu_{MS} SS and La-O(2)-Cu_{MS} MS paths. Based on the symmetry of the structure, the aforementioned expansion results in *both* contraction and expansion of the La-Cu_{MS} distance which then contribute to static disorder in this distance. It is estimated for the concentrations of Ba under consideration that about 50% of all La-Cu_{MS} paths are affected. Assuming a vibrational zero point motion for the unaffected paths similar to that found for La_{2-x}Sr_xCuO₄ at low x , the total disorder in La-Cu_{MS} distance becomes $\sigma_{\text{CuMS}}^2 = 0.5 \times (0.004) + 0.5 \times [0.004 + (0.05)^2] = 0.0053 \text{ \AA}^2$. This is not enough to account for the observed $\sigma^2 \sim 0.008 \text{ \AA}^2$ (table 6.6) obtained in the La K -edge XAFS. Since a single σ^2 is refined in the fits for the La-Cu_{MS} and La-O(2)-Cu nearly collinear MS paths at nearly the same distance, it is thinkable that the larger σ^2 obtained partially compensates for a larger than average deviation from collinearity which is not accounted for in the model. Ba induced displacements in both O(2) (intervening atoms) and Cu (end atoms) could in principle result in deviations from the three body configuration determined in the diffraction studies. A measurement of the effective “buckling” angle (averaged over all Cu sites) of the Cu-O(2)-La three body configuration, as determined from \hat{c} -axis polarized Cu K -edge XAFS, seems to confirm this assumption. As discussed in the next section, the effective “buckling” angle measured by XAFS, $\sqrt{\langle \theta^2 \rangle}$ (the average being over all Cu central atoms)

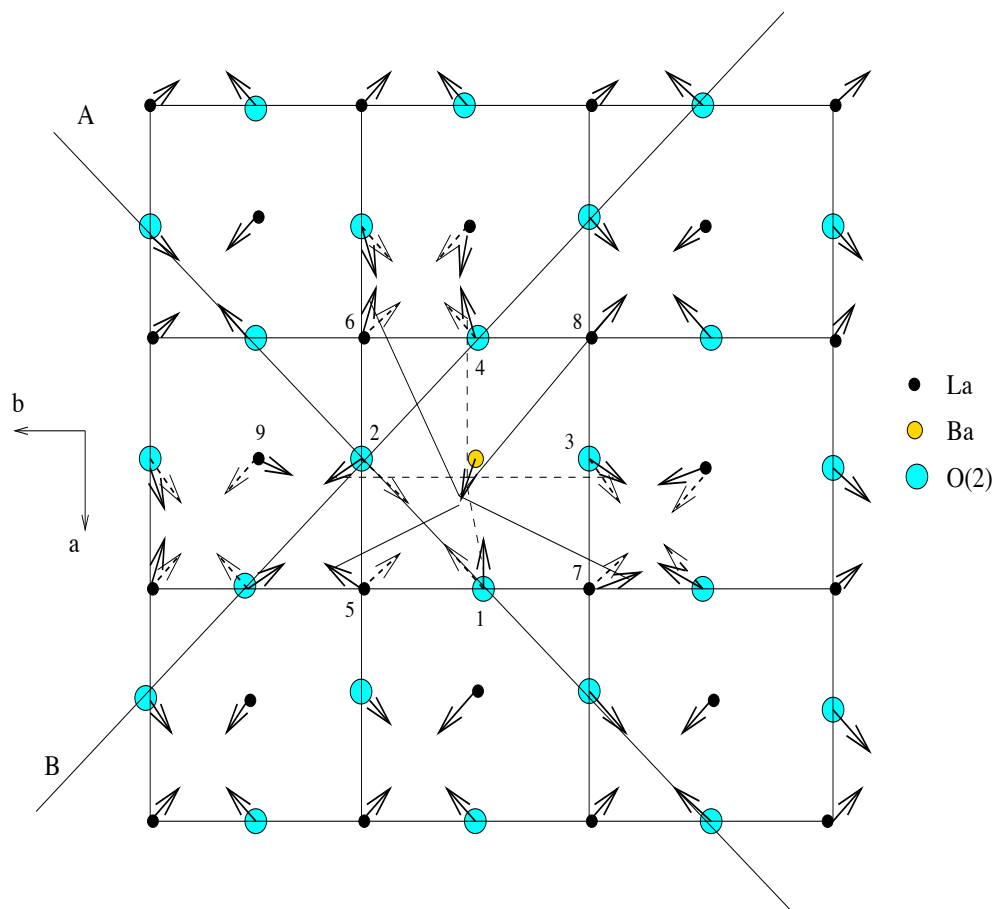


Figure 6.18: Schematic representation of O(2) and correlated La/Ba atomic displacements consistent with the Ba K -edge data. Two arrows are placed when the actual local displacement differs from the ideal LTT one. Arrows are not drawn to scale. This represents a *possible*, likely scenario, but by no means uniqueness is claimed. Correlated displacements in neighboring cells are deduced and therefore ought to be taken on a *hypothetical* basis. The arrows are not drawn to scale; the O(2) displacements (relative to the undistorted HTT phase) being much larger than the La/Ba ones.

Table 6.10: Parameters used for the background removal shown in fig. 6.20. Fourier components are minimized in the region $[0, r_{\text{bkg}}]$. Fourier transform k -weight, range and Hanning window sill widths are also shown.

	E_0 (KeV)	$r_{\text{bkg}}(\text{\AA})$	$k_{\text{min}}(\text{\AA}^{-1})$	$k_{\text{max}}(\text{\AA}^{-1})$	kw	$dk(\text{\AA}^{-1})$
$\hat{e} \parallel \hat{c}$	8.980	1.3	0.5	last point	1	0.2
$\hat{e} \perp \hat{c}$	8.980	1.2	0.5	last point	1	0.2

is $\approx 2\langle\theta\rangle$, $\langle\theta\rangle$ being the long-range- averaged ‘‘buckling’’ angle determined by the average atomic positions found in the diffraction studies.

To end this section, a summary of the Ba induced distortions measured by Ba K -edge XAFS is schematically shown in fig. 6.19. It is interesting to note the very different nature of the Ba induced distortions in $\text{La}_{2-x}\text{Ba}_x\text{CuO}_4$ compared to the Sr induced distortions in $\text{La}_{2-x}\text{Sr}_x\text{CuO}_4$ (fig. 5.35). Their differences are the most likely origin for the different structural ground states (LTT vs LTO) of these systems in the superconducting region of the phase diagram.

6.3 Cu K -edge measurements

6.3.1 Experimental results

Samples for the Cu K -edge measurements are from the same batch as those used in the La and Ba measurements. Details on sample preparation, characterization and experimental setup are given in chapters 3 & 4. A Si(111) double crystal monochromator was used and the second crystal was detuned for harmonic rejection (the intensity of the fundamental was reduced by about $\sim 20\%$). Polarized measurements were done by rotating the c -axis of the oriented powder relative to the electric field of the synchrotron radiation. Measurements were done at $T=10\text{K}$, 30K , 50K , 80K , 140K and 240K . Figure 6.20 shows raw absorption data for $x = 0.125$ at $T=10\text{K}$ in both polarization conditions, after pre-edge subtraction and normalization by the edge step. The background function, obtained with the parameters listed in table 6.10 is also included in the plots. Reproducibility scans for $x = 0.125$ at $T=10\text{K}$ are shown in fig. 6.21.

The analysis procedure used here is the same described above; i.e., both polariza-

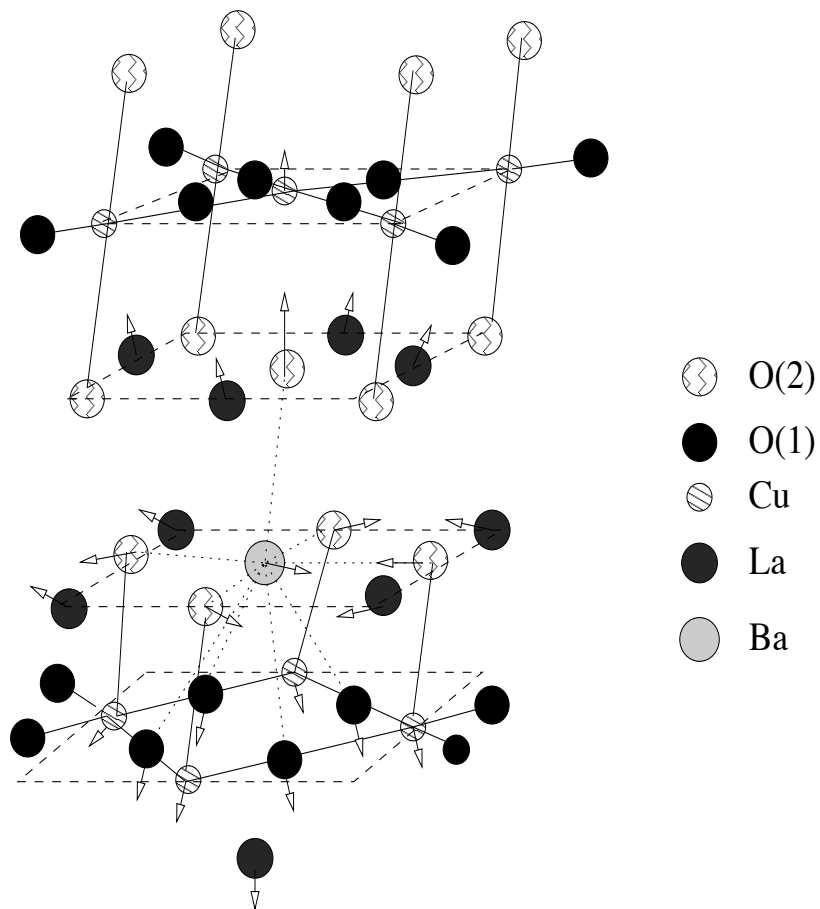


Figure 6.19: Schematic representation of the pattern of atomic displacements induced by Ba substitution in $\text{La}_{2-x}\text{Ba}_x\text{CuO}_4$ as determined by Ba K -edge XAFS. The arrows are intended as an approximate representation of the orientation of the actual atomic displacements.

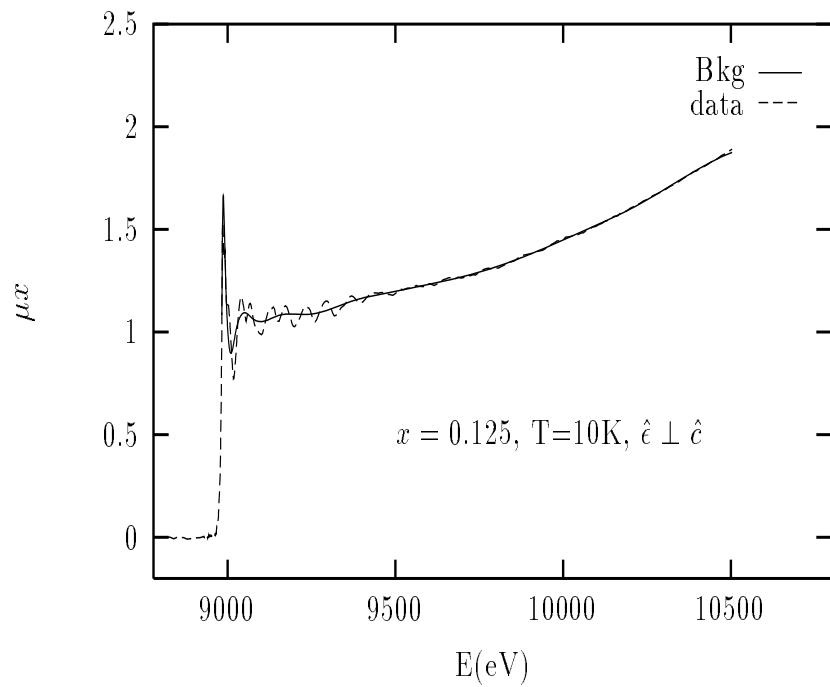
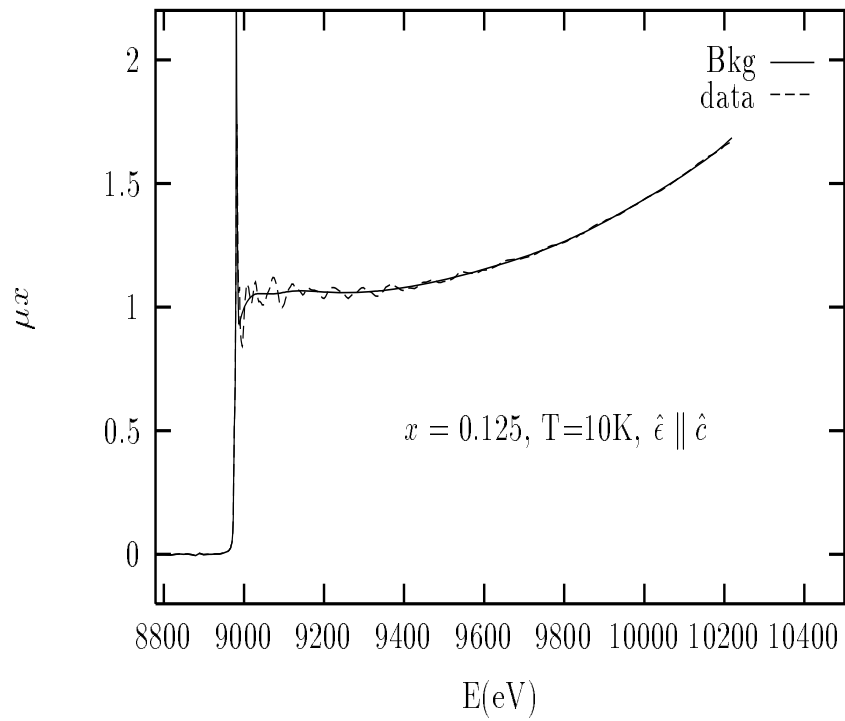


Figure 6.20: Cu K -edge absorption data in $\text{La}_{2-x}\text{Ba}_x\text{CuO}_4$ for $x = 0.125$ at $T = 10\text{K}$. Both polarization conditions are shown, together with the background function obtained with the parameters in table 6.10.

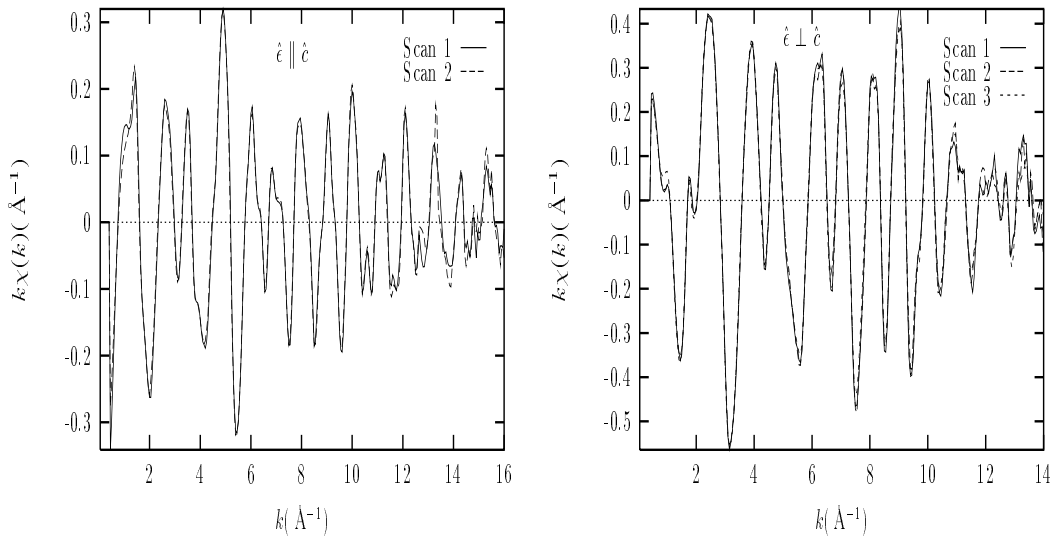


Figure 6.21: $k\chi(k)$ reproducibility data for Cu K -edge, $x = 0.125$ in $\text{La}_{2-x}\text{Ba}_x\text{CuO}_4$ at $T=10\text{K}$. Left: \hat{c} -polarization; right: in-plane, \widehat{aa} -polarization

tions are refined simultaneously and the structural parameters of the scattering paths that contribute to both polarizations are constrained to be the same. The appropriate angular average for each polarization, as explained in appendix B, is performed in the FEFF6 calculation, using the atomic positions as determined in the diffraction studies. [74] Tables 6.11 & 6.12 list SS and MS paths used in fitting the Cu K -edge XAFS data.

Data in the k -space region $k = [3, 14] \text{\AA}^{-1}$ was Fourier transformed and fits were performed in the $r = [1.6, 5.0] \text{\AA}$, $r = [1.4, 4.5] \text{\AA}$ regions of r space for \hat{c} , \widehat{aa} polarizations, respectively. Besides constraining the structural parameters of those paths that contribute to both polarized XAFS, additional constraints were imposed. A single “linear expansion” coefficient was varied for the Cu-O(1) and Cu-O(1') distances; i.e., their changes from the average structure values are constrained to be proportional to their half path length. Attempts to vary these distances independently resulted in large correlations with their σ^2 value and no improvement in the quality of fit. This is expected since the splitting in distances is small and cannot be distinguished from an effective σ^2 . A different σ^2 was refined for the Cu-O(1) and Cu-O(2) SS paths, as this significantly improved the fit. σ^2 's of nearly collinear MS paths were related to those of the SS paths as described in appendix C. For the smaller MS paths with oxygen atoms at the end of the path (table 6.11) these constraints neglect

Table 6.11: Theoretical SS photoelectron paths used in the Cu K -edge fits to the experimental XAFS signal in the r -space regions $r = [1.6, 5.0]$ Å, $r = [1.4, 4.5]$ Å for \hat{c} , \widehat{aa} polarizations, respectively. Values for interatomic distances correspond to the average structure of $x = 0.125$ at 15K. [74]

Path	r_{eff} (AA)	Degeneracy	Polarization
Cu _c -O(1')-Cu _c	1.891	(×2)	\widehat{aa}
Cu _c -O(1)-Cu _c	1.893	(×2)	\widehat{aa}
Cu _c -O(2)-Cu _c	2.413	(×2)	\hat{c}
Cu _c -La-Cu _c	3.226	(×4)	\hat{c} , \widehat{aa}
Cu _c -La-Cu _c	3.272	(×4)	\hat{c} , \widehat{aa}
Cu _c -O(1')-Cu _c	4.228	(×4)	\widehat{aa}
Cu _c -O(1)-Cu _c	4.229	(×4)	\widehat{aa}
Cu _c -O(2)-Cu _c	4.381	(×2)	\hat{c} , \widehat{aa}
Cu _c -O(2)-Cu _c	4.486	(×4)	\hat{c} , \widehat{aa}
Cu _c -O(2)-Cu _c	4.589	(×2)	\hat{c} , \widehat{aa}
Cu _c -O(2)-Cu _c	4.94	(×4)	\hat{c}
Cu _c -O(2)-Cu _c	5.033	(×4)	\hat{c}

Table 6.12: Theoretical MS photoelectron paths (and SS paths of nearly the same length) used in fitting the Cu K -edge XAFS data in the r -regions $r = [1.6, 5.0] \text{ \AA}$, $r = [1.4, 4.5] \text{ \AA}$ for \hat{c} , $\hat{a}\hat{a}$ polarizations, respectively. Values for the interatomic distances correspond to $x = 0.125$ at 15K. [74]

Path	$r_{\text{eff}}(\text{AA})$	Degeneracy	Type	Polarization
$\text{Cu}_c\text{-Cu-Cu}_c$	3.782	($\times 4$)	SS	$\hat{a}\hat{a}$
$\text{Cu}_c\text{-O}(1')\text{-O}(1')\text{-Cu}_c$	3.782	($\times 2$)	DS	$\hat{a}\hat{a}$
$\text{Cu}_c\text{-Cu-O}(1')\text{-Cu}_c$	3.782	($\times 4$)	DS	$\hat{a}\hat{a}$
$\text{Cu}_c\text{-O}(1')\text{-Cu}_c\text{-O}(1')\text{-Cu}_c$	3.782	($\times 2$)	TS	$\hat{a}\hat{a}$
$\text{Cu}_c\text{-O}(1')\text{-Cu}_c\text{-O}(1')\text{-Cu}_c$	3.782	($\times 2$)	TS	$\hat{a}\hat{a}$
$\text{Cu}_c\text{-O}(1')\text{-Cu-O}(1')\text{-Cu}_c$	3.782	($\times 2$)	TS	$\hat{a}\hat{a}$
$\text{Cu}_c\text{-Cu-O}(1)\text{-Cu}_c$	3.784	($\times 4$)	DS	$\hat{a}\hat{a}$
$\text{Cu}_c\text{-O}(1)\text{-O}(1)\text{-Cu}_c$	3.787	($\times 2$)	DS	$\hat{a}\hat{a}$
$\text{Cu}_c\text{-O}(1)\text{-Cu}_c\text{-O}(1)\text{-Cu}_c$	3.787	($\times 2$)	TS	$\hat{a}\hat{a}$
$\text{Cu}_c\text{-O}(1)\text{-Cu}_c\text{-O}(1)\text{-Cu}_c$	3.787	($\times 2$)	TS	$\hat{a}\hat{a}$
$\text{Cu}_c\text{-O}(1)\text{-Cu-O}(1)\text{-Cu}_c$	3.787	($\times 2$)	TS	$\hat{a}\hat{a}$
$\text{Cu}_c\text{-La-Cu}_c$	4.773	($\times 2$)	SS	\hat{c}
$\text{Cu}_c\text{-La-O}(2)\text{-Cu}_c$	4.777	($\times 4$)	DS	\hat{c}
$\text{Cu}_c\text{-O}(2)\text{-La-O}(2)\text{-Cu}_c$	4.781	($\times 2$)	TS	\hat{c}
$\text{Cu}_c\text{-O}(2)\text{-O}(2)\text{-Cu}_c$	4.827	($\times 2$)	DS	\hat{c}
$\text{Cu}_c\text{-O}(2)\text{-Cu}_c\text{-O}(2)\text{-Cu}_c$	4.827	($\times 2$)	TS	\hat{c}
$\text{Cu}_c\text{-O}(2)\text{-Cu}_c\text{-O}(2)\text{-Cu}_c$	4.827	($\times 2$)	TS	\hat{c}

Table 6.13: Fourier transform parameters, fitting regions and quality of fit factors for fits shown in figs. [6.22- 6.25]. $S_0^2 = 0.91(6)$ was obtained in the fits, the uncertainty including the small variation between samples. A McMaster correction $\sigma_{mm}^2 = 0.00052 \text{ \AA}^2$ was used to correct for edge step normalization.

	$k_{\min}(\text{\AA}^{-1})$	$k_{\max}(\text{\AA}^{-1})$	$dk(\text{\AA}^{-1})$	kw	$r_{\min}(\text{\AA})$	$r_{\max}(\text{\AA})$
$\hat{e} \parallel \hat{c}$	3	14	1.5	2	1.6	5
$\hat{e} \perp \hat{c}$	3	14	1.5	2	1.4	4.5
$x = 0.125$	$\chi_\nu^2 = 46$	$R=0.011$				
$x = 0.15$	$\chi_\nu^2 = 40$	$R=0.01$				

correlations in the displacements of the end oxygen atoms (appendix C). This is a reasonable approximation here since the MS signals at $r \sim 3.78 \text{ \AA}$ and $r \sim 4.77 \text{ \AA}$ are dominated by the focusing MS paths with Cu and La atoms as the end atoms (table 6.11), respectively. The total number of independent points was $N_I = 48$ and a total number of $N_P = 16$ parameters were used, resulting in $\nu = (N_I - N_P) = 32$ degrees of freedom. Fits obtained for $x = 0.125$ and $x = 0.15$ in both polarization conditions are shown in figs. [6.22- 6.25].

Table 6.13 includes quality of fit factors, Fourier transform parameters and fitting regions, and best fit S_0^2 values.

As already mentioned, the XAFS of the Cu site is the *less* sensitive to the occurrence of the structural phase transitions. This is because the CuO_6 octahedra's tilts are centered on the Cu atoms, and the small tilt angles involved ($\leq 3^\circ$) result in small changes in its interatomic distances across the different phase transitions. For example, at the LTT to LTO phase transition ($T \sim 60\text{K}$) the changes in Cu-O(1), Cu-O(2), Cu-Cu and Cu-La_{MS} interatomic distances is $\leq 0.005 \text{ \AA}$. [74, 75] The most significant change consists of a redistribution of Cu-La distances [74], but yet the small changes involved at the LTT to LTO transition result in static disorder of about 0.0005 \AA^2 which can be accommodated by a small change in σ^2 . This lack of sensitivity is consistent with the observation of no changes in local structure from $T=4\text{K}$ to 300K in the Cu K -edge powder XAFS work of Boyce *et. al* in $\text{La}_{1.8}\text{Ba}_{0.2}\text{CuO}_4$. [129] Whether *local* atomic displacements consistent with the long range averaged displacements found at the structural phase transitions measured by diffraction are present is still

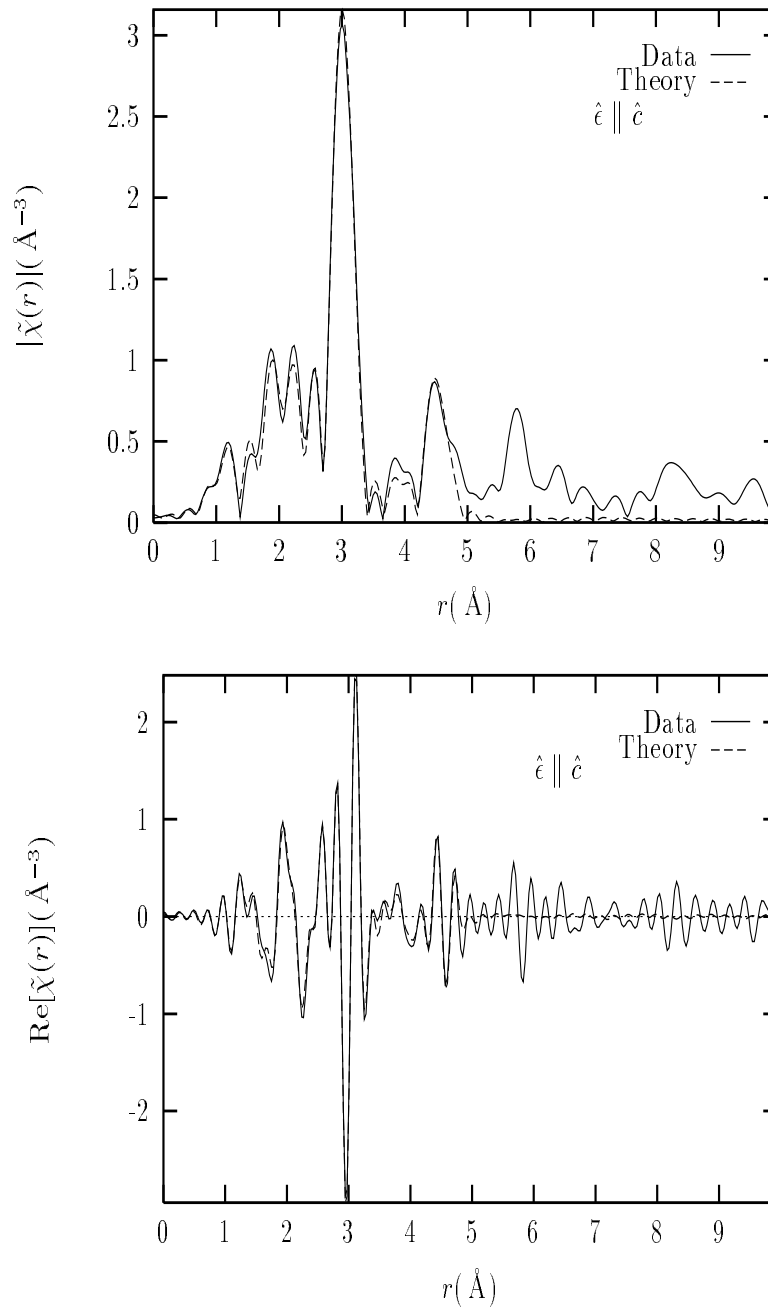


Figure 6.22: Fit results for the $x = 0.125$ sample at $T=10$ K. The magnitude (top) and the real part (bottom) of the complex Fourier transform are shown for $\hat{e} \parallel \hat{c}$

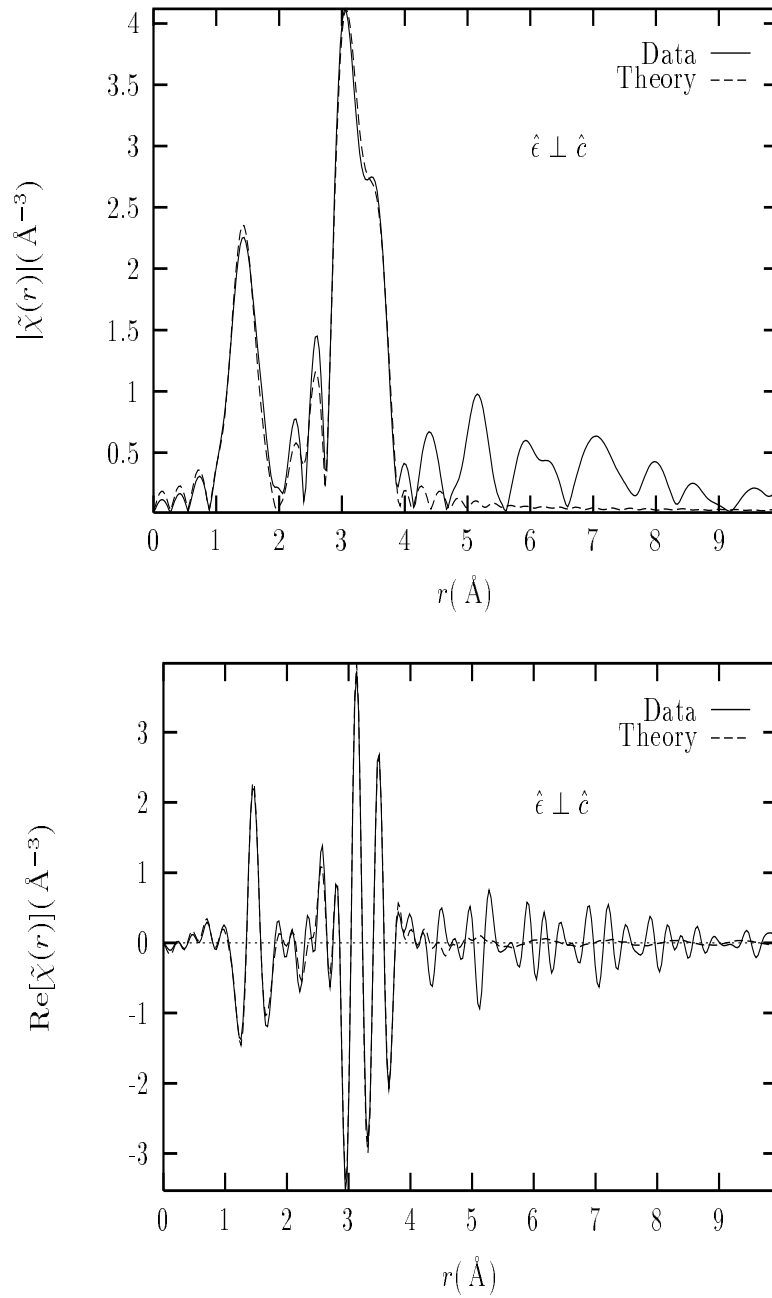


Figure 6.23: Fit results for the $x = 0.125$ sample at $T=10$ K. The magnitude (top) and the real part (bottom) of the complex Fourier transform are shown for $\hat{e} \perp \hat{c}$

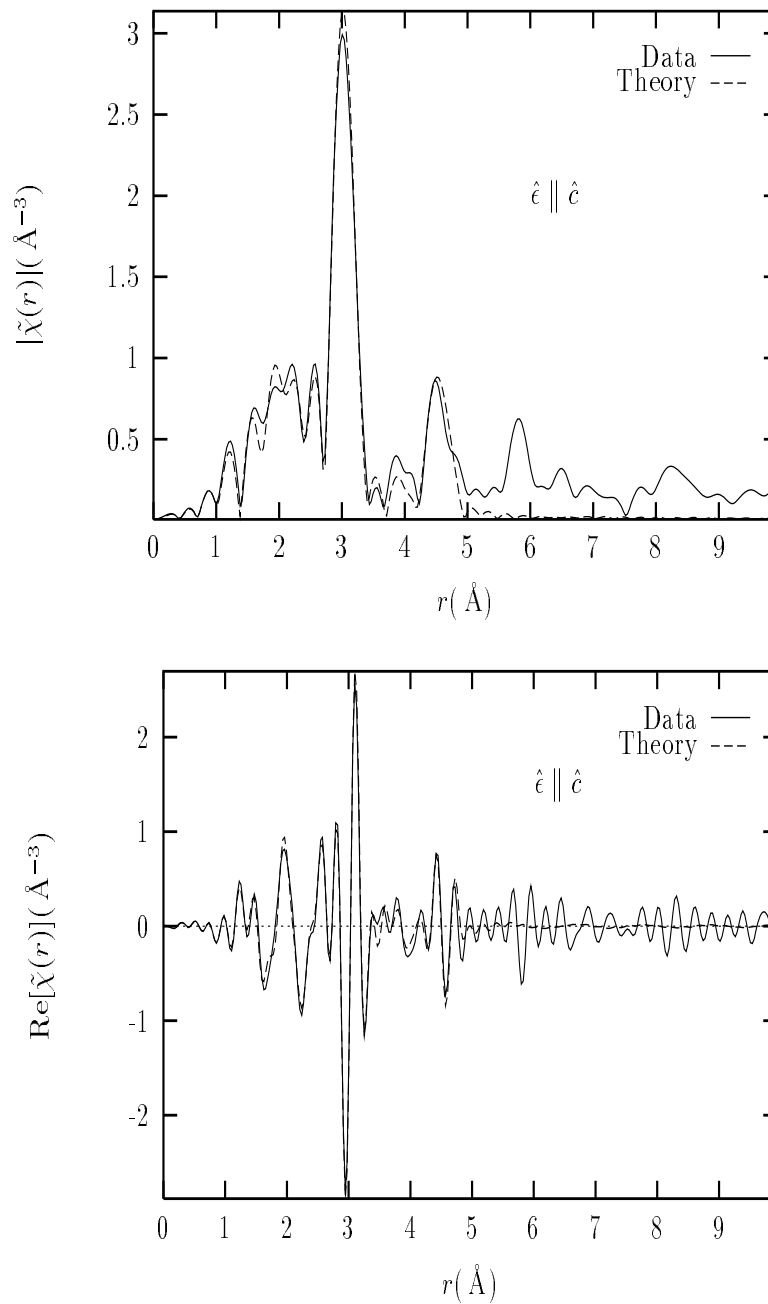


Figure 6.24: Fit results for the $x = 0.15$ sample at $T=10$ K. The magnitude (top) and the real part (bottom) of the complex Fourier transform are shown for $\hat{e} \parallel \hat{c}$

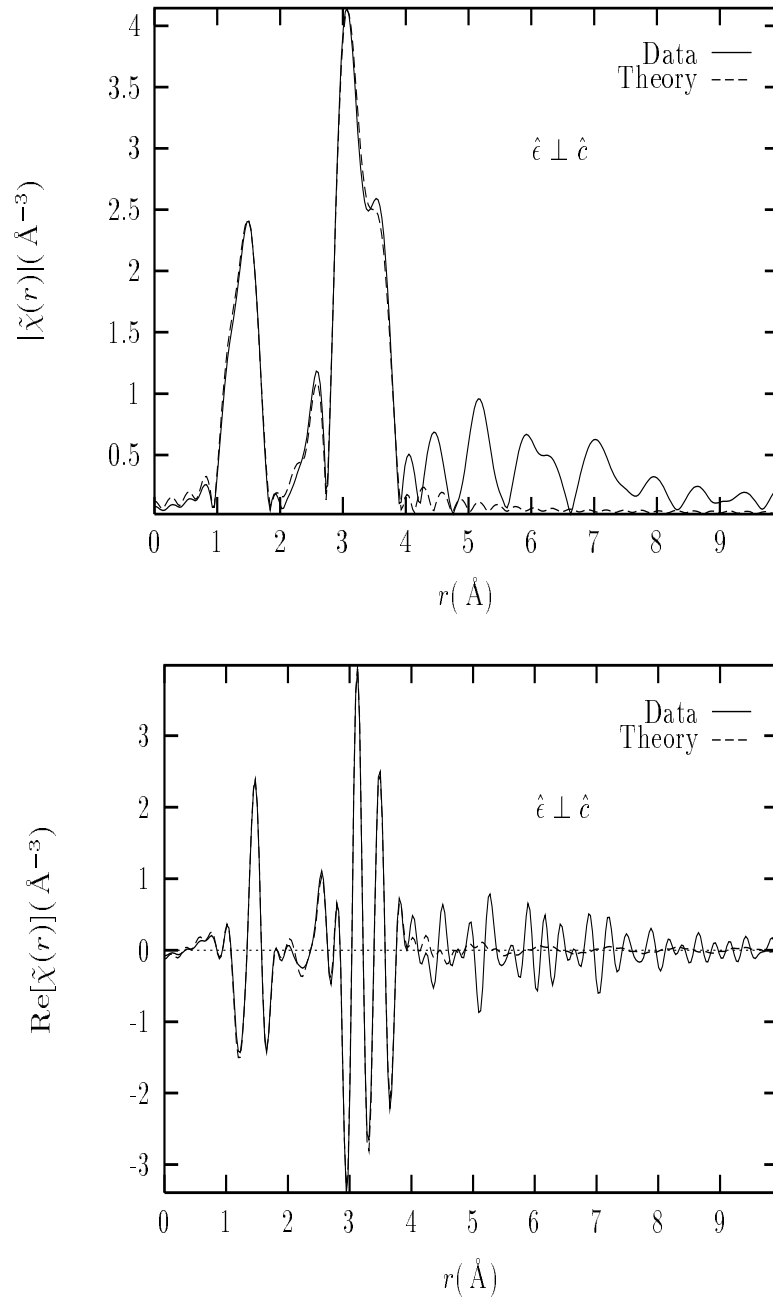


Figure 6.25: Fit results for the $x = 0.15$ sample at $T=10$ K. The magnitude (top) and the real part (bottom) of the complex Fourier transform are shown for $\hat{e} \perp \hat{c}$

an open question. Strong evidence in support of an *instantaneous* temperature *independent* local structure in a $\leq 5 \text{ \AA}$ scale is found in the PDF studies of Billinge *et. al* [133], implying that dynamical fluctuations of octahedra tilts (with the related loss of long range order in their tilt pattern over longer length scales) are responsible for the phase transitions. Irrespective of this question, the XAFS of the Cu site is nearly insensitive to the *average* atomic displacements found by diffraction, *even if* they are also present in the *local* structure.

In this spirit, the Cu *K* edge XAFS data at several temperatures spanning the two different structural phase transitions (LTT to LTO at $T \sim 60 \text{ K}$; LTO to HTT at $T \sim 200 \text{ K}$) were analyzed using an LTT model for the local structure. The main purpose here is not to address the effect of the structural phase transitions on the local structure (minor in the Cu XAFS) but to determine the structural ground state ($T=10 \text{ K}$) as accurately as possible. The Cu site is the most suitable for investigating the local structure of the CuO_2 planes, in particular whether local atomic displacements commensurate with charge density wave (CDW) formation exist in the $x = 0.125$ sample. CDW formation is one possible suggested mechanism for the observed T_c suppression at $x = 0.125$. [63, 152]

Figs. [6.26- 6.29] show fit results obtained using the LTT model for all temperatures. It should be noted that the Cu local structure was successfully modeled at all temperatures using the LTT model, in agreement with either the lack of sensitivity of the Cu site to the structural changes or/and the absence of those changes in a local level. [133]

6.3.2 Discussion

The possibility of an increased splitting of Cu-O(1), Cu-O(1') distances (or a related anomalous σ^2) as a function of temperature was thoroughly checked here, as such anomalous behavior was reported in the Cu *K*-edge powder XAFS study of Lanzara *et. al* [152] to occur around the onset of the LTO to LTT phase transition in $x = 0.125$ doped $\text{La}_{2-x}\text{Ba}_x\text{CuO}_4$. In their study, a systematic increase in σ^2 for the Cu-O(1), Cu-O(1') distances was reported below about $T=60 \text{ K}$, the anomalous increase totaling $\Delta\sigma^2 \approx 0.002 \text{ \AA}^2$ at $T=10 \text{ K}$. The increased σ^2 was attributed to the onset of local structural fluctuations of the CuO_2 planes as a response to the formation of a charge density wave (CDW) below about the temperature of the appearance of the LTT phase. [152]

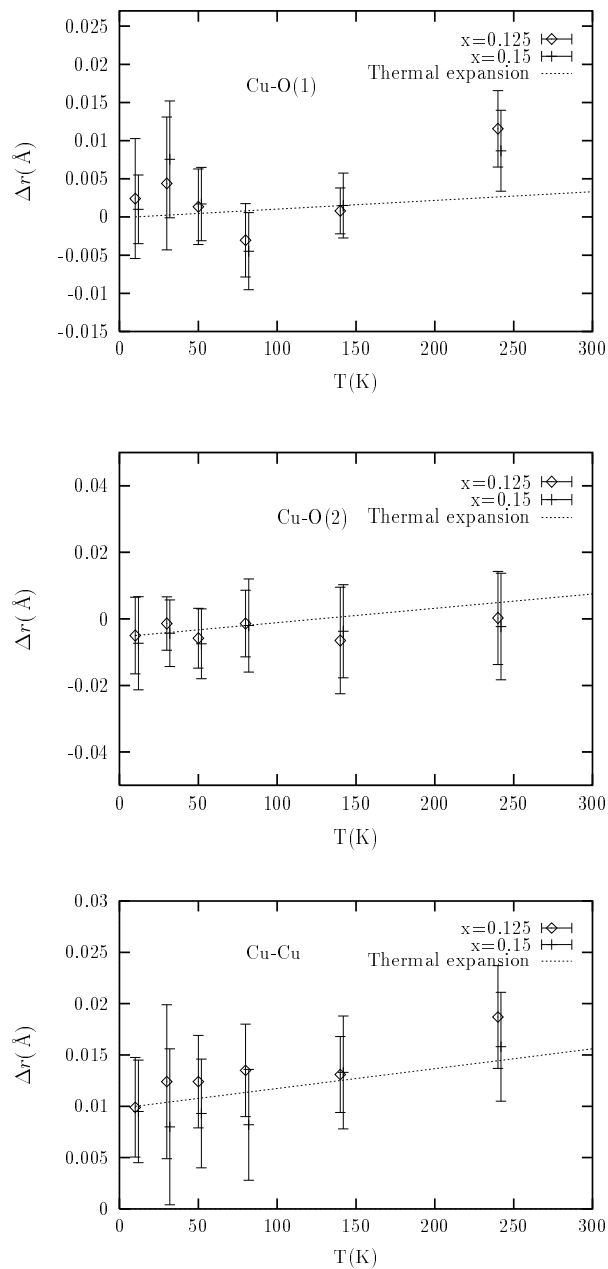


Figure 6.26: Fit results as obtained in the analysis of Cu K -edge polarized XAFS data for $x = 0.125, 0.15$. From top to bottom: Cu-O(1), Cu-O(2), Cu-Cu distances. Δr is the measured change in distance relative to the diffraction results of Katano *et. al* [74], listed in tables 6.11 & 6.12. The slope of the thermal expansion lines are from reference 126. $x = 0.15$ results displaced by 2K for clarity.

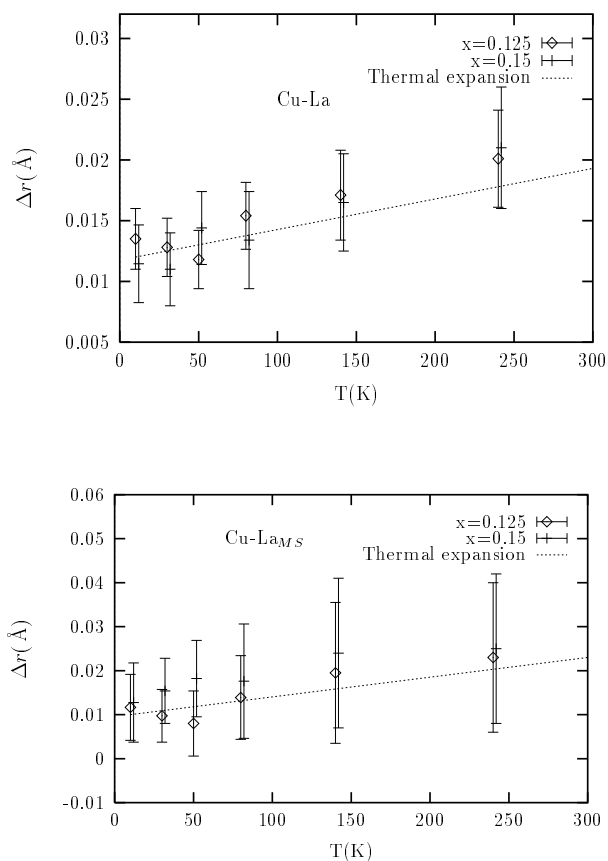


Figure 6.27: Fit results as obtained in the analysis of Cu K -edge polarized XAFS data for $x = 0.125, 0.15$. From top to bottom: Cu-La, Cu-La_{MS} distances. Δr is the measured change in distance relative to the diffraction results of Katano *et. al* [74], listed in tables 6.11 & 6.12. The slope of the thermal expansion lines are from reference 126. $x = 0.15$ results displaced by 2K for clarity.

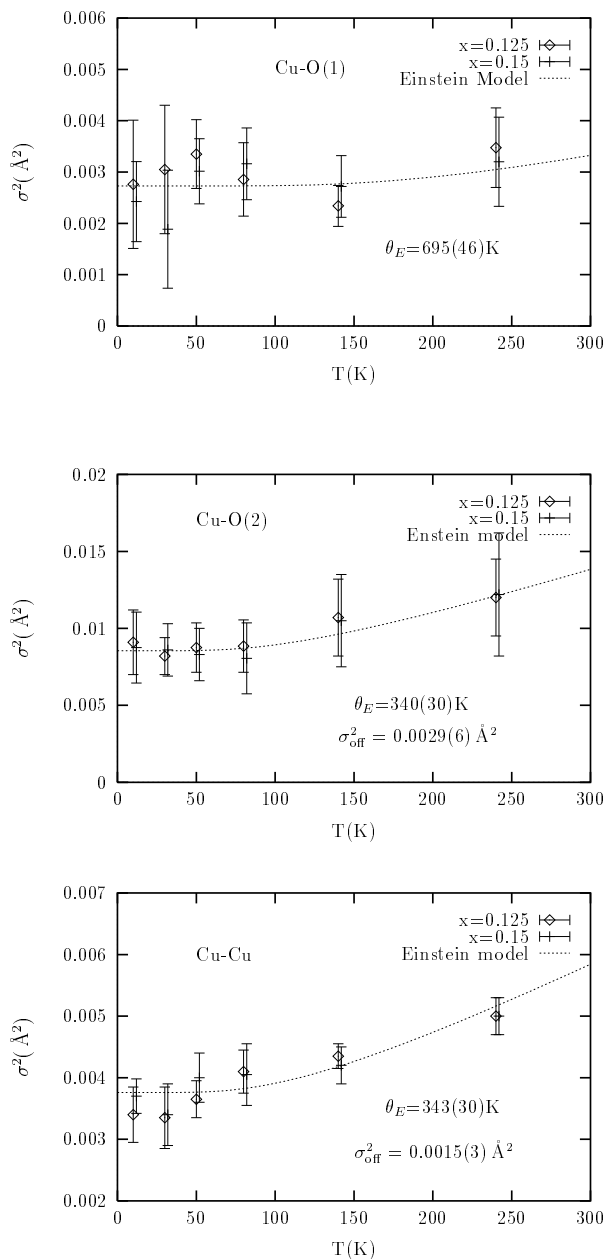


Figure 6.28: Fit results as obtained in the analysis of Cu K -edge polarized XAFS data for $x = 0.125, 0.15$. From top to bottom: Cu-O(1), Cu-O(2), Cu-Cu XAFS Debye Waller factors. Fits of the disorder in bond length (using $x = 0.125$ data) to an Einstein model also shown. Einstein temperatures together with the additional static disorder σ_{off}^2 required (when shown) in fitting the data also shown. $x = 0.15$ results displaced by 2K for clarity.

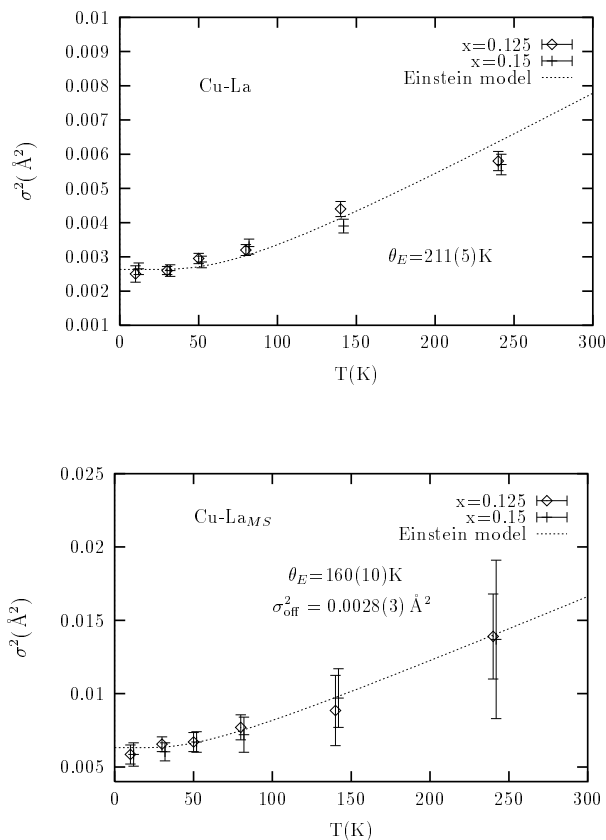


Figure 6.29: Fit results as obtained in the analysis of Cu K -edge polarized XAFS data for $x = 0.125, 0.15$. From top to bottom: Cu-La, Cu-La_{MS} XAFS Debye Waller factors. Fits of the disorder in bond length (using $x = 0.125$ data) to an Einstein model also shown. Einstein temperatures together with the additional static disorder σ_{off}^2 required (when shown) in fitting the data also shown. $x = 0.15$ results displaced by 2K for clarity.

As shown in fig. 6.28, whereas a small increase in σ^2 ($\Delta\sigma^2 \lesssim 0.0005 \text{ \AA}^2$) cannot be ruled out in our measurements of the Cu-O(1) disorder (or a corresponding increase in splitting of distances of $\Delta r \lesssim 0.022 \text{ \AA}$), an increase in σ^2 of the magnitude reported by Lanzara *et. al* is inconsistent with our results. Moreover, the results obtained here for the $x = 0.125$ and $x = 0.15$ samples are the same within the uncertainties, imposing strong limitations on theories invoking the existence of a CDW, and the related local atomic displacements commensurate with it, as the reason for T_c suppression in $\text{La}_{2-x}\text{Ba}_x\text{CuO}_4$ with $x = 0.125$. Possible origins of the discrepancy between this work and that of ref. 152 include the treatment in the latter of the first shell signal as composed only of Cu-O(1) neglecting the Cu-O(2) apical contribution in the powder XAFS signal or/and the underestimation of the uncertainties in the parameters. The polarized data as obtained here allowed a complete separation of the planar Cu-O(1) signal from the smaller but not negligible Cu-O(2) apical signal.

Self consistency requires that the Cu-La distances and disorder obtained from the Cu K -edge analysis match the La-Cu distances and disorder obtained in the analysis of the La K -edge data. This is indeed the case. For example, for $x = 0.125$ at $T=10\text{K}$, Cu-La distances of $3.240(3) \text{ \AA}$, $3.280(3) \text{ \AA}$ are obtained, compared to La-Cu distances of $3.235(3) \text{ \AA}$, $3.282(3) \text{ \AA}$ obtained from La XAFS. The disorder in Cu-La bond length is $\sigma^2 = 0.0022(3) \text{ \AA}^2$, compared to $\sigma^2 = 0.0019(3) \text{ \AA}^2$ obtained in the La XAFS study.

The observed changes in distances with temperature are in good agreement with the overall thermal expansion of this material. Since the thermal expansion coefficient is highly anisotropic, the actual changes in distances from 10K to 300K observed in the neutron diffraction work of Jorgensen *et. al* [126] are added in figures 6.26 & 6.27. An anomalously short Cu-O(1) distance is observed at $T \sim 80\text{K}$, close to the LTT to LTO transition temperature [67, 75] and to the temperature where the anomalous increase in resistivity and reduction in Hall coefficient are observed. [61, 62] The observed deviation is small ($\Delta r \leq 0.005 \text{ \AA}$) and barely outside the uncertainties so care should be exercised in assigning any physical meaning to it. In addition the same anomaly is observed for both concentrations, ruling out a correlation with the anomalies observed in the transport properties mentioned above, since the latter are observed *only* for $x \sim 0.125$.

In the Einstein model for lattice vibrations the mean squared deviation of each atom about the lattice site corresponds to that of a one dimensional quantum har-

monic oscillator with a characteristic frequency $\omega_E = K_B\theta_E/\hbar$, K_B being Boltzmann's constant. [153] The XAFS mean square disorder in this approximation can be written as

$$\sigma^2 = \frac{\hbar^2}{2M_r K_B \theta_E} \coth\left(\frac{\theta_E}{2T}\right) \quad (6.2)$$

where the reduced mass of the *pair* of atoms (central atom and backscatterer) is used. The expression in eq. 6.2 neglects correlations in the vibrations of the atoms forming the pair (appendix C). The experimental values determined in the fits do include correlations and therefore by fitting the temperature dependence of σ^2 to the expression in eq. 6.2 a θ_E is obtained which effectively reflects these correlations. Such fits are shown for different bonds in figs. 6.28 & 6.29 where the fits were performed using the σ^2 values for $x = 0.125$. Refined Einstein temperatures are included. For the polyatomic structure here, the expression in eq. 6.2 should be a good approximation for describing the *thermal* component of the disorder, including vibrational zero point motion. [153] However, if *static* disorder is present which is unaccounted for in the fitting model, an additional temperature-independent, constant disorder σ_{off}^2 has to be added to eq. 6.2 to successfully reproduce the experimental data. This static disorder was needed in obtaining good fits to the temperature dependence of some bonds and their values for those cases are included in the plots. The presence of significant static disorder is not surprising, as the large Ba distortions found in the Ba XAFS analysis significantly affect the Cu environment, as discussed below.

The fact that very good fits are obtained using the harmonic Einstein model indicates that deviations from harmonic behavior are small. Next it is interesting to compare the characteristic Einstein temperatures obtained here for the Cu-O(1) and Cu-O(2) bonds with values obtained in previous Cu XAFS studies. Boyce *et. al* [129] reported $\theta_E = (610 \pm 80)K, (1000 \pm 200)K$ for Cu-O(1) in $\text{La}_{1.8}\text{Sr}_{0.2}\text{CuO}_4$ and $\text{La}_{1.8}\text{Ba}_{0.2}\text{CuO}_4$, respectively. [129] Tranquada *et. al* reported $\theta_E = (595 \pm 50)K, (550 \pm 40)K$ for Cu-O(1) in $\text{La}_{1.85}\text{Sr}_{0.15}\text{CuO}_4$ and $\text{La}_{1.7}\text{Ba}_{0.3}\text{CuO}_4$, respectively. [130] This values compare well to the value found here (fig. 6.28). Because of the large scatter in their data for the disorder in the Cu-O(2) bond (powder was used in their experiment), Boyce *et. al* [129] could only estimate an upper limit of $\theta_E \sim 300K$ for this bond in $\text{La}_{1.8}\text{Ba}_{0.2}\text{CuO}_4$. This value compares well with the one obtained here (fig. 6.28).

Now I turn to the discussion of the observed static disorder in some distances. The La-O(2) apical and Ba-O(2) apical distances differ significantly, as measured from the La and Ba *K*-edges (tables 6.5 & 6.8). In addition, since the La/Ba-O(2)-Cu_{MS} path is nearly collinear, the Cu-O(2) distance near a La/Ba atom can be obtained by subtracting the La/Ba-O(2) distance from the La/Ba-Cu_{MS} one. Those distances, as obtained from La, Ba XAFS analysis, are summarized in fig. 6.30 together with the probability of the different configurations neighboring a Cu atom. All numbers correspond to $x = 0.125$ at T=10K. The average, local, Cu-O(2) distance that results from the appropriately weighted configurations is

$$r[\text{Cu} - \text{O}(2)] = 0.879 \times (2.414) + 0.117 \times \left(\frac{2.414 + 2.25}{2} \right) + 3.9 \cdot 10^{-3} \times 2.25 = 2.404 \text{ \AA}, \quad (6.3)$$

in very good agreement with $r = 2.408 \pm 0.011 \text{ \AA}$ obtained from the Cu *K*-edge XAFS analysis. In terms of static disorder, if the only contribution comes from the disorder of the O(2) atoms,

$$\begin{aligned} \sigma_{\text{off}}^2[\text{Cu} - \text{O}(2)] &= 0.879 \times (2.414 - 2.408)^2 & (6.4) \\ &+ 0.117 \times \left[\frac{(2.414 - 2.408)^2 + (2.25 - 2.408)^2}{2} \right] = 1.5 \cdot 10^{-3} \text{ \AA}^2. \end{aligned}$$

This contribution is not enough to account for the observed static disorder in fig. 6.28. As found in the Ba XAFS analysis, the Cu atoms neighboring the Ba atoms are displaced by $\Delta r \sim 0.05 \text{ \AA}$ away from Ba. Since the Ba atoms are randomly distributed, and assuming the Cu are displaced mostly along the \hat{c} axis, the effect of the Cu displacements will result in an equal number of shorter and longer Cu-O(2) bonds (relative to the average, local distance) next to Ba, i.e., its effect will be additional static disorder. For the concentrations of Ba at hand, about 50% of the Cu-O(2) bonds are affected. Its contribution to static disorder is then $\sigma_{\text{off}}^2 = 0.5 \times (0.05)^2 = 1.25 \times 10^{-3} \text{ \AA}^2$. Since these Cu distortions and the O(2) distortion contributing to eq. 6.4 are uncorrelated, the total static disorder in Cu-O(2) distance becomes $\sigma_{\text{off}}^2 \approx 2.75 \times 10^{-3} \text{ \AA}^2$, in agreement with the fitted value in fig. 6.28.

On the other hand, the static disorder obtained for the Cu-La_{MS} and Cu-Cu distances is too large to be explained as solely due to Ba induced disorder in the Cu-La_{MS} and Cu-Cu distances. Nearly collinear MS paths contribute at about these

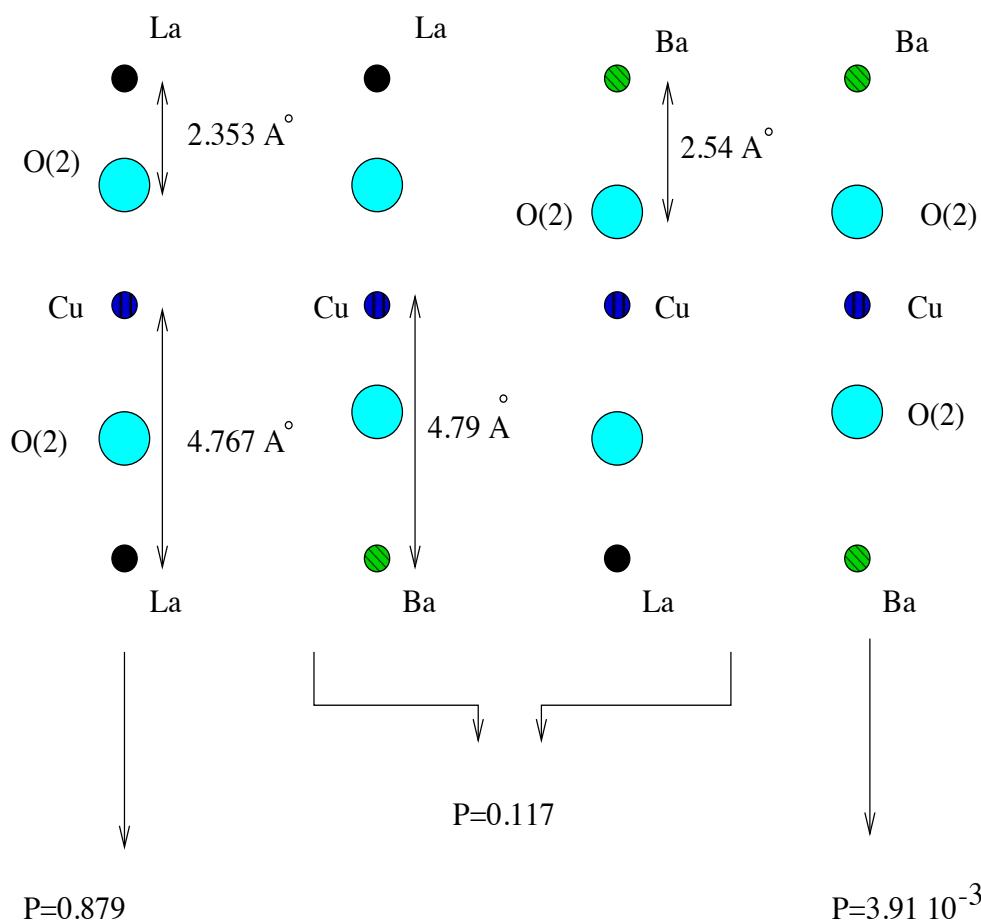


Figure 6.30: Schematic representation of the different local atomic configurations for Cu atoms in $\text{La}_{2-x}\text{Ba}_x\text{CuO}_4$, together with their probabilities. La/Ba-O(2) and La/Ba-Cu distances, obtained from La and Ba *K*-edge XAFS analysis are shown.

same distances (table 6.12) and their disorder is constrained in the fits to be the same as that of the SS path of nearly the same length. Therefore an effective σ^2 for the SS and MS paths at nearly the same distance is obtained. It is then reasonable to expect that Ba-induced deviations from the three body-nearly collinear arrangement of atoms forming these MS paths, which result in local increases in “buckling” angle of the Cu-O(1)-Cu and Cu-O(2)-La atomic arrangements, lower the resulting signal as discussed below. This decrease can be partially compensated for by an increased σ^2 , since the buckling angle was set in the fits to the smaller, long range averaged value determined by diffraction. If the magnitude of the local buckling angle is temperature independent, as suggested by the PDF studies of Billinge *et. al* [133], a constant offset to the Einstein model behavior, as obtained here, could somewhat compensate for the unaccounted, increased buckling.

6.3.3 Measuring the CuO_6 octahedra tilt angle

A measurement of the effective buckling angle in the Cu-O(1)-Cu and Cu-O(2)-La three body atomic arrangement was performed here to investigate this issue. The sensitivity of MS XAFS to changes in buckling angle is mostly due to the p.e. scattering amplitude at the intervening O(1) and O(2) atoms being strongly peaked in the forward direction and rapidly decreasing with scattering angle. [78,92] For example, the amplitude of the DS $\text{Cu}_c\text{-O(1)-Cu-Cu}_c$ path as obtained by the curved wave criteria in FEFF6 is $\sim 40\%$ larger than that of the $\text{Cu}_c\text{-Cu-Cu}_c$ SS path of nearly the same length. This is due to the enhancement of the p.e. wave function at the position of the end atoms as compared to its value in the absence of the intervening, “focusing” atom. As the deviation from collinearity increases the enhancement decreases, lowering the overall amplitude of the scattering path. The dependence of the effective scattering amplitude and phase on buckling angle is illustrated in appendix A for the $\text{Cu}_c\text{-O(1)-Cu-Cu}_c$ DS path.

A detailed description of the method used here to measure the buckling angle, α and β in fig. 6.31, is given in appendix A, including examples of modified *paths.dat* files and *feffit.inp* files used in the modeling, which combines FEFF6 and FEFFIT. Main differences of this method as compared to others [93,94,99] include the proper parameterization of the MS half path length in terms of the buckling angle, $\Delta r(\alpha, \beta)$, and accounting for the k -dependence in the correction to the effective scattering amplitude, $F_k(\alpha, \beta)$, as explained in appendix A.

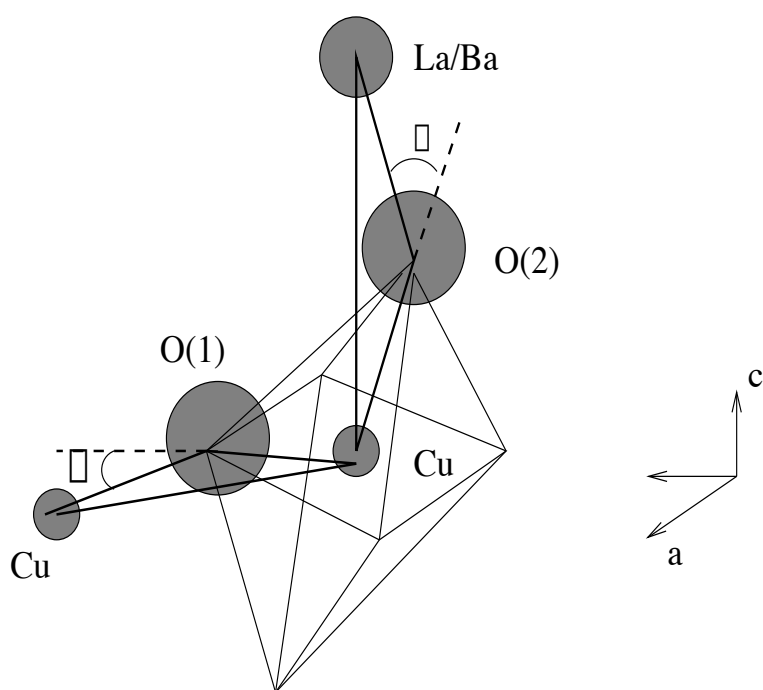


Figure 6.31: Schematic representation of the buckling angles α and β determined from MS analysis of Cu-O(1)-Cu and Cu-O(2)-La signals using $\widehat{a\hat{a}}$ and \hat{c} polarized Cu K -edge data.

The σ_{off}^2 previously obtained by fitting the temperature dependence of the disorder in the Cu-O(1)-Cu and Cu-O(2)-La distances (figs. 6.28 & 6.29) to an Einstein model could, in principle, arise from increased deviations from collinearity *and* static disorder of other nature which is *not* well described by changes in buckling angle as modeled here following appendix A. Therefore enough flexibility has to be included in the model to allow for static disorder of *other* source besides buckling. This is done here by fitting *all* the temperatures simultaneously and constraining the vibrational component of the disorder to follow an Einstein model *but* allowing for an offset of static nature. In addition, the buckling angle is varied *for each temperature*, following the recipe in appendix A. Even though the PDF work of Billinge *et. al* [133] implies a constant magnitude of the local buckling angle for all temperatures, the temperature dependent buckling angle introduced here allows for changes due to the presence of the structural phase transitions at $T \sim 60, 200$ K (the long range averaged buckling angle is zero in the HTT phase, above $T \sim 200$ K). Changes in distance due to natural thermal expansion are allowed in the model as well.

Since each of the signals of interest contribute in one polarization only, *all* temperatures were refined simultaneously for each polarization in the r -space region of interest ($r = [3.7, 5] \text{ \AA}$; $r = [3, 4] \text{ \AA}$ for $\epsilon \parallel, \perp \hat{c}$, respectively) while all other variables were set to their best fit values as obtained in the simultaneous fittings to both polarizations at each temperature. Since the MS signal under study dominates the XAFS signal in the region of r -space being fitted, setting the parameters of neighboring shells to their best fit values did not affect the refinement of the MS signals, as corroborated by allowing the parameters of neighboring shells to vary as well. The length of legs forming the MS paths are parameterized in terms of the scattering angles α, β and the SS half path length, as explained in appendix A. The SS half path length is allowed to vary for each temperature to account for deviations from the average structure, including thermal expansion. The effective scattering amplitude is parameterized in terms of α (and β) by calculating the effective scattering amplitude for three different scattering angles using FEFF6 and constructing a correction of the form $F_k(\alpha) = F_{k, \alpha_{\text{avg}}}(\gamma_k + \zeta_k \alpha^2)$ (for the scattering angles considered here, $(\alpha, \beta) \leq 20^\circ$, this functional form accurately describes the dependence on scattering angle; see appendix A). α_{avg} is the scattering angle found in the average structure studies [74] and γ_k, ζ_k are k -dependent coefficients obtained by fitting the (α, β) dependence of F_k (done separately for DS, TS paths and for each value of k). The

effective scattering phase ($\phi(k)$ in the total phase expression $2kr_{\text{eff}} + 2\phi_c(k) + \phi(k)$) is set to the value corresponding to the average structure's scattering angle. Its dependence on scattering angle has a measurable effect on distance determination but does not affect the measurement of the angle, as discussed below.

Two models are compared for which the buckling angle is either set to the average structure value at 10K ($\alpha = 5.9^\circ$, $\beta = 6.9^\circ$ for Cu-O(1)-Cu and Cu-O(2)-La, respectively), independent of temperature (as implied from the PDF study of ref. 133), or varied and allowed to change as a function of temperature. In both models the disorder is constrained to follow an Einstein model but an offset is allowed (σ_{off}^2) to account for static disorder, even when the buckling angle is varied. The SS distances are varied and the MS distances parameterized as described in appendix A.

Results obtained in the two models are compared in table 6.14. The effective buckling angle obtained in the second model is shown in fig. 6.32 for both MS paths. Also shown are the long range averaged values obtained in the diffraction work of Katano *et. al* [74]. The distances obtained when using the effective scattering phase that corresponds to the average structure's three body configuration [$\phi_k(\alpha = 5.9^\circ; \beta = 6.9^\circ)$] are within uncertainties the same for both models and the same as those shown in figs. 6.26 & 6.27. To check the effect of having set $\phi(k)$ to the value corresponding to the average structure's configuration, the values of $\phi(k)$ calculated by FEFF6 corresponding to $\alpha = 14^\circ, \beta = 15^\circ$ were used instead. This did not affect the refined values for the buckling angles but it did result in an offset of the measured distances of $\Delta r \sim 0.003 \text{ \AA}, 0.006 \text{ \AA}$ for Cu-O(1)-Cu and Cu-O(2)-La, respectively. This is in agreement with the observation of, e.g., $\Delta\phi(k = 8 \text{ \AA}^{-1}) \approx 0.1$ radians for the DS paths in going from $6\text{-}7^\circ$ to $14\text{-}15^\circ$, corresponding to a change in distance of about $\Delta r \sim 0.005 \text{ \AA}$ (in fact what is relevant to distance determination is the change in *slope* of $\phi(k)$ but this gives a good estimate). The rate of distance's change with temperature, however, is nearly the same for both $\phi(k)$ values.

The improvement obtained when varying the buckling angle is statistically significant, as the ratio of χ_ν^2 values obtained in both models is $\approx (1 + 2\sqrt{2/\nu})$, the fit with the lowest χ_ν^2 being better. The improvement of the second model can also be seen visually, as shown in fig. 6.33.

The results obtained by setting the buckling angle to its average structure value (model 1) correspond well to those previously obtained by fitting each temperature data set independently. This gives an independent check of the overall fitting pro-

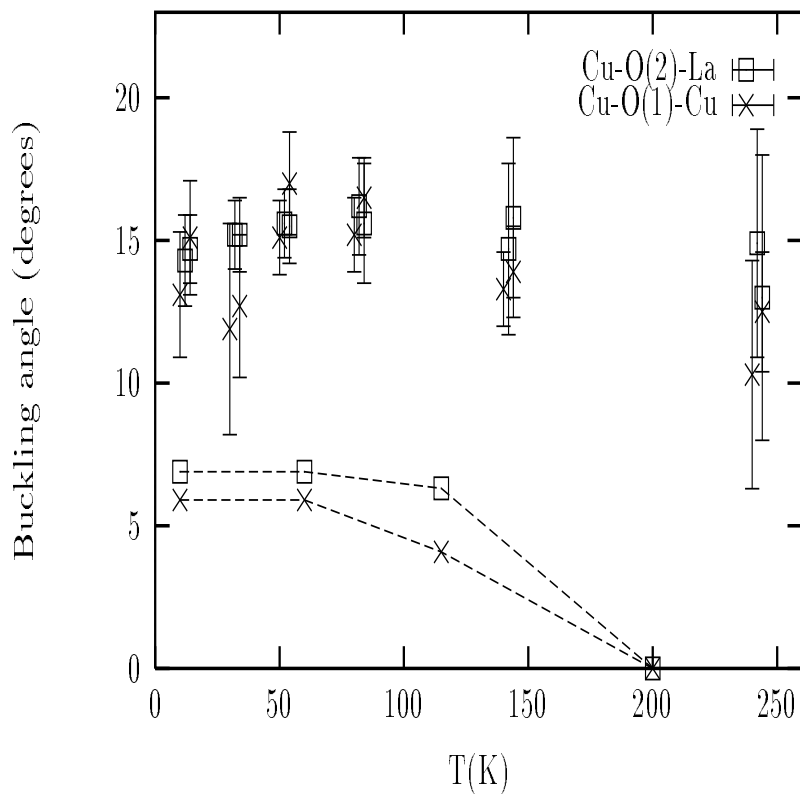


Figure 6.32: Buckling angle for Cu-O(1)-Cu and Cu-O(2)-La three body configurations as determined in the fittings of the $x = 0.125$ and $x = 0.15$ samples. The corresponding average structure's values as obtained in refs. 74,75 are shown in the lower panel. Lines through the average structure results are guide to the eye.

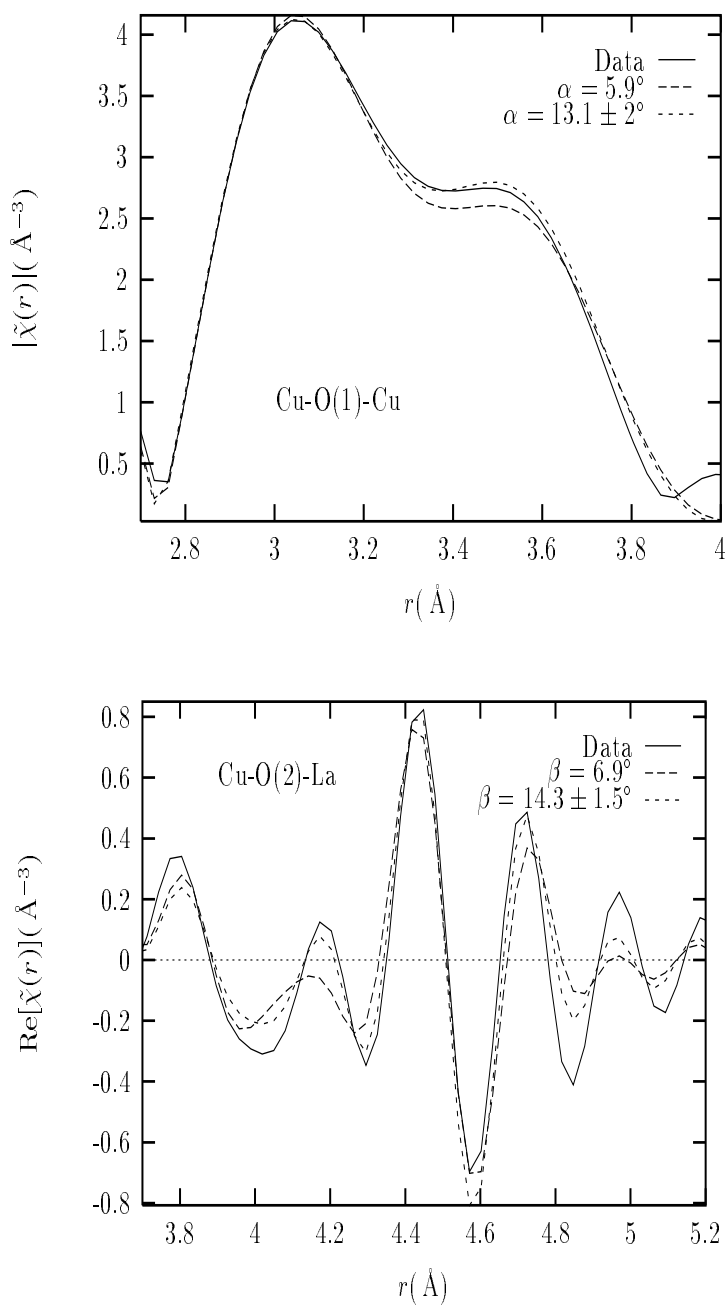


Figure 6.33: Comparison between the two models described in the text. Top: Cu-O(1)-Cu signal; bottom: Cu-O(2)-La signal. The region of r space fitted is emphasized. The improvement obtained by varying the buckling angle is readily seen. Fits here correspond to $x = 0.125$ at $T=10\text{K}$.

Table 6.14: Comparison between models for which the buckling angle is set to the average structure value at T=10K or allowed to vary as a function of temperature. Data for both Cu-O(1)-Cu and Cu-O(2)-La paths is shown. Numbers here correspond to the $x = 0.125$ sample; results for $x = 0.15$ are, within uncertainties, the same.

Cu-O(1)-Cu					
Model	$\theta_E(K)$	$\sigma_{\text{off}}^2(\text{\AA}^2)$	N_I	N_P	χ_ν^2
$\alpha = 5.9^\circ$	357(35)	0.0018(3)	42	8	45.5
$\alpha = \alpha(T)$	296(14)	0.0002(7)	42	13	32.1
Cu-O(2)-La					
Model	$\theta_E(K)$	$\sigma_{\text{off}}^2(\text{\AA}^2)$	N_I	N_P	χ_ν^2
$\beta = 6.9^\circ$	158(16)	0.0030(6)	55	8	33.9
$\beta = \beta(T)$	174(24)	(-0.0004 ± 0.0016)	55	13	23.58

cedure. Varying the buckling angle in model 2, accounted for most of the static disorder as can be seen by the negligible σ_{off}^2 values obtained in model 2. The uncertainties obtained in the σ_{off}^2 values of model 2 give an upper limit for the static disorder of other nature, beside an increased deviation from collinearity; i.e., 0.0007\AA^2 , 0.0016\AA^2 for Cu-O(1)-Cu, Cu-O(2)-La, respectively. In addition, it is interesting to note that the vibrational zero point motion obtained in model 2 for Cu-O(2)-La_{MS} paths ($0.0030(5) \text{\AA}^2$ as deduced from the values of θ_E and M_r using eq. 6.2) compares well to the vibrational zero point motion of La-O(2)-Cu_{MS} obtained in the La *K*-edge XAFS of La_{2-x}Sr_xCuO₄ at T=20K and low x ; $0.004(1) \text{\AA}^2$ (table 5.5).

It should be noted that fitting the different temperature's data sets simultaneously and constraining the vibrational component of the disorder to follow an Einstein model resulted in no significant correlations between the buckling angle and Einstein temperature parameters, as seen from the relatively small uncertainties in the measurement of these parameters. This is in part expected due to the different k -dependence in the effect that an increased buckling angle or an increased σ^2 have on the XAFS.

6.3.4 Comparing local and average buckling angles

As seen from the parameterization $F_k(\alpha) = F_{k,\alpha_{\text{avg}}}(\gamma_k + \zeta_k \alpha^2)$, XAFS measures buckling angle, α , by measuring the *local* α^2 averaged over all absorbing Cu atoms; i.e., $\alpha = \sqrt{\langle \alpha^2 \rangle}$. This is different from the measurement of buckling angle determined in the conventional diffraction studies. There, the long range averaged atomic positions are determined (only periodic components of the atomic displacements, consistent with the space group used in the refinement contribute) and then the buckling angle is determined from the average atomic positions; i.e., $\alpha = \langle \alpha \rangle$ where the average is performed using the long range order, periodic component of the atomic displacements. It is clear from the results presented in this chapter that significant deviations from the long range averaged atomic displacements exist in $\text{La}_{2-x}\text{Ba}_x\text{CuO}_4$, mostly resulting from Ba induced disorder. These local atomic displacements are random, as Ba randomly substitutes for La in the lattice. Even if correlations between these local atomic displacements exist (which is probably the case), their order is of short range nature as they are not observed in the diffraction studies. For example the local atomic displacements of the O(1) atoms next to Ba found in the Ba *K*-edge refinements will contribute to the XAFS measurement of buckling angle but, since they are random, they will not contribute to the value determined by diffraction. It is not surprising, then, that the buckling angle's values measured here and shown in fig. 6.32 are larger than the values determined by diffraction. However, the results here have tremendous significance, as discussed below, since the values determined by XAFS are the *actual* local buckling angles and better reflect what is actually happening in the structure at the local level.

6.3.5 On the relation between buckling and tilt angles

Since the buckling angle determined by XAFS contains contributions from both periodic and random atomic displacements, it should be kept in mind that the buckling angle measured here is an effective angle with contributions from regions of the local structure with *different* ordering; i.e., by no means the structure can be seen as having a single valued buckling angle, but a distribution of angles whose average over all Cu central atoms results in the value reported in fig. 6.32. The buckling angle is related to the tilt angle of the CuO_6 octahedra, as schematically shown in fig. 6.31; for an ordered structure the buckling angle is about twice as big as the tilt angle (exactly twice for Cu-O(1)-Cu, a factor of 2.35 for Cu-O(2)-La). However, relating

the buckling angles measured here to those corresponding to local *rigid* tilts of CuO_6 octahedra is not obvious. A better representation of the buckling angle here would be *independent* “tilts” of the O(1) and O(2) atoms from the \widehat{aa} plane and \hat{c} direction, respectively. On the other hand, the buckling angles obtained here for Cu-O(1)-Cu and Cu-O(2)-La atomic configurations (fig. 6.32) show a similar temperature dependence, even though no relation between them is assumed in the fits. This most likely indicates that a significant contribution of the measured buckling angle here is related to a *correlated* motion of O(1) and O(2) atoms, as in a rigid tilt of CuO_6 octahedra. The “tilt” angles obtained here are about a factor of 2 larger than the values obtained from the long range averaged atomic displacements of diffraction. For the structural ground state at $T=10\text{K}$, they are about $6 \pm 1^\circ$ compared to about 3° found in the diffraction studies. [74, 75]

6.3.6 Implications for T_c suppression at $x = 0.125$

As already mentioned, two possible mechanisms for T_c suppression at $x = 0.125$ in $\text{La}_{2-x}\text{Ba}_x\text{CuO}_4$ are currently under debate. These are (a) CDW formation due to a commensuration effect at $x = 1/8$ hole content, resulting in partial hole localization and commensurate local atomic displacements [63, 69–71] and (b) a density of states (DOS) effect in which the LTT deformation potential couples to the electronic states at the Fermi level resulting in a reduced DOS for $x = 0.125$ (in a rigid band picture). [66, 73] The main conceptual difference between the two pictures is in the origin of the instability towards the LTT phase: in (a) it is of Peierls-like origin (transition triggered by the coupling to the carriers) while in (b) it is of ionic nature and the carriers are affected by the potential change.

If a CDW is the structural ground state of $\text{La}_{2-x}\text{Ba}_x\text{CuO}_4$ at $x = 0.125$, local atomic displacements commensurate with it would occur. By comparing the results for the $x = 0.125$ and $x = 0.15$ samples in figs. [6.26- 6.29] it is clear that no significant differences exist in the local structure of these two samples. Even if the CDW was dynamic in nature, a commensuration effect at $x = 1/8$ (and its absence for $x = 0.15$) would result in differences in the σ^2 values of the two concentrations. This was not observed. The size of the error bars in figs. [6.26- 6.29] limit differences in local atomic displacements between the two samples to about $\Delta r \leq 0.005 \text{ \AA}$, which imposes strong limitations on theories evoking CDW formation at $x = 0.125$ at the basis of T_c suppression. In addition, careful diffraction work on both $x = 0.125$ and

$x = 0.15$ by Billinge *et. al* revealed the same fraction of LTT phase for both x values at all temperatures. [67] It is then concluded that the $x = 0.125$ and $x = 0.15$ samples have the same *short and long* range order and therefore the anomalies observed in the transport properties for $x = 0.125$ [61, 62] are not due to structural differences between the samples.

On the other hand, a DOS effect does not require differences in the structure of the two samples to account for T_c suppression and the transport anomalies observed at $x = 0.125$ since, in a rigid band picture, the Fermi level is tuned relative to the features of the DOS by adding hole carriers. In this picture, the Van Hove singularity (VHS) at the Fermi level is split by the appearance of the LTT order [66, 73] and the Fermi level at $x = 0.125$ corresponds to the minimum of the split VHS. The presence of LTT order is required but not sufficient in this picture to bring about the anomalies in the transport properties. Based on the electronic structure results of Pickett *et. al* and Norman *et. al* [66, 73], the splitting of the VHS in the LTT phase is very sensitive to the *magnitude* of the tilt angle of the CuO_6 octahedra. For example, by using the tilt angle values found in the diffraction studies, a very mild effect on the $\text{DOS}(E_F)$ was found by Norman *et. al* [73]. The tilt angle values used in the work of Pickett *et. al* resulting in the splitting of the VHS are about a factor of 2 larger than the diffraction values and therefore the applicability of this results to the real structure was questioned. [66, 73] The XAFS results, however, indicate that the situation in $\text{La}_{2-x}\text{Ba}_x\text{CuO}_4$ corresponds to local tilt angles which are larger than the diffraction values. Even though the XAFS results revealed a disordered ground state which cannot be described by a periodic, ordered band structure calculation, the finding of *local* buckling which corresponds to tilt angles about a factor of 2 larger than the diffraction values is extremely important in determining the applicability of the DOS model. It is clear that more sophisticated electronic structure calculations have to be performed, which include the effect of random disorder introduced with Ba and the resulting increased buckling, before conclusions can be made. Despite this, the information provided by XAFS seems to indicate that a DOS effect (and not CDW formation) is the most likely origin for the T_c suppression and transport anomalies in $\text{La}_{2-x}\text{Ba}_x\text{CuO}_4$ for $x = 0.125$.

6.3.7 On the nature of the temperature-induced LTT \rightarrow LTO \rightarrow HTT structural phase transitions

The measurement of the buckling angle here clearly demonstrates that the tilt angle of the CuO_6 octahedra does not vanish at the LTO \rightarrow HTT phase transition ($T \approx 200\text{K}$). In fact the results are consistent with a nearly temperature independent magnitude of the local tilt angle. This result is in agreement with the PDF work of Billinge *et. al* [133] in which it was found that the local tilts are always LTT-like, with correlation lengths of about $\sim 10 \text{ \AA}$ at about $T=80\text{K}$ (LTO phase). Thermally activated fluctuations of LTT tilts among locally equivalent configurations, it was argued, results in spatial disordering of the tilts relative to each other over long range leading to the phase transformations measured by diffraction. [133] The buckling angles found here are larger than the ones assumed in the modeling of the PDF data. [133] As the effect of the increased buckling angles found here results in local disorder without large changes in the averaged, local atomic positions (deviations in the local atomic positions from the diffraction values are very significant only within $\sim 5 \text{ \AA}$ from the Ba atoms, but these displacements are random), its effect on the PDF obtained in the neutron scattering studies can be compensated by an increased disorder in the relevant distances. The effect is even more obscured there by the fact that the PDF of neutron scattering contains *all* pair correlations and therefore the radial distribution function at a particular distance typically has contributions from many pairs. XAFS measures partial pair and three body correlations (between central atom and other atoms) resulting in greater sensitivity in the measured signal to evaluate the above mentioned effects.

Whether changes occur in the *direction* of the local CuO_6 octahedra's tilts at the LTT \rightarrow LTO phase transition ($T \sim 60\text{K}$) cannot be addressed from the Cu XAFS results due to the lack of sensitivity at the Cu site to the presumed change in tilt direction from $\langle 110 \rangle$ to $\langle 100 \rangle$ (*Bmab* representation) found in the diffraction studies, as already discussed. A complete analysis of the temperature dependence of the La *K*-edge XAFS in $\text{La}_{2-x}\text{Ba}_x\text{CuO}_4$ across the phase transformations is under way so a definite statement on this matter cannot be made at this point. However, some supportive evidence in favor of *absence* of change in the local tilt direction at the LTT \rightarrow LTO phase boundary is obtained from the temperature dependence of the Fourier transformed data, shown in fig. 6.34. The large rearrangement in local La-O(2) planar distances expected *if* changes in tilt direction occur consistent with the

diffraction studies can be seen in fig. 6.35 where FEFF6 calculations of $\hat{e} \perp \hat{c}$ polarized La K -edge XAFS of the LTT and LTO phases corresponding to the average structure results [74] are shown. The large changes in La-O(2) distances predicted by the crystal structure are not observed in the data. Despite the fact that only a detailed analysis can reveal the actual changes in La-O(2) and further neighbor's distances across the phase transitions, this most likely indicates that the local tilts are LTT-like for all temperatures and that the LTT \rightarrow LTO \rightarrow HTT phase transitions are of order-disorder nature, in agreement with the PDF results of Billinge *et. al* [133] and the tilt-direction-dependent energy surface found for $\text{La}_{2-x}\text{Ba}_x\text{CuO}_4$ in the self-consistent local-density-functional approximation (LDA) calculations of Pickett *et. al*.

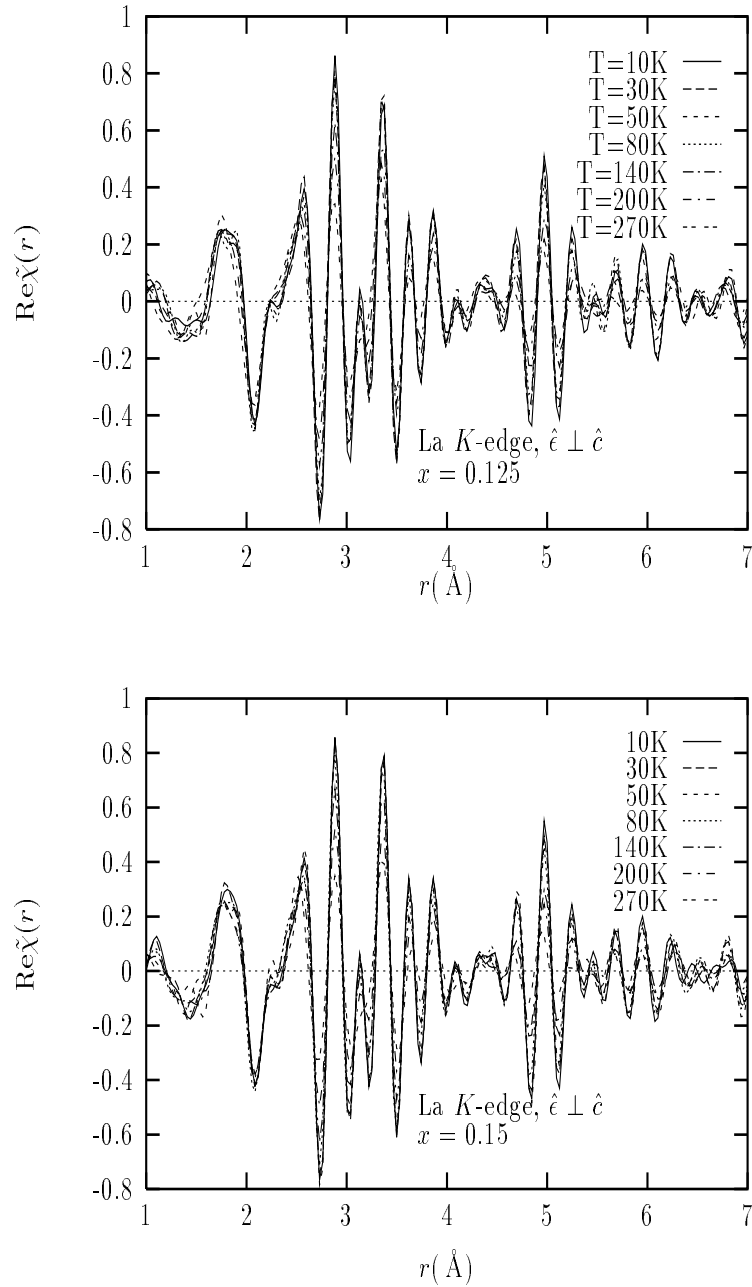


Figure 6.34: Real part of the complex Fourier transform of $k^2\chi(k)$ data as obtained at the La K -edge, $\hat{\epsilon} \perp \hat{c}$ for the temperatures shown. Top: $x = 0.125$, bottom: $x = 0.15$.

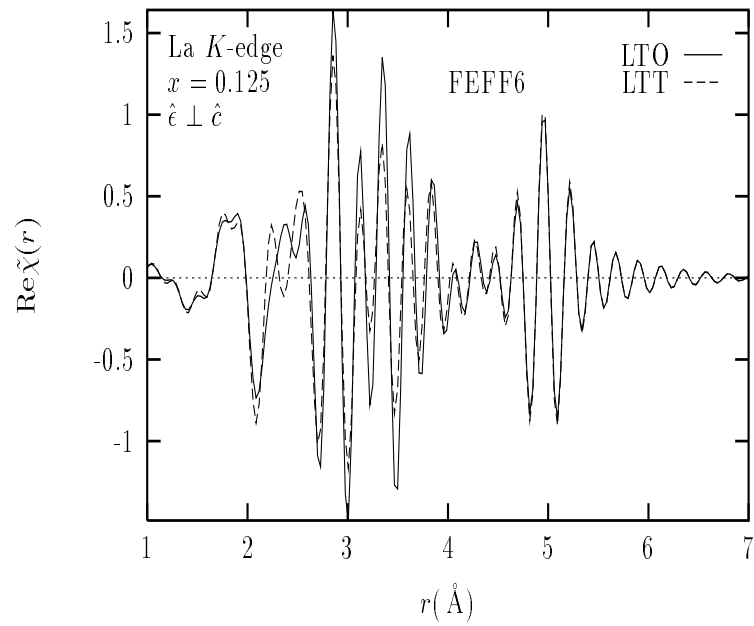


Figure 6.35: Real part of the complex Fourier transform of $k^2\chi(k)$ obtained by FEFF6 at the La K -edge, $\hat{\epsilon} \perp \hat{c}$, for both LTT and LTO structures. Atomic coordinates used in the calculation correspond to $x = 0.125$ at $T=15\text{K}$ and $T=115\text{K}$ as found by Katano *et. al* [74]. No thermal disorder is included in these calculations.

Chapter 7

SUMMARY AND CONCLUSIONS

In this chapter a summary of the most significant results obtained in this thesis is presented. Emphasis is placed on the implications with respect to the structural, magnetic and superconducting properties of the $\text{La}_{2-x}\text{Sr}_x\text{CuO}_4$ and $\text{La}_{2-x}\text{Ba}_x\text{CuO}_4$ cuprates.

7.1 *On the nature of the dopant and temperature induced structural phase transitions in $\text{La}_{2-x}(\text{Sr},\text{Ba})_x\text{CuO}_4$*

One of the main contributions of this thesis is the finding by XAFS of an important order-disorder component in all structural phase transitions in $\text{La}_{2-x}(\text{Sr},\text{Ba})_x\text{CuO}_4$. XAFS measurements at the La *K*-edge were essential in addressing this question, as the La environment is highly sensitive to the different structural modifications. It should be noted that most of the quantitative XAFS work previously done in these cuprates was at the Cu site, the *least* sensitive to the structural modifications (in terms of changes in its interatomic distances). The highly complicated oxygen environment around the La atoms (nine oxygens, six distances), however, required that polarization dependent XAFS be performed on oriented samples effectively increasing the amount of information. This required, among others, implementing a novel method of sample preparation for the $\text{La}_{2-x}\text{Ba}_x\text{CuO}_4$ system, as its polycrystalline grain size was prohibitively small for powder composed only of single crystallites to be obtained by conventional sieving methods (chapter 4), and novel approaches in modeling the data (chapters 5 & 6).

7.1.1 *The $\text{La}_{2-x}\text{Sr}_x\text{CuO}_4$ system: Dopant and temperature induced LTO \rightarrow HTT structural transitions*

A thorough study of the Sr and temperature induced LTO \rightarrow HTT structural phase transitions in $\text{La}_{2-x}\text{Sr}_x\text{CuO}_4$ revealed that the CuO_6 octahedra tilts *persist* in the HTT phase, contrary to the findings of the crystallographic studies. The long range

averaged zero tilt angle of the HTT phase measured by diffraction techniques must therefore result from a loss of spatial coherence in the arrangement of octahedra tilts and not from the vanishing of the local atomic displacements from the high symmetry HTT positions. The large “thermal” ellipsoids obtained for the O(2) atoms in the Rietveld refinements of the crystallographic studies are consistent with the lower symmetry atomic displacements present in the local structure found by XAFS, which are larger for the O(2) atoms. The persistence of local LTO tilts in the HTT phase was first suggested by Egami *et. al* [50,51] using pair distribution function analysis (PDF) of neutron scattering data. However, the ability of PDF analysis to reveal the details of the local structure is limited due to the fact that *all* pair correlations contribute to the signal making its interpretation more difficult. XAFS measures *partial* pair and three body correlations (only those including the central atom) and therefore, coupled with polarization dependent measurements, results in a highly sensitive measurement of the local atomic environment. This allowed us to reveal, among others, that the dopant and temperature induced phase transitions are of different nature. The Sr-induced transition at low temperature has both displacive and order-disorder components; i.e., the CuO_6 octahedra’s tilt angle initially decreases with Sr content up to $x \sim 0.15$ after which the local tilt angle stops changing. As the phase boundary is approached ($x \sim 0.21$ at $T=10\text{K}$) the CuO_6 octahedra become disordered relative to each other to result in the long range averaged zero tilt angle measured by diffraction. The LTO-like tilts persist well above the LTO to HTT boundary.

On the other hand the temperature-induced phase transition is purely of order-disorder character, i.e., the local tilt angle remains constant throughout the whole temperature range measured here (10K-300K) even though the structural phase transition is completed at $T \sim 200\text{K}$. The difference in the local and long range averaged structures implicitly requires the existence of a new structural length scale, i.e., the correlation length of CuO_6 octahedra tilts, ζ_{tilts} . Below about $x \approx 0.15$ and $T \approx 100\text{K}$ the short range order is the same as the long range order and therefore ζ_{tilts} is several hundred angstroms. For higher x and T local LTO tilts persist but become uncorrelated outside ζ_{tilts} to give rise to the long range averaged HTT phase; i.e., ζ_{tilts} decreases as the phase boundary is approached. Only a lower limit for the correlation length of tilts can be obtained from the XAFS measurement, as no indication of disorder was found in the $5 - 10 \text{ \AA}$ cluster probed by the photoelectron in the XAFS

regime. The extent of the correlations can be obtained by techniques sensitive to the intermediate range order ($10 - 30 \text{ \AA}$) in the atomic arrangement, such as PDF analysis of neutron scattering data. [52] A detailed picture of how the Sr and T-induced disorder arise cannot be obtained from the XAFS measurements alone and requires information on a longer length scale. Some statements, however, can be made. Sr induced disorder at low temperature must be quasi-static, as the temperature required to activate thermal fluctuations of the CuO_6 octahedra among equivalent minima of the energy surface is estimated at about 120K (potential barrier $\sim 10 \text{ meV}$) [66]. Evidence for static disorder introduced with Sr was found from the Sr K edge studies performed here, indicating that local distortions associated with Sr are responsible for the loss of periodicity in the tilt arrangement of the CuO_6 octahedra. Temperature induced disorder is most likely dynamic, with the CuO_6 octahedra fluctuating between equivalent minima of the energy surface. Since the time scale for such thermally induced hopping is no faster than the lattice times ($\tau_{\text{latt}} \approx 10^{-13} \text{ sec}$) and therefore much slower than the XAFS time scale ($\tau_{\text{XAFS}} \approx 10^{-16} \text{ sec}$), XAFS will measure the instantaneous tilt configuration corresponding to one of the equivalent minima. It should be noted that XAFS cannot distinguish between dynamic and static disorder.

Irrespective of the mechanism of disorder, its presence could have profound implications on the properties of these cuprates. Sr induced disorder at low temperature was found to be significant above about $x \sim 0.15$. This is the “overdoped” regime for which T_c decreases with Sr content. Since the relevant length scale for superconductivity is the intrinsic superconducting coherence length, $\zeta_{\text{SC}} \approx 10 - 20 \text{ \AA}$, if $\zeta_{\text{tilts}} \lesssim \zeta_{\text{SC}}$ the structural disorder is expected to affect the superconducting properties and could contribute to the decrease in T_c and eventual loss of superconductivity at high Sr content. Of course additional contributions to the decrease of T_c in the overdoped regime could come from changes in the chemical potential with Sr doping and related changes in the density of states at the Fermi level. Another important length scale is the instantaneous correlation length of the 2D antiferromagnetic (AF) spin fluctuations of the Cu^{+2} moments in the Cu-O planes, of about $\zeta_{\text{AF}} \approx 10 \text{ \AA}$. Short ranged, 2D AF fluctuations coexist with superconductivity in these cuprates. ζ_{AF} was found by inelastic neutron scattering to gradually decrease with Sr in $\text{La}_{2-x}\text{Sr}_x\text{CuO}_4$. [24] The introduction of disorder with Sr at distances larger than ζ_{tilts} , which itself decreases with Sr content as the distance between Sr atoms decreases, could significantly contribute to the decrease in correlation length of AF fluctuations of the Cu^{+2}

moments.

7.1.2 The $\text{La}_{2-x}\text{Ba}_x\text{CuO}_4$ system: temperature induced LTT \rightarrow LTO \rightarrow HTT structural phase transitions

Whereas a detailed investigation of the sequence of temperature -induced structural transformations in $\text{La}_{2-x}\text{Ba}_x\text{CuO}_4$ is still under way, enough evidence was found in the XAFS studies performed in this thesis in favor of a purely order-disorder mechanism for the transitions. Measurements at the La K -edge revealed that the *direction* of the CuO_6 octahedra local tilts does not change from $\langle 110 \rangle$ to $\langle 100 \rangle$ ($Bmab$ representation) at the LTT \rightarrow LTO transition, as determined in the crystallographic studies. The large rearrangement in La-O(2) planar distances that would result from such a change in tilt direction was not observed in our data. The La-O(2) distances can be successfully described assuming an LTT model for *all* temperatures measured here (10K-300K), even though the sample has undergone, when averaged over the long length scales measured by diffraction, two structural modifications. In addition, the tilt angle of the CuO_6 octahedra was measured directly using Cu K -edge data by exploiting the sensitivity of XAFS, via multiple scattering in nearly collinear paths, to three body correlations. In this way the buckling angle of Cu-O(1)-Cu and Cu-O(2)-La atomic configurations was measured and found to be nearly independent of temperature (10K-300K), indicating the existence of local octahedra tilts well above the LTO \rightarrow HTT phase boundary. Details on the method used here to determine the buckling angle, which differs somewhat from previously described ones, are given on appendix A and the results of such an analysis are described in more detail below in this section.

The results here are in agreement with self consistent local density functional approximation (LDA) calculations of the energy surface of $\text{La}_{2-x}\text{Ba}_x\text{CuO}_4$ which show that the LTT modification is the lowest energy configuration (at $T=0\text{K}$) and that the HTT structure is a local *maximum* of the energy surface (at $T=0\text{K}$). [66] The XAFS results here of the HTT phase support the picture in which the shape of the potential at high temperature (300K) is similar to that found in the LDA calculations at $T=0\text{K}$; i.e., a four-well potential with four equivalent LTT minima with the HTT phase corresponding to a local maximum of the energy surface. Preferential occupation of two sites would result in the LTO phase measured by diffraction whereas random occupation of the four sites will result in the average HTT phase. The

preferential occupation of two sites at intermediate temperatures can not be predicted by the $T=0\text{K}$ calculation as that would require including entropy contributions due to partial disordering of the LTT domains together with correlation energy due to the interaction between domains, i.e., at intermediate temperatures a compromise is obtained between entropy contribution to the free energy (disorder) and interaction between domains that would tend to preserve some degree of ordering (elastic energy) particularly in these structures for which the CuO_6 octahedra are coupled by their vertexes. The thermally activated disorder of tilts together with the long range averaged tilt direction obtained from spatial superposition of local tilts (bold arrows) are schematically represented in fig. 7.1. For simplicity the LTT phase is represented with all CuO_6 octahedra tilted in the same direction whereas in the actual LTT structure neighboring octahedra tilt in opposite directions and the tilt axis changes from $\langle 110 \rangle$ to $\langle -110 \rangle$ in going from $z = 0$ to $z = 0.5$ (unit cell units) along the \hat{c} -axis of the unit cell.

The existence of local LTT tilts of the CuO_6 octahedra in the average LTO and HTT phases was previously noted in the PDF studies of Billinge *et. al.* [133] Our results are in qualitative agreement with this previous work but major quantitative differences exist between our findings here and the description of Billinge *et. al.* First we were able to measure the Ba local atomic environment and the La atomic environment *separately*, by tuning the x-ray energy to the absorption threshold of either specie. Since Ba substitutes at the La site with a relative concentration of only a few %, the PDF at the La/Ba-(O, Cu, La) distances is dominated by the La contribution, in addition to contributions from other pairs at about the same distances. The Ba XAFS revealed the presence of major structural distortions induced by Ba doping, which extend as far as 5 \AA from the Ba sites, essentially affecting the whole lattice for the $x = 0.125, 0.15$ doping levels measured here. Ba induced disorder is seen in the La and Cu XAFS and results, among others, in the LTT structural ground state at $T=10\text{K}$ having a considerable amount of static disorder. This can be seen, e.g., by the large static offsets required for several Cu-neighbors bonds in order to fit the temperature dependence of the vibrational component of the mean squared disorder to an Einstein model. It can also be seen directly on the La XAFS signal by comparing Ba doped samples to the Sr doped ones. The large internal disorder in the LTT ground state (the most important phase as it is the underlying structure in the superconducting regime) can also be seen in the measurement of the

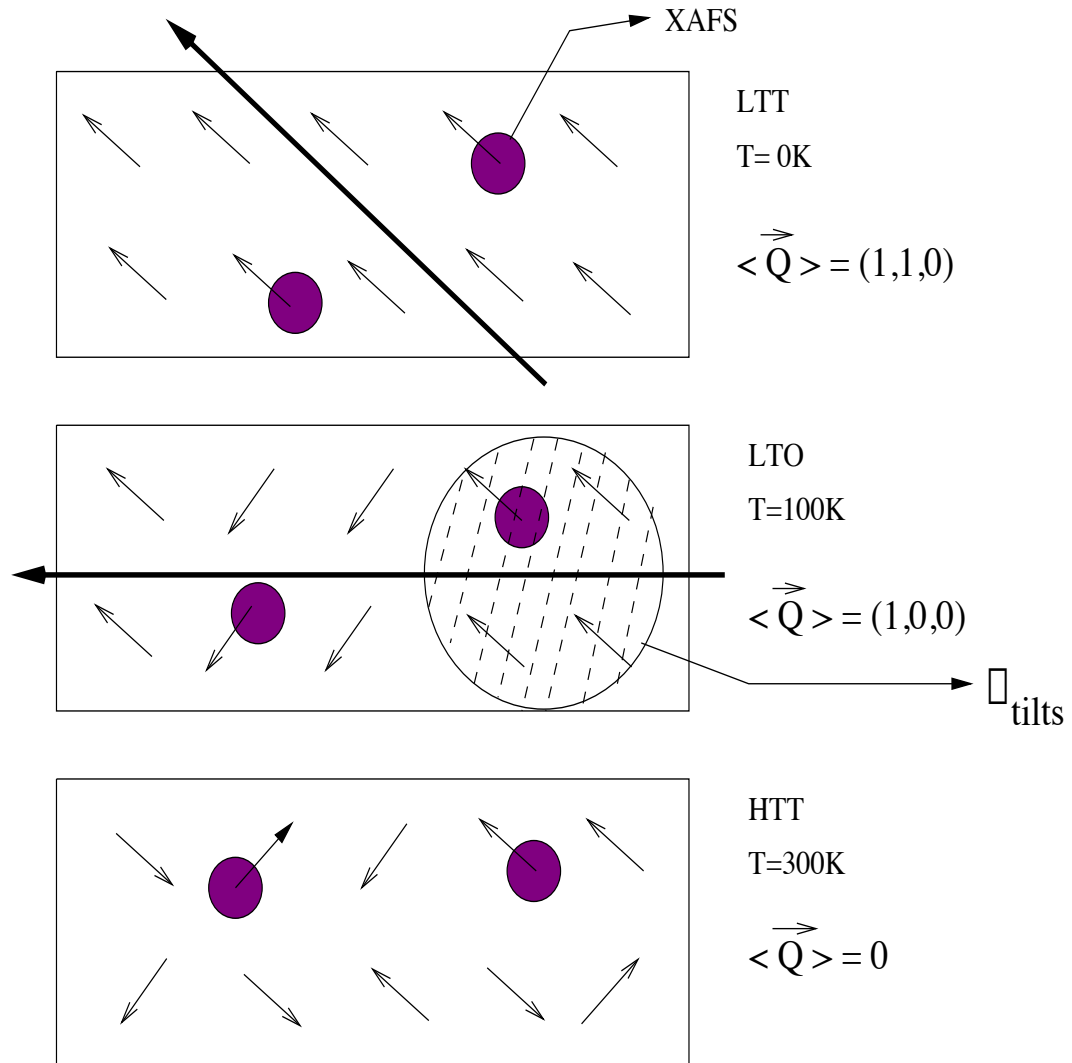


Figure 7.1: Schematic representation of thermally induced order-disorder structural phase transitions in $\text{La}_{2-x}\text{Ba}_x\text{CuO}_4$. The local tilts are LTT-like at all temperature and are ordered over a length scale ζ_{tilts} . The tilt direction obtained by averaging over long range is shown by the bold arrows. The XAFS length scale is indicated by the small circles and is about 5-10 Å.

Cu-O(1)-Cu and Cu-O(2)-La buckling angles. Our results revealed a local buckling angle, averaged over all Cu sites, about 2 times larger than the values determined in the diffraction and PDF studies; i.e., $\sqrt{\langle\theta^2\rangle} \approx 2\langle\theta\rangle$. This is consistent with the presence of large local atomic displacements from the average lattice positions, which are random as expected from random Ba substitution. Diffraction techniques determine the buckling angle from the long range, periodic component of the atomic positions. Since $\theta = \bar{\theta} + \delta\theta$ diffraction measures

$$\langle\theta\rangle = \langle\bar{\theta}\rangle + \langle\delta\theta\rangle = \bar{\theta} \quad (7.1)$$

since the deviation from the average buckling angle resulting from the random atomic displacements induced by Ba is also random and averages to zero. On the other hand XAFS measures the square of the buckling angle, averaged over all Cu central atoms; i.e.,

$$\langle\theta^2\rangle = \langle\bar{\theta}^2\rangle + \langle\delta\theta^2\rangle + \langle 2\bar{\theta}\delta\theta \rangle = \bar{\theta}^2 + \langle\delta\theta^2\rangle \quad (7.2)$$

The results here indicate that the root mean squared deviation in buckling angle is *larger* (by almost a factor of 2) than its average value, averaged over all central atoms. Even though the correspondence between the buckling angle measured here and the tilt angle is not completely transparent, due to small displacements of the end atoms (Cu, La) contributing to the measurement of the buckling angle in addition to the large contributions of the intervening O(1) and O(2) atoms, it is clear that the concept of a unique, single valued tilt angle of the CuO_6 in $\text{La}_{2-x}\text{Ba}_x\text{CuO}_4$ is ill defined and a very broad distribution of angles is present locally.

The significant amount of disorder present in the structural ground state of $\text{La}_{2-x}\text{Ba}_x\text{CuO}_4$ is the most likely reason for the anomalously broad diffraction peaks observed in the LTT phase of this system. [49] In addition, a disordered LTT phase could explain the lower maximum T_c 's attainable in the $\text{La}_{2-x}\text{Ba}_x\text{CuO}_4$ system (30K) compared to the $\text{La}_{2-x}\text{Sr}_x\text{CuO}_4$ system ($T=40\text{K}$) for which structural disorder was found here to be small in the underdoped and optimally doped samples.

7.2 On the nature of local distortions around (Sr, Ba) dopant atoms

A significant part of this thesis has been devoted to the study of the local atomic environment around the dopant atoms and its implications for the dopant induced

changes in structural, electronic and magnetic properties of these cuprates. XAFS has the great advantage of being able to tune to the dopant atoms and isolate their contribution from the majority La atoms. This, coupled with the polarization dependent measurements, enabled us to quantitatively determine, for the first time, the effect of (Sr, Ba) substitution on the local structure. As an example, we were able to show that, contrary to previous assertions [55], the O(2) apical oxygen to Sr is fully occupied.

Whereas we found that both dopant atoms induce large local distortions in their immediate atomic surroundings, the nature of these distortions differ significantly for both types of ions. Local atomic displacements nearby Ba ions, even though quite anisotropic, are well represented by an overall lattice expansion, with the strain field extending at least up to about 5 \AA from the Ba ions. This is consistent with the much larger ionic radius of the Ba^{+2} ion (1.35 \AA) compared to that of the La^{+3} ion (1.15 \AA) for which it substitutes in the lattice. The distortions around the Sr^{+2} ions (1.13 \AA ionic radius), however, cannot be attributed to a size effect as, e.g., some O(1) oxygen atoms distort to get closer to Sr while others get further away from it. Even more significant is the finding here of a double site configuration for the O(2) apical oxygen to Sr with the two sites separated by about 0.3 \AA , indicating charge redistribution effects are at the basis of the Sr induced lattice distortions. No anomalies were found in the La-O(2) apical distances indicating the dopant induced holes have a large amplitude at the position of the dopant atoms. The hole donated by the Sr together with its associated lattice distortions is therefore a polaron. Its existence and prominent concentration dependence, as discussed below, is neglected in all current theories of high T_c superconductivity as well in attempts to explain the unusual normal state transport properties of these cuprates. As an example, the large concentration dependence observed for the two site configuration, the site closer to the Cu-O planes becoming predominant at high x , could relate well to the increase in \hat{c} -axis conductivity with Sr to become metallic-like for $x \gtrsim 0.2 - 0.25$. [30, 32]

7.2.1 *Polaronic nature of the Sr induced holes in $\text{La}_{2-x}\text{Sr}_x\text{CuO}_4$*

The strong concentration dependence found here for the relative occupancy of the O(2) apical-to-Sr double site configuration cannot be explained by changes in the potential at one Sr site resulting from the introduction of additional Sr atoms (interaction between Sr atoms), as very significant changes were found between $x = 0.075$

and $x = 0.15$ (3.75% and 7.5 %, respectively) even though the Sr atoms are quite dilute at these concentrations. On the other hand a strong concentration dependence of the *ratio* of Sr induced holes with O(2) $2p_z$ -Cu $3d_{3z^2-r^2}$ and O(1) $2p_{x,y}$ -Cu $3d_{x^2-y^2}$ orbital character, respectively, is found in polarized XANES studies [25, 26], the dopant induced holes with O(2) $2p_z$ -Cu $3d_{3z^2-r^2}$ character becoming predominant at high Sr content. A one to one correspondence between the two O(2) apical sites next to Sr observed here and the two different types of holes found in the XANES studies is proposed by Polinger *et. al* [149], in which each type of hole induces either an enhanced Jahn Teller (EJT) distortion or an anti Jahn Teller (AJT) distortion of the CuO_6 octahedra containing the O(2) apical to Sr and therefore the one affected the most by charge redistribution (the hole is peaked around the Sr). A schematic representation of the two JT polaronic distortions related to each type of hole is shown in fig. 7.2.

The lack of a measurable temperature dependence in the occupancy of the two sites found by XAFS indicates that the electronic states associated with each type of hole corresponding to each of the two sites are not discrete but rather broader than $k_B T$ (up to $T=300\text{K}$). Otherwise the relative occupation of the two sites would be expected to follow a Boltzmann distribution $e^{-\Delta E/K_B T}$, with ΔE the energy difference between the two hole states, which was not observed. This is consistent with each type of hole belonging to an electronic *band* in the solid. Whether the presence of the aforementioned JT polarons introduced with Sr is related to the mechanism of pairing is not clear at present and would require further investigation.

The possibility of the existence of a double site for the O(2) apical oxygen to Ba in $\text{La}_{2-x}\text{Ba}_x\text{CuO}_4$ was explored for both $x = 0.125$ and $x = 0.15$ samples measured here. Whereas the fits to the 10K isolated Ba-O(2) apical signal could be improved with a 2 site configuration with relative occupancies of (79(4)%, 21(4)%), (81(4)%, 19(4)%) for the (AJT, EJT) sites for $x = 0.125$, $x = 0.15$, respectively, in quite good agreement with the Sr results at similar concentrations shown in fig. 5.34, a single site model better described the Ba-O(2) signal at $T=140\text{K}$, 300K . A reasonable temperature dependence is obtained for the σ^2 in the isolated Ba-O(2) distance if a single site model is assumed for 10, 140 and 300K. This is different than the behavior observed in the Sr-doped case, where the occupation of the two sites was found to be nearly temperature-independent with the two sites model resulting in large fit improvements at all temperatures studied. Therefore, for the two values of x studied

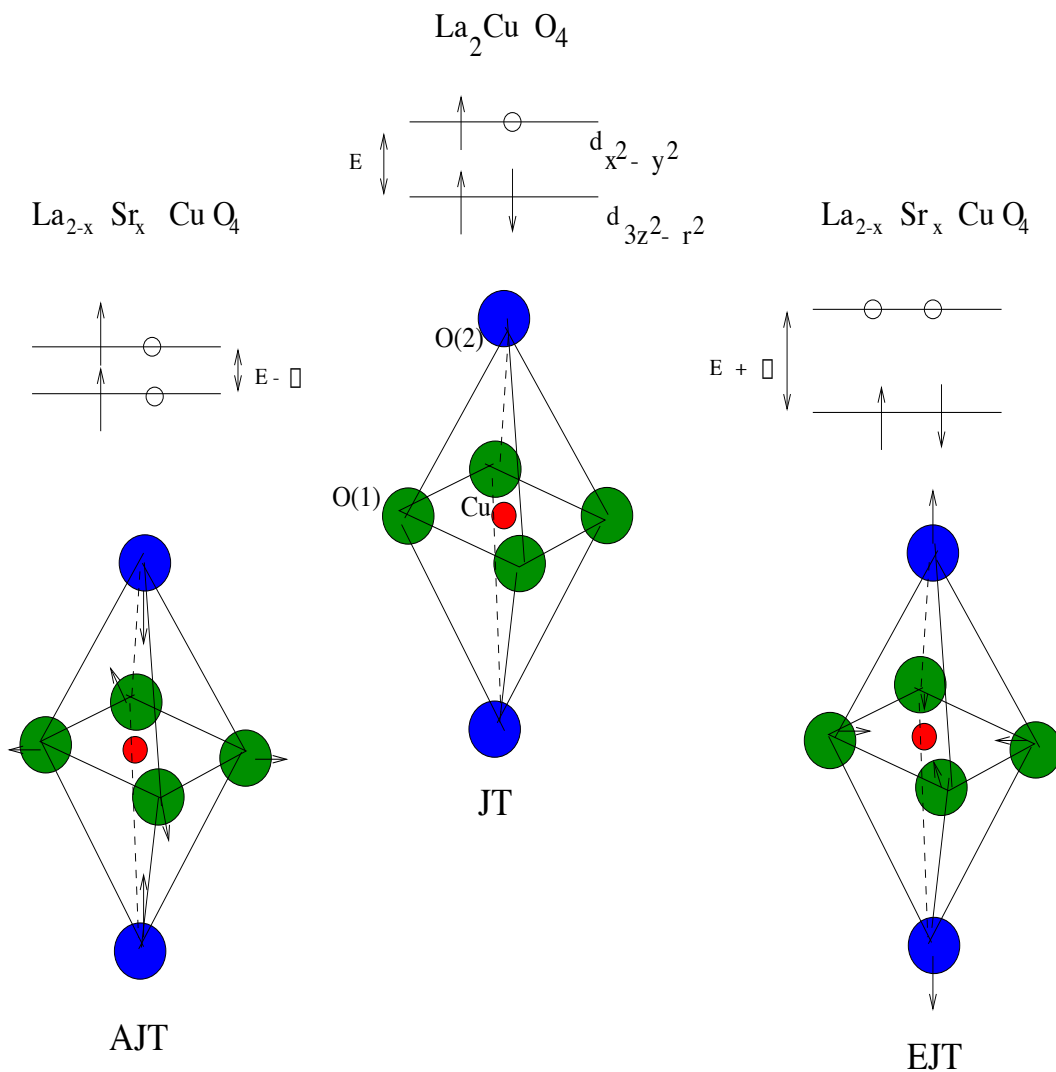


Figure 7.2: Schematic representation of Jahn Teller polarons induced by Sr doping of holes into molecular orbitals with different character. The CuO_6 octahedra for $x = 0$ is JT distorted; each type of hole introduces an enhanced JT distortion (EJT) or anti JT distortion (AJT), respectively, resulting in the two O(2) apical sites observed about the Sr sites. At high Sr content the AJT polarons become dominant, consistent with the XANES measurements [25,26] and the predominant occupancy of the long Sr-O(2) distance (short Cu-O(2) distance) found by XAFS.

here for $\text{La}_{2-x}\text{Ba}_x\text{CuO}_4$, no significant evidence in favor of two sites is found. Further measurements on $\text{La}_{2-x}\text{Ba}_x\text{CuO}_4$ at lower values of x , where the two site configuration is more evident in the Sr-doped system (fig. 5.34), are required to make a definitive conclusion.

Whether the prominent appearance of out-of-plane $O(2) 2p_z$ -Cu $3d_{3z^2-r^2}$ dopant induced holes, as evident from the XANES studies [25,26] and the predominant population of AJT sites found by XAFS at high x , is favorable or detrimental for the mechanism of pairing leading to the high T_c 's is not clear at this point, as the role that holes with out of plane orbital character play in determining the superconducting properties is yet an open question. What is clear is that the doped holes have not only in-plane orbital character but a significant fraction of them are doped into out-of-plane orbitals, which become dominant at high x . Theories that rely on single band effective Hamiltonians involving only in-plane Cu $3d_{x^2-y^2}$, $O(1) 2p_{x,y}$ orbital character for the doped holes are including only a minority of the donated holes and their conclusions must be viewed with caution. Even if the out-of-plane character of the doped holes has a detrimental effect on superconductivity, its prominent appearance with Sr doping has to be accounted for in explaining the superconducting and normal state properties as a function of x . Moreover, a recent paper by P. W. Anderson [154] cites experimental evidence for his theory of high T_c superconductivity in $\text{La}_{2-x}\text{Sr}_x\text{CuO}_4$ which postulates that superconductivity is produced by interlayer coupling of Cu-O planes through coherent pair tunneling which places the $O(2) 2p_z$ -Cu $3d_{3z^2-r^2}$ states in the forefront of importance for understanding superconductivity.

7.2.2 *On the effect of (Sr, Ba) distortions on the magnetic properties*

Both Sr and Ba doping introduce significant distortions in neighboring Cu-O planes resulting in the loss of periodicity in their atomic arrangement. These distortions result in increased buckling of the Cu-O planes around the dopant atoms, which could affect the spin dynamics of the Cu^{+2} moments. Doping La_2CuO_4 with (Sr, Ba) results in loss of 3D AF order, but short range 2D AF spin fluctuations of the Cu^{+2} moments persists in the Cu-O planes in the superconducting regime. Marked differences have been found in the magnetic dynamics of the doped systems when compared to the parent compound, which go beyond a decrease in the instantaneous correlation length of the AF fluctuations with Sr doping [24], e.g., spin wave damping/softening with Ba-doping. [23] Knowledge of the local distortions of the Cu-O

planes induced with doping, as detailed in this thesis, should help clarify the causes of the changes induced with doping on the spectrum of magnetic excitations. Obviously the addition of extrinsic holes into the Cu-O planes with significant weight on the O(1) atoms bridging the Cu atoms [27] is the major contribution to the loss in AF long range order at low x . [28] However, understanding the magnetic dynamics at higher values of x in the superconducting regime, including differentiating between spin wave softening (reduction in spin-wave velocity, which implies a reduction in the AF exchange coupling constant J) and spin-wave damping (energy broadening due, e.g., disorder) [23] might require accounting for the structural disorder of the Cu-O planes found here, whose effect increases with doping.

7.3 On the origin of T_c suppression in $\text{La}_{2-x}\text{Ba}_x\text{CuO}_4$ with $x = 0.125$

A direct comparison of the local structures of $x = 0.125$ and $x = 0.15$ $\text{La}_{2-x}\text{Ba}_x\text{CuO}_4$ samples revealed no significant differences between the two, despite superconductivity being strongly suppressed for $x = 0.125$ (fig. 4.11). Our measurements at the Cu K -edge put an upper limit of $\Delta r \lesssim 0.005 \text{ \AA}$ for the differences between both samples in Cu interatomic distances up to its fifth neighboring shell of atoms. This imposes severe limitations on models that invoke charge density wave (CDW) formation due to a commensurability effect at $x = 1/8$ at the basis of T_c suppression, as it constrains the size of attendant atomic displacements of such a CDW to below the value mentioned above. Whereas the existence of a CDW was postulated in $\text{La}_2\text{NiO}_{4.125}$ [72] and in $\text{La}_{1.48}\text{Nd}_{0.4}\text{Sr}_{0.12}\text{CuO}_4$ [71] based on the observation of superstructure reflections in neutron diffraction, a CDW was never observed in $\text{La}_{1.875}\text{Ba}_{0.125}\text{CuO}_4$. It is currently argued [72, 155] that charged stripes could exist in $\text{La}_{1.875}\text{Ba}_{0.125}\text{CuO}_4$ but are dynamic in nature and therefore fail to order and are not visible in the neutron studies.

It is important to emphasize that even if the CDW is dynamic, its presence would result in instantaneous local atomic displacements which, when averaged over all central atoms, should result in increases in the σ^2 values measured by XAFS. From our measurements, the difference between $x = 0.125$ and 0.15 in mean square disorder at 10K in the planar Cu-O(1) distances which should be affected the most by the postulated charge modulations, is of about $\Delta\sigma^2 \lesssim 3(3) \times 10^{-4} \text{ \AA}^2$. Whereas this result cannot rule out a CDW as the electronic ground state of $\text{La}_{1.875}\text{Ba}_{0.125}\text{CuO}_4$, models invoking its presence should be consistent with the upper limits imposed by

XAFS on the extent of the lattice modulation associated with the postulated ordering of doped charges.

A density of states (DOS) effect, in which the Van Hove singularity (VHS) near E_F is split by the appearance of the LTT long range order therefore reducing the DOS at the Fermi level has been postulated based on LDA electronic structure calculations. [66] The validity of this mechanism has been questioned [73] due to the ~ 2 times larger magnitude of the CuO_6 octahedra LTT tilts used in the LDA calculations as compared to the tilt angle values measured by diffraction techniques. Our direct XAFS measurements of the buckling angles in Cu-O(1)-Cu and Cu-O(2)-La three-body configurations, which involves the aforementioned octahedra tilts, reveal that large, random, deviations from the average tilt angle exist at a *local* level, with the width of the tilt angle distribution (one σ assuming a Gaussian distribution) being ~ 2 times *larger* than its average value. A single valued magnitude of the tilt angle in $\text{La}_{2-x}\text{Ba}_x\text{CuO}_4$ cannot describe the highly disorder LTT structural ground state since large local deviations in tilt angle exist across the structure. The factor of 2 larger tilt angle used in the LDA calculations is not unreasonable for some octahedra, as that corresponds to half a standard deviation in the tilt angle distribution. The LDA calculations, however, are based on a periodic structure with a single valued tilt angle, which is certainly not the case in $\text{La}_{2-x}\text{Ba}_x\text{CuO}_4$. Whereas more sophisticated calculations are required to mimic the effect of random Ba substitution and the distribution of tilt angles associated with it, the XAFS results clearly demonstrate that a DOS effect cannot yet be ruled out as the mechanism for T_c suppression at $x = 0.125$, since even if the local structures of $x = 0.125$, $x = 0.15$ are the same, the change in doping could tune the Fermi level to the minimum of the split VHS for $x = 0.125$.

BIBLIOGRAPHY

- [1] J. G. Bednorz and K. A. Müller. *Z. Phys. B*, 64:189, 1986.
- [2] B. J. Jonsson, T. Turkki, V. Strom, Z. Igbal, and K. V. Rao. *Journal of Applied Physics*, 79:6583, 1996.
- [3] A. Fukuoka, A. Tokiwa-Yamamoto, M. Itoh, R. Usami, S. Adachi, and K. Tanabe. *Physical Review B*, 55:6612, 1997.
- [4] S. Kumari, A. K. Singh, and O. N. Srivastave. *Superconductor Science & Technology*, 10:235, 1997.
- [5] Z. Z. Sheng and A. M. Hermann. *Nature (London)*, 332:55, 1988.
- [6] R. M. Hazen, L. W. Finger, R. J. Angel, C. T. Perwitt, N. L. Ross, C. G. Hadidiacos, P. J. Heaney, D. R. Veblen, Z. Z. Sheng, A. El Ali, and A. M. Hermann. *Physical Review Letters*, 60:1657, 1988.
- [7] D. Pines. *Physica C*, 282-287:273, 1997.
- [8] V. J. Emery, S. A. Kivelson, and O. Zachar. *Physical Review B*, 56:6120, 1997.
- [9] P. W. Anderson. *Science*, 235:1196, 1987.
- [10] P. W. Anderson, G. Baskaran, Z. Zou, and T.Hsu. *Physical Review Letters*, 58:2790, 1987.
- [11] T.Barnes and M. D. Kovarik. *Physical Review B*, 42:6159, 1990.
- [12] L. F. Mattheiss. *Physical Review Letters*, 58:1028, 1987.
- [13] W. Weber. *Physical Review Letters*, 58:1371, 1987.

- [14] H. Kamimura, S. Matsuno, Y. Suwa, and H. Ushio. *Physical Review Letters*, 77:723, 1996.
- [15] H. Kamimura. *Japanese Journal of Applied Physics*, 26:L627, 1987.
- [16] H. Aoki and H. Kamimura. *Solid State Communications*, 63:665, 187.
- [17] M. Suzuki and M. Hikita. *Japanese Journal of Applied Physics*, 28:1368, 1989.
- [18] H. Ding, M. R. Norman, J. C. Campuzano, M. Randeria, A. F. Bellman, T. Yokoya, T. Takahashi, T. Mochiku, and K. Kadowaki. *Physical Review B*, 54:R9678, 1996.
- [19] D. Haskel, E. A. Stern, D. G. Hinks, A. W. Mitchell, J. D. Jorgensen, and J. I. Budnick. *Physical Review Letters*, 76:439, 1996.
- [20] P. G. Radaelli, D. G. Hinks, A. W. Mitchell, B. A. Hunter, J. L. Wagner, B. Dabrowski, K. G. Vandervoort, H. K. Viswanathan, and J. D. Jorgensen. *Physical Review B*, 49(6):4163–4175, 1994.
- [21] D. Haskel, E. A. Stern, D. G. Hinks, A. W. Mitchell, and J. D. Jorgensen. *Physical Review B*, 56:R521, 1997.
- [22] Y. Endoh, K. Yamada, R. J. Birgeneau, D. R. Gabbe, H. P. Jenssen, M. A. Kastner, C. J. Peters, P. J. Picone, T. R. Thurston, J. M. Tranquada, G. Shirane, Y. Hidaka, M. Oda, Y. Enomoto, M. Suzuki, and T. Murakami. *Physical Review B*, 37(13):7443, 1988.
- [23] G. Aeppli, S. M. Hayden, H. A. Mook, Z. Fisk, S-W. Cheong, D. Rytz, J. P. Remika, G. P. Espinosa, and A. S. Cooper. *Physical Review Letters*, 62(17):2052, 1989.
- [24] R. J. Birgeneau, D. R. Gabbe, H. P. Jenssen, M. A. Kastner, P. J. Picone, T. R. Thurston, G. Shirane, Y. Endoh, M. Sato, K. Yamada, Y. Hidaka, M. Oda, Y. Enomoto, M. Suzuki, and T. Murakami. *Physical Review B*, 38(10):6614, 1988.

- [25] C. T. Chen, L. H. Tjeng, J. Kwo, H. L. Kao, P. Rudolf, F. Sette, and R. M. Fleming. *Physical Review Letters*, 68(16):2543, 1992.
- [26] E. Pellegrin, N. Nücker, J. Fink, S. L. Molodstov, A. Gutierrez, E. Navas, O. Strebel, Z. Hu, M. Domke, G. Kaindl, S. Uchida, Y. Nakamura, J. Markl, M. Klauda, G. Saemann-Ischenko, A. Krol, J. L. Peng, Z. Y. Li, and R. L. Greene. *Physical Review B*, 47(6):3354, 1993.
- [27] J. B. Grant and A. K. McMahan. *Physical Review Letters*, 66:488, 1991.
- [28] A. Aharony, R. J. Birgeneau, A. Coniglio, M. A. Kastner, and H. E. Stanley. *Physical Review Letters*, 60(13):130, 1988.
- [29] B. Ellman, H. M. Haeger, D. P. Katz, T. F. Rosenbaum, A. S. Cooper, and G. P. Espinosa. *prb*, 39:9012, 1989.
- [30] Y. Nakamura and S. Uchida. *Physical Review B*, 47:8369, 1993.
- [31] S. Kambe, K. Kitazawa, M. Naito, A. Fukuoka, I. Tanaka, and H. Kojima. *Physica C*, 160:35, 1989.
- [32] S. Sreedhar and P. Ganguly. *Physical Review B*, 41:371, 1990.
- [33] M. Braden, P. Schweiss, G. Heger, W. Reichardt, Z. Fisk, K. Gamayunov, I. Tanaka, and H. Kojima. *Physica C*, 223:396, 1994.
- [34] V. B. Grande, H.K. Muller-Buscbaum, and M. Schweizer. *Z. anorg. allg. chem.*, 428:120, 1977.
- [35] R. D. Shannon. *Acta Crystallogr.*, A 32:751, 1976.
- [36] K. K. Singh, P. Ganguly, and J. B. Goodenough. *J. Solid State Chem.*, 52:254, 1984.
- [37] W. E. Pickett. *Rev. Mod. Phys.*, 61:433, 1989.
- [38] S. Sugano, Y. Tanabe, and H. Kamimura. *Multiplets of Transition-Metal Ions in Crystals*. Academic Press, New York and London, 1970.

- [39] J. Rodriguez-Carvajal, M. T. Fernandez-Diaz, and J. L. Martinez. *J. Phys.: Condens. Matter*, 3:3215, 1991.
- [40] H. A. Jahn and E. Teller. *Proc. R. Soc. London, Ser. A*, 161:220, 1937.
- [41] E. Teller. *Physica A*, 114:14, 1982.
- [42] *Multiplets of Transition-Metal Ions in Crystals*. Academic Press, New York and London, 1970.
- [43] H. Takagi, R. J. Cava, M. Marezio, B. Batlogg, J. J. Krajewski, W. F. Peck Jr., P. Bordet, and D. E. Cox. *Physical Review Letters*, 68:3777, 1992.
- [44] J. B. Torrance, A. Bezing, A. I. Nazzari, T. C. Huang, S. S. P. Parkin, D. T. Keane, S. J. LaPlaca, P. M. Horn, and G. A. Held. *Physical Review B*, 40:8872, 1989.
- [45] T. Nagano, Y. Tomioka, Y. Nakayama, K. Kishio, and K. Kitazawa. *Physical Review B*, 48:9689–9696, 1993.
- [46] J. D. Jorgensen, D. G. Hinks, B. A. Hunter, R. L. Hitterman, A. W. Mitchell, P. G. Radaelli, B. Dabrowski, J. L. Wagner, H. Takahashi, and E. C. Larson. In Y. Bar-Yam, T. Egami, J. Mustre de Leon, and A. R. Bishop, editors, *Lattice Effects in High T_c Superconductors*, page 84, Singapore-New Jersey, 1992. World Scientific.
- [47] N. Yamada and M. Ido. *Physica C*, 203:240, 1992.
- [48] B. Dabrowski, Z. Wang, K. Rogacki, J. D. Jorgensen, R. L. Hitterman, J. L. Wagner, B. A. Hunter, P. G. Radaelli, and D. G. Hinks. *Physical Review Letters*, 76:1348, 1996.
- [49] J. D. Axe, A. H. Moudden, D. Hohlwein, D. E. Cox, K. M. Mohanty, A. R. Moodenbaugh, and Y. Xu. *Physical Review Letters*, 62:2751, 1989.
- [50] T. Egami, W. Dmowski, J. D. Jorgensen, D. G. Hinks, D. W. Capone, C. U. Segre, and K. Zhang. *Reviews of Solid State Science*, 1(2):247–257, 1987.

- [51] T. R. Sendyka, T. Egami, B. A. Hunter, J. D. Jorgensen, D. G. Hinks, and A. W. Mitchell. In Y. Bar Yam, T. Egami, J. Mustre de Leon, and A. R. Bishop, editors, *Lattice Effects in High- T_c Superconductors*, pages 111–117, Santa Fe, New Mexico, 1992. World Scientific.
- [52] S. J. L. Billinge and T. Egami. *Physical Review B*, 47(21):14386, 1993.
- [53] E. D. Isaacs, G. Aeppli, P. Zschack, S-W. Cheong, H. Williams, and D. J. Buttry. *Physical Review Letters*, 72:3421, 1994.
- [54] W. Dmowski, R. J. McQueeney, T. Egami, Y. P. Feng, S. K. Sinha, T. Hinatsu, and S. Uchida. *Physical Review B*, 52(9):6829, 1995.
- [55] Z. Tan, M. E. Filipkowski, J. I. Budnick, E. K. Heller, D. L. Brewes, B. L. Chamberland, C. E. Bouldin, J. C. Woicik, and D. Shi. *Physical Review Letters*, 64:2715, 1990.
- [56] J. D. Jorgensen, B. Dabrowski, S. Pei, D. R. Richards, and D. G. Hinks. *Physical Review B*, 40:2187, 1989.
- [57] Z. Y. Wu, C. R. Natoli, and M. Benfatto. *Physica B*, 208&209:491, 1995.
- [58] K. Yoshimura, T. Imai, T. Shimizu, Y. Ueda, K. Kosuge, and H. Yasuoka. *Journal of the Physical Society of Japan*, 58:3057, 1989.
- [59] P. C. Hammel, A. P. Reyes, S. W. Cheong, Z. Fisk, and J. E. Schirber. *Physical Review Letters*, 71:440, 1993.
- [60] T. Suzuki and T. Fujita. *Physica C*, 159:111, 1989.
- [61] A. R. Moodenbaugh, Y. Xu, M. Suenaga, T. J. Folkerts, and R. N. Shelton. *Physical Review B*, 38:4596, 1988.
- [62] M. Sera, Y. Ando, S. Kondoh, K. Fukuda, M. Sato, I. Watanabe, S. Nakashima, and K. Kumagai. *Solid State Communications*, 69:851, 1989.
- [63] S. Barisic and J. Zelenko. *Solid State Communications*, 74:367, 1990.

- [64] Y. Maeno, A. Odagawa, N. Kakehi, T. Suzuki, and T. Fujita. *Physica C*, 173:322, 1991.
- [65] S. Katano, Y. Ueda, A. Hayashi, and N. Môri. *Physica B*, 213&214:81, 1995.
- [66] W. E. Pickett, R. E. Cohen, and H. Krakauer. *Physical Review Letters*, 67:228, 1991.
- [67] S. J. L. Billinge, G. H. Kwei, A. C. Lawson, J. D. Thompson, and H. Takagi. *Physical Review Letters*, 71:1903, 1993.
- [68] S. Katano, S. Funahashi, N. Môri, Y. Ueda, and J. A. Fernandez-Baca. *Physical Review B*, 48:6569, 1993.
- [69] R. E. Peierls. *Ann. Phys. Leipzig*, 4:121, 1930.
- [70] R. E. Thorne. Charge density wave conductors. *Physics Today*, MAY(:):42, 1996.
- [71] J. M. Tranquada, B. J. Sternlieb, J. D. Axe, Y. Nakamura, and S. Uchida. *Nature*, 375:561, 1995.
- [72] J. M. Tranquada, D. J. Buttrey, V. Sachan, and J. E. Lorenzo. *Physical Review Letters*, 73:1003, 1994.
- [73] M. R. Norman, G. J. McMullan, D. L. Novikov, and A. J. Freeman. *Physical Review B*, 48:9935, 1993.
- [74] S. Katano, J. A. Fernandez-Baca, S. Funahashi, N. Môri, Y. Ueda, and K. Koga. *Physica C*, 214:64, 1993.
- [75] E. Takayama-Muromachi, F. Izumi, and T. Kamiyama. *Physica C*, 215:329, 1993.
- [76] Y. Zhu, A. R. Moodenbaugh, Z. X. Cai, J. Taftø, M. Suenaga, and D. O. Welch. *Physical Review Letters*, 73:3026, 1994.

- [77] E. A. Stern. *Physical Review B*, 10:3027, 1974.
- [78] P. A. Lee and J. B. Pendry. *Physical Review B*, 11:2795, 1975.
- [79] J. J. Rehr and R. C. Albers. *Physical Review B*, 41:8139, 1990.
- [80] J. J. Rehr, R. C. Albers, C. R. Natoli, and E. A. Stern. *Physical Review B*, 34:4350, 1986.
- [81] J. J. Rehr, J. Mustre de Leon, S. I. Zabinsky, and R. C. Albers. Theoretical x-ray absorption fine structure standards. *Journal of the American Chemical Society*, 113(14):5135–5140, 1991.
- [82] J. Mustre de Leon, J. J. Rehr, and S. I. Zabinsky. *Ab initio* curved-wave x-ray-absorption fine structure. *Physical Review B*, 44(9):4146–4156, 1991.
- [83] J. J. Rehr, R. C. Albers, and S. I. Zabinsky. *Physical Review Letters*, 69(23):3397, 1992.
- [84] S. I. Zabinsky, J. J. Rehr, A. Ankudinov, R. C. Albers, and M. J. Eller. *Physical Review B*, 52:2995, 1995.
- [85] A. Ankudinov and J. J. Rehr. *Physical Review B*, 51(2):1282, 1995.
- [86] J. J. Sakurai. *Advanced Quantum Mechanics*. Addison-Wesley, 1967.
- [87] Olavi Keski-Rahkonen and Manfred O. Krause. *Atomic Data and Nuclear Data Tables*, 14:139, 1974.
- [88] L. I. Schiff. *Quantum Mechanics*. McGraw-Hill Book Company, Singapore, 1988.
- [89] B. K. Teo and P. A. Lee. *Journal of the American Chemical Society*, 101:2815, 1979.
- [90] E. A. Stern and S. M. Heald. *Basic Principles and Applications of EXAFS*, chapter 10, pages 979–980. North-Holland, New York, 1983.

- [91] J. J. Rehr, E. A. Stern, R. L. Martin, and E. R. Davidson. *Physical Review B*, 17(3):560, 1978.
- [92] E. A. Stern. *Theory of EXAFS*, pages 3–51. John-Wiley & sons, 1988.
- [93] A. Frenkel, E. A. Stern, A. Voronel, M. Qian, and M. Newville. *Physical Review B*, 49(17):11662, 1994.
- [94] A. Frenkel, E. A. Stern, A. Voronel, M. Qian, and M. Newville. *Physical Review Letters*, 71:3485, 1993.
- [95] E. A. Stern, M. Newville, B. Ravel, Y. Yacoby, and D. Haskel. *Physica B*, 208&209:117, 1995.
- [96] M. Newville, P. Līviņš, Y. Yacoby, J. J. Rehr, and E. A. Stern. *Physical Review B*, 47(21):14126, 1993.
- [97] B. Ravel. ATOMS: Crystallography and XAFS. This documentation is part of the UWXAFS3.0 package.
- [98] B. Ravel. Ph. D Thesis, University of Washington 1997.
- [99] M. Newville. FEFFIT: Using FEFF to model XAFS in R-space. This documentation is part of the UWXAFS3.0 package.
- [100] M. Newville, B. Ravel, D. Haskel, J. J. Rehr, E. A. Stern, and Y. Yacoby. *Physica B*, 208&209:154, 1995.
- [101] J. J. Rehr, C. H. Booth, F. Bridges, and S. I. Zabinsky. *Physical Review B*, 49(17):12347, 1994.
- [102] E. A. Stern. *Physical Review B*, 48(13):9825, 1993.
- [103] W. H. McMaster, N. Kerr-Del Grande, J. H. Mallett, and J. H. Hubbell. *Compilation of X-ray Cross Sections. Lawrence Radiation Laboratory Report UCRL-50174*. National Bureau of Standards, Springfield, VA, 1969.

- [104] G. Bunker. *Nuclear Instruments and Methods*, 207:437, 1983.
- [105] E. A. Stern, Y. Ma, and O. Hanske-Petitpierre. *Physical Review B*, 46(2):687, 1992.
- [106] P. A. Lee and G. Beni. *Physical Review B*, 15:2862, 1977.
- [107] D. Haskel, B. Ravel, M. Newville, and E. A. Stern. *Physica B*, 208&209:151, 1995.
- [108] P. R. Bevington. *Data Reduction and Error Analysis for the Physical Sciences*. McGraw-Hill, New York, 1969.
- [109] T. M. Hayes and J. B. Boyce. *Extended X-Ray Absorption Fine Structure Spectroscopy*, volume 37 of *Solid State Physics*, pages 173–351. Academic Press, New York, 1982.
- [110] E. A. Stern and K. Kim. *Physical Review B*, 23:3781, 1981.
- [111] E. E. Koch, editor. *Handbook of Synchrotron Radiation*. North-Holland, New York, 1983.
- [112] Neil W. Ashcroft and N. David Mermin. *Solid State Physics*. Holt, Rinehart and Winston, 1976.
- [113] M. E. Rose and M. M. Shapiro. *Physical Review*, 74:1853, 1948.
- [114] A. Hofmann. *SSRL ACD-NOTE*, 38:1–55, 1986.
- [115] D. E. Farrell, B. S. Chandrasekhar, M. R. Deguire, M. M. Fang, V. G. Kogan, J. R. Clem, and D. K. Finnemore. *Physical Review B*, 36:4025, 1987.
- [116] V. G. Kogan. *Physical Review B*, 38:7049, 1988.
- [117] J. M. Tranquada, A. I. Goldman, A. R. Moodenbaugh, G. Shirane, S. K. Sinha, D. Vakin, and A. J. Jacobson. *prb*, 37:519, 1988.

- [118] K. Fukuda, S. Shamoto, M. Sato, and K. Oka. *Solid State Communications*, 65:1323, 1988.
- [119] J. D. Livingston, H. R. Hart, and W. P. Wolf. *Journal of Applied Physics*, 64:5806, 1988.
- [120] J. D. Jackson. *Classical Electrodynamics*. John Wiley & Sons, New York, 1975.
- [121] D. G. Hinks. Personal communication.
- [122] B. E. Warren. *X-ray Diffraction*. Addison-Wesley, New York, 1969.
- [123] G. Thomas and M. J. Goringe. *Transmission Electron Microscopy of Materials*. John Wiley & Sons, 1981.
- [124] A. R. Moodenbaugh, U. Wildgruber, Y. L. Wang, and Y. Xu. *Physica C*, 245:347, 1995.
- [125] B. Ravel. Personal communication.
- [126] J. D. Jorgensen, H. B. Schüttler, D. G. Hinks, D. W. Capone, K. Zhang, M. B. Brodsky, and D. J. Scalapino. *Physical Review Letters*, 58:1024, 1987.
- [127] C. Rial, E. Moran, M. A. Alario-Franco, U. Amador, and N. H. Andersen. *Physica C*, 270:51, 1996.
- [128] H. Scher and R. Zallen. *Journal of Chemical Physics*, 53:3759, 1970.
- [129] J. B. Boyce, F. Bridges, T. Claeson, T. H. Geballe, C. W. Chu, and J. M. Tarascon. *Physical Review B*, 35(13):7203–7206, 1987.
- [130] J. M. Tranquada, S. M. Heald, A. R. Moodenbaugh, and M. Suenaga. *Physical Review B*, 35(13):7187–7190, 1987.
- [131] A. Bianconi, N. L. Saini, A. Lanzara, M. Missori, R. Rossetti, H. Oyanagi, H. Yamaguchi, K. Oka, and T. Ito. *Physical Review Letters*, 76(18):3412, 1996.

- [132] N. L. Saini, A. Lanzara, H. Oyanagi, H. Yamaguchi, K. Oka, T. Ito, and A. Bianconi. *Physical Review B*, 55(18):12759, 1997.
- [133] S. J. L. Billinge, G. H. Kwei, and H. Takagi. *Physical Review Letters*, 72(14):2282–2285, 1994.
- [134] N. Sicron, B. Ravel, Y. Yacoby, E. A. Stern, F. Dogan, and J. J. Rehr. *Physical Review B*, 50:13168, 1994.
- [135] B. Ravel, N. Sicron, Y. Yacoby, E. A. Stern, F. Dogan, and J. J. Rehr. *Ferroelectrics*, 164:265, 1995.
- [136] B. Rechav, Y. Yacoby, E. A. Stern, and J. J. Rehr M. Newville. *Physical Review Letters*, 72(9):1352, 1994.
- [137] A. Frenkel, E. A. Stern, and F. A. Chudnovsky. *Solid State Communications*, 102:637, 1997.
- [138] A. Frenkel, F. M. Wang, S. Kelly, R. Ingalls, D. Haskel, E. A. Stern, and Y. Yacoby. *Physical Review B*, 56:10869, 1997.
- [139] E. A. Stern and Y. Yacoby. *J. Phys. Chem. Solids*, 57:1449, 1996.
- [140] Y. Yacoby and E. A. Stern. *Comments Cond. Mat. Phys.*, 18:1, 1996.
- [141] W. E. Pickett, H. Krakauer, D. A. Papaconstantopoulos, and L. L. Boyer. *Physical Review B*, 35:7252, 1987.
- [142] F. Cordero, C. R. Grandini, G. Cannelli, R. Cantelli, F. Trequattrini, and M. Ferretti. *Physical Review B*, page Scheduled for 1 March issue, 1998.
- [143] C. Friedrich, B. Büchner, M. M. Abd-Elmeguid, and H. Mickliz. *Physical Review B*, 54:R800, 1996.
- [144] D. Haskel, E. A. Stern, and H. Shechter. *Physical Review B*, Scheduled for 1 April issue, 1998.

- [145] S. D. Conradson, I. D. Raistrick, and A. R. Bishop. *Science*, 248:1394, 1990.
- [146] J. Mustre de Leon, S. D. Conradson, I. Batistic, and A. R. Bishop. *Physical Review Letters*, 65:1675, 1990.
- [147] T. Egami, B. H. Toby, S. J. L. Billinge, H. D. Rosenfeld, J. D. Jorgensen, D. G. Hinks, B. Dabrowski, M. A. Subramanian, M. K. Crawford, W. E. Farneth, and E. M. McCarron. *Physica C*, 185-189:867, 1989.
- [148] D. Haskel. In progress, 1998.
- [149] V. Polinger, D. Haskel, and E. A. Stern. To be published. 1998.
- [150] Landolt-Börnstein. *New Series*, volume 7. K-H-Hellwege, 1958.
- [151] T. Egami. *Solid State Communications*, 63:1019, 1987.
- [152] A. Lanzara, N. L. Saini, T. Rossetti, A. Bianconi, H. Oyanagi, H. Yamaguchi, and Y. Maeno. *Solid State Communications*, 97:93, 1996.
- [153] E. Sevillano, H. Meuth, and J. J. Rehr. *Physical Review B*, 20:4908–4911, 1979.
- [154] P. W. Anderson. *Science*, 279:1196, 1998.
- [155] V. J. Emery and S. A. Kivelson. *Physica C*, 209C:597, 1993.

Appendix A

MEASURING BUCKLING ANGLES WITH XAFS

In this section a detailed explanation of the method used in measuring the buckling angle θ of a nearly collinear three-atom configuration using XAFS is presented. This method self-consistently accounts for changes in half-path length of the multiple scattering paths as a function of the buckling angle, $\Delta r(\theta)$, as well as for a k -dependent correction to the effective scattering amplitude, $F_k(\theta)$.

The method was implemented in this thesis to measure the *local* tilt angle of the CuO_6 octahedra in $\text{La}_{2-x}\text{Ba}_x\text{CuO}_4$ with respect to the \hat{c} and $\hat{a}\hat{b}$ orientations, respectively.

Figure A.1 schematically represents the single and multiple scattering paths considered. For generality, the three legs involved (r_1 , r_2 and r_3) are assumed to have different lengths. The buckling angle is defined as $\theta = 180 - \widehat{ABC}$ and is allowed to change. The SS half path length, r_3 , is allowed to change as well.

The half-path length correction to the DS and TS paths is given by

$$\Delta r_{DS} = \frac{(\Delta r_1(\theta) + \Delta r_2(\theta, \Delta r_3 = 0)) + \Delta r_2(\Delta r_3, \theta = \theta_{\text{avg}}) + \Delta r_3}{2} \quad (\text{A.1})$$

$$\Delta r_{TS} = \frac{(2\Delta r_1(\theta) + 2\Delta r_2(\theta, \Delta r_3 = 0)) + 2\Delta r_2(\Delta r_3, \theta = \theta_{\text{avg}})}{2} \quad (\text{A.2})$$

where the change in r_2 depends on both θ and Δr_3 and was treated above in the spirit of partial derivatives,

$$\delta r_2 = \left. \frac{\partial r_2}{\partial \theta} \right|_{\Delta r_3=0} \delta \theta + \left. \frac{\partial r_2}{\partial r_3} \right|_{\theta=\theta_{\text{avg}}} \delta r_3 \quad (\text{A.3})$$

We first derive the term $\Delta r_2(\Delta r_3, \theta = \theta_{\text{avg}})$. Using the law of cosines,

$$r_3^2 = r_1^2 + r_2^2 - 2r_1r_2\cos(180 - \theta_{\text{avg}}) \quad (\text{A.4})$$

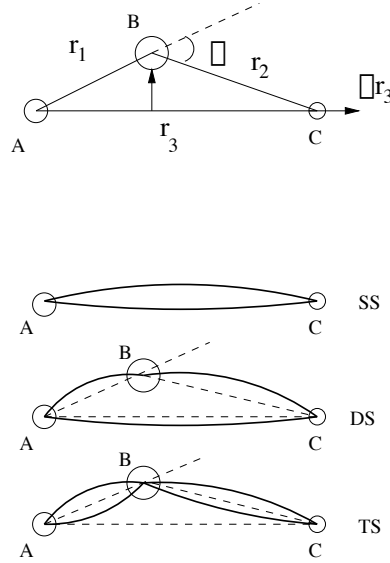


Figure A.1: Schematic representation of nearly collinear multiple scattering paths.

For a given change Δr_3 ,

$$(r_3 + \Delta r_3)^2 = r_1^2 + (r_2 + \Delta r_2)^2 + 2r_1(r_2 + \Delta r_2)\cos\theta_{\text{avg}} \quad (\text{A.5})$$

Substituting eq. A.4 into eq. A.5 and neglecting second order corrections to Δr we obtain

$$\Delta r_2 \Big|_{\theta=\theta_{\text{avg}}} = \frac{r_3 \Delta r_3}{(r_2 + r_1 \cos\theta_{\text{avg}})} \quad (\text{A.6})$$

where r_1 , r_2 , r_3 and θ_{avg} in eq. A.6 are fixed to their values in the average structure to be used as the theoretical standard in FEFFIT.

The parameterization of $\Delta r_{1,2}(\theta)$ is done by geometrical construction of modified MS paths with different buckling angles. For this purpose, atoms A and C are left fixed at their average positions and atom B is moved (usually perpendicular to AC direction) by five different arbitrary amounts corresponding to θ values in the range $[0^\circ, 15^\circ]$. r_1 and r_2 are recorded as function of θ . What we are interested in is the *change* in distance with buckling angle *relative* to the average structure value, which is going to be used as our fitting standard in FEFFIT. We then obtained the *change* $\Delta r_{1,2}(\theta)$ from the average structure value; i.e., $\Delta r_{1,2}(\theta = \theta_{\text{avg}}) = 0$. We fit these values to an expression of the form $\Delta r_{1,2} = \alpha_{1,2}\theta^{y_{1,2}} + \beta_{1,2}$. If, by construction,

Table A.1: First leg length r_1 as function of θ and its deviation from the average structure, Δr_1 .

θ (degrees)	r_1 (Å)	Δr_1 (Å)
0	1.8910	$-2.55 \cdot 10^{-3}$
3	1.8916	$-1.90 \cdot 10^{-3}$
5.9	1.8935	0
10	1.8982	$4.70 \cdot 10^{-3}$
15	1.9073	0.0138

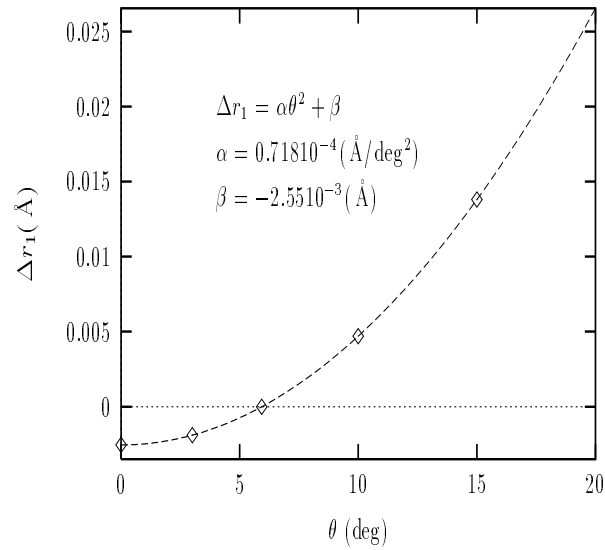
the simulated distortion of the B atom \vec{d}_B ($\vec{r}_{B'} = \vec{r}_{B,\text{avg}} + \vec{d}_B$) leads to a three atom configuration that has the symmetry $\vec{d}_B \rightarrow -\vec{d}_B$, then the lowest order is quadratic in θ and $y_{1,2} = 2$.

Figure A.2 shows such a parameterization for $\Delta r_1(\theta)$ for the nearly in-plane, collinear multiple scattering path Cu-O(1)-Cu in $\text{La}_{1.875}\text{Ba}_{0.125}\text{CuO}_4$ at 10K, where $\theta_{\text{avg}} = 5.9^\circ$ and the Cu-Cu distance is 3.7819 Å. The intervening O(1) atom was arbitrarily moved perpendicular to the Cu-Cu direction corresponding to the different buckling angles shown in table A. In this case $r_1 = r_2$, but in general each leg has to be parameterized separately.

In what follows the parameterization of $F_k(\theta)$ is detailed. The overall idea is to use FEFF6 theory to calculate the effective scattering amplitude for three different, artificial, atomic configurations corresponding to three different θ 's: the average structure value plus two others. This is obtained by changing the atomic coordinates of the intervening atom in the file *paths.dat* to the values corresponding to the particular θ 's of interest and running the third module of FEFF6 (mfeff) using the altered *paths.dat*. Only the relevant DS and MS paths need to be left in *paths.dat*. The same *phase.bin* file obtained by FEFF6 using the atomic coordinates of the average structure is used for the three different angles; i.e., the overlapped-atomic potentials are assumed to be the same for the three cases.

Figures A.3 and A.4 show two *paths.dat* files corresponding to the average structure value, $\theta = 5.9^\circ$, and to the modified $\theta = 14^\circ$, respectively, for the Cu-O(1)-Cu DS and TS paths discussed above.

In this way, $F_k(\theta_i)$'s are obtained for the three different configurations (third

Figure A.2: Parameterization of Δr_1 as function of θ .

LaBaCu0, x=0.125 LTT average structure from Katano et.al
 Rmax 6.9767, keep limit 0.000, heap limit 0.000 Feff 6.01a
 Plane wave chi amplitude filter 2.50%

```

-----
20   3   4.000  index, nleg, degeneracy, r= 3.7844
      x         y         z      ipot  label      rleg      beta
2.674190  2.674190  0.000000  3  'Cu   '      3.7819  177.0351
1.337090  1.337090  0.097940  1  'O    '      1.8935   5.9299
0.000000  0.000000  0.000000  0  'Cu   '      1.8935  177.0350
24   4   2.000  index, nleg, degeneracy, r= 3.7869
      x         y         z      ipot  label      rleg      beta
-1.337090 -1.337090 -0.097940  1  'O    '      1.8935   5.9299
-2.674190 -2.674190  0.000000  3  'Cu   '      1.8935  180.0000
-1.337090 -1.337090 -0.097940  1  'O    '      1.8935   5.9299
0.000000  0.000000  0.000000  0  'Cu   '      1.8935  180.0000
  
```

Figure A.3: *paths.dat* file corresponding to $\theta_{\text{avg}} = 5.9^\circ$

```

LaBaCuO, x=0.125 LTT structure modified from Katano et.al
Rmax 6.9767, keep limit 0.000, heap limit 0.000      Feff 6.01a
Plane wave chi amplitude filter 2.50%
-----
20   3   4.000  index, nleg, degeneracy, r= 3.7961
   x         y         z      ipot  label      rleg      beta
2.674190   2.674190   0.000000   3 'Cu    '      3.7819  173.0000
1.337090   1.337090   0.232180   1 'O     '      1.9052  14.0000
0.000000   0.000000   0.000000   0 'Cu    '      1.9052  173.0000
24   4   2.000  index, nleg, degeneracy, r= 3.8103
   x         y         z      ipot  label      rleg      beta
-1.337090  -1.337090  -0.232180   1 'O     '      1.9052  14.0000
-2.674190  -2.674190   0.000000   3 'Cu    '      1.9052  180.0000
-1.337090  -1.337090  -0.232180   1 'O     '      1.9052  14.0000
0.000000   0.000000   0.000000   0 'Cu    '      1.9052  180.0000

```

Figure A.4: *paths.dat* file corresponding to $\theta_{\text{avg}} = 14.0^\circ$

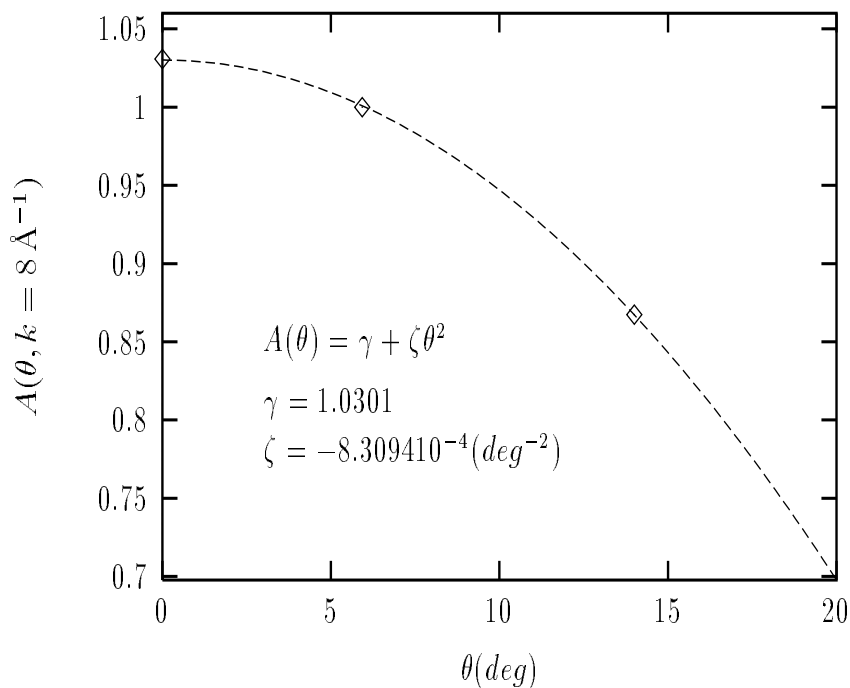


Figure A.5: Parameterization of $A(\theta, k = 8 \text{ \AA}^{-1})$ as a function of θ for the DS path.

column in corresponding *feffxxx.dat* files). What we are interested in is to construct a correction to the DS and TS paths of the *average* structure configuration to be used as the standard in the fit. Hence, the average structure's effective scattering amplitude has to be multiplied by $A(\theta, k) = F_k(\theta) / F_k(\theta_{\text{avg}})$ so the correction is 1 if $\theta = \theta_{\text{avg}}$. The correction $A(\theta, k)$ is obtained by fitting the three values $A(\theta_i, k_j)$ ($i = 1, 2, 3$) to an expression of the form $A(\theta, k_j) = (\gamma_{k_j} + \zeta_{k_j}\theta^m)$ for each value of k_j . As before, the lowest order is quadratic in θ ($m = 2$) if the three atom configuration is symmetric under $\vec{d}_B \rightarrow -\vec{d}_B$.

Figure A.5 shows such a parameterization for the DS path Cu-O(1)-Cu considered above ($\theta_{\text{avg}} = 5.9^\circ$) as obtained for $k = 8 \text{ \AA}^{-1}$. FEFF6 calculation was performed for $\theta = 0^\circ$ and $\theta = 14^\circ$ in addition to θ_{avg} . The parameterization is done for every value of k in the *feffxxx.dat* files and $\gamma(k)$, $\zeta(k)$ are obtained. The procedure is then repeated for the TS path and the same functional form of $A(\theta)$ is used (the next leading term, $\mathcal{O}(\theta^4)$, can be shown to be small). The k -dependent coefficients γ and ζ will of course be different for the DS and TS paths.

Figure A.6 shows $\gamma(k)$ and $\zeta(k)$, respectively, obtained for the DS path mentioned above.

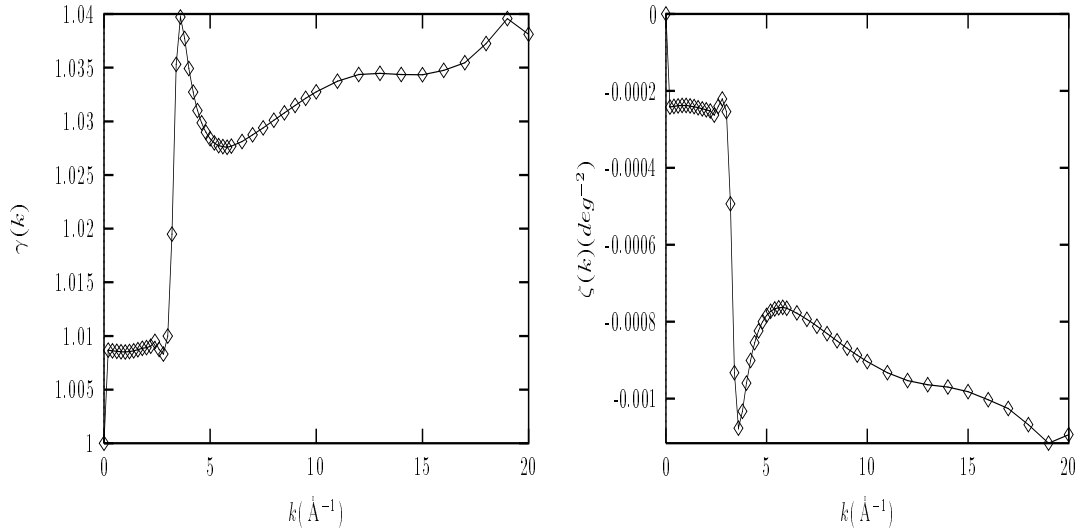


Figure A.6: $\gamma(k)$ and $\zeta(k)$, as defined in the text, as obtained for the Cu-O(1)-Cu DS path.

The modified effective scattering amplitude to be used in the fit has the form

$$F_k(\theta) = F_{k,\theta_{avg}} A_k(\theta) = F_{k,\theta_{avg}} [(\gamma_k + \zeta_k \theta^2)] \quad (\text{A.7})$$

In order to introduce the k -dependent correction into FEFFIT, the θ -independent and θ -dependent terms were considered separately. Instead of using a single PATH paragraph for the DS and TS paths, each was split into two PATH paragraphs. The theoretical standard used in the first PATH is modified such that its effective scattering amplitude (column 3 in *feffxxx.dat*) is replaced by $F_{k,\theta_{avg}} \gamma_k$ while that for the second PATH is replaced by $F_{k,\theta_{avg}} \zeta_k$. The amplitude of the second PATH is then multiplied by the parameter θ^2 which is varied in the fit (the amplitude is varied via the PATH parameter S_0^2).

The relevant portions of the *feffit.inp* file are shown in figures A.7& A.8.

To end this section, I plot in figures A.9& A.10 the θ dependence of the effective scattering amplitude, F_k , and of the effective scattering phase, $\phi_b(k)$. The method used here neglects the change in $\phi_b(k)$ with θ (the overall XAFS phase for a Gaussian distribution of atoms about an effective mean distance r_{eff} from the central atom is given by $\phi(k) = 2kr_{eff} + 2\phi_c(k) + \phi_b(k)$, where $\phi_c(k)$ is the central atom phase shift). For example, the change in $\phi_b(k = 8 \text{ \AA}^{-1})$ for the Cu-O(1)-Cu and Cu-O(2)-La

```

% LaBaCu0 x=0.125 Cu K-edge ab- polarization 10K
% using polarized theory, data april 97.
% Theory is Katano at 15K for x=0.125 LTT structure
set sigmm= 0.00052  !! McMaster correction
set amplitude=0.94
set e0=-3.3
guess ein =200 !Einstein temperature for Cu-Cu
guess off =0
guess theta = 6
set h=0.00255
set i=3.782
set j=1.8935
set ct= 0.0000718*( theta^2 )
%SS in plane Cu-Cu
guess dr5=0.0
%DS in plane Cu-O(1)-Cu
set dr11= ( 2*(ct - h) + (i*dr5)/(j* (1+cos(5.93*pi/180))) + dr5 )/2
set dr94=dr11
%TS in plane Cu-O(1)-Cu
set dr15= ( 2*(ct - h) + (i*dr5)/(j* (1+cos(5.93*pi/180))) )
set dr95=dr15
%Cu-Cu MS in plane
set ss5= eins2(10,ein,31.773) + off
set ss11=ss5
set ss94=ss11
set ss15=ss5
set ss95=ss15

!!&& program: "feffit"

```

Figure A.7: Relevant portion of the *feffit.inp* file containing variables used in fitting the buckling angle (θ) about the \widehat{ab} plane in $\text{La}_{2-x}\text{Ba}_x\text{CuO}_4$.


```

e0 0 e0
s02 0 amplitude
path 5 feff0014.dat
id 5 Cu-Cu SS deg=4.000 r_eff=3.782
delr 5 dr5
sigma2 5 ss5 + sigmm
path 11 dscons.dat
id 11 Cu-Cu-0(1) DS deg=4.000 r_eff=3.784
delr 11 dr11
sigma2 11 ss11 + sigmm
path 94 dsthet.dat
id 94 Cu-Cu-0(1) deg=4.000 r_eff=3.784
delr 94 dr94
sigma2 94 ss94 + sigmm
s02 94 amplitude*(theta^2)
path 15 tscons.dat
id 15 Cu-0(1)-Cu-0(1) TS deg=2.000 r_eff=3.787
delr 15 dr15
sigma2 15 ss15 + sigmm
path 95 tsthet.dat
id 95 Cu-0(1)-Cu-0(1) TS deg=2.000 r_eff=3.787
delr 95 dr95
sigma2 95 ss95 + sigmm
s02 95 amplitude*(theta^2)

!!&& program: "generic"

```

Figure A.8: Relevant portion of the *feffit.inp* file containing PATH paragraphs used in fitting the buckling angle (θ) about the \hat{ab} plane in $\text{La}_{2-x}\text{Ba}_x\text{CuO}_4$. FEFF6 theoretical standards for the DS and TS paths are modified as described in the text.

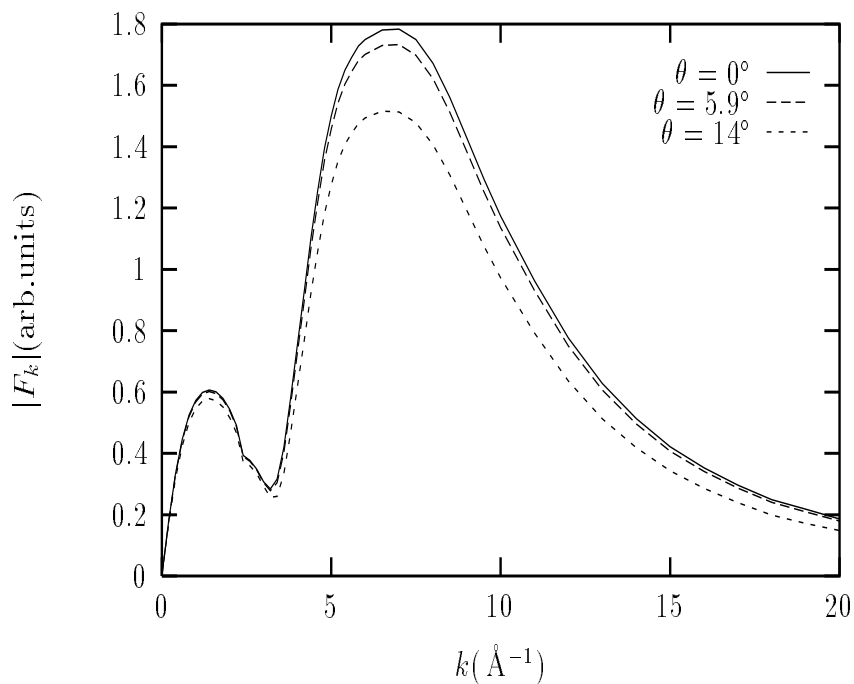


Figure A.9: F_k dependence on θ for the Cu-O(1)-Cu DS path.

DS paths when the buckling angle changes from $6\text{-}7^\circ$ to $14\text{-}15^\circ$ is about 0.1 radians, corresponding to a change in distance of about $\Delta r \approx 0.005 \text{ \AA}$ (what is relevant to distance determination is the change in *slope* of $\phi_b(k)$, but this gives a good estimate). To check the effect of neglecting the θ dependence of $\phi_b(k)$, fits were performed separately by using $\phi_b(k, \theta = \theta_{\text{avg}})$ or $\phi_b(k, \theta = 14 - 15^\circ)$ as calculated by FEFF6 for the different buckling angles. The measurement of θ did not change but the measurement of the distance was offset by about $\sim 0.003 - 0.006 \text{ \AA}$ for Cu-O(1)-Cu and Cu-O(2)-La, respectively. The method here is then reliable for buckling angle determination (for angles $0 \leq \theta \leq 20$) but has a limit on distance determination to within about $r \approx 0.006 \text{ \AA}$.

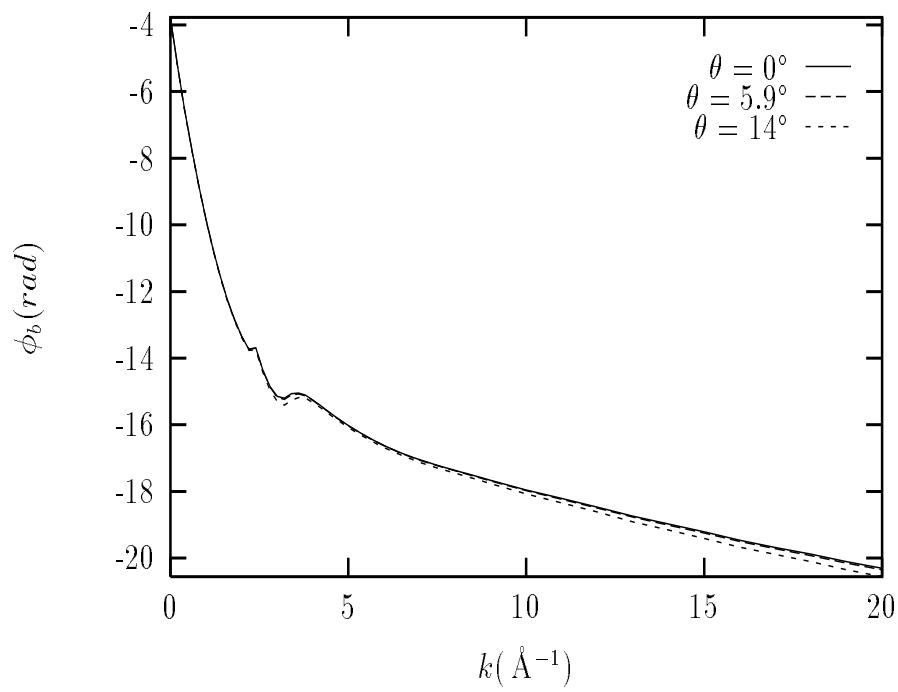


Figure A.10: ϕ_k dependence on θ for the Cu-O(1)-Cu DS path.

Appendix B

ANGULAR AVERAGING IN XAFS

In this appendix different angular averages of the dipole interaction term, $\langle \hat{r} \cdot \hat{e} \rangle_{\theta, \phi}$ are obtained which are pertinent to the experimental situation found in our oriented-powder experiments, i.e., powder which is oriented along the \hat{c} -axis but is random in the $\hat{a}\hat{b}$ orientation. In particular relations are derived between the XAFS of a completely random powder, χ_{ran} , and the polarized XAFS χ_c and χ_{ab} measured in the experiments on the magnetically-aligned powder.

Most of the following section is based on AQM of Sakurai, SSP chapter Hayes and Boyce, Schiff QM. We start by deriving the expression for the absorption cross section for the process of interest in XAFS, i.e., the excitation of a deep core electron by an X-ray photon. The absorption coefficient, $\mu(E)$, is given by

$$I(E) = I_0(E)e^{-\mu(E)x} \quad (\text{B.1})$$

where $I(E)$ and $I_0(E)$ are the intensities of the transmitted and incoming beams and x is the thickness of the sample. $\mu(E)$ contains the contribution to the absorption of all atoms in the crystal

$$\mu(E) = \sum_i n_i \sigma_i(E) \quad (\text{B.2})$$

with n_i the number of atoms of type i per unit volume and $\sigma_i(E)$ their contribution to the cross section.

The transition rate (probability per unit time) for a X-ray induced absorption in which the system goes from an initial, bound state $|i\rangle = |i, n_{\vec{k}, \alpha}\rangle$ to an unbound final state $|f\rangle = |f, (n_{\vec{k}, \alpha} - 1)\rangle$ is given by Fermi's Golden Rule [86]

$$\Omega_{i \rightarrow f}(\omega) = \frac{2\pi}{\hbar} |\langle f | H_I | i \rangle|^2 \delta(E_f - E_i - \hbar\omega) \rho(E_f). \quad (\text{B.3})$$

Here H_I is the interaction Hamiltonian between the radiation field and the atomic core electron; $\rho(E_f)$ is the density of unoccupied states at the final energy E_f ; $\hbar\omega$ is

the energy of the incoming photon which satisfies $E_f - E_i = \hbar\omega$. $n_{\vec{k},\alpha}$ is the number of photons with wave number \vec{k} and polarization α .

The cross section is the transition rate normalized by the incoming photon flux;

$$\sigma(\omega) = \frac{\Omega(\omega)}{nc} \quad (\text{B.4})$$

with n the number of photons per unit volume and c the velocity of light.

The interaction of the radiation field and the electrons is obtained by modifying the electron momentum; $\vec{p} \rightarrow \vec{p} - e\vec{A}/c$, where \vec{A} is the quantized radiation field given by

$$\vec{A}(\vec{r}, t) = \frac{1}{\sqrt{V}} \sum_{\vec{k}} \sum_{\alpha} c\sqrt{2\pi\hbar/\omega} [a_{\vec{k},\alpha}(t)\vec{\epsilon}^{(\alpha)} e^{i\vec{k}\cdot\vec{r}} + a_{\vec{k},\alpha}^{\dagger}(t)\vec{\epsilon}^{(\alpha)} e^{-i\vec{k}\cdot\vec{r}}] \quad (\text{B.5})$$

where $a_{\vec{k},\alpha}^{\dagger}, a_{\vec{k},\alpha}$ are creation and annihilation operators which create and annihilate photons with wave number \vec{k} and polarization α . $\vec{\epsilon}^{(\alpha)}, \alpha = 1, 2$ are linear polarization unit vectors perpendicular to \vec{k} (transverse field) which form an orthogonal basis to describe the polarization state of the photon.

The single particle Hamiltonian describing the deep core electron and its interaction with the X-ray field is given by

$$H = H_0 + H_I = \frac{1}{2m} \left(\vec{p} - \frac{e\vec{A}}{c} \right)^2 + V(\vec{r}) \quad (\text{B.6})$$

with $V(\vec{r})$ being the electrostatic potential binding the electron to the atom. The perturbation introduced by the field, H_I , is then given by

$$H_I = \left[\frac{-e}{2mc} (\vec{p} \cdot \vec{A}(\vec{r}, t) + \vec{A}(\vec{r}, t) \cdot \vec{p}) + \frac{e^2}{2mc^2} \vec{A}(\vec{r}, t) \cdot \vec{A}(\vec{r}, t) \right] \quad (\text{B.7})$$

The commutation relations $[x, p_x] = i\hbar$ can be generalized to $[x^n, p_x] = ni\hbar x^{n-1}$ and even further to

$$[f(\vec{r}), p_x] = i\hbar \frac{\partial}{\partial x} f(\vec{r}). \quad (\text{B.8})$$

Using the relations given in eq. B.8 one has $\vec{p} \cdot \vec{A} = \vec{A} \cdot \vec{p} - i\hbar \vec{\nabla} \cdot \vec{A}$. However, because of the transversality condition (Coulomb gauge) $\nabla \cdot \vec{A} = 0$ and we obtain

$$H_I = \left[\frac{-e}{mc} (\vec{A}(\vec{r}, t) \cdot \vec{p}) + \frac{e^2}{2mc^2} \vec{A}(\vec{r}, t) \cdot \vec{A}(\vec{r}, t) \right] \quad (\text{B.9})$$

When evaluating the matrix element $\langle f, (n_{\vec{k}, \alpha} - 1) | H_I | i, n_{\vec{k}, \alpha} \rangle$ given in eq. B.3, with H_I given in eq. B.9 and $\vec{A}(\vec{r}, t)$ given in eq. B.5, it is clear that only the term in \vec{A} containing the annihilation operator $a_{\vec{k}, \alpha}(t)$ leads to a non-zero matrix element. The term $(\vec{A} \cdot \vec{A})$ in H_I does not contribute to the absorption either since it changes the total number of photons by 0 or ± 2 .

The matrix element then becomes

$$\begin{aligned} \langle f, (n_{\vec{k}, \alpha} - 1) | H_I | i, n_{\vec{k}, \alpha} \rangle &= \frac{-e}{mc} \langle f, (n_{\vec{k}, \alpha} - 1) | \sqrt{\frac{2\pi\hbar c^2}{\omega V}} a_{\vec{k}, \alpha}(0) e^{i\vec{k} \cdot \vec{r} - i\omega t} \vec{p} \cdot \vec{\epsilon}^{(\alpha)} | i, n_{\vec{k}, \alpha} \rangle \\ &= \frac{-e}{m} \sqrt{\frac{2\pi\hbar n_{\vec{k}, \alpha}}{\omega V}} \langle f | e^{i\vec{k} \cdot \vec{r}} \vec{p} \cdot \vec{\epsilon}^{(\alpha)} | i \rangle e^{-i\omega t} \end{aligned} \quad (\text{B.10})$$

where the time evolution of a, a^\dagger is obtained by solving Heisenberg equation of motion to give $a_{\vec{k}, \alpha} = a_{\vec{k}, \alpha}(0) e^{-i\omega t}$; $a_{\vec{k}, \alpha}^\dagger = a_{\vec{k}, \alpha}^\dagger(0) e^{i\omega t}$. In addition the relations $a^\dagger |n\rangle = \sqrt{n+1} |n+1\rangle$ and $a |n\rangle = \sqrt{n} |n-1\rangle$ have been used to derive eq. B.10. That the state described by $a |n\rangle$ represent a state with the number of photons reduced by 1 is readily seen by applying the photon number operator N on that state; i.e., $Na |n\rangle = N\sqrt{n} |n-1\rangle = (n-1)\sqrt{n} |n-1\rangle = (n-1)a |n\rangle$.

Next we neglect the spatial variation in the amplitude of the radiation field over the dimensions on which the electron is localized. This is equivalent to assume that $\lambda_\gamma \gg r_e^-$. For hard X-rays, $\lambda = (2\pi/k) \approx 1 \text{ \AA}$, while for the relatively heavy elements studied here ($Z \gtrsim 29$), $r_e^- \sim \sqrt{\hbar/(2\omega_0 m_e)} \lesssim 0.02 \text{ \AA}$, with $\hbar\omega_0$ the binding energy of a 1s deep core electron. The dipole approximation allows us then to write

$$e^{i\vec{k} \cdot \vec{r}} = 1 + i\vec{k} \cdot \vec{r} - \frac{(\vec{k} \cdot \vec{r})^2}{2} + \dots \approx 1 \quad (\text{B.11})$$

Finally we use the commutation relations $[\vec{r}, H_0] = [\vec{r}, \vec{p}^2/(2m)] = i\hbar\vec{p}/m$ to get

$$\begin{aligned} \langle f | \vec{p} \cdot \vec{\epsilon}^{(\alpha)} | i \rangle &= \langle f | \frac{-im}{\hbar} [\vec{r}, H_0] \cdot \vec{\epsilon}^{(\alpha)} | i \rangle \\ &= \frac{-im}{\hbar} \langle f | \vec{r} \cdot \vec{\epsilon}^{(\alpha)} E_i - E_f \vec{r} \cdot \vec{\epsilon}^{(\alpha)} | i \rangle = \frac{im}{\hbar} (\hbar\omega) \langle f | \vec{r} \cdot \vec{\epsilon}^{(\alpha)} | i \rangle \end{aligned} \quad (\text{B.12})$$

Combining eqs. B.13, B.3 and B.4 we obtain the final expression for the cross section,

$$\sigma(\omega) = 4\pi^2 \alpha_{fs} \hbar \omega | \langle f | \vec{r} \cdot \vec{\epsilon}^{(\alpha)} | i \rangle |^2 \delta(E_f - E_i - \hbar\omega) \rho(E_f). \quad (\text{B.13})$$

Here $\alpha_{fs} = e^2 / (\hbar c)$ is the fine-structure constant.

In this thesis the K -shell absorption of different types of atoms in different solid-state environments has been measured ($1s$ initial state) and hence the discussion here is limited to that case. In addition, only single scattering (SS) is considered here since the relations derived at the end of this section were used to determine bond orientations from SS paths only.

The $\cos\theta$ dependence of the dipole interaction $\vec{r} \cdot \vec{\epsilon}$ together with the $1s$ initial state being spherically symmetric ($l = 0$) require for the final state $|f\rangle$ to have a $\cos\theta$ angular dependence ($l = 1, m = 0$) for the matrix element in eq. B.13 to be non-zero.

Since $|i\rangle$ is highly localized next to $\vec{r} = 0$, the overlap of $|f\rangle$ and $|i\rangle$ is only significant next to the origin. Due to the presence of neighboring atoms around the central atom being excited, the final state $|f\rangle$ next to the origin is a superposition of an outgoing wave and an incoming, backscattered, wave $|f\rangle = |f_{\text{out}}\rangle + |f_{\text{in}}\rangle$. The variation with photon energy of the interference between this two parts gives the modulation of the absorption coefficient called XAFS. Following Stern [92], the outgoing part can be represented as the real part of a Hankel function with $l = 1$,

$$|f_{\text{out}}\rangle = \text{Re}[h_1(kr)] \cos\theta = \text{Re}\left[\frac{e^{ikr}}{kr} + \frac{ie^{ikr}}{(kr)^2}\right] \cos\theta \quad (\text{B.14})$$

whereas the backscattering part can be written as

$$|f_{\text{in}}\rangle = \text{Re}[i(h_1(kr))(h_1^2(kr_j)) f(\pi) \cos\theta 3\cos^2\theta_j e^{2i\delta_1}]. \quad (\text{B.15})$$

\vec{r}_j denotes the position of the scattering atom; $f(\pi)$ the backscattering amplitude; $\theta_j = \cos^{-1}\hat{\epsilon} \cdot \hat{r}_j$ the angle between the polarization vector of the X-rays and \hat{r}_j (the absorbing atom is at the origin); δ_1 the scattering phase shift of the $l = 1$ component of the partial wave decomposition of the scattered wave.

The final state is then given by

$$|f \rangle = \text{Re} \left[h_1(kr) \cos\theta [1 + i h_1^2(kr_j) 3 \cos^2\theta_j f(\pi) e^{2i\delta_1}] \right] \quad (\text{B.16})$$

The modulation to the absorption coefficient, within the single scattering approximation, is obtained by substituting the expression for $|f \rangle$ into eq. B.13 to obtain,

$$\mu(k) = \mu_0(k)[1 + \chi(k)] = [1 - \text{Im} \sum_j h_1^2(kr_j) 3(\hat{\epsilon} \cdot \hat{r}_j)^2 f(\pi) e^{2i\delta_1}] \quad (\text{B.17})$$

where μ_0 is the absorption coefficient of the embedded central atom without the scattering correction and a sum over all neighboring atoms, j , was added. It is worth noting that μ was defined in eq. B.2 as a sum over contributions of all types of atoms present in the sample. In the actual experiment, however, the energy is varied across the 1s excitation threshold of a particular element (central atom). Below that threshold the absorption is due to other atoms and other edges of the central atom. These contributions, however, are smoothly varying across the absorption edge of interest and can be subtracted to obtain the contribution to the absorption of the edge of interest in the atom of interest.

The term $(\hat{\epsilon} \cdot \hat{r}_j)^2$ appearing in $\chi(k)$ is what we are interested in here. The polarization dependence of the XAFS is all given by this term. In what follows we derive relations between the XAFS of a randomly oriented sample (polycrystal) and the polarized XAFS measured in our oriented samples. As mentioned before, our magnetically aligned powder is oriented along the \hat{c} axis but random in the $\hat{a}\hat{b}$ orientation. As shown in figure B.1, a neighboring atom A is located at $\vec{r}_A = r(\sin\theta_A \cos\phi_A, \sin\theta_A \sin\phi_A, \cos\theta_A)$. The polarization vector (electric field) is represented by $\vec{E} = E(\sin\theta \cos\phi, \sin\theta \sin\phi, \cos\theta)$. The synchrotron radiation used in our experiments is linearly polarized in the plane of the orbit. At the experimental station, the direction of the electric field is fixed and what varies is the orientation of the sample relative to the field. For simplicity, we will assume the sample orientation is fixed and we will average over the electric field orientation. These two scenarios are equivalent.

$$\int_{\pi}^0 d\cos\theta (1 - \cos^2\theta) = \frac{4}{3}; \int_{-\phi_A}^{2\pi-\phi_A} \cos^2\phi' d\phi' = \pi; \int_{-\phi_A}^{2\pi-\phi_A} \cos\phi' d\phi' = 0 \quad (\text{B.20})$$

we obtain

$$\chi_{\text{ran}} \propto \frac{1}{4\pi} \left[\frac{4\pi}{3} \sin^2\theta_A + 0 + \frac{4\pi}{3} \cos^2\theta_A \right] = \frac{1}{3} \quad (\text{B.21})$$

For the \hat{c} -axis polarized XAFS, the electric field vector is given by $E = E(0, 0, \hat{z})$ (see fig. B.1) and we have

$$\chi_c \propto \left\langle (\hat{E} \cdot \hat{r}_A)^2 \right\rangle_{\theta, \phi} = \cos^2\theta_A \quad (\text{B.22})$$

For the \hat{ab} polarized XAFS, the electric field is randomly oriented in the \hat{ab} plane and given by $E = E(\cos\phi, \sin\phi, 0)$ (fig. B.1); then

$$\begin{aligned} \chi_{\text{ab}} \propto \left\langle (\hat{E} \cdot \hat{r}_A)^2 \right\rangle_{\theta, \phi} &= \left\langle (\cos\phi \sin\theta_A \cos\phi_A + \sin\theta_A \sin\phi_A \sin\phi)^2 \right\rangle_{\theta, \phi} \\ &= \left\langle \sin^2\theta_A \cos^2(\phi - \phi_A) \right\rangle_{\theta, \phi} \end{aligned} \quad (\text{B.23})$$

The integral to evaluate is then

$$\chi_{\text{ab}} \propto \frac{1}{4\pi} \sin^2\theta_A \int_0^{2\pi} \int_0^{\pi} \sin\theta d\theta d\phi \cos^2(\phi - \phi_A) = \frac{\sin^2\theta_A}{2} \quad (\text{B.24})$$

Summarizing, for single scattering K -edge XAFS, the relations between the XAFS of a randomly oriented powder and the polarized XAFS measured in our \hat{c} -axis oriented powder (randomly oriented in the \hat{ab} -plane) are given by

$$\begin{aligned} \chi_c &= 3 \cos^2\theta_A \chi_{\text{ran}} \\ \chi_{\text{ab}} &= 3 \frac{\sin^2\theta_A}{2} \chi_{\text{ran}} \end{aligned} \quad (\text{B.25})$$

These relations were used in the Sr K -edge XAFS analysis of $\text{La}_{2-x}\text{Sr}_x\text{CuO}_4$ to find out the angle formed by some bonds with the \hat{c} axis. As is shown in this thesis,

Sr introduces severe distortions in the nearest neighbors oxygen environment. If the angles sustained by some bonds (with respect to the \hat{c} -axis) are different than the ones derived from the average structure atomic positions, a FEFF6 calculation of polarized XAFS using those positions will be incorrect and errors in the amplitude of the XAFS will be introduced. We therefore used a random FEFF6 calculation and corrected it for polarization effects by fitting simultaneously both \hat{c} and \hat{ab} polarized XAFS while correcting the amplitude of some single scattering paths using eq. B.25 and varying θ_A . The simultaneous refinement helps not only in reducing the number of variables in the fit but ensures self consistency of the answer, i.e., for bonds that contribute to both polarizations the optimized angle should best fit both \hat{c} and \hat{ab} polarized XAFS.

Appendix C

XAFS DEBYE WALLER FACTORS

In this section we derive some useful relations between the σ^2 's of some SS paths and those of the collinear, focussing, MS paths involving the same atoms from which SS occurs. The different paths considered are schematically represented in figure C.1 where the c -suffix denotes the central atom position along the path. The atomic labeling corresponds to paths encountered in the Cu K -edge $\hat{a}\hat{b}$ polarized XAFS of $\text{La}_{2-x}(\text{Sr},\text{Ba})_x\text{CuO}_4$ but the relations derived here apply in general for similar scattering geometries.

Consider, e.g., the SS_3 path $\text{Cu}_c \rightarrow \text{Cu}_3 \rightarrow \text{Cu}_c$, where the index 3 stands for third near neighbor. If the *equilibrium* position of the Cu_3 is denoted by \vec{r}_0 (relative to the central atom) while its *instantaneous* position is denoted by \vec{r}_i , then the mean square deviation in *half path length* about the average position is

$$\left\langle (\vec{r}_i - \vec{r}_0)^2 \right\rangle_i \equiv \sigma_{\text{SS}_3}^2 \quad (\text{C.1})$$

where $\langle \rangle_i$ indicates an average over a given distribution of atoms in the third shell (e.g., gaussian) about the equilibrium half path length distance. It is worth noting that since XAFS is so fast (core hole-lifetime $\sim 10^{-15}$ sec) compared to lattice times (10^{-13} sec), for each absorption event (each core-hole production) XAFS will measure

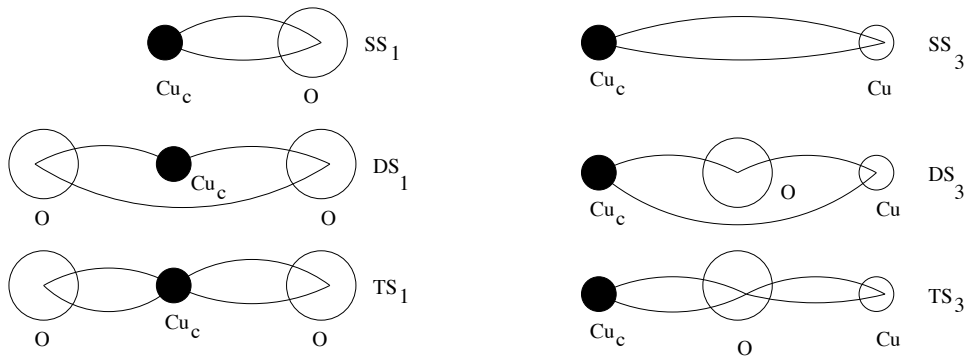


Figure C.1: Schematic representation of SS and collinear, focussing MS paths for which σ^2 relations were derived.

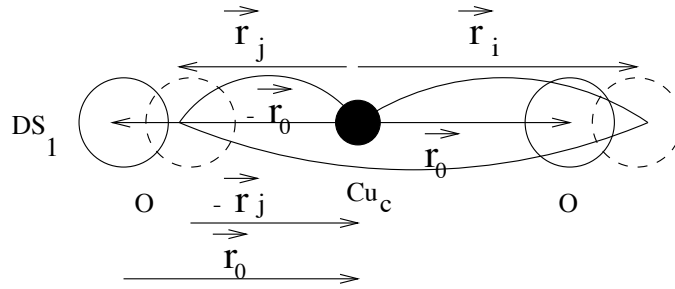


Figure C.2: Average and instantaneous positions of atoms used to determine $\sigma_{\text{DS}_1}^2$.

the instantaneous distribution of atoms in the j^{th} -shell. Each energy-point measurement of the absorption coefficient, however, is composed of at least 10^6 such events and hence a configurational average over all participating central atoms is obtained.

Consider the double scattering (DS_3) collinear MS path $\text{Cu}_c \rightarrow \text{Cu}_3 \rightarrow \text{O}_1 \rightarrow \text{Cu}_c$. If the instantaneous position of the O atoms is denoted by \vec{r}_l , then

$$\sigma_{\text{DS}_3}^2 = \left\langle \left(\frac{\vec{r}_i - \vec{r}_0 + \vec{r}_i - \vec{r}_l - \vec{r}_0/2 + \vec{r}_l - \vec{r}_0/2}{2} \right)^2 \right\rangle_{il} = \left\langle (\vec{r}_i - \vec{r}_0)^2 \right\rangle_i = \sigma_{\text{SS}_3}^2. \quad (\text{C.2})$$

In the case at hand (DS_3 , TS_3) the O atoms are, on the average, halfway between the Cu atoms. The same relation derived here holds, however, for an intervening atom *anywhere* in between the end atoms since the total path length is constant irrespective of the position of the intervening atom; the only assumption in eq. C.2 is collinearity of the three atoms involved.

In the same way as described above, it can be shown that $\sigma_{\text{TS}_3}^2 = \sigma_{\text{DS}_3}^2 = \sigma_{\text{SS}_3}^2$ where TS_3 stands for the triple scattering path $\text{Cu}_c \rightarrow \text{O}_1 \rightarrow \text{Cu}_3 \rightarrow \text{O}_1 \rightarrow \text{Cu}_c$.

For the DS_1 focusing MS path $\text{Cu}_c \rightarrow \text{O}_1 \rightarrow \text{O}_1 \rightarrow \text{Cu}_c$, however, correlations between the displacements of the oxygen atoms at the ends of the path might be important.

As schematically shown in figure C.2, if the instantaneous positions of the oxygen atoms at the ends of the path are \vec{r}_i and \vec{r}_j and their average positions are \vec{r}_0 and $-\vec{r}_0$

(assuming there is inversion symmetry about Cu_c), the $\sigma_{\text{DS}_1}^2$ for this path is given by

$$\begin{aligned} & \left\langle \left(\frac{\vec{r}_i - \vec{r}_0 + \vec{r}_i - \vec{r}_j - 2\vec{r}_0 - \vec{r}_j - \vec{r}_0}{2} \right)^2 \right\rangle_{ij} = \\ & \left\langle (\vec{r}_i - \vec{r}_0)^2 \right\rangle_i + \left\langle (\vec{r}_j + \vec{r}_0)^2 \right\rangle_j - 2 \left\langle (\vec{r}_i - \vec{r}_0) \cdot (\vec{r}_j + \vec{r}_0) \right\rangle_{ij} = \\ & 2 \cdot \sigma_{\text{SS}_1}^2 - 2 \left\langle (\vec{r}_i - \vec{r}_0) \cdot (\vec{r}_j + \vec{r}_0) \right\rangle_{ij} \end{aligned} \quad (\text{C.3})$$

where $\sigma_{\text{SS}_1}^2$ is the mean square disorder for path SS_1 . If the displacements of the end atoms are 100% correlated (i.e., in phase motion where $\vec{r}_i - \vec{r}_0 \parallel \vec{r}_j + \vec{r}_0$) and in addition, the size of displacement is the same for both end atoms ($|\vec{r}_i - \vec{r}_0| = |\vec{r}_j + \vec{r}_0|$, which holds for the case of inversion symmetry about Cu_c), we obtain $\sigma_{\text{DS}_1}^2 = 2\sigma_{\text{SS}_1}^2 - 2\sigma_{\text{SS}_1}^2 = 0$. Vibrational modes for which the *instantaneous* total path length remains unchanged do not contribute to the mean square displacement. XAFS, then, probes the vibronic spectrum in a distinct manner, i.e., it is less sensitive to long wavelength modes in which atoms move in phase with each other.

If the motion of the end atoms, however, is uncorrelated, then the average over the dot product of the vector displacements is zero and we obtain $\sigma_{\text{DS}_1}^2 = 2\sigma_{\text{SS}_1}^2$.

In the same way, it can be shown that $\sigma_{\text{TS}_1}^2 = \sigma_{\text{DS}_1}^2$, where the path TS_1 is shown in figure C.1.

To end this chapter, the difference between the Debye-Waller factors (DWF) measured in Diffraction experiments (u^2) and those measured in XAFS (σ^2) is emphasized. Figure C.3 shows the average atomic positions (lattice sites) represented by \vec{r}_i, \vec{r}_j and the instantaneous positions denoted by \vec{r}'_i, \vec{r}'_j .

In a diffraction experiment, the mean square displacement of each atomic species about their average lattice site is measured. The diffraction DWF's for atoms i, j are then given by

$$\begin{aligned} u_i^2 &= \left\langle (\vec{r}'_i - \vec{r}_i)^2 \right\rangle_{i'} \\ u_j^2 &= \left\langle (\vec{r}'_j - \vec{r}_j)^2 \right\rangle_{j'} \end{aligned} \quad (\text{C.4})$$

where the average is done over the distribution of instantaneous positions.

XAFS measures the disorder in half path length (or equivalently in “bond length”). In single scattering the partial pair distribution function (PPDF) is measured where only pair correlations involving the central, absorbing, atom contribute to the XAFS

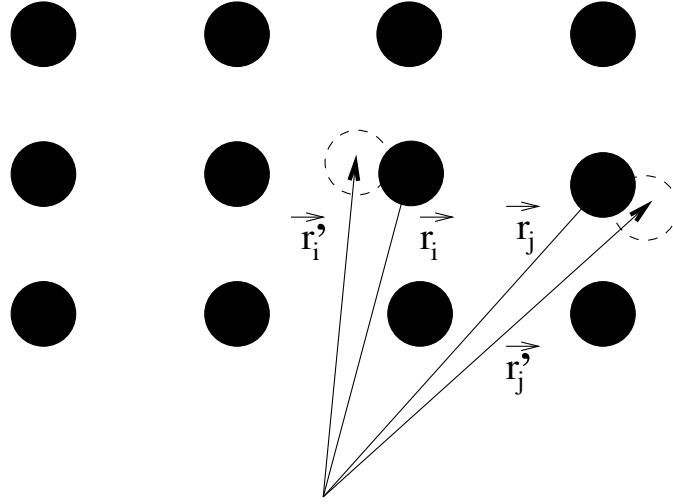


Figure C.3: Lattice sites and instantaneous positions of atoms i and j .

signal. Hence, what contributes to disorder in XAFS is the change in bond length between the central atom, i , and the scatterer, j , giving by

$$\begin{aligned}
 \sigma_{ij}^2 &= \left\langle (\vec{r}'_j - \vec{r}'_i - (\vec{r}_j - \vec{r}_i))^2 \right\rangle_{i,j'} \\
 &= \left\langle (\vec{r}'_j - \vec{r}_j - (\vec{r}'_i - \vec{r}_i))^2 \right\rangle_{i,j'} \\
 &= \left\langle (\vec{r}'_j - \vec{r}_j)^2 \right\rangle_{j'} + \left\langle (\vec{r}'_i - \vec{r}_i)^2 \right\rangle_{i'} - 2 \left\langle (\vec{r}'_j - \vec{r}_j) \cdot (\vec{r}'_i - \vec{r}_i) \right\rangle_{j',i'} \\
 &= u_i^2 + u_j^2 - 2 \left\langle \vec{u}_{i,i'} \cdot \vec{u}_{j,j'} \right\rangle_{i',j'} \tag{C.5}
 \end{aligned}$$

By combining the disorder measured by diffraction with the one measured by XAFS it is possible, in principle, to infer about the size of the correlation term in eq. C.5.

VITA

Daniel Haskel was born in Montevideo, Uruguay, on April 8, 1966 to Miriam and Elias Haskel. He moved to Israel in 1985 where he graduated with a B. A. in physics from the Technion (Israel Institute of Technology) in 1989 and with a MSc. degree in physics in 1992 from the same institution. His master's thesis was on *The effect of impurities on dynamical properties of alloys* using Mössbauer spectroscopy. He married Ileana Oreamuno, whom he met while at the Technion, in Costa Rica August 5, 1990. He started his graduate studies at the University of Washington in August 1992. His first son, Ilan, was born August 22, 1997, an event which made the last year of his student life the best ever.